NASA-CR-195532

NASW-4435

LOITA

Lunar Optical/Infrared Telescope Array

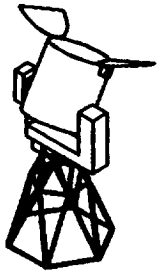

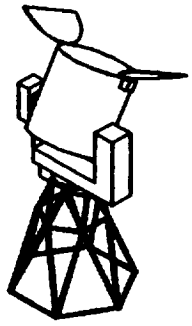

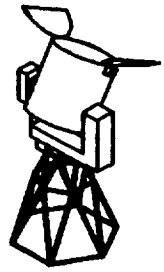

NASA/USRA Advanced Design Program

June 1993

Department of Aerospace & Ocean Engineering

Virginia Polytechnic Institute & State University

Abstract

LOITA (Lunar Optical/Infrared Telescope Array) is a lunar-based interferometer composed of 18 alt-azimuth telescopes arranged in a circular geometry. This geometry results in excellent uv coverage and allows baselines up to 5 km long. The angular resolution will be 25 micro-arcsec at 500 nm and the main spectral range of the array will be 200 to 1100 nm. For infrared planet detection, the spectral range may be extended to nearly 10 μm.

The telescope mirrors have a Cassegrain configuration using a 1.75 m dia. primary mirror and a 0.24 m dia. secondary mirror. A three-stage (coarse, intermediate, and fine) optical delay system, controlled by laser metrology, is used to equalize path lengths from different telescopes to within a few wavelengths.

All instruments and the fine delay system are located within the instrument room. Upon exiting the fine delay system, all beams enter the beam combiner and are then directed to the various scientific instruments and detectors.

The array instrumentation will consist of CCD detectors optimized for both the visible and infrared as well as specially designed cameras and spectrographs. For direct planet detection, a beam combiner employing achromatic nulling interferometry will be used to reduce star light (by several orders of magnitude) while passing the planet light.

A single telescope will be capable of autonomous operation. This telescope will be equipped with 4 instruments: Wide Field and Planetary Camera, Faint Object Camera, High Resolution Spectrograph, and Faint Object Spectrograph. These instruments will be housed beneath the telescope.

The array pointing and control system is designed to meet the fine pointing requirement of 1 micro-arcsec stability and to allow precise tracking of celestial objects for up to 12 days. During the lunar night, the optics and the detectors will be passively cooled to 70-80 K temperature. To maintain a continuous communication with the Earth a relay satellite placed at the L4 libration point will be used in conjunction with the Advanced Tracking and Data Relay Satellite System (ATDRSS). Electrical power of about 10 kW will be supplied by a nuclear reactor based on the SP-100 technology. LOITA will be constructed in 3 phases of 6 telescopes each. The total mass of the first operational phase is estimated at 58,820 kg. The cost of the fully operational 1^{ST} phase of the observatory is estimated at $8.9 billion.

LOITA's primary objectives will be to detect and characterize planets around nearby stars (up to 10 parsec away), study physics of collapsed stellar objects, solar/stellar surface features and the processes in nuclear regions of galaxies and quasars. An interferometric array such as LOITA will be capable of achieving resolutions 3 orders-of-magnitude greater than Hubble's design goal. LOITA will also be able to maintain higher signal-to-noise ratios than are currently attainable due to long observation times available on the Moon.

LOITA

Lunar Optical/Infrared Telescope Array

Project Advisors: Prof. A. Jakubowski
Aerospace & Ocean Engineering Department
Virginia Polytechnic Institute & State University

Davy A. Haynes
NASA Langley Research Center

Project Leaders: Geoffrey Pierce
Neil Thomas

Team Members

Preliminary Array Requirements:	Kevin Martin, Geoffrey Pierce, Neil Thomas
Telescope Optics:	Geoffrey Pierce
uv Coverage & Array Geometry:	Neil Thomas
Beam Control at Telescope:	Kevin Martin, Geoffrey Pierce, Neil Thomas
Delay Lines:	Geoffrey Pierce
Image Construction:	Neil Thomas
Beam Combination & Instrumentation:	Seth Chiaramonte, Sheri Davis
Planet Detection Schemes:	Seth Chiaramonte, Geoffrey Pierce
Metrology:	Neil Thomas, Kevin Wood
Pointing Control:	Kelly Matney, Greg Sheppard
Optical Structure:	Kevin Martin, Geoffrey Pierce
Telescope Structure:	David Grubb, Brian Hartt, Kevin Martin
Motors & Gears:	Marc Luek
Instrument Room:	Geoffrey Pierce
Thermal Control:	Scott Schorn
Power:	Marc Luek, Tim Mahoney
Communications:	Neil Thomas
Lunar Environment:	Sheri Davis, Kevin Wood
Site Selection:	Neil Thomas, Kevin Wood
Launch Scenario:	Geoffrey Pierce
Construction & Assembly:	Marc Luek, Tim Mahoney, Neil Thomas
Cost Analysis:	Geoffrey Pierce

Table of Contents

List of Tables

List of Figures

List of Appendices

I. Introduction

Astronomy has always been limited by the state of the art in telescope resolving ability. Space and lunar based interferometry promises great increases in telescopic performance. The Hubble Space Telescope increased resolution by an order of magnitude over systems under the earth's atmosphere. Space based interferometers will again push these limits back orders of magnitudes. This type of ability will lead to many answers and, as good science always does, will no doubt pose many more questions.

Of particular interest to this project is the search for other planetary systems. It is likely that a powerful space based interferometer could even detect Earth-like planets within several parsecs. Another field of astronomy that would gain from such a system is that of stellar evolution. Great strides could be made by observing star formation regions at the level of resolution achievable through interferometry. Insight into the death of stars could be gained through the observation of collapsed objects such as white dwarfs, neutron stars, and black holes. Detailed imaging of accretion disks surrounding such objects could be possible. Surveys concerning basic stellar properties such as angular momentum could also be performed by resolving stellar surfaces on a large sample of local stars, which would tell us more about our own sun through comparison.

Much could be learned about galaxies as well. The formation of galaxies could be investigated by observing the motion of different types of stars within various types of galaxies. Observations could probe into the dense cores of radio galaxies and quasars. High resolution measurement of motion within the known universe would lead to information concerning dark matter as well as Hubble flow and the expansion of the universe. Also of particular interest will be high-resolution imaging of gravitational lenses. The first wave of observations concerning these and other topics will surely lead to even more observations. Almost every branch of astronomy could expect an answer to some of its more difficult questions.

I.1 Scope of Project

The goal of this project is to design an interferometric array for operation on the far side of the moon to the subsystem level. LOITA (Lunar Optical/Infrared Telescope Array) operates across the visible spectrum of light with some capability in the near infrared and ultraviolet.

I.2 Design Requirements

The primary requirements established by NASA/Space Exploration Initiative Office are:

1. The array shall consist of optical elements with an observational spectrum of 5 nm to 5 mm in wavelength (the primary operating mode will be in the visible spectrum).

2. The array baseline (length) must be sufficient to enable resolution of Earth-type planets at distances of up to 10 parsecs.

3. The array total collection area must be sufficient to provide a signal-to-noise ratio (S/N) of not less than 10.0 for a median wavelength of 500 nm.

4. The individual array elements are constrained to an optical aperture diameter of not greater than 2.0 m.

5. The individual array elements must be identical system components.

6. The array shall be located on the lunar far side at a latitude between 10° North and South (an equatorial region) and shall not be located any closer than 15° to either limb.

A number of additional requirements, assumptions, and criteria have been developed during the design process. These include:

1. All subsystems are designed for minimal achievable mass.

2. All data handling and system control is directed from the Earth.

3. Emplacement and operation of the system is to be done with minimal maintenance and repair.

4. The pointing and control system should be stable to 10^{-6} arcseconds.

5. The system needs to operate reliably in the harsh lunar environment.

6. The system should be capable of forming true images of the observed source.

7. The system will be inoperative during the lunar day.

8. Current trends in technology have been extrapolated to the forecasted time of construction and implementation of the system (2010 - 2020).

I.3 History

Modern long-baseline optical interferometry began with the I2T (Interféromètre à Deux Télescopes) by Labeyrie in 1974. It is presently being upgraded to include active fringe tracking as well as a third telescope. The first stellar interferometer to demonstrate photoelectric fringe detection and phase-coherent fringe tracking was the Mark I stellar interferometer by Shao and Staeling in 1979. This instrument was succeeded by the Mark II and then the Mark III which is

currently operating on Mt. Wilson. Results of observations made with the Mark III include wide-angle astrometric measurements, studies of binary stars, and determination of stellar diameters.

I.4 Current Projects

Two interferometers are currently under development by the U.S. Naval Research Lab and the U.S. Naval Observatory. The Big Optical Array will operate at visible/near-infrared wavelengths using 6 siderostats in a Y-shaped array with a 250 m radius. The Naval Observatory Astrometric Interferometer will be a four-element interferometer with orthogonal baselines of 25 m designed primarily for astrometry.

There are a number of other interferometer projects currently underway. These include: the GI2T (Grand Interféromètre à Deux Télescopes) at CERGA, France - a successor to the I2T with baselines of 70 m; the SUSI (Sydney University Spatial Interferometer) prototype at Sydney, Australia - a two-element interferometer with baselines up to 640 m; and IOTA (Infrared/Optical Telescope Array), at Mt. Hopkins, is a three-element interferometer for visible/infrared observations with baselines up to 45 m.

The potential of space interferometry has been known for some time and many groups have studied possible configurations. Two such studies are POINTS (Precision Optical Interferometer in Space) and OSI (Orbiting Stellar Interferometer).

POINTS uses two interferometers (4 siderostats) to look at two stars about 90° apart. POINTS articulates the two interferometers and ties the two together via a laser metrology truss. To keep the costs low, the design uses a short 2 m baseline with 25 cm apertures.

OSI consists of three interferometers (6 siderostats) with collinear baselines. The baseline lengths extend to 20 m with 0.5 m apertures. Two of the interferometers lock onto guide stars to provide attitude control while the third interferometer switches among a number of stars, measuring the position of the delay line at which fringes are found. The interferometers are tied together with a laser optical truss.

Other space-based systems include: SAMSI (Spacecraft Array for Michelson Spatial Interferometry), an orbiting spatial interferometer comprised of three free-flying spacecraft, two collector telescopes and a central mixing station; TRIO, a kilometric array stabilized by solar sails comprised of two to four free-flying telescopes and a focal station; and COSMIC (Coherent Optical System of Modular Imaging Collectors), a high-resolution, large collecting area telescope.

The lunar surface as a location for optical interferometers has been addressed in a number of studies. These include: NASA Publication 2489, "Future Astronomical Observatories on the Moon;" LOVLBI (Lunar Optical Very Long Baseline Interferometer) by Langley Research Center;

VLFA (Very Low Frequency Array, NASA Conference Publication 3039); and LOUISA (Lunar Optical/Ultra-violet/Infrared Synthesis Array), consisting of 42 1.5 m mirrors distributed in two concentric circles 10 km in diameter.

I.5 Design Team Approach

The priorities of the group were predominantly centered on the optical systems. The array was designed with the primary objective of resolving Earth-like planets at 10 parsecs in mind. Although the system will have many uses, planet detection was deemed to be the most demanding. This was the primary consideration in the development of the array geometry as well as the design of the pointing control system. The ability of the system to form true images of the source was also of importance. This requirement placed strong demands on the metrology system and delay lines. A key group decision involved the location of the instruments: should they be centrally located, or placed within each telescope?

Other items of importance included: the power source, type of materials employed in the structures, types of instruments and detectors to be used, beam combination, type of motor and gear system to move the telescopes, and radiation protection for the entire system.

I.6 Design Summary

The recommended design is that of a circular array consisting of 18 unevenly spaced elements located in the crater Hertzsprung. The layout of the complete system is shown in Figure 1. The maximum baseline is 5 km. Each telescope within the array contains a primary mirror 1.75 m in diameter and a secondary mirror 0.23 m in diameter. The operating spectrum of the array extends from 300 nm - 10 μm. All instruments, detectors, data processing and transmission equipment as well as control computers are centrally located near the center of the array in the instrument room. The planet detection technique employed is an adaptation of achromatic nulling interferometry. The array will receive power from a SP-100-like nuclear reactor. Data handling and command functions are routed through a satellite positioned at L4 which is capable of handling data at a maximum rate of 600 Mbits/sec.

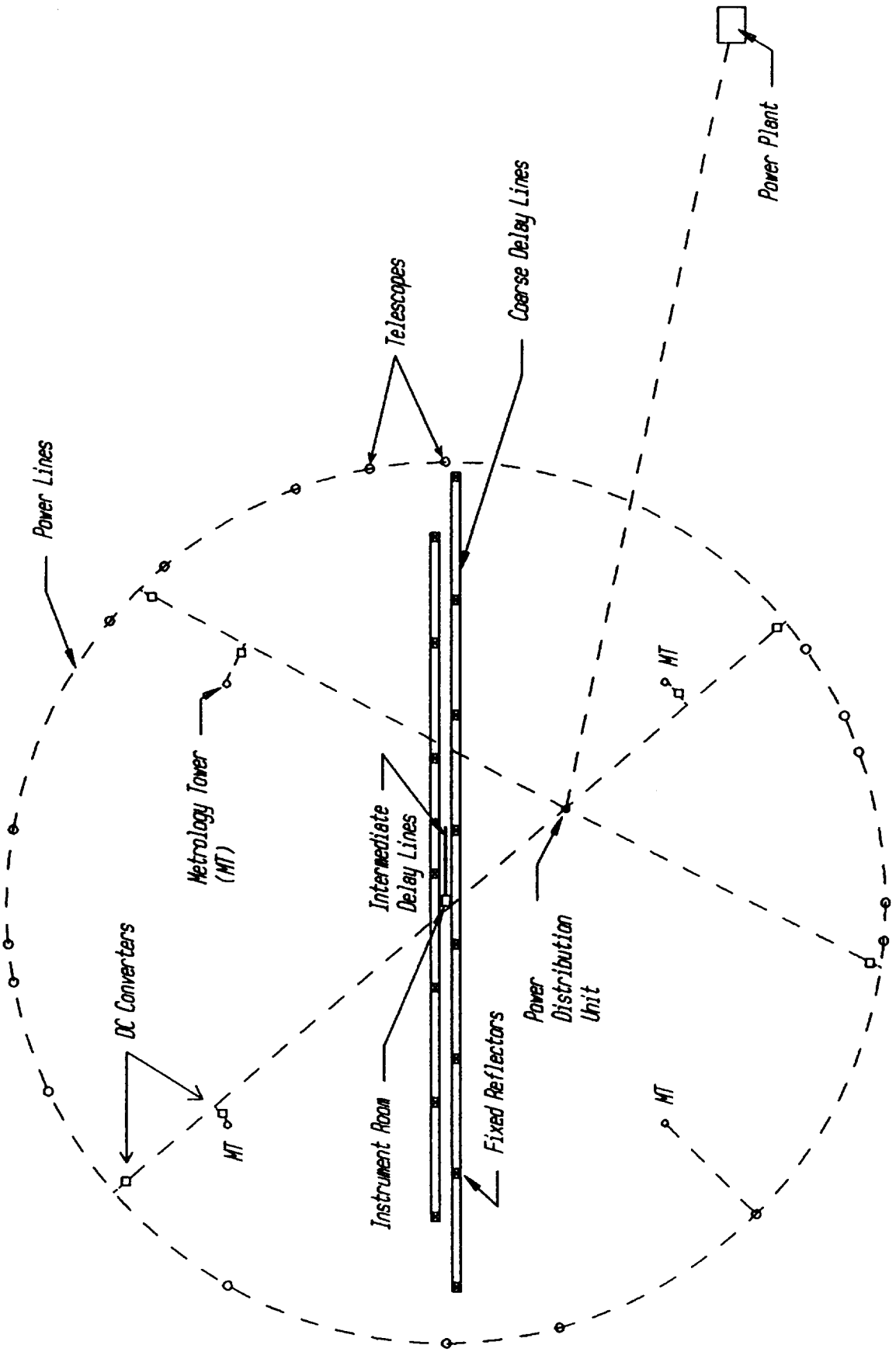

FIG. 1. LOITA Layout

II. Background

An image formed by a single lens telescope (filled aperture) is created by focusing the light waves collected from a source. When the telescope is pointed directly at a point source the waves travel identical distances and are in phase as they reach the focus. For an off-axis source some waves strike the lens before others, as shown in Figure 2a. This path difference causes various phases of the incident light to reach the focus at any given instant. If this path difference is half a wavelength ($\lambda/2$) between two points D/2 apart (where D is the diameter of the lens) the light waves are completely out of phase and cancel. Geometry shows that the angular distance between the two minimums surrounding the primary maximum at the telescope's axis is approximately λ/D. No matter how small the angular size of the source is, it will be smeared to at least this size on the focal plane. This angle is therefore the resolution of the telescope. If the source is further off-axis the light waves begin to add again until a second maximum is reached at a path difference of one wavelength. A series of diminishing maximum and minimum amplitudes (interference fringes) are thus created over a range of off axis angles (θ) as shown in Figure 2b. A polar diagram of this effect (Figure 2c) is useful in visualizing the effectiveness of a telescope over a range of off axis viewing.

The filled aperture principles of resolution can be applied to a two element interferometer. The two telescopes act as two sections of a filled aperture lens. As before, the primary maximum occurs when there is no path length difference as seen in Figure 3a. As with a single aperture, path length differences (Figure 3a) will create a series of maximums and minimums. The angular width of the primary amplitude maximum (resolution) will in this case be λ/B where B is the distance between the two telescopes (baseline length). The resolution of an interferometer, therefore, does not depend on the size of a single lens but upon the separation of its elements. The interference fringes have a higher frequency, depending on the distance between the two telescopes as shown in Figures 3b and c. Each point source will be smeared less, thereby allowing the resolution of smaller angularities.

When viewing an object that is not directly overhead it is necessary to introduce a delay into one of the light paths. This insures that only parts of a single wavefront are being combined and hence, a point source will create a primary maximum when it is directly on axis. Otherwise interference would occur due to the geometry of the array and not due to the off axis components of the source.

An extended object may be considered as a composite of point sources. In this case, the overall interference fringe will be a combination of each fringe from the sources in the field of

view. This image is formed in the uv plane which is perpendicular to the incoming light path. The mixture of interference fringes can be decomposed into each of its elements through Fourier analysis. Each separated fringe pattern yields the location and brightness of its corresponding 'point' source. Thus, an image with resolution λ/B is produced.

II.1 Imaging

When the light from any two telescopes is combined, the interference patterns produce the Fourier transform of the actual image. This image will be transmitted directly to the earth to be processed. A detailed examination of reconstruction techniques, therefore, is not required in the design of the array. A qualitative knowledge of the requirements for various techniques, however, is necessary so that the array can be designed accordingly. There are two primary approaches to interferometric optical imaging: Michelson (pairwise) and Fizeau combination.

Michelson (pairwise) combination is similar to that used in radio interferometry. In this system, fringes on all $n(n-1)/2$ baselines (for an n-element system) are measured simultaneously. Beam combination in a pairwise interferometer, such as LOITA, can be accomplished in either the pupil plane by using beam splitters, or in the image plane with a combining telescope. LOITA utilizes pupil plane interferometry.

In Fizeau combination, the various interferometer apertures are re-imaged at the pupil of a combining telescope exactly as they are seen by the incident wavefront. However, with this type of combination, there are large sidelobes, which the signal processing must account for.

A complex visibility function $\Gamma(u,v)$ can be obtained by collecting fringe visibility data for baselines of various lengths and orientations. Each separate baseline observation yields a complex value of $\Gamma(u,v)$ at a particular point on the uv plane. These observations take the form of fringes that are perpendicular to the baseline and whose period depends on the baseline length. The amplitude component is measured from the contrast of fringes. It is the phase component of $\Gamma(u,v)$ that poses the greatest difficulty.

The Fourier transform, Ft, is applied once the uv plane sampling is finished. The Ft separates the fringe patterns with different periods. Differences in fringe periods correspond to differences in the phase of the wave fronts collected by different telescopes. The difference depends on baseline length, telescope pointing, the specifics of the beam combiner, and naturally, any delay line errors.

By taking the Ft of the complex visibility function the image of the source is obtained. The resolution of its features along a particular axis are limited by the variety of baseline lengths. A small object would be best imaged by many long baselines with little concern for moderate and

short baselines (there are no large features to resolve). Conversely, a more dispersed object such as a nebula would need a better spread of baseline lengths.

Observations of the amplitude alone can lead to many worthwhile measurements. Although reliable images of complex objects are not attainable, measurements of symmetric objects such as stars and accretion disk can be made. This is the basic operating principle of the adding interferometer which only produces axi-symmetric images.

True image reconstruction is a necessity for a project of this scope. This requires knowledge of both phase measurements and fringe contrasts at many points throughout the uv plane. The processed image is convolved with a point-spread function (PSF). If uv coverage is poor, then the PSF will have sidelobes and hence, the image will suffer. The quality of the image can be aided by deconvolving with processes such as CLEAN or Maximum Entropy. This simply reinforces the design goal of avoiding sparse uv coverage. Anything less than a full aperture will most likely benefit from deconvolution techniques, but this is a topic for a discussion on earth-based data processing.

In creating a true image via a coherent interferometer the unmistakable goal is to determine both the phase and the amplitude of the complex visibility. Many techniques have been developed to accomplish this. The following is a summary of the more popular methods and their relevance to the design of LOITA.

A very direct method of measuring the phase of the complex visibility function involves vibrating the path length of one of the beams being interfered. This is accomplished by placing a vibrating (40 Hz)[38] mirror in the beam path which lengthens and shortens the effected beam a quarter wavelength. By comparing the change of the fringe during this process it is possible to determine the phase. The mathematical basis for this technique is shown in Appendix A.

Another technique is that of phase-closure. This technique requires at least three telescopes, but becomes increasingly powerful with an increasing number of telescopes. Phase-closure techniques are commonly used in Earth-based systems since atmospheric effects tend to cancel out, leaving only baseline dependant features. SELFCAL and RSC are two popular methods of phase-closure processing. This approach is based on the fact that any combination of two telescopes will contain phase errors from each element. The phase error is often produced in a random fashion. A least-squares-like fit can be used to determine the phase of the source by examining the measured phases of all the telescopes. The error can then be removed to reveal the phase portion of the visibility function.

Another powerful tool in determining phase is the use of redundant baselines. As with phase-closure, a combination of any two telescopes will contain errors from each. Any two

redundant baselines should have the same visibility function under a given set of circumstances. Errors can be calculated and removed by this type of comparison. Unfortunately, redundant baselines reveal data about the same points on the uv plane, thereby reducing the overall coverage of the array.

There are currently several efforts in the development of phaseless true image reconstruction. All efforts require a model or 'guess' at what the form of the image is. They also demand much greater uv sampling. Therefore, these methods are not considered appropriate for this project.

LOITA is designed to meet several requirements for flexibility in the determination of phase. It should have removable in-line vibrating mirrors. It should have substantially more than three telescopes for phase-closure. Lastly, it should have some amount of redundancy for redundant spacing calibration.

II.2 Resolution and Observable Bandwidth

The goal of resolving an Earth-like planet at 10 parsecs requires a resolution of 0.01 milli-arcseconds. This represents a worst-case scenario. Figure 4 shows a plot of the resolution obtained over a range of baselines at the primary observing wavelength of 500 nm. Resolution of an Earth-like planet at 10 parsecs requires a maximum baseline of 12 km, however, a Jupiter-like planet at 10 parsecs can be resolved with a baseline less than 2 km. It can be seen that a resolution of 0.025 milli-arcseconds can be achieved with a maximum baseline of 5 km. A 5 km maximum baseline would permit resolution of an Earth-like planet at a distance of 3 parsecs. To keep the cost and complexity of the facility at manageable levels, the 5 km maximum baseline was selected for this system. This will still permit resolution of planets around hundreds of nearby stars.

Figure 5 shows the maximum wavelength at which an object can be resolved for a given baseline. It can be seen for a baseline of 5 km, resolution of an Earth-like planet at 10 parsecs dictates a maximum observable wavelength of 200 nm. This level of resolution at 3 parsecs dictates a maximum observable wavelength of about 600 nm. As also shown in the figure, resolution of a Jupiter-like planet at 10 parsecs is achievable with a baseline of under 3 km. Wavelengths above the stated limits, however, can be viewed with reduced resolving ability. The lower bound of the observable bandwidth will be limited by the coating used on the mirrors and beamsplitters. The observable wavelengths are therefore limited to between 300 nm and 10 μm.

II.3 Collecting Area and Signal-to-Noise Ratio

The required collecting area of a telescope system is determined through studies of signal to noise ratio requirements. To calculate the required collecting area of this array, the problem of detecting an Earth-like planet at 10 parsecs is considered. The signal-to-noise ratio is found by the following equation:

$$\frac{S}{N} = \mathrm{SQRT}\left\{ \frac{2\,\Omega_S\, A\, \delta v\, t}{\lambda^2 \left(e^{hv/kT} - 1\right)} \right\}$$

where, $\Omega_S = D_S^2/(4d^2)$ = solid angle of source

D_S = diameter of the source

d = distance to the source

A = collecting area

$v = c / \lambda$ = frequency

c = speed of light

λ = wavelength

δv = bandwidth

t = observation time

h = Planck's constant

k = Boltzmann constant

T = temperature of source

This equation relates the brightness of the source, the collecting area, and the observation time to S/N. The primary assumptions in this analysis were: the planet is 10^{-9} times fainter than its star, the star luminosity and temperature are the same as that of the sun: T = 5800 K, $\delta v/v = 1$ (for a smaller bandwidth, $\delta v/v < 1$), and near-perfect masking of the parent star.

This analysis was carried out for various wavelengths, observation times of 3 and 12 days and for distances up to 10 parsecs for both Earth-like and Jupiter-like planets. The results of this analysis are shown in Figure 6. This figure shows that for a signal to noise ratio of 10, the total required collecting area (assuming CCD efficiency of 70%) of the array is 38.5 m^2 to detect an Earth-like planet at a distance of 10 parsecs with an exposure time of 12 days at 500 nm. The total required collecting area of the array is less than 10 m^2 to detect a Jupiter-like planet at 10 parsecs at 500 nm.

II.4 Planet Detection Techniques

A number of techniques may be employed in the search for nonsolar planets, including both direct and indirect methods for planet detection. Two existing indirect techniques are astrometry and radial velocity measurement. The fundamental problem of direct imaging is that the light from the parent star must be suppressed so that the planet's light is not washed out. Direct imaging of the planet would require apodization of the aperture. Interferometric imaging would necessitate the suppression of starlight by interference in order to detect a planet.

Astrometry

This technique could be used to indirectly detect a planet orbiting a star. The motion of the star would be measured and thus, the size of the planet or orbiting body could be inferred from that information as in the case of the astrometric binary.

Astrometric techniques are employed in the proposed Astrometric Imaging Telescope (AIT).[24] The technique is based on the concept of the Multichannel Astrometric Photometer which measures the centroid position of the stars in two orthogonal coordinates. This same measurement technique is currently used in ground-based systems. The AIT's imaging capability relies on a high efficiency coronagraph. Once space-borne, the AIT will be able to image planetary systems.

Radial Velocity Measurement

Radial velocity can be measured by observing the Doppler shift of a star. If observations were carried out over a period of a number of years, a periodicity could be found. This periodicity would suggest that a body was orbiting the star. As in the case of astrometry, the planet itself would not be observed, but its influence on the star would. Again, this technique would depend on observations made in visible light.

Spectrometric Techniques

Since Earth's oxygen was most likely created by life, an abundance of oxygen in the atmosphere of another planet would be a strong indication that life existed there. Burke[8] and others have suggested looking for the oxygen A-band absorption as well as ozone absorption by utilizing the greater spectroscopic resolution that can be obtained by the dispersed-fringe correlator. Although this method may not assist in the initial detection of a nonsolar planet, it would be instrumental in determining whether a newly discovered planet was capable of supporting life.

II.4.1 Detection By Imaging

Earthlike planets are completely undetectable by their gravitational influence on the parent star and can only be found by direct imaging. Calculations show that infrared observations may be more conducive to planet detection. There is an intensity factor of 10^5 favoring infrared over visible radiation as a medium for planetary detection.[6] However, in the near-infrared, the advantage of viewing in the infrared becomes minimal and may be outweighed by the added burden of cooling the optics and detectors. Because of this, the choice of wavelength is important. The optimal wavelength for detection of Earthlike planets is 10 μm.

Apodization

Diffraction of the starlight at the edge of the telescope aperture obscures the planetary light. This is the greatest obstacle in utilizing direct imaging for the detection of planets and is not avoided by placing the telescope in space. To overcome the problem of diffraction it is necessary to shade the aperture so that the transmission of light falls off gradually from the center to the edge making the edge imperceptible. This results in a reduction of the side-lobe level and the aperture of the system is said to be apodized. However, this reduction results in a greater width of the central peak of the point spread function. Because of this, a planet residing relatively near the star could be absorbed by the wider central peak.

Two types of apodizers for telescopes are possible. Both types must be located at any real plane conjugate to the telescope aperture. In other words, both are placed over the opening to the telescope. This is necessary so that light rays from every object are distributed over the apodization device in exactly the same manner throughout.

One type of apodizer consists of a diaphragm that alters the shape of the aperture as shown in Figure 7. The second type is a filter designed to cut transmission of light gradually, towards the edge of the aperture (see Figure 7). Both possibilities would allow for imaging while in use although they can slightly reduce the aperture size. With the proper design, detection of a star's companion separated from the star 0.5 arcsec at 10pc with a brightness ratio of about 10^{-8} would be possible on a ground based system. Normally, distinction between two 'neighboring' objects is possible only at a greater separation and a much larger brightness ratio than stated above. It would not be unreasonable to assume that the brightness ratio could decrease further and still be detected by an array on the moon.

In order to utilize apodization to its fullest, any such masks or filters would have to be rotated about its center in order to have nulls created by the apodizer blank out starlight in the supposed region of the planet. This task would be extremely complicated when using an array of

18 telescopes. It would require at least one motor to rotate each of the 18 apodizers into position and a system to check each apodizer to make sure all of them were synchronized. Even without using rotation, a system would have to be designed in order to position the apodizers over each of the telescope apertures when they are needed and out of the way when they are not.

Coronographic Technique

Another apodization technique is that of the coronographic telescope such as the proposed Circumstellar Imaging Telescope (CIT)[36] and the Astrometric Imaging Telescope.[24] The method employed uses the combination of a coronagraph to reduce the diffraction of starlight by the telescope and a super-smooth mirror to reduce scattered light.

A telescope such as the CIT would be able to reduce the diffracted light in the wings of the Airy Pattern by a factor of 1000 over the field of view of the instrument. Center light from a bright object in the field of view is blocked out with an occulting spot in the focal plane as in the Lyot coronagraph. The pupil of the telescope is imaged and masked off to remove light diffracted from the edges and support structures of the primary and secondary mirrors. By apodizing both the pupil and focal planes in multiple stages, objects close to the central source can also be imaged. This is an improvement over other apodization techniques. However, this improvement can only be realized if the scattering due to figure errors in the primary mirror is at least 1000 times less than the diffraction of a conventional mirror.[36] Because of this requirement, very strong constraints on the surface errors of the telescope are imposed.

II.4.2 Interferometric Imaging

Detection of interferometric fringes due to a faint nonsolar planet is not possible unless the bright fringes due to the central star are suppressed. One method which would accomplish this task was that of the spinning interferometer proposed by Bracewell.[5] Another method, proposed by Shao and Colavita[30,32], is the achromatic nulling interferometer.

Spinning Interferometer

This method consists of a two-element interferometer in which the light from the mirrors is combined 180° out of phase so as to provide a null on-axis, where the star is located. The entire system is then rotated about this axis so that the planet signal is modulated as the fringe pattern sweeps through the sky. This system is not capable of synthesizing images of complex objects unless many telescope pairs of varying baselines were in use.

Achromatic Nulling Interferometer

In this method[30,32], light from two apertures is split at a beamsplitter into two paths, one in plane, and one out of plane. Each beam is then reflected from a dihedral, then recombined at the beamsplitter as shown in the Figure 8. Output from the beamsplitter is fed through single-mode optical fibers to the detectors. The optical fibers act as spatial filters to eliminate the propagation of scattered light, thus eliminating the need for super-smooth optics. The beamsplitter need not be precisely 50/50 since it is used once in reflection and once in transmission in each arm. Unlike the method of inserting a phase delay into the interferometer to produce a null, the null in this case is achieved by a polarization flip. Since the quarter-wavelength phase shift is eliminated, the null is achromatic. This is strictly a method for planet detection. True imaging of the planet will not be possible since a phase shift is required in order to obtain all components of the complex visibility.

This is the technique that has been selected for LOITA; its implementation will be discussed later.

II.5 Lunar Environment

The table below presents a comparison of advantages and disadvantages of Earth-based and space-based interferometer systems.

Location	Pros	Cons
Earth	•Easily serviced and repaired •Relatively low cost •Relatively few unsolved technological problems	•Short observation times •Atmospheric interference •Need space for large systems •Light/radio pollution
Earth Orbit	•No Atmosphere •Light-weight due to reduced gravity •Long observation times (depending on type and altitude of orbit)	•Cost: servicing and maintenance •Thermal cycling •Technological problems: construction, transport, deployment •Cosmic radiation

Lunar Surface	•Stable base for large telescopes •Hard vacuum for diffraction limited imagery •Long observation times •Stable baselines for interferometry •Absence of light/radio pollution •Ample material on surface for shielding •Absence of magnetic field •Light-weight structures	•Cost •Transportation to and landing on Moon •Cosmic radiation •Thermal cycling •Dust contamination of support systems •Crew requirements for assembly •Require data link with relay station

The pros listed for the lunar surface are very inviting to scientists. Fairly light structures could be used since the gravity of the Moon is 1/6 that of Earth and there is no weather to add excess loads on the structures. There is a large, stable platform to support large structures. Also, the long uninterrupted observation period of 14 days would mean images could be formed over shorter time periods.

When LOITA is constructed in 15-20 years, some of the negative aspects could possibly be reduced. For instance, if a lunar base were established previous to building the array, some of the costs would decrease. Astronauts stationed at the base would be tasked with making routine repairs. The base would have a communications link with the Earth, so the array could use the same system.

Putting the array in an orbit around the Earth has some of the same advantages as the moon. The structures could be lighter because of no gravity, and there is no atmosphere to interfere with the observation. This possibility, however, also has a very high cost of servicing like the lunar site. It also presents more difficult technological problems of construction and deployment.

The third option is putting the array on Earth. The biggest advantage is that the cost would be much lower than for an orbital or lunar site. It would be easily serviced and repaired, and there are no unsolved technological problems. However, on the Earth there would be relatively short night observation times. Also, the atmosphere's distortion of the incoming light must be taken into

account when producing the final image. Lastly, a place would need to be found on Earth large enough for the array and far enough away from any disturbances.

II.5.1 Geology of the Moon

The lunar surface contains a harsh set of environmental constraints such as high thermal gradients, a high vacuum, enormous levels of radiation, low gravity, an apparent lack of water resources, meteoroid impacts, and an abundance of fine-grained particle material. The surface area of the moon is approximately equal to that of Africa and Western Europe combined.

The top 30 cm of lunar soil is made up of grain-sized particles which are slightly cohesive. Meteoroid impacts over the centuries have blasted the soil, creating craters and layers of scattered debris from the ejecta patterns. The density of the soil varies over short distances in both the horizontal and vertical directions, but in general, the lunar surface has a sufficient bearing capacity to support most structures at most locations. Subsurface layers of the moon, which are made up of crushed rubble from extensive meteoroid impacts, are such that seismic waves are quickly damped near the disturbance. Typical ground motions are about 1 nm. This is important for optical interferometry where one must track the baseline to within a fraction of the wavelength being studied.

During several Apollo missions, experiments were carried out to determine the properties of the lunar surface. One of the properties which was measured was the density of the soil. This is an important aspect to structural support on any surface because the density of the soil is directly proportional to the structural weight that can be supported. Measurements were taken at several depths and are shown below.

Depth (cm)	Bulk Density (g/cm^3)	Relative Density Dr (%)
0-15	1.50 ± .05	65 ± 3
0-30	1.58 ± .05	74 ± 3
30-60	1.74 ± .05	92 ± 3

From this table, it is apparent that the most stable depth to place the base of a structure is at least 30 cm. It could become important to place the structure deeper into the soil if the weight of the object becomes very large.

The moon has a very thin atmosphere. Table 1 lists the components of the lunar atmosphere and their concentrations. The low density of the atmosphere is ideal for high vacuum materials processing and for high resolution astronomy.

There is a large temperature variation at the surface ranging from 100 K at night to 385 K during the lunar day. The proper materials and equipment used should be selected in order to withstand this variation. However, 30 cm below the surface the temperature is approximately 250 K, and varies only 2-4 K. Therefore, the foundations of the equipment could be placed below the surface to avoid the extreme temperature variation.

There are occasional moonquakes at and near the lunar surface, but they average only 1-2 on the Richter Scale. Table 2 shows a comparison of moonquakes with earthquakes. Seismic waves are present, but they are quickly dampened near the disturbance due to the surface of crushed rubble from meteoroid impacts.

The moon has a very small magnetic field -- 3 to 330 gamma at the surface, while the earth's is about 30,000 gamma at the equator. Because of this small field and nearly absent lunar atmosphere, solar particles hit the surface unimpeded. There are three sources of radiation with different energies and fluxes hitting the moon. The first is high energy (1 to 10 GeV/nucleon) galactic cosmic rays with a flux of about $1/cm^2/sec$ and a penetration depth of a few meters. The second is solar flare particles with energies 1 to 100 MeV/nucleon, a flux of about $100/cm^2/sec$, and a penetration depth of 1 cm. The third source is from solar wind particles with energies 1000 eV, a flux of about $10^8/cm^2/sec$, and a penetration depth of about 10^{-8} cm.

Because of their high energy level and high flux, solar flare particles are the most dangerous to electronic equipment. The equipment's exposure to this radiation should be somehow limited. The best alternative to protect the majority of the equipment would be to cover the equipment with a layer of lunar soil, which could shield the equipment from solar radiation.

The effects of lunar soil particles, or dust, will be a reasonably difficult problem to solve in the design process. The large electrical conductivity change associated with visible and ultraviolet (UV) irradiation, combined with very low electrical conductivity and dielectric losses, can produce an extremely efficient electrostatic charging mechanism. This process is initiated with the lunar terminator, or sunrise. "The sharp gradient in UV flux across the solar terminator (boundary between day and night) may generate clouds of electrostatically-supported dust, and set them into motion as the terminator moves across the moon."[126] This creates a dust storm which could extend 10 meters above the lunar surface. These particles could adhere to surfaces, creating a coating of dust. This increase in irradiation begins some 40 hours before sunrise and ends about 30 hours after it. The electrical conductivity is lowest during the lunar night, so the soil will have the highest electrostatic chargeability at night. Nighttime surface activities that disturb the lunar soil could generate thick coatings of dust on exposed surfaces. Clearly, all exposed equipment on the lunar surface must be protected. The telescopes, electronic equipment, delay lines, and

communications equipment must be sealed from such dust storms. The best method to close off the telescopes would be to place a large door which could seal-off the end of the telescope during such harsh conditions. Shown below is a table of the adhesion strength of lunar soil to certain surfaces.

ADHESION STRENGTH OF LUNAR SOILS

PAINTED SURFACES	10000 dynes/cm^2
METALLIC SURFACES	2000-3000 dynes/cm^2

II.5.2 Meteorites

The role of meteorites in this design will be an important design consideration because of the relatively large micrometeorite flux present on the lunar surface. From Figures 9, 10, and 11, it is apparent that meteorites could possibly damage, or even destroy the entire lunar observatory. It would be impossible to design a structure which could withstand the force created by a large meteorites, but the structure must be able to withstand the unending flux of micrometeorites. For instance, a 1 gram micrometeorite will on average strike within an area of 1 square kilometer once a year. The kinetic energy of a 1 gram meteorite would be approximately 451068.51 Joules. The equation for calculating the kinetic energy is

$$\log E = \log m + 2 \log V + 9.70$$

where the kinetic energy, E, is expressed in ergs, the mass, m, in grams, and the velocity of the meteorite, V, in km/sec. The average flux of this 1 gram micrometeorite is 1 per cm^2 per 273.97 years. There is a definite possibility that one or more of the telescopes could be destroyed from a meteorite impact, but the risks are not exceptionally large. The majority of these micrometeorites are so small that they leave craters of only about 0.1 micrometers in diameter. A particle of mass 10^{-8} grams would be associated with an energy of 0.0045 Joules. The structures used to support and surround the telescopes must be able to withstand many impacts with particles of this size.

One method which could be used to deal with the protection of the telescopes consists of two thin layers of metals used to cover each individual telescope. One layer would be placed over the second, and a small gap of 3-4 inches left between the two. The outer layer of metal would serve as a barrier to reflect most of the micrometeorites. If, by chance, one of the micrometeorites were to pass through the first layer of shielding, the kinetic energy associated with the meteorites would be reduced so that it would not pass through the second layer of metal. The gap between the two layers would serve as a means of ejecting the micrometeorites from the structure. The

objects would slide, or roll, down between the two layers of metal and fall harmlessly to the lunar surface. These layers of metal shielding could be left open to the environment because the dust, radiation, and other environmental phenomenon would not be able to interfere with the structure's ability to fulfill its objective.

II.6 Site Selection

Several conditions must be considered in the selection of a site. Some are dictated by the qualities of the moon itself, while others are dependant on the type of intended observations. The mare section of Hertzsprung on the far side of the moon is shown to be ideal by examining the following parameters:

1) Lunar libration
2) Communication link requirements
3) Desirable observations
4) Topography

1) The observatory is placed on the far side of the moon due to the light polluting effects of the earth. A map of the far side showing the suitable locations is given in Figure 12. More than half of the moon's surface is exposed to the earth due to an apparent wobble of the moon called libration. Libration is primarily due to inclination of the moon's orbit about the earth. Hence, the border between the near and far side is constantly shifting up to 6° behind either limb. Therefore, the observatory is constrained to a safe distance of 15° from either limb.

2) It is shown in the communications section that an L5 or L4 link can theoretically reach up to 60° behind the limb. The libration of the moon, however, reduces this figure to 54°. Non-flat terrain, in addition, would restrict this communication zone further. Requiring that the relay satellite appear at least 9° above the horizon demands that the array be positioned no more than 45° behind the limb.

3) The detection of an earth-like planet is one of LOITA's primary goals. The five most likely candidate star systems within 12 light years are given in Table 4. The location of the observatory must be such that a maximum number of these systems are observable. The declination of these sources are marked across the lunar map in Figure 12. This shows the lunar locations where the particular source appears to pass directly overhead (not accounting for the 5° difference in the axis

of the moon and the celestial sphere). An observatory within 90° of this 'overhead line' could theoretically observe the source. A value of 80° is assumed, however, to account for the moon axis' inclination and a non-flat horizon. It can be seen that all five of the sources are within this range of Hertzsprung. The most important source, Tau Ceti, passes only 20° from the zenith. The worst case is that of Alpha Centauri which still passes 25° above a flat horizon.

4) There are basically two distinct terrains present on the lunar surface. According to Taylor, the highlands area are very old and heavily cratered, while the maria are much younger.[128] Masursky defines a mare as "a dark, level, relatively smooth part of the lunar surface (so distinct from the lunar highlands or terrae that most large mare areas on the near side are visible from Earth with the unaided eye). Most geologists now agree that they are underlain by solidified (basaltic) lava flows."[121] At one time, the maria were seas of liquid lava which have solidified to make basalt, a volcanic rock. A smoother site is important for the construction and operation of this array. If the site is fairly "rough", then it would be nearly impossible for the telescopes to communicate via line of sight with some central instrumentation building. The delay lines could not be constructed along a horizontal plane, but instead would have to take on a jagged shape. Without a colossal amount of reshaping the lunar surface, the delay lines would have to bend at the top of hills, or crater rims. Laser metrology would be very difficult to carry out over rough terrain. An extreme example would call for reflecting the laser around, or over mountains. Obviously, a clear line of sight is important to the operation of a lunar array.

The crater Hertzsprung is located at a latitude of 2.0° N and a longitude of 128.1° W. Hertzsprung has a diameter of 520 kilometers. The mare of Hertzsprung is approximately 160 km from east to west, and approximately 200 km from north to south, which is many times larger than would be required for our array. Figure 13 shows that the walls around Hertzsprung are approximately 4 km tall. If the array is placed at the center of the mare section of the crater, then the viewing would be restricted to 2.86° above the horizon. Figure 14 shows the basis for this restriction.

Andersson has helped to define a new system of naming and locating craters on the lunar surface. This enables us to learn about new, smaller craters located within our selected site of Hertzsprung. Figure 15 shows a 24 hour clockface which is used to define these new letter designations. According to Andersson,

> The letter designation scheme for the far-side
> was devised for maximum ease in locating craters
> on maps, and works as follows: each "patronymic"

> crater is considered to be the center of a 24 hour clockface in which the numbers have been replaced with Roman capital letters, with Z at the north point. Thus each letter represents a fixed azimuth from the patronymic crater, and the chosen subsidiary craters are lettered according to their closest azimuths.[113]

Using this lettering scheme, eleven different, smaller craters have been discovered inside Hertzsprung. These are as follows:

Crater	Latitude	Longitude	Diameter
Hertzsprung D	3.3° N	125.4° W	45 km
Hertzsprung H	1.3° S	124.4° W	21 km
Hertzsprung K	0.5° S	127.6° W	27 km
Hertzsprung L	0.4° N	127.8° W	33 km
Hertzsprung M	7.5° S	128.9° W	36 km
Hertzsprung P	0.0° N	129.3° W	22 km
Hertzsprung R	0.1° S	131.8° W	33 km
Hertzsprung S	0.6° N	132.5° W	47 km
Hertzsprung U	5.2° N	133.3° W	39 km
Hertzsprung X	3.8° N	129.1° W	24 km
Hertzsprung Y	8.8° N	131.2° W	23 km

All of these requirements and restraints must be taken into account when the final site selection is made. The array should be located in the mare section of Hertzsprung, but, if possible, ought not be positioned in one of these smaller craters. A more detailed study of the mare section of Hertzsprung will be required before the final site selection can be determined. This would enable a determination of the exact position of each telescope, instrument room, metrology system, power plant, communications station, etc.

TABLE 1. COMPOSITION OF THE LUNAR ATMOSPHERE AT NIGHT (from ref.9)

Gas	Concentration (mol/m^3)
H_2	1.1×10^{-15}
^4He	6.6×10^{-14}
^{20}Ne	1.3×10^{-13}
^{36}Ar	5.0×10^{-15}
^{40}Ar	1.2×10^{-14}
O_2	3.0×10^{-16}
CO_2*	5.0×10^{-15}

*Carbon gasses (CO_2, CO, CH_4) probably dominate the daytime lunar atmosphere.

TABLE 2. COMPARISON OF MOONQUAKE AND EARTHQUAKE INTENSITIES
(from ref.9)

	Moon	Earth
Number of events/year	5 shallow (m 2.2)* 500 deep (m 1.6)*	10^4 (m 4)*
Energy release of largest event	2×10^{10} J (shallow) 1×10^6 J (deep)	10^9 J
Magnitude of largest event	4.8 (shallow) 3.0 (deep)	9
Seismic enery release/year	2×10^{10} J/yr (shallow) 8×10^6 J/yr (deep)	10^{18} J/yr

* m = magnitude on the Richter Scale

TABLE 3. MICROMETEORITE FLUXES ON THE MOON
(from ref.9)

Crater diameter (μm)	Craters/m^2/yr
00.1	30000
1.0	1200
10	300
100	0.6
1000	0.0001

TABLE 4. FIVE STARS WITHIN 12 LY MOST LIKELY TO HAVE EARTH-LIKE PLANET
(in order of likelihood)

	Star	Declination	Apparent Magnitude
1.	Tao Ceti	-16°	3.5
2.	Epsilon Indi	-57°	4.7
3.	61 Cygni	+38°30'	5.2 / 6.0
4.	Alpha Centauri	-60°38'	0.0 / 1.4
5.	Epsilon Eridani	-09°38'	3.7

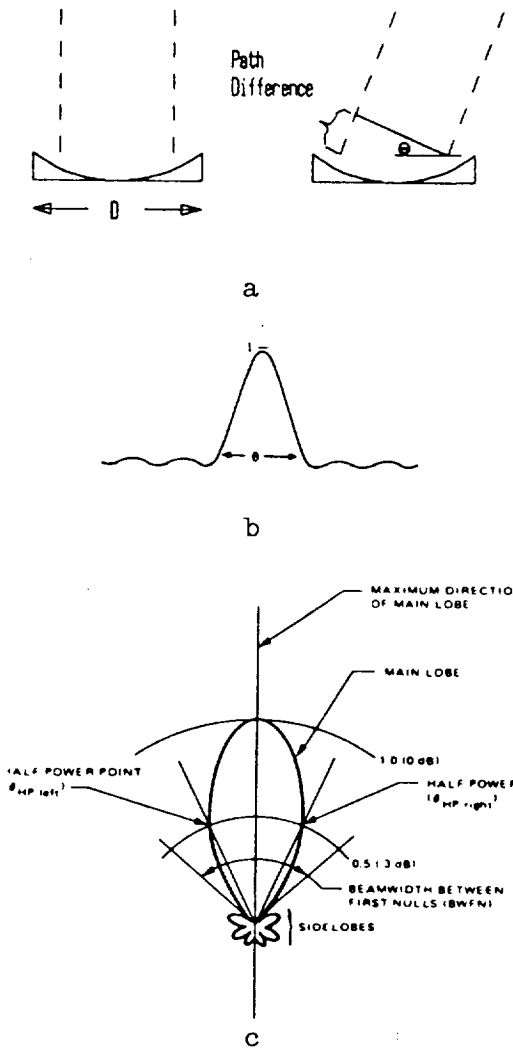
Path
Difference
D
a
b
MAXIMUM DIRECTION
OF MAIN LOBE
MAIN LOBE
1.0 (0 dB)
HALF POWER POINT
0.5 (-3 dB)
BEAMWIDTH BETWEEN
FIRST NULLS (BWFN)
SIDELOBES
c

FIG. 2

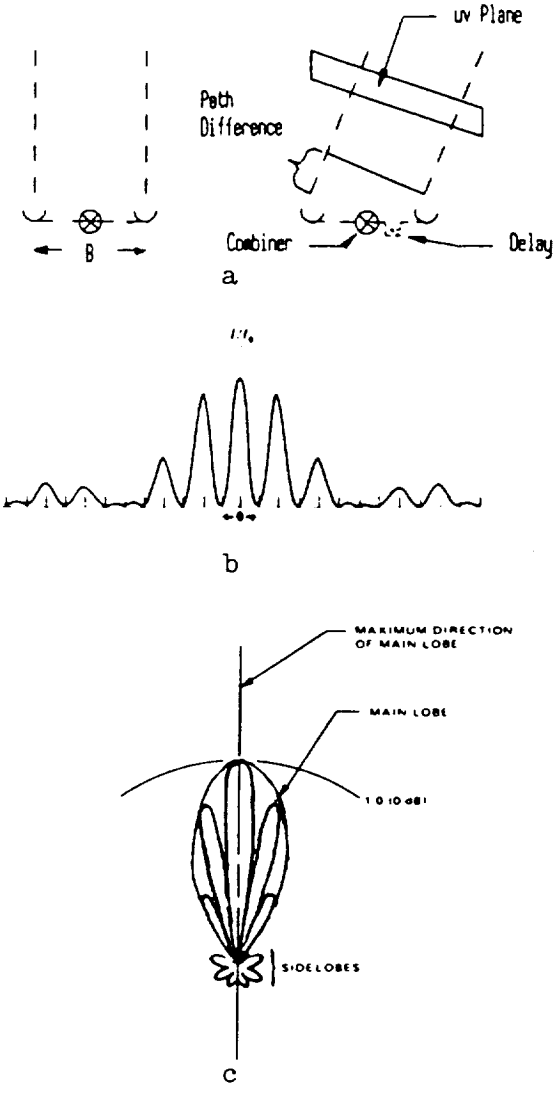
uv Plane
Path
Difference
B
Combiner
Delay
a
b
MAXIMUM DIRECTION
OF MAIN LOBE
MAIN LOBE
1.0 (0 dB)
SIDELOBES
c

FIG. 3

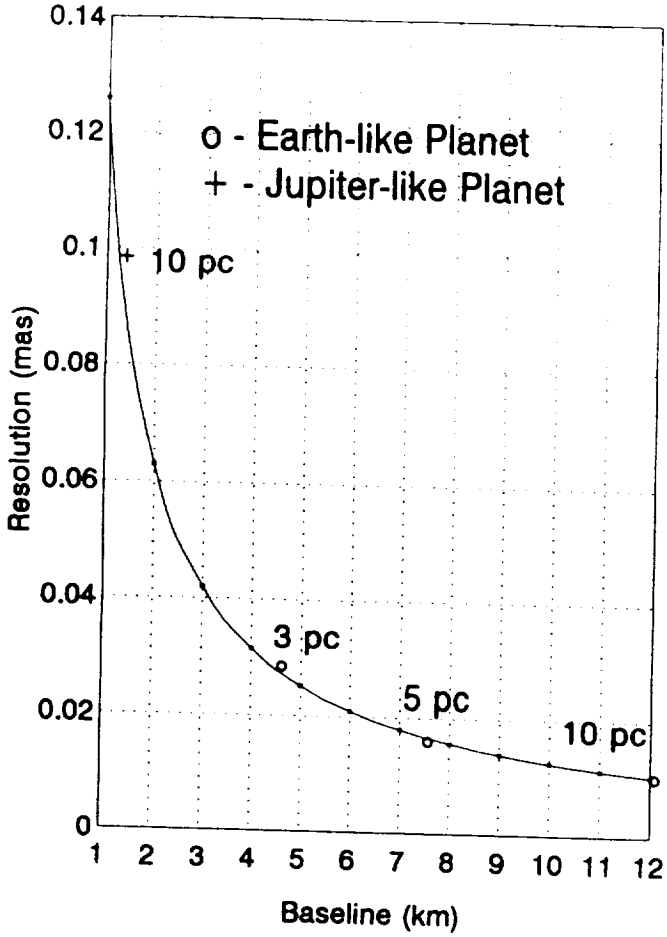

FIG. 4. Resolution vs. Baseline at 500 nm

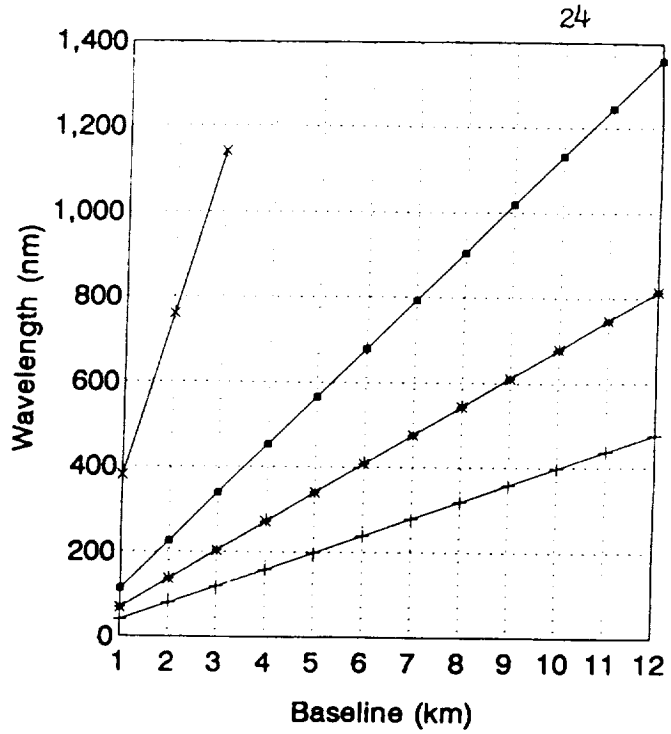

FIG. 5. Limiting Resolvable Wavelength vs. Baseline

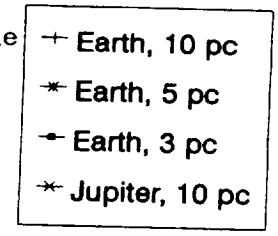

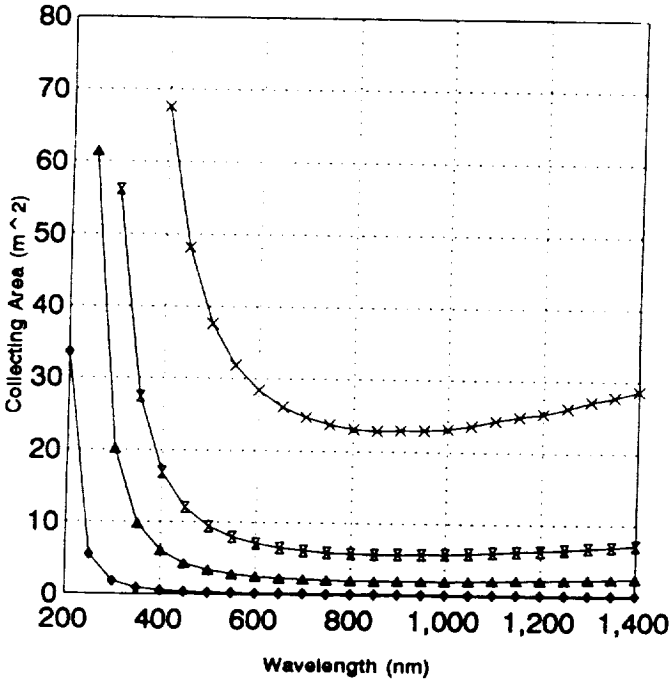

12 day observation time

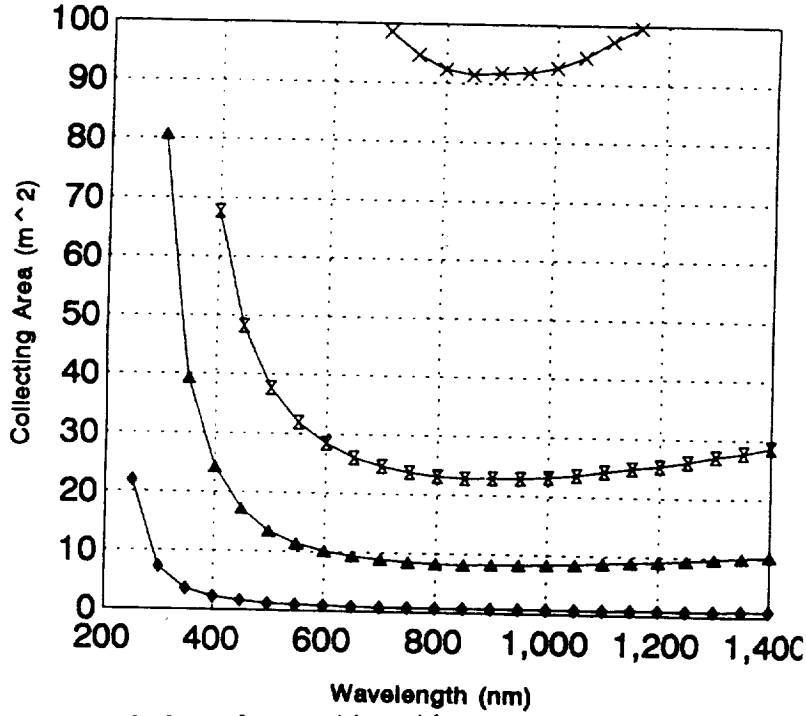

3 day observation time

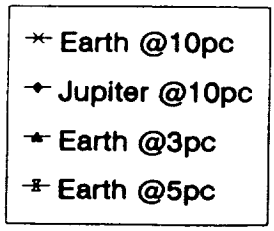

FIG. 6. Collecting Area vs. Wavelength for S/N = 10

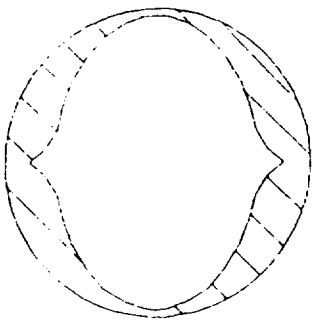

Example of diaphragm

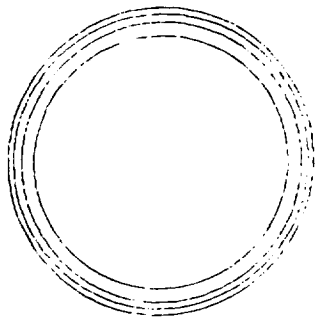

Example of filter

FIG. 7. Types of Apodizers

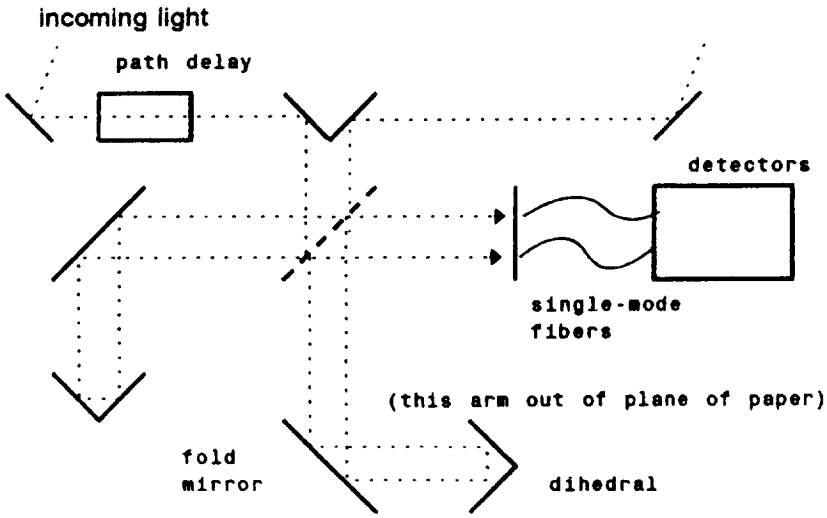

FIG. 8. Achromatic Nulling Interferometer

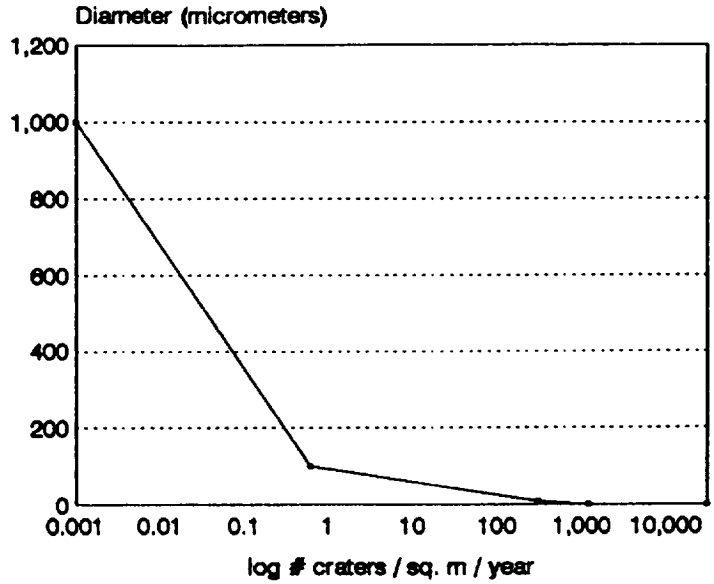

FIG. 9. Micrometeorite Fluxes on the Moon

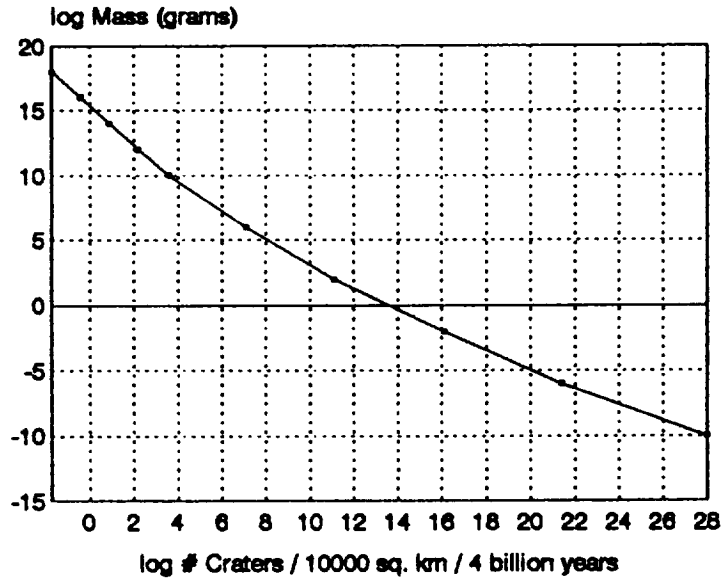

FIG. 10. Number of Craters vs. Mass of Meteorite

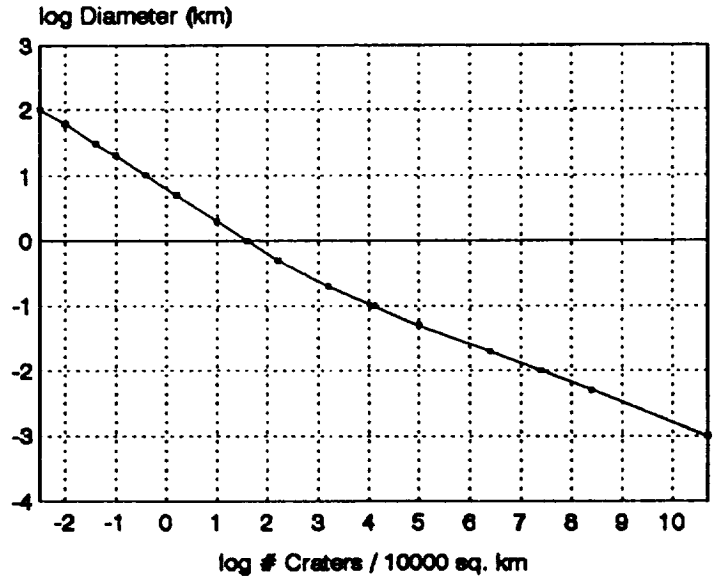

FIG. 11. Number of Craters vs. Crater Diameter

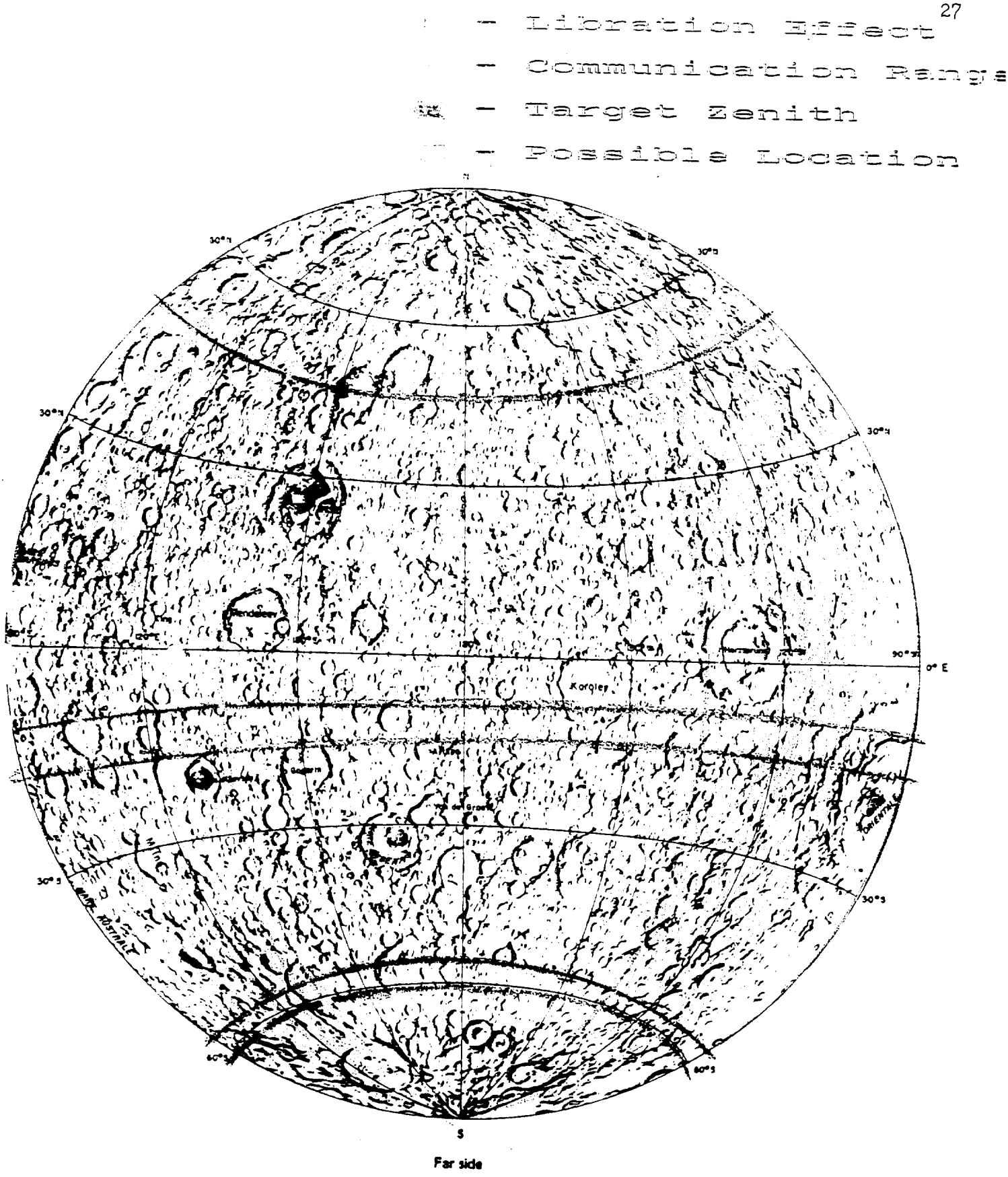

FIG. 12. Possible Array Locations on Moon

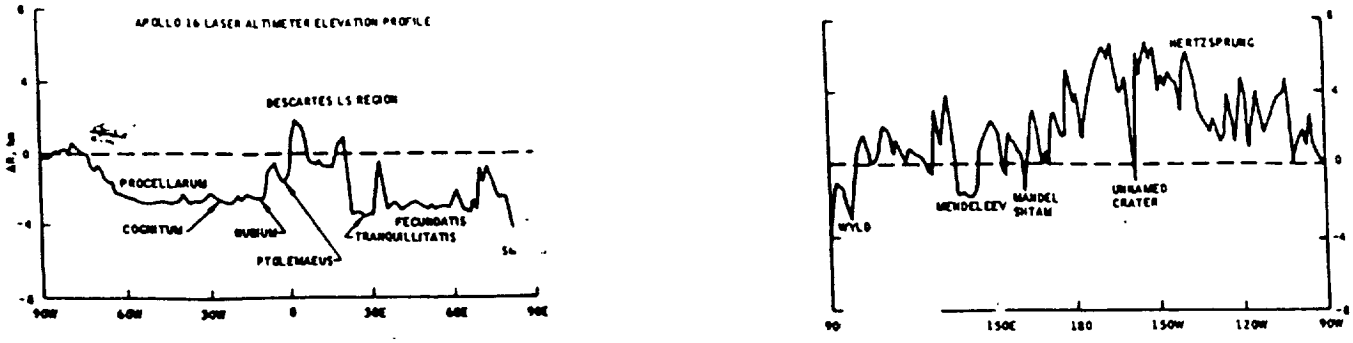

FIG. 13. Hertzsprung Altimeter Profile
(taken from reference 117)

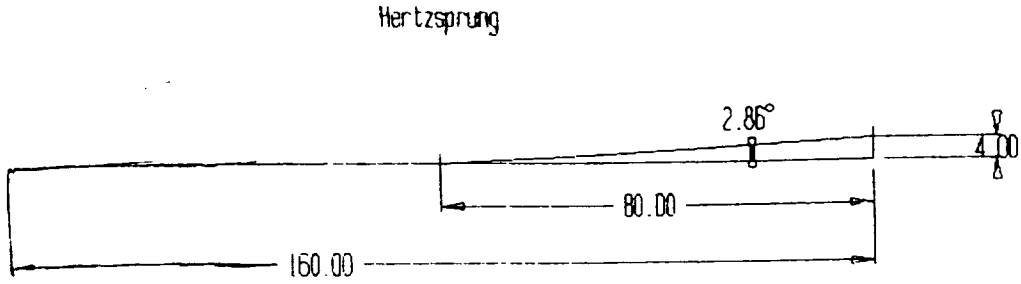

All dimensions in kilometers

FIG. 14. Restricted Horizon

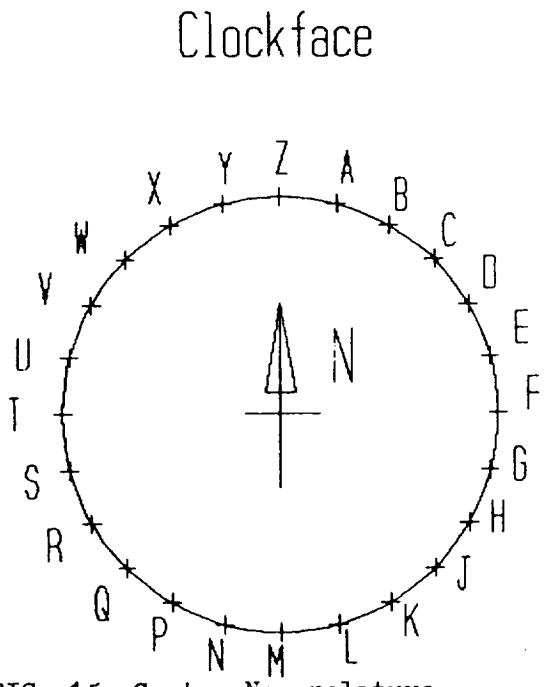

FIG. 15. Crater Nomenclature

III. Optics

III.1 Array Size

The number of telescopes and the size of each were selected through the use of a mass minimization trade-off study shown in Appendix B. One of the primary objectives of the design of the telescope array is to minimize the mass of the system. This is very important because of the cost and technical problems involved with lifting large masses into space.

For each individual mirror system used, there is an associated mass of structural components and instrumentation. With this information, several primary diameters ranging from 1 m to 2 m were considered. For each diameter considered, the approximate collecting area and mass of the mirror system was computed, taking into account the primary area blocked by the secondary mirror. Once the area for a single telescope was established, the number of telescopes required to meet the collecting area requirement could be found. With the total number of telescopes needed for a given primary diameter known, the total system mass for that diameter was computed. It was this number which was to be minimized. The results of this trade-off study suggest that the primary diameter should be between 1.5 and 1.9 m (see Figure 16). The selected primary mirror diameter was 1.75 meters; the diameter of the secondary mirror is 24 cm. The array will consist of 18 individual telescope units of this size to meet the total required collecting area. The total system mass was initially estimated to be 21000 kg (this number does not include the mass of the power system or data processing equipment). The following assumptions were made: 1) the thickness to diameter ratio of the mirror is 1:25, 2) the density of the optical material (Zerodur^{TM}) is 2205 kg/m^3, 3) the mirror mass/solid mirror mass (construction efficiency) is 0.25, and the mirror is of light-weight honeycomb structure, 4) the mass of the mirror structure is 8x the mass of the primary mirror, and 5) the mass of the base and support structure is 500 kg.

III.2 Telescope Optics

A systematic study was performed which considered a number of geometries. This study made use of a paraxial ray-trace routine which included a third-order error analysis of coma and astigmatism. Once a nominal range of mirror diameters that minimized the system mass was established, each primary mirror diameter within this range was examined. For each diameter, a range of separations between the primary and secondary mirrors was also examined. The separation range was 0.5 to 2.5 m. The selected geometry is that of a standard cassegrain telescope with parabolic primary and secondary mirrors which minimizes coma and astigmatism.

Based primarily on optical performance, error analysis, and mass considerations, the recommended design calls for a 1.75 m diameter primary mirror, with a 0.24 m diameter secondary mirror. The separation between reflecting surfaces is 1.5 m, as shown in Figure 17. The collecting area of the aperture is approximately 2.36 m^2. Therefore, the total collecting area of the array is 42.5 m^2. Both the primary and secondary mirrors are coated with Aluminum (reflecting surface) and Magnesium Fluoride (protective coating).

III.3 uv Coverage and Array Geometry

The arrangement of the telescopes comprising the array was primarily determined by the uv coverage. Two popular array configurations (circular and Y-shaped) were examined.

A computer program (Appendix C) was developed to process a given telescopic arrangement at a given location on the moon and plots the uv coverage for a point source at a given celestial location. This program was based on the basic baseline - uv formula[26]. The calculated uv locus trace out ellipses in the uv plane as the moon rotates. The given plots show the potential locus of uv coverage given all of the possible baselines over a full exposure of 360°. Such an observation will not actually be attainable experimentally due to blockage from the horizon. Plots of a full exposure, however, provide valuable qualitative features concerning a given configuration. A real exposure will sweep out arcs of these ellipses dependent on the exposure time. This is an important consideration when predicting the results of an exposure but is irrelevant when comparing one configuration to another. The program assumes that the moon's spin axis is along the celestial pole. This is an invalid assumption due the moon's tilt and the tilt of its orbit about the earth. Again, this is an important consideration in exposure calculations, but is not important in comparing configurations.

It is important when examining a uv coverage plot to realize that coverage furthest from the origin corresponds to the amount of high resolution imaging[40]. The dimensions of the various arrays considered are such that the maximum baseline is the same for all cases. The actual size, and therefore the dimensions on the uv plane are ignored at this point. Only the qualitative features of the coverage are important for this study.

The array analysis is done for a target declination of 20°. This is a typical declination and should show trends between various configurations that are representative of the coverage at any angle. The preliminary analysis was done for six member configurations. Obviously a fair comparison must be between options with the same number of telescopes. Six was chosen because it is easily handled but should be expressive enough for an accurate analysis. This type of configuration could be employed as a first-stage proof-of-concept construction.

The proposed configuration given by the System Study Final Report[16] was the first possibility fed into the program. The uv coverage is shown in Figure 18a. The uv coverage as calculated via the program FAKE[16] is supplied in Figure 18b for comparison. The exact agreement shows the validity of plots made with the program developed by this group.

A number of variations of a Y-type, 6 element array were considered. Figure 19a shows the coverage for Case 1, a Y-type arrangement with two telescopes mid-way between the center and the outermost telescopes and one at the center. The coverage is relatively even but irregular in overall shape. Figures 19b and 19c show how the coverage changes for Cases 2 and 3 as the intermediate telescopes are moved inward or outward, respectively. The coverage clumps and separates in both cases. Figure 20a shows Case 4, another variation where the center telescope is moved outward to the third limb. This configuration leaves large gaps in coverage. Figure 20b displays the effect of simply rotating the array relative to the moon for Case 5. It too displays severe clumping and only isolated coverage. Thus, Y-type designs demand great care in the positioning of telescopes along the three limbs. Y-type would also require a simultaneous study in the effects of local North - South orientation. This study would necessarily include consideration of the local N - S coordinates as related to the celestial sphere over a month (consider moon and moon orbit tilt). Clearly, the conventional earth based Y-type configuration has, in our opinion, limited applicability to a lunar project.

An evenly spaced six element circular array is considered in Figure 21a. While the coverage is relatively even, it exhibits fewer ellipses than Figure 18 (8 as compared with 14). If the telescopes are unevenly spaced, however, as in Figure 21b, the coverage increases many fold. Doing this avoids redundant coverage from parallel baselines of the same length. The coverage spans the uv plane and is evenly distributed within. Comparing with Figure 18, it is clear that the unevenly spaced, circular design is far superior to the conventional Y-type configuration.

A more detailed examination of the circular configuration was then made for 18 telescopes, the number used in the actual design. If uv coverage is adequate for this number then it should be selected. This yields over 10 times as many baselines as was considered adequate[9]. The coverage of an evenly distributed ring of 18 telescopes is shown in Figure 22a. It is spherical and very evenly filled. Redundant baselines are eliminated by systematically increasing the angular separation between each successive telescope. At this point the uv coverage is complete (within the resolution of the printer) as shown in Figure 22b. The coverage for a source at 0° is shown in Figure 22c. At a target declination of 0° the ellipses reduce to horizontal lines. The given configuration, however, still manages to provide very full coverage. Table 5 is a list of telescope coordinates.

Typical uv coverage of the Very Large Array (VLA) is shown in Figure 23. The VLA has 27 telescopes in a Y-type design and is therefore comparable to the design considered above. Figures 22b and 22c compare favorably with the VLA which employees 9 extra elements. In particular, the circular design does not exhibit the overall irregularity in uv coverage that the VLA does.

A pair of concentric circles is examined in Figure 24. Coverage is reduced, however, for high resolution imaging.

A spiral configuration was briefly examined (not shown) but demonstrated little promise.

A more detailed examination of coverage will be performed now that the final configuration is determined. The uv program developed will now be used to show the coverage at various exposure durations. Figure 25a shows the coverage for a 12.5 day exposure in which the target passes from 15° above one horizon to 15° above the other horizon. Coverage is still evenly formed and distributed, although density has certainly decreased. Figure 25b shows the same coverage for a target declination of 0°.

Another important aspect is that of "snapshot" coverage. This is the uv coverage achieved with an exposure short enough that the motion of the moon does not appreciably move the array. The uv plane therefore consists of a point for each baseline. Figure 26 shows the snapshot (1 hour) coverage of LOITA for a source at the zenith. The coverage displays a relatively even distribution from the origin. This corresponds to an even sampling over the range of resolutions.

In summary, the unevenly spaced circular array appears to be the superior option for several reasons: 1) The array can be easily designed for a desired uv coverage pattern by experimenting with the placement of telescopes one at a time. 2) The array does not have a particular North - South orientation to be concerned with as one designs the arrangement of telescopes along the ring. 3) Very good uv coverage can be achieved with a number of telescopes corresponding to the optimal array mass. 4) Uniform coverage is maintained over the range of possible source locations. 5) Uniform coverage is achieved at integration times ranging from the full lunar night down to snapshot exposures.

An array composed of stationary elements was selected over one with movable elements. The primary advantage of having movable elements is increased uv coverage over shorter exposure periods. The fixed-position, 18-member design, however, gives acceptable uv coverage. In addition, the precision required to move and measure non-stationary telescopes during an exposure appears beyond the immediately foreseeable future technologies.

III.4 Optical Train

The optical train from the telescope entrance to the optical combiners will now be examined. The primary mirror reflects the light to the secondary mirror, creating an afocal beam 23 cm in diameter. This beam width was established on the basis of diffraction effects calculated from the Rayleigh criterion. At this diameter, the beam will be able to propagate across path lengths of 7500 m with small losses in fringe visibility due to diffraction. Once reflected off the secondary mirror, the beam is bounced through four reflections to the base of the telescope and then to the entrance to the coarse delay system as shown in Figure 27.

III.4.1 Delay Lines

Delay lines are needed so that the path lengths of all 18 incoming beams can be equalized. This is necessary in order to retrieve any data through the interference pattern (fringes). The layout of the delay lines is shown in Figure 28. When designing the delay lines, careful considerations were made on how to best avoid polarization effects. This problem was overcome by designing the lines such that each beam strikes the same number of mirrors, and is reflected through rectangular paths.[31] Light from each array element must reach the beam recombination station at the same time. Since our maximum baseline is 5000 m, the maximum path difference which must be accounted for is approximately 7500 m; these lengths must be corrected to nanometer accuracy in order to be able to construct true images. This task is accomplished through a three-tiered delay system, coarse, intermediate and fine. The optical configuration for a single telescope is shown in Figure 29.

The coarse delay system reduces the path differences to within 600 m. Light from individual array elements travels in a North-South direction until it encounters one of a set of two parallel East-West delay bands. The northern band handles light coming from all elements east of the instrument room (located 30m East of the center of the array along the East-West axis of the array), while the southern band handles light from elements west of the instrument room. Upon reaching these bands, the light hits a positionable mirror which deflects it to one of several fixed reflectors 24 cm in diameter (10 on the North band and 11 on the South), depending upon the path delay required. A schematic of the reflector is shown in Figure 30. In each delay band, the stationary mirrors are placed at approximately 600 m spacings, and tiered vertically such that the reflected beam may be directed over unused mirrors. Tables 6 and 7 show the location and relative heights of each reflector. The maximum height of the reflectors relative to the initial beam height is 1.9 m. The light bounces back from this mirror to another positionable reflector, which routes the beam to the intermediate delay system.

Light from the East-West delay bands is passed through a series of reflectors before entering the intermediate delay system. At this point, all 18 beams are in a single horizontal plane, and parallel to one another, traveling in an East-West direction.

The intermediate delay system is comprised of a set of reflective units. A schematic of one such unit is also shown in Figure 30. Light hits the top portion of this unit, and is folded through two reflections to exit the lower portion of the unit in the opposite direction. There are 18 of these reflectors, each mounted on its own set of 380 m long rails. The reflectors traverse the length of the rails during an observation. All beams exit the intermediate delay system in a parallel plane, slightly lower than the entry plane. This system reduces path length differences to within 2 m.

The fine delay system is housed within the instrument room. At the entrance to the instrument room, the parallel beams are compressed to a diameter of 2 cm each, spaced 30 cm apart. For each beam, the fine delay system employs a single linearly positionable reflector. The position of these reflectors must be controlled to nanometer accuracy. So that true images may be constructed, the final mirror of the fine delay system can be oscillated at a frequency of 40 Hz (as previously discussed). All beams exiting the fine delay system are equivalent in path length down to a few wavelengths. This set of beams hits a row of reflectors which reduce the spacing to 1 cm between beams. The maximum compensation of the fine delay system is 2 m.

At this point, all beams are in a single horizontal plane, and each beam has the same path length from the observed source. All beams encounter a beamsplitter which bleeds off approximately 10% of the light to the optical feedback for the pointing and control system. The remaining light enters the beam combiner, and is directed to the various detectors.

III.5 Beam Combination

At the end of the fine delay system there are 18 parallel light beams. These beams will be sent to one of two combiners. The main combiner will process beams in the wavelength ranges of 200 to 1000 nm, while the secondary combiner will be for beams having infrared wavelengths of 1 to 10 μm. Figure 31 shows a diagram of the main beam combiner. Each beam has a 2 cm diameter and the beams are 4 cm apart. Going into the main combiner, these beams are split into two parts and deflected 90° apart into 2 sets of 18 beams. Each set of beams is then reflected back 90° by aluminum coated mirrors placed at 45° angles to the beams' paths.

After these reflections, the paths of the two sets of beams will cross. At these intersections, beam splitters are placed to combine the light from two different telescopes. These beam splitters can be moved horizontally in order to combine the beams from different pairs of telescopes.

Passing the incoming beams through the combiner results in two sets of 18 combined beams. The beams are then sent to the aperture of one of the instruments which are all located 2.05 meters from the beam combiner (see Figure 32). From the combiner, each beam enters a prism made of fused silicon, SiO_2 (see Figure 33). The prisms have a height of 4 cm and angles of 30°, 75°, and 75°; the thickness is 3 cm. There are two such prisms at each of the 36 total combined beams (2 sets of 18), and two prisms at each of the six apertures (the four instruments and two null positions). Two prisms are needed to correctly direct the beams into the instruments. See Figure 34 for the aperture plane of the instrument package. The null positions are locations to which beams that aren't being processed are directed.

Before the main combiner, after the polarizer, up to six of the 18 beams will be reflected to the secondary beam combiner by movable mirrors. These mirrors are coated for infrared wavelength ranges from 1 to 10 μm. This secondary combiner will be initially constructed for six beams, but can be expanded to accommodate all 18 beams.

The same types of reflectors and splitters in the main combiner will be used in the secondary combiner. All of the reflective surfaces will be coated to optimize the infrared wavelength range specified above. The primary use of the secondary combiner is the study of infrared light in the search for planets. Figure 32 shows the placement of the instruments at the secondary combiner.

To obtain closure phases for imaging, more complicated schemes for combining three or more beams will be necessary.

III.6 Instruments

LOITA will utilize pupil plane interferometry which offers a variety detection schemes. Fringe detection and visibility measurements can be most easily accomplished in the pupil plane because imaging the fringes in that plane allows increased tolerance to the path length errors. Note that in order to resolve fringes in the focal plane of a system with a focal length f, it must be possible to resolve a distance of $f\lambda/B$. Assuming 4 μm pixel size projected for the detector, resolving fringes at 500 nm requires f = 40 km!

III.6.1 Array Instrumentation/Detectors

The instruments/detectors will be packaged together in a case of aluminum in order to allow for easier transport and placement. See Figure 34 for a diagram of the enclosure of the instruments. LOITA's instruments/detectors will include imagers and spectrographs for the spectral ranges of 200 - 400 nm (UV), 400 nm - 1 μm (visible - near IR), and 1 - 10 μm (IR). The

field of view (FOV) will vary from a few arcsec to 1 milli-arcsec and will depend on the bandwidth of the detected signals (FOV ~ $(\lambda/\delta\lambda)(\lambda/B)$). Low and medium spectral resolution CCD spectrometers will be used for imaging. Very large format CCDs will be needed for the wide-field imaging. A 1 arcsec field in visible light will require $50{,}000^2$ pixels. Assuming 4 μm pixels, the detector size will be at least 20 x 20 cm and it will be constructed as a mosaic (at least in the east-west direction) of monolithic CCD detectors. To minimize gaps in sky coverage due to inevitable, small spacings between CCDs, the largest possible CCDs (e.g., $10{,}000^2$) will be utilized (shown in Figure 35). To accommodate possible field curvature introduced by the optics, in the image forming plane, the CCDs can be bent. Finally, to maintain reasonable readout times, multiple simultaneous outputs will be incorporated.

Because the interferometric resolution is reduced in the infrared, the IR detectors will need somewhat less pixels. At 10 μm, the 4 arcsec field requires $10{,}000^2$ pixels.

An instrument containing a fiber optic cable and a CCD detector is used with the secondary (IR) combiner for planet detection purposes. The detector in this instrument is optimized for 1 to 10 μm ranges. This instrument will be discussed in a following section.

III.6.2 Astrometry

LOITA is expected to have great astrometric capability of near 0.1 μarcsec. Achieving this level of astrometric accuracy with a 5 km interferometer will require: (a) 2.5 nm accuracy in baseline measurements, (b) maintaining the angle between the telescopes used for astrometry to 0.1 microarcsec accuracy, and (c) extreme precision in fabrication and assembly of retroreflectors and optical components involved in the path length and baseline metrology. Therefore, the interferometers selected for astrometry would be furnished with specialized metrology and tracking/pointing systems and/or optical components capable of providing required levels of accuracy. Development of these systems entails significant technical challenges.

Wide-angle astrometry will use three or more connected interferometer baselines and a dedicated pupil-plane beam combiner. The phase and amplitude of the fringes will be measured using path length modulation over a wavelength in one interferometer leg. The detectors will be broad-band photon counters (avalanche photodiodes). It may be pointed out that 0.1 microarcsec astrometric accuracy should allow an indirect detection of an Earth/Sun - like system up to a distance of 12 parsec.

III.6.3 Single Telescope Option

One telescope will be capable of operating independently of the array to perform focal plane direct imaging. The telescope will perform direct imaging in the focal plane after removal of the tertiary (fold) mirror. This telescope will be equipped with four instruments: Wide Field and Planetary Camera, Faint Object Camera, High Resolution Spectrograph, and the Faint Object Spectrograph. These instruments are based upon those used aboard the Hubble spacecraft. The instruments would be housed beneath the telescope. All instruments are operated at a minimum temperature of 70 K to optimize performance. The telescope would offer significantly better performance than the Hubble Space Telescope because of excellent stability, long observation times and improved pointing/tracking capability allowed by the lunar location. Conceivably, this telescope could even detect large planets around nearby stars by using long exposures, photon-counting mode, coronagraphic masks and electronic image subtraction when the telescope is rotated about its optical axis to various angles on the detector. The process of image subtraction would remove the pattern of stray light while leaving the planet image at various angles corresponding to those at which exposures were made.

III.6.3.1 Wide Field and Planetary Camera

The Wide Field and Planetary Camera (WFPC) shown in Figure 36 has an estimated mass of 250 kg. The WFPC is estimated to use about 150 W of power during a normal operation. The WFPC consists of two cameras: the Wide Field Camera (WFC) and the Planetary Camera (PC). The WFC is used to image large areas of the sky and study galaxies or clusters of galaxies. The PC is used with short exposure times for higher resolution of images of planets and galaxies, and possible extra-solar planets.

III.6.3.2 Faint Object Camera

The Faint Object Camera (FOC) has a mass is 320 kg and uses 150 W of power during normal operation. The capabilities of the FOC include imaging of the faintest objects (such as possible planets) as well as providing the sharpest images of bright objects. A schematic of the FOC is shown in Figure 37.

The FOC is made up of two cameras -- one with an effective focal ratio of F/9.6 to provide the high resolution of bright objects; the other has an effective focal ratio of F/19.2 which is used to image possible planets near bright stars. The second camera also has the option of having a focal ratio of F/57.6 for even higher resolutions of a smaller FOV.

III.6.3.3 Spectrographs

The High Resolution Spectrograph (HRS) is used to produce a detailed spectrum of partial UV, visible, and infrared spectra. The mass of the HRS is 225 kg with a peak power requirement of 200 W. A schematic of this instrument is shown in Figure 38. The Faint Object Spectrograph (FOS) is used in creating a detailed spectrum of very faint objects detected by the telescopes. The entrance to the instrument (see Figure 39) has multiple aperture capabilities by using a motorized disc containing a variety of apertures. The disc contains apertures for maximum light, optimum spectral resolution and to isolate targets in crowded fields. The overall mass is approximately 250 kg, and the estimated peak power requirement is 200 W.

III.6.4 Infrared Detector for Planet Detection

This instrument is located with the secondary combiner (see Figure 32). A schematic is shown in Figure 40. It consists of a fiber optic cable and a CCD detector. The focal ratio for this instrument is 115.2. The detector is coated to optimize the wavelength ranges of 1-10 μm.

The fiber optic cable will be used with beams that have gone through the star-light cancellation process. It will be a used in the search for extra-solar planets. If a planet is detected then the light beam may be redirected through the main combiner to one of the other instruments for further study.

The fiber optic cable will act as a filter for stray light. It will be single-mode and made of a Germanium (Ge) core and a pure silicon (Si) cladding. The cable performs better when the core material has an index of refraction only slightly higher than the cladding. For Ge, n = 4.00 and for Si, n = 3.45. The diameter of the core is 8 microns, and the diameter of the cladding is 30 microns. The fiber is supported by a silica tube of diameter 160 μm.

The light from the aperture is focused by a lens onto the fiber optic cable. The cable is approximately 1.5 meters long. When the light comes out of the cable it is focused by a lens onto the CCD detector, and the image is read out.

III.7 Planet Detection Scheme

Of the detection techniques that were examined, apodization and nulling interferometry were selected as being the most feasible solutions. Nulling interferometry has been selected over apodization as the planet detection scheme for LOITA. The nulling interferometry system offers ease of installation and operation since its components are centrally located within the instrument room instead of at each telescope. Observations with the specific aim of detecting nonsolar planets will be made in the infrared. This system will be able to achieve starlight cancellation at a level of

10^8. For detection at a wavelength of 10 μm, the required pointing/tracking accuracy will be 40 microarcsec (10% of the angular resolution).

III.7.1 Selected Design

The technique employed in this design is an adaptation of the achromatic nulling interferometer[30,32]. Two separate and independent polarizing arms are used for any pair of beams. The polarizing arms are shown schematically in Figure 41. The primary feature is that the light path through each arm is identical in length so that the nulling is due to only a polarization flip, rather than interference. As can be seen in the figure, a majority of the structure of each arm is identical.

The polarizing arms will be situated in the lower level of the instrument room just ahead of the beam combiner. When not in use, the top-most reflectors on each arm will retract straight down so that they are not in the beam path. Also, each arm will rest on a set of tracks (perpendicular to the beams) so that they can be moved from one beam to another. All of the reflecting surfaces will be coated with aluminum and will have tolerances matching those of the primary mirror.

For any telescope pair, one beam would travel through arm 1 while the other beam would travel through arm 2. Upon leaving the polarizing arms, the beams travel to the combiner where they are combined. The nulling actually occurs at the combiner. The combined beam is then reflected to the Infrared Detector.

Before any observation can be made, the baselines to be used must be selected. For planet detection, only two baselines are absolutely necessary (one North-South and one East-West, utilizing 4 telescopes). With this system, a maximum of nine baselines can be utilized during one observation.

III.7.2 Choice of Wavelength

The primary factor in determining the wavelength at which these observations will be made was the time required to detect the planet. The signal-to-noise ratio determines the required observation time to detect a planet.

Calculations were first performed assuming that an Earth-like planet could be detected through observations made in the visible spectrum (500 nm) and that the planet was 10^{-9} times as bright as the parent star. The calculations revealed that the detection of an Earth-like planet at 3 parsecs required an observation time of 61 days (10 nm bandwidth, utilizing all 18 telescopes). Since the array will have many missions, a single application that absorbs 4.5 months of

observation time is unreasonable. Therefore, detection of Earth-like planets in the visible spectrum is not feasible.

In the infrared, the planet emits its own radiation. The ratio of infrared powers received in a narrow band from the star and planet is given by:

$$P_p/P_s = (T_p/T_s)(D_p/D_s)^2,$$

where T is the temperature and D is the diameter. Using the following values: $T_p = 128$ K, $T_s = 5800$ K, $D_p = 12756$ km (Earth), and $D_s = 1.39 \times 10^6$ km, we find

$$P_p/P_s = 1.86 \times 10^{-6}.$$

There is a component of stellar infrared radiation reflected from the planet, but it is negligible. Now, for a wavelength of 1000 nm and a bandwidth of 10 nm, the required observation time is only 4.5 hours to detect an Earth-like planet at 3 parsecs (utilizing only 4 telescopes). The same calculation was performed for a Jupiter-like planet at 10 parsecs. P_p/P_s is then 2.27×10^{-4} and the required observing time is 30 minutes (4 telescopes).

Since the required observing time is greatly reduced, observations with the specific task of detecting planets will be made in the infrared. The observation time is further reduced as the wavelength is increased.

TABLE 5. TELESCOPE LOCATIONS

given in meters
origin is at center of array

Telescope	X (East-West)	Y (North-South)
1	2500	0
2	1606.965	1915.11
3	-1056.545	2265.765
4	-2414.81	-647.045
5	855.05	-2349.23
6	1915.11	1606.965
7	-2500	0
8	1433.94	-2047.88
9	-434.12	2462.015
10	0	-2500
11	-217.885	2490.485
12	1056.54	-2265.77
13	-2165.06	1250
14	2349.23	855.045
15	-217.885	-2490.485
16	-1767.75	-1767.75
17	434.11	2462.02
18	2462.015	434.125

TABLE 6. NORTH DELAY BAND

all dimensions in meters
Height is relative to initial beam height

Distance East	Height	Distance West	Height
0	0.0	600	0.46
600	0.23	1200	0.23
900	0.46	1800	0.0
1200	0.69		
1500	0.92		
1800	1.15		
2100	1.38		

TABLE 7. SOUTH DELAY BAND

Distance West	Height	Distance East	Height
0	0.0	340	1.15
480	0.23	940	0.92
1080	0.46	1240	0.69
1800	0.69	1840	0.46
2205	0.92	2140	0.23
		2440	0.0

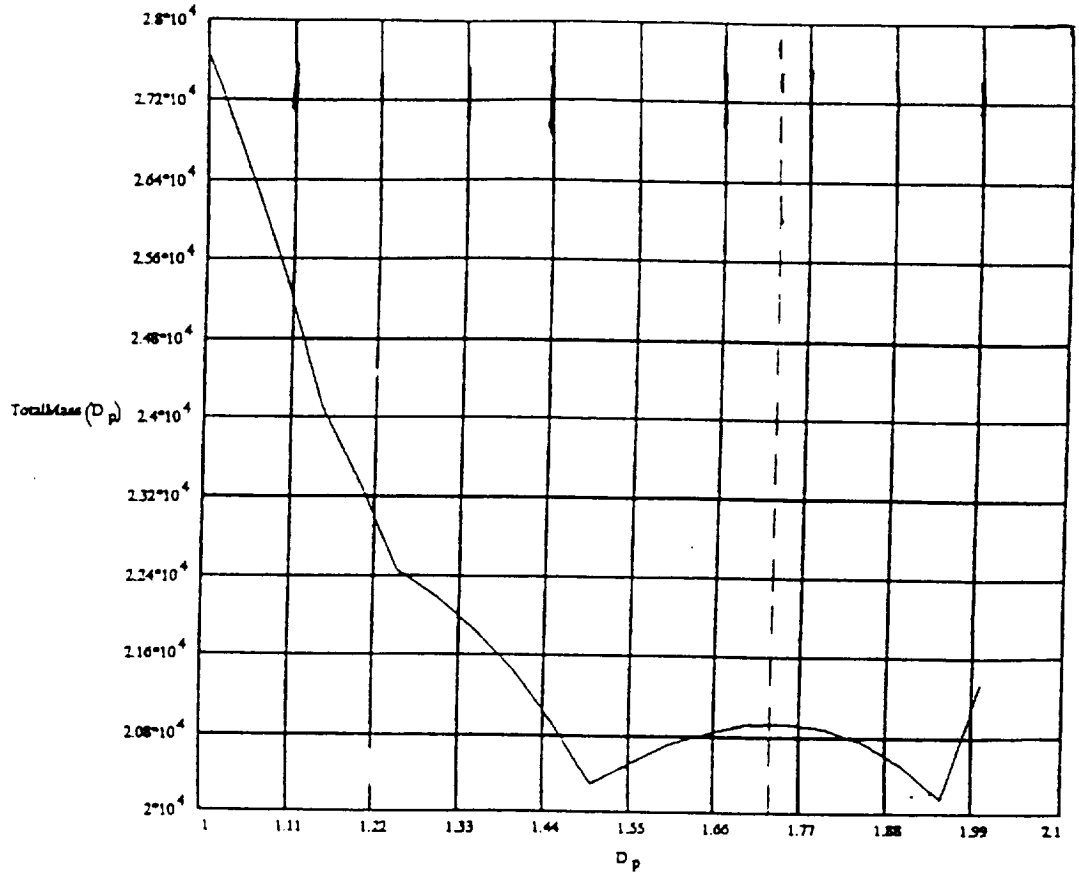

TotalMass - Total array mass (kg)

D_p - Diameter of primary mirror (m)

FIG. 16. Total Array Mass vs. Primary Diameter

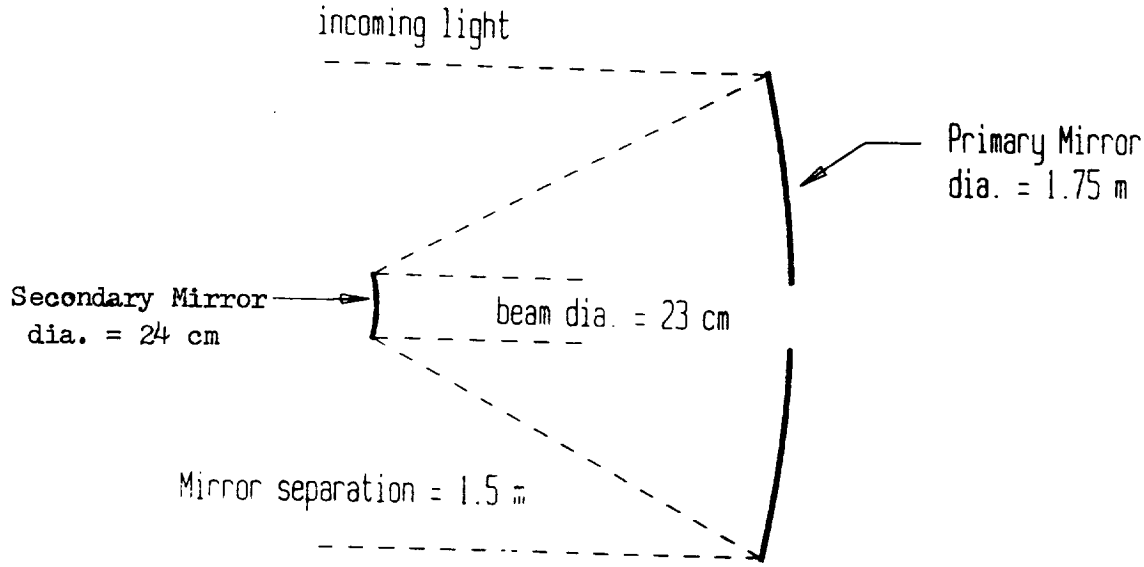

FIG. 17. Telescope Optics

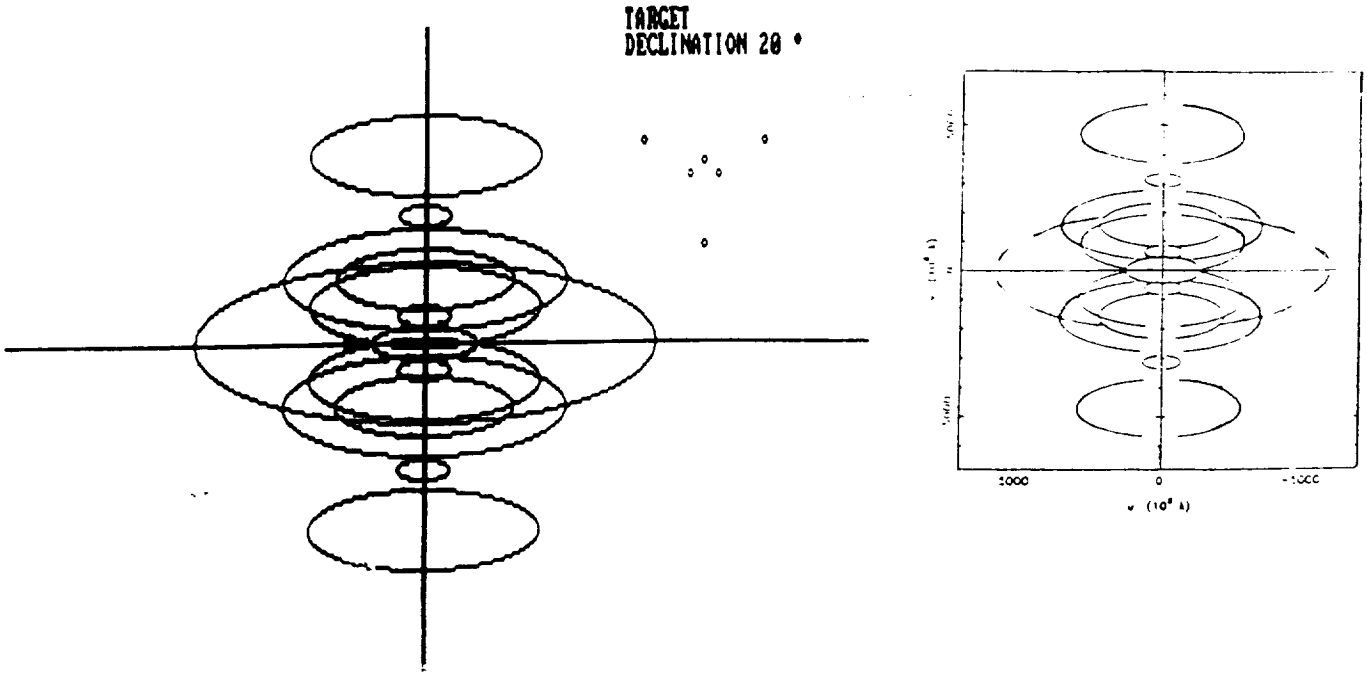

a. Our Program

b. FAKE (ref.16)

FIG. 18. Comparison of Our Program and FAKE

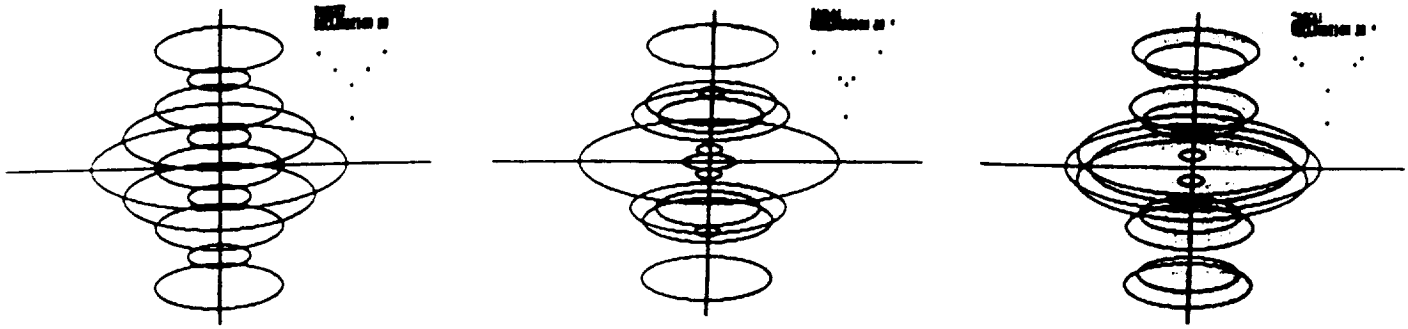

a. Case 1

b. Case 2

c. Case 3

FIG. 19. 6 Element Y-Type Configurations

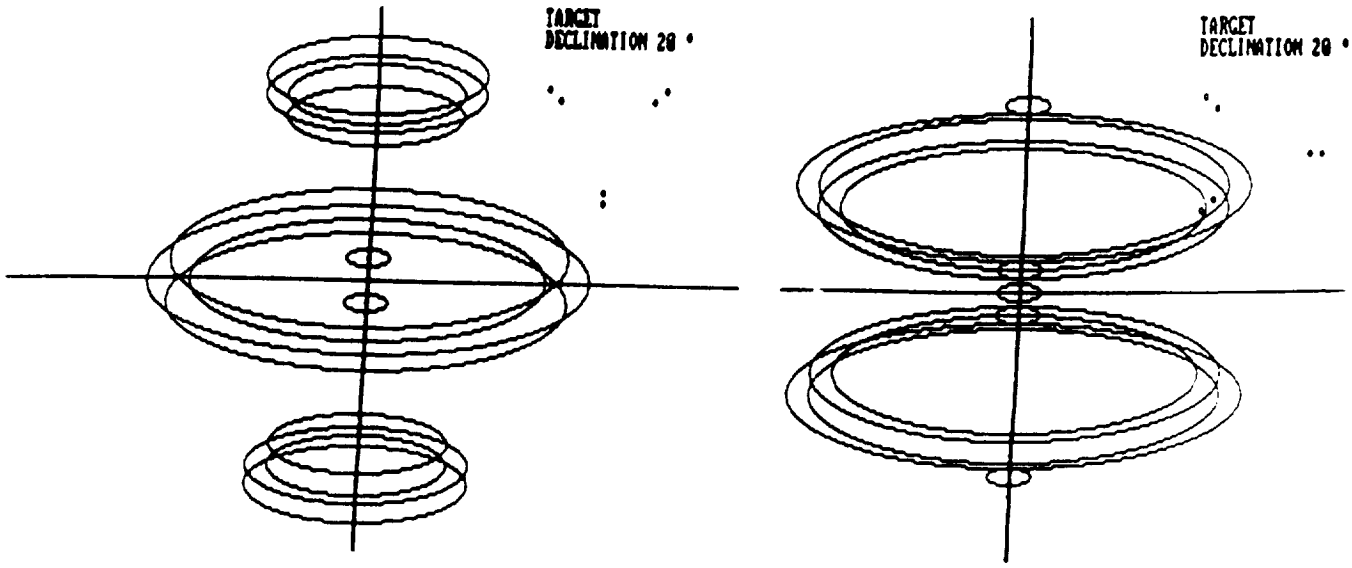

a. Case 4 b. Case 5

FIG. 20. Coverage Effected by Rotation of Y-Type

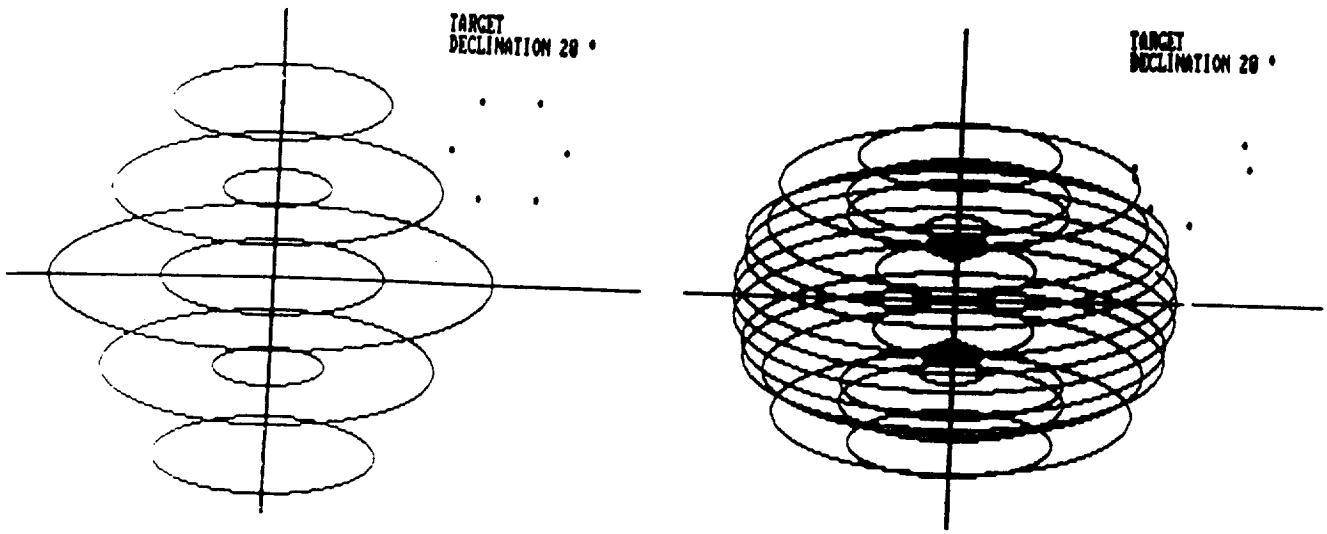

a. Evenly Spaced b. Unevenly Spaced

FIG. 21. Effect of Spacing on 6
Element Circular Array

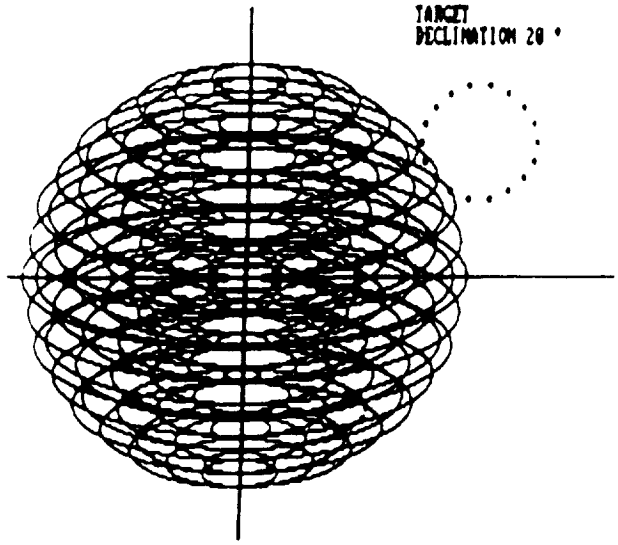

a. Evenly Spaced

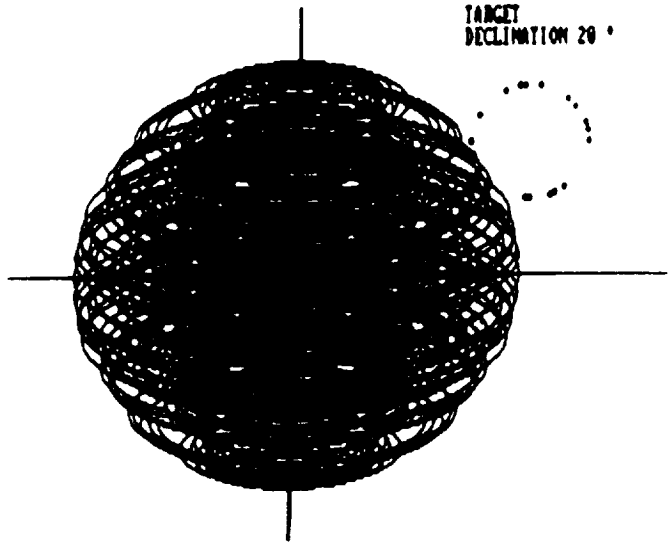

b. Unevenly Spaced

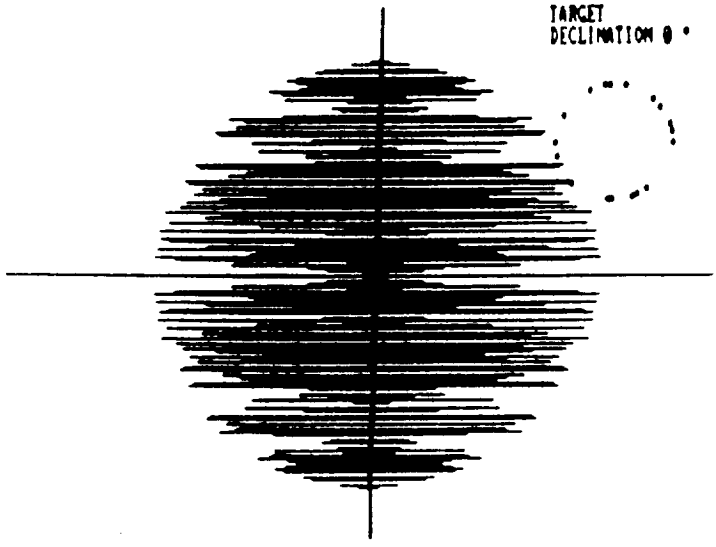

c. Unevenly Spaced, Target Declination of 0

FIG. 22. 18 Element Circular Array

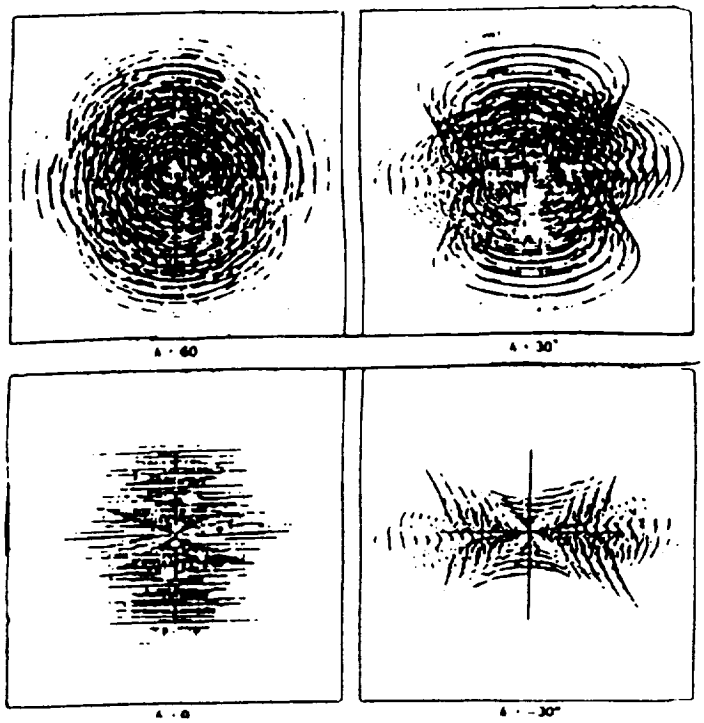

FIG. 23. Y-Type, VLA Coverage
(ref. 16)

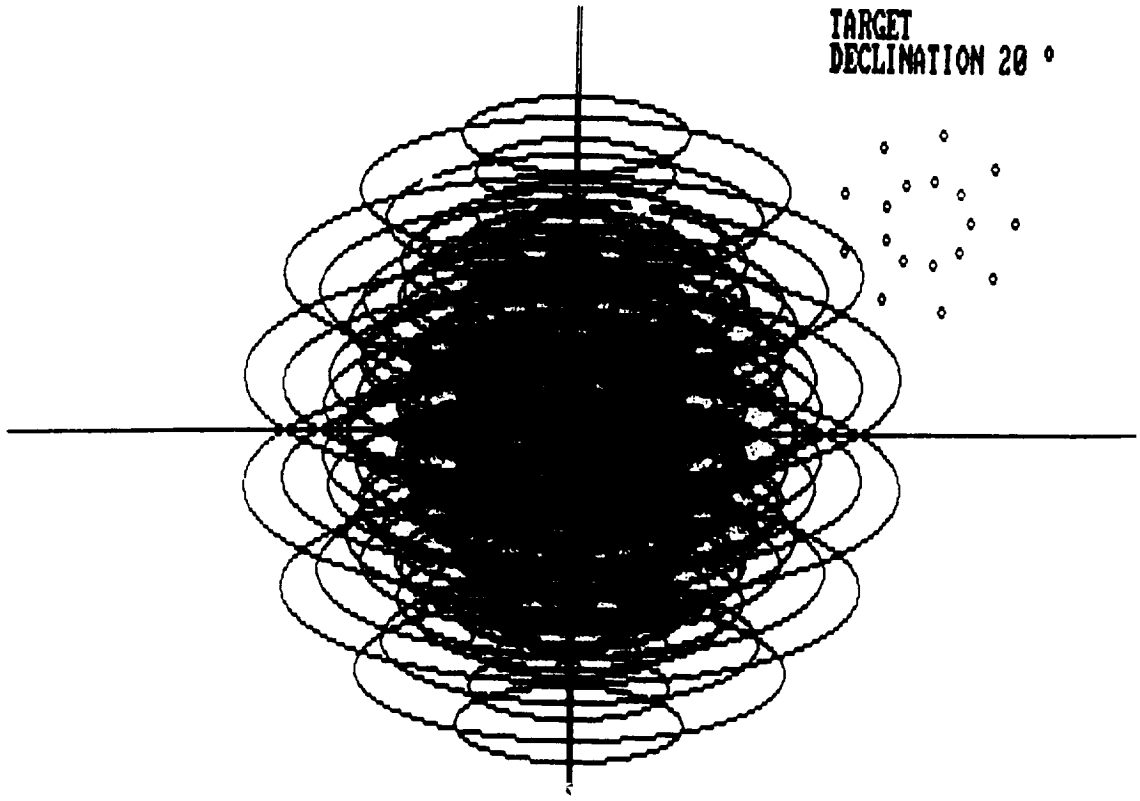

FIG. 24. Concentric Circles with 18 Elements

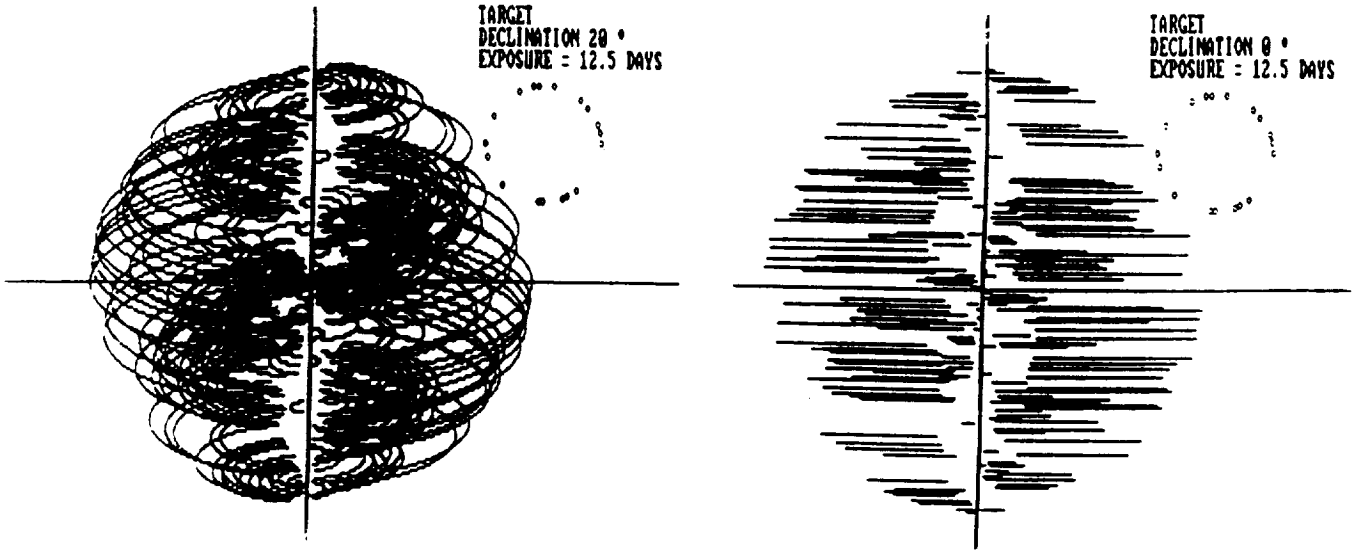

a. 12.5 Day Exposure

b. 12.5 Day Exposure, Target Declination of 0°

FIG. 25. Finite Exposure

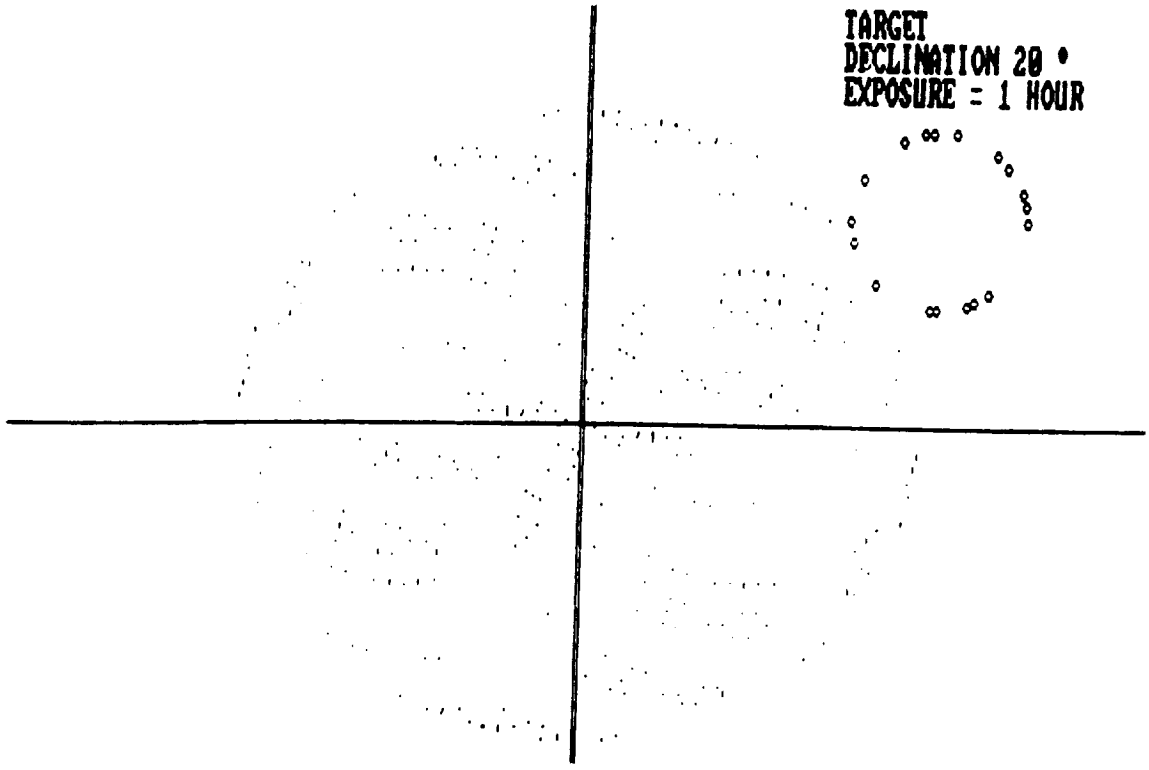

FIG. 26. Snapshot Coverage (1 Hour)

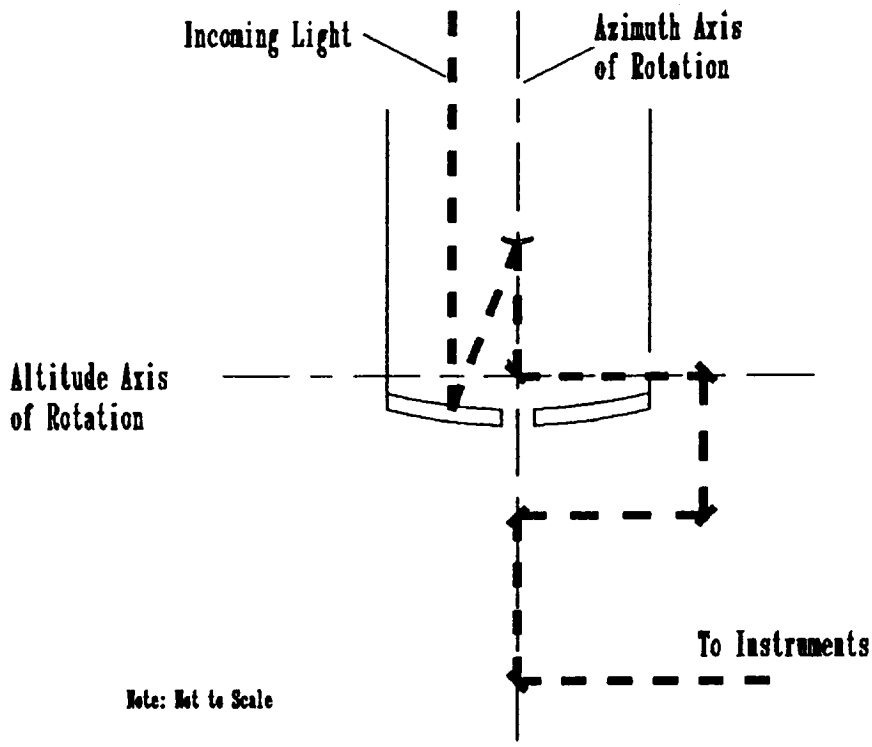

FIG. 27. Beam Control

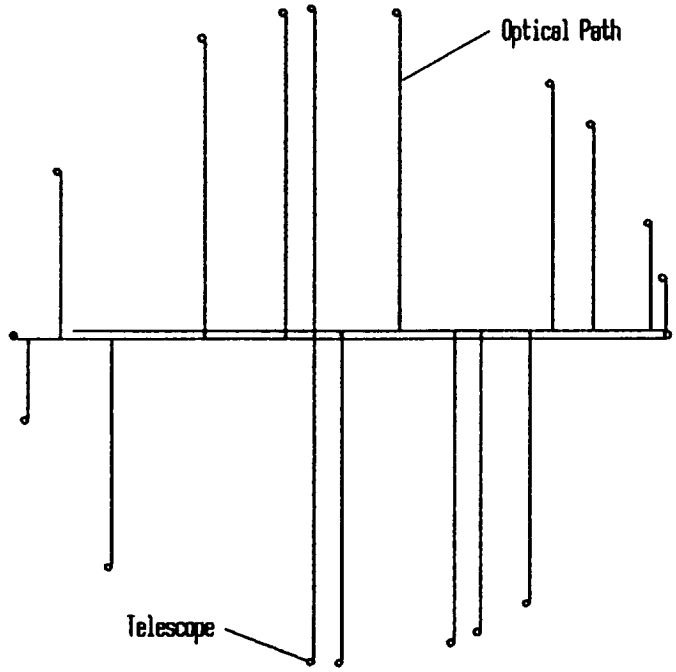

FIG. 28. Optical Paths

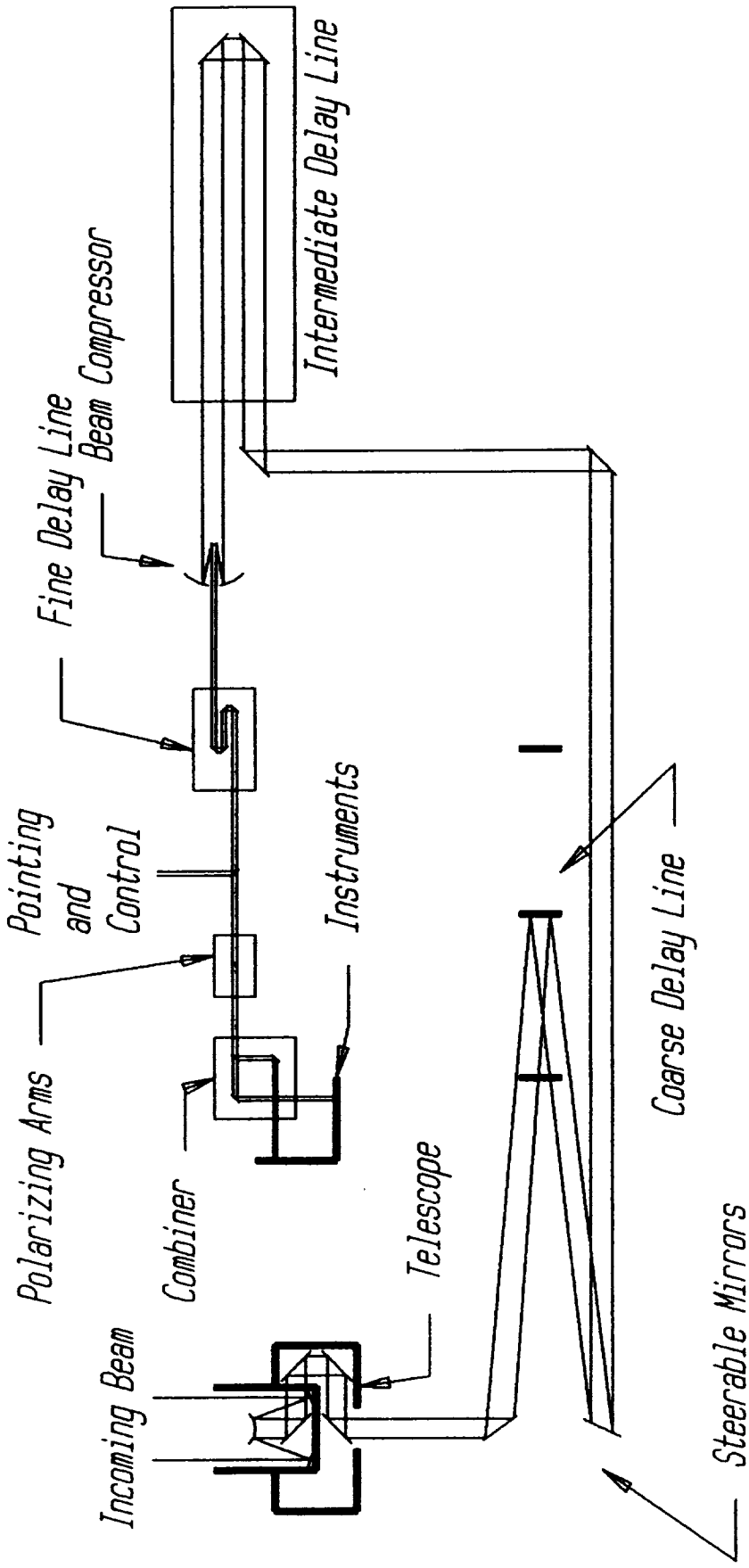

FIG. 29. LOITA Optical Configuration

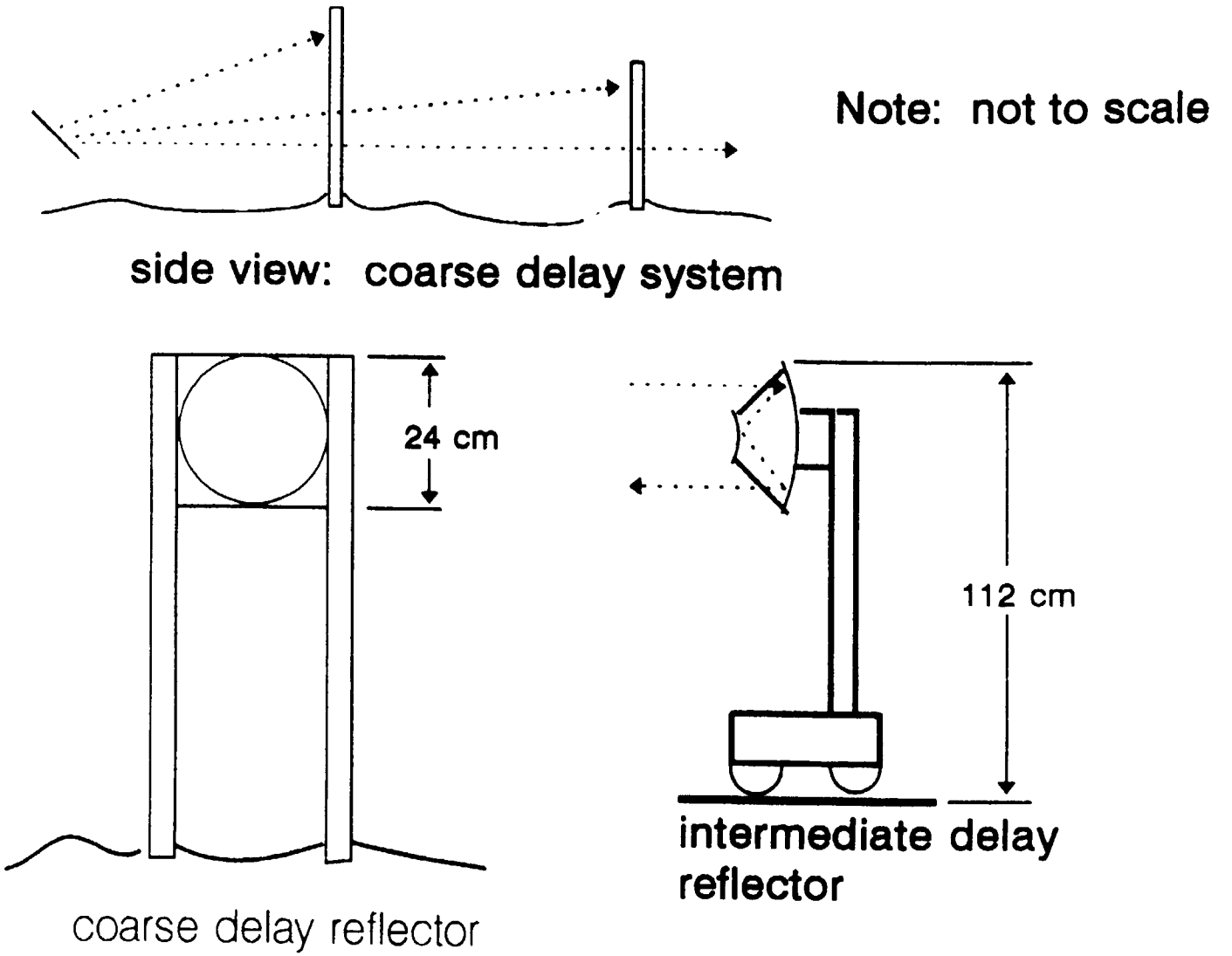

FIG. 30. Schematic of the Reflectors

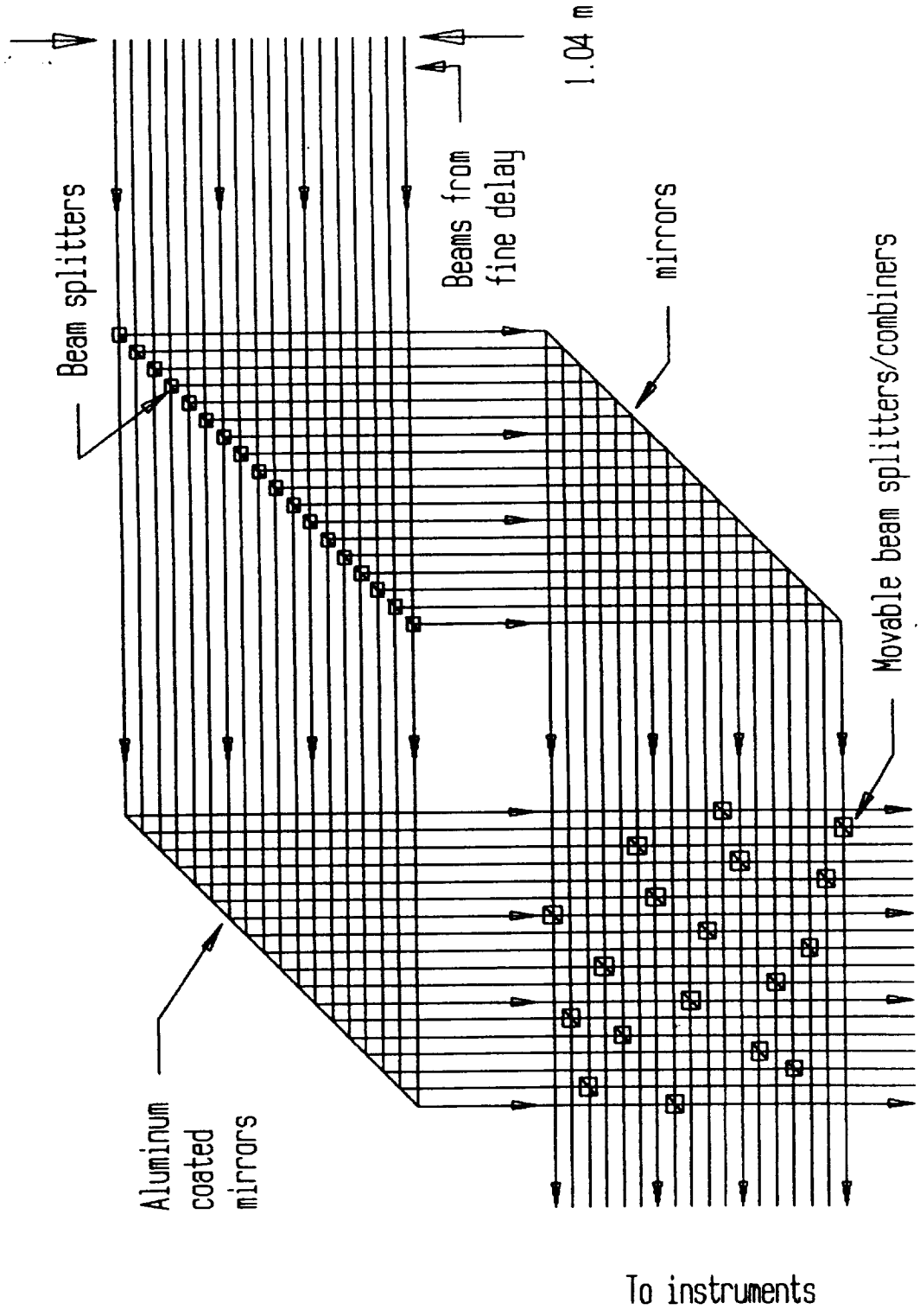

FIG. 31. Beam Combiner

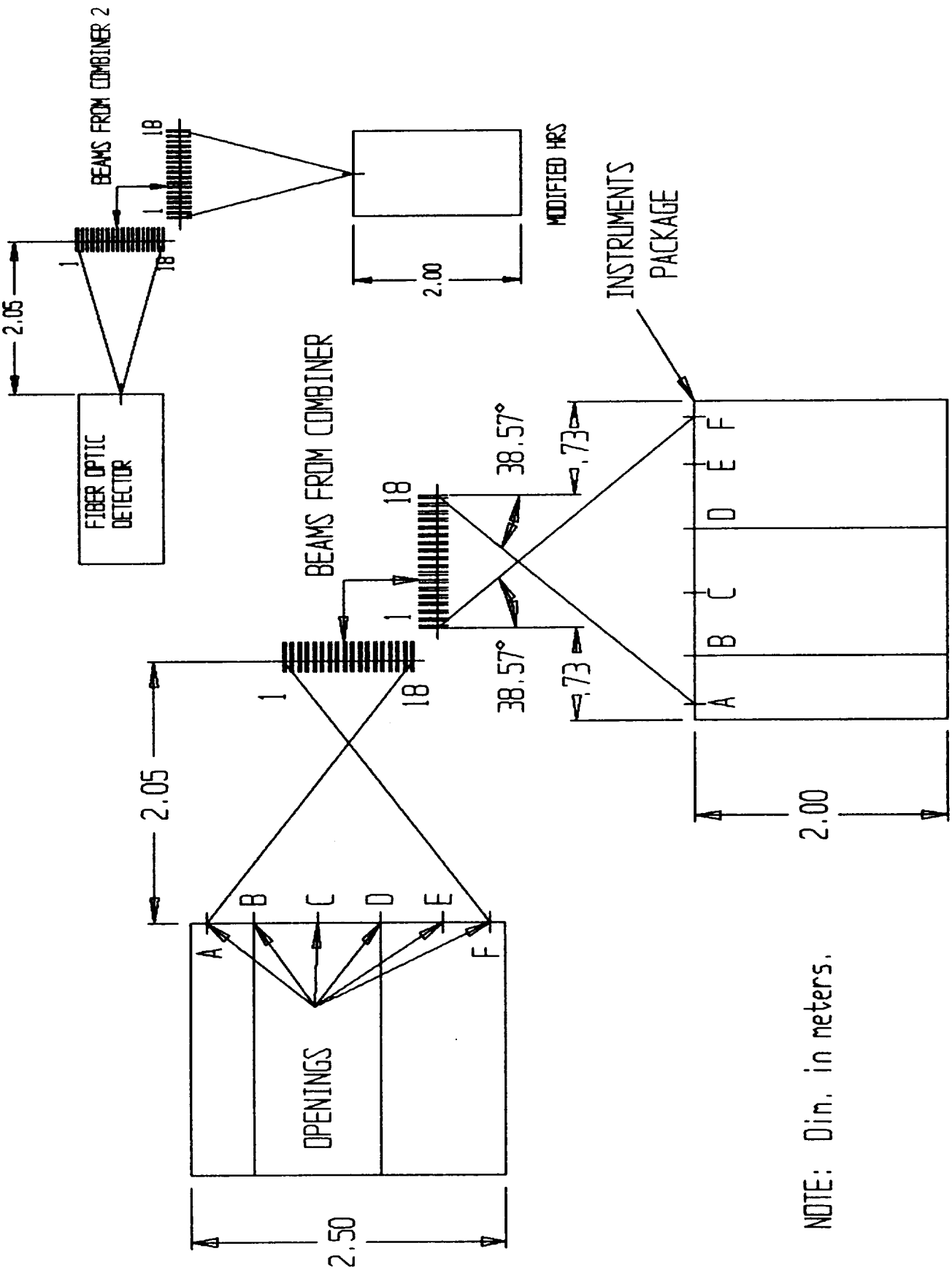

FIG. 32. Reflecting of Beams into Instruments

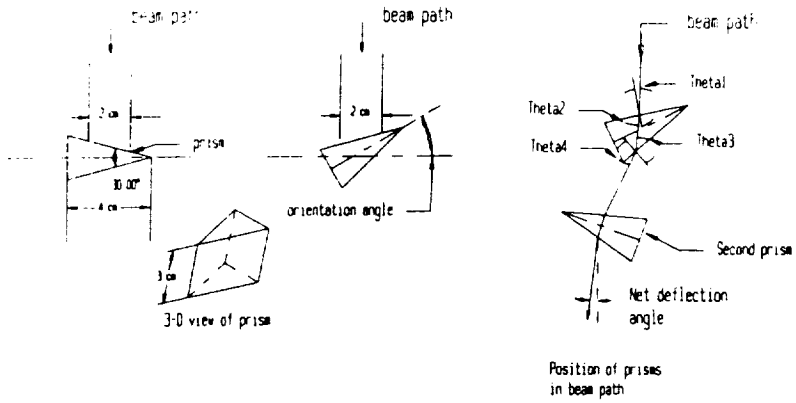

FIG. 33. Schematic of Prisms

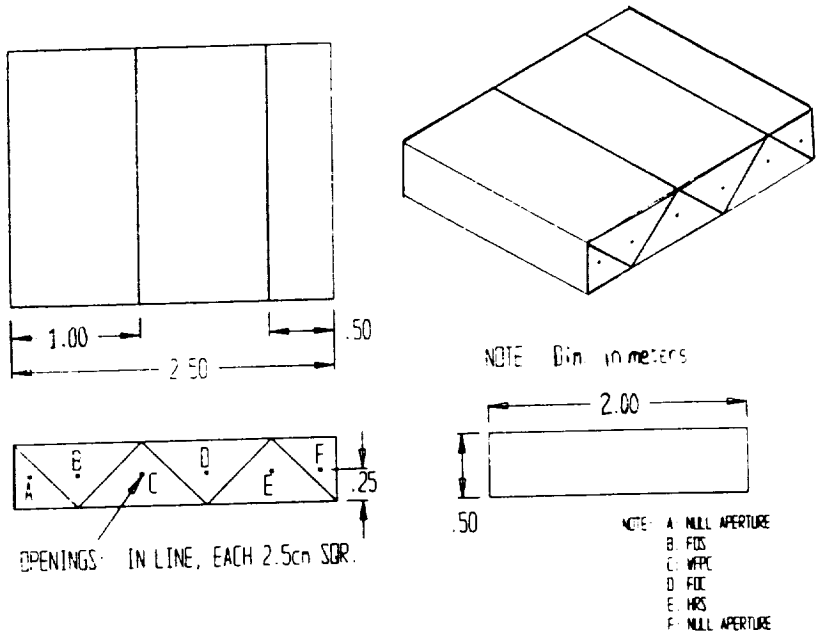

FIG. 34. Structural Enclosure of Instrument Package

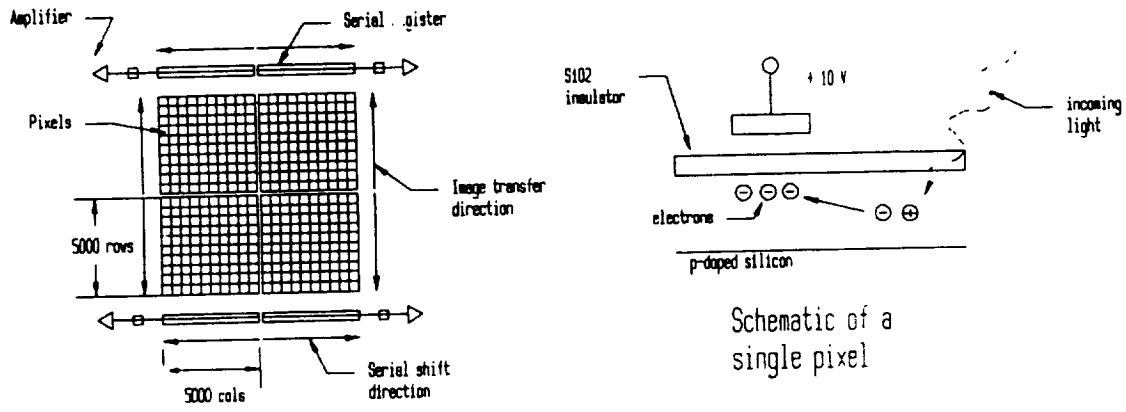

FIG. 35. Schematic of CCD

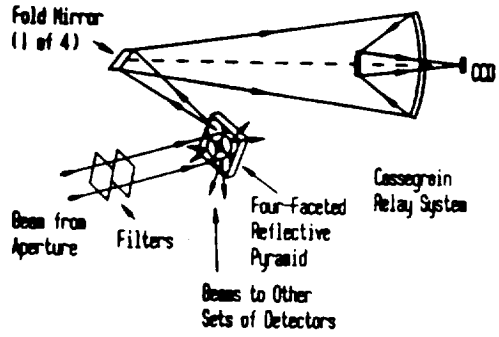

FIG. 36. Schematic of Wide Field and Planetary Camera (WFPC)

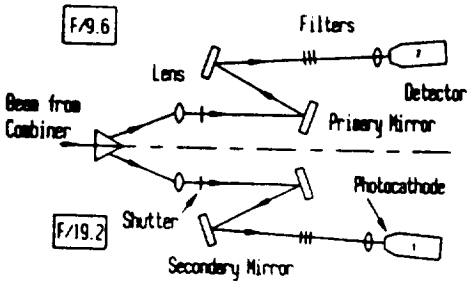

FIG. 37. Schematic of Faint Object Camera (FOC)

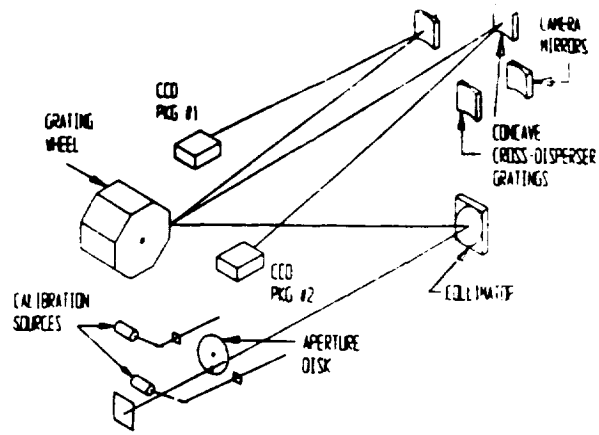

FIG. 38. Schematic of High Resolution Spectrograph (HRS)

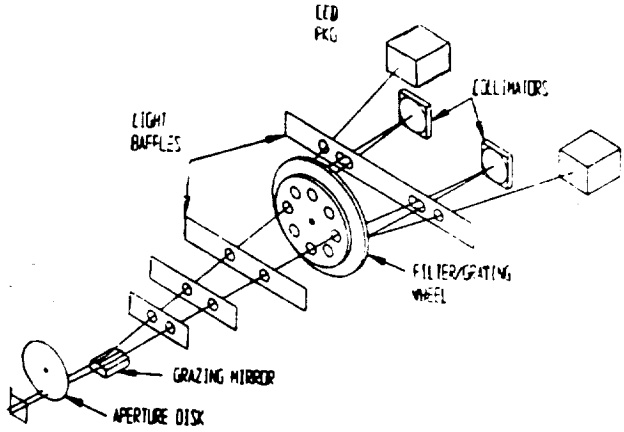

FIG. 39. Schematic of Faint Object Spectrograph (FOS)

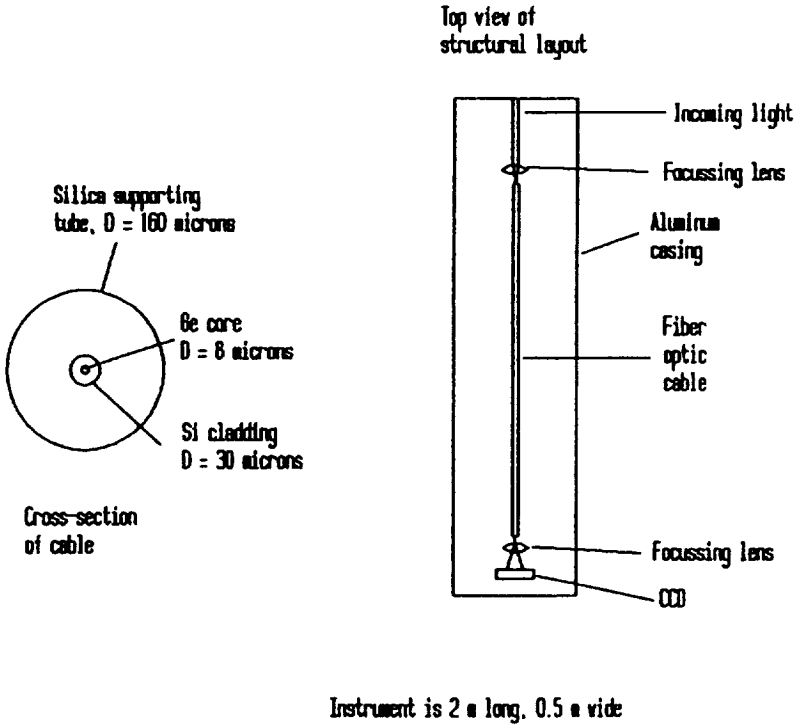

FIG. 40. Infrared Detector

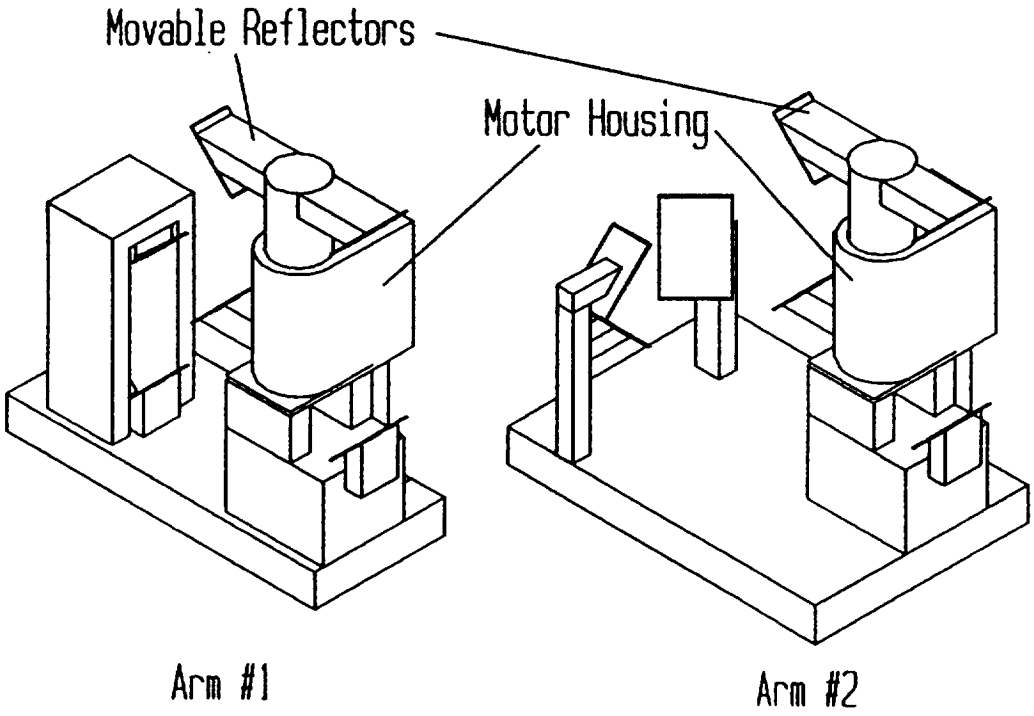

FIG. 41. Polarizer Arms

IV. Metrology

In order to accomplish the objectives of this array, it is necessary to make very accurate measurements of large distances. The only technique that presently appears capable of meeting these requirements is laser metrology. This section analyzes the various requirements associated with the project and investigates the application of this technology.

Two different types of measuring systems are required for the operation of LOITA. One is used to fix the geometry of the array. This is accomplished via external metrology towers which work in tandem to locate the position of each telescope. The other system is used internally to determine the path length of the complete optical train for each member of the array. This data is used to maintain equal path lengths between all of the telescopes.

IV.1 Internal Metrology

The accuracy of the internal metrology system must be such that it is possible to maintain equal optical path lengths from each telescope, through the delay system, and on to the beam combiner. The optical paths must be continuously corrected so that coherence is maintained between light beams coming from each of the telescopes. Image reconstruction is accomplished through Fourier analysis of the combined light beams. Error in the equalization will result in a degraded image quality. Maintaining the optical path lengths within three or less wavelengths (1200 nm) of each other should provide adequate fringes for quality image reconstruction.

There are two different types of laser metrology systems that are used to measure distances in this realm of accuracy. The first, and simplest, is the time of flight or pulse method. The other, is that of interferometric metrology. Separate discussions of these techniques follow.

IV.1.1 Pulse Metrology

Time of flight metrology is a radar-like technique that utilizes laser beams instead of radio waves. A laser pulse is emitted from a source and passes through a beam splitter as detailed in Figure 42. The camera registers both the initial pulse, and then the targeting pulse. Geometry shows that this results in a measurement of the laser travel time from the beam splitter to the target. The primary source of error in such a system is the temporal accuracy of the detection unit. It has been demonstrated that modern sweep cameras can measure the incoming pulse with a temporal width on the order of 1 ps[73]. This corresponds to an error of 300,000 nm.

IV.1.2 Interferometric Metrology

A more promising technique of distancing is that of interferometric laser metrology. A schematic of a laser interferometer is shown in Figure 43. A laser emits a continuous beam which enters a beam splitter. As in the pulse method, one of the beams is directed to a stationary mirror that is located near the laser. The other beam is sent onward to the reflector positioned on the target to be distanced. Both beams return to the beam splitter where they are recombined and interfered. The interference fringes are monitored by a CCD or a simple photoreceiver. Any change in the path length of either of the laser beams will be indicated by a motion of the interference fringes. The beam reflected from the plane mirror is used as the reference wave. Hence, any motion of the reflector can be ascertained. This simple approach does not yield the absolute distance, however, unless this distance is less than the laser wavelength.

Very powerful techniques for ranging using absolute distance interferometry (ADI) have been recently developed using data from more than one laser wavelength[70]. Two observations are performed for each distance measurement. The laser is first set to frequency 1 and allowed to travel through the system. The phase (θ_1) of the interference is recorded. This is the phase of the laser beam after traveling the path length difference between the stationary mirror and the reflector. Measurements are then made after the laser is switched to frequency 2. The phases are given by,

$$\theta_1 = z / \lambda_1 \quad \text{and} \quad \theta_2 = z / \lambda_2$$

where z is the difference in path lengths traveled by the two beams between the time they are split and when they interfere on the CCD, and λ is laser wavelength. Either measurement alone is ambiguous in determining the absolute distance because all distances that contain multiples of the particular wavelength have the same phase. Combining the two, however, yields,

$$\text{(a)} \qquad \theta_1 - \theta_2 = \theta_L = z \left(1/\lambda_2 - 1/\lambda_1 \right) \approx z/\lambda_L$$

where

$$\text{(b)} \qquad \lambda_L = \lambda^2 / (\lambda_2 - \lambda_1)$$

and λ_L is called the synthetic wavelength. The distance that can now be determined without ambiguity must be within this synthetic wavelength. By thinking of the many complete waves and the one incomplete wave that occur over the distance z, it can be noted that,

$$\text{(c)} \qquad z = (N_1 + \theta_1) \lambda_1$$

where N_1 is an integer, and phase is measured in fractions of a wave. Combining (c) and (a)-(b) yields,

$$(N_1 + \theta_1) \lambda_1 = (\theta_L) (\lambda_L)$$

which determines N_1. Substituting N_1 into (c) yields z, the absolute path length distance between the stable mirror and the reflector. The smallest difference between two frequencies in a tunable laser is approximately 0.1 Å. The corresponding synthetic wavelength is 0.036 meters. The

geometry of the array will be known within this level before the use of any metrology. Interferometric metrology alone, therefore, will be capable of measuring the necessary distances.

The error of such a system can depend on several factors.[70] On the moon, however, only the instability of the laser frequency will be important. Any difference in the actual wavelength from the wavelength being used in the above calculations will result in an error. Instabilities of $\delta(\lambda)/\lambda$ are currently obtainable below 10^{-9} and may reach less than 10^{-12} in the foreseeable future. This results in metrology errors of 7500 nm and 75 nm, respectively (with a 600 nm laser over a 7.5 km measurement). This system will be capable of equalizing path lengths from within 19 waves, downward to potentially less than a fifth of wave.

IV.1.3 Laser Selection

The process of selecting a laser involves examining several criteria. The laser should have a wavelength larger than 400 nm so that the reflectance of the reflector will be relatively large (>90%).[77] This detail will be discussed a little later. The output power of the laser should be such that the beam entering the detection system has sufficient strength to permit fringe analysis. Beam divergence should be kept to a minimum so that the overall efficiency of the laser can be maximized. The lifetime of the laser should be as large as possible to prevent frequent replacements of the units. Table 8 gives detailed information concerning this list of criteria for four promising lasers.[70] A brief analysis of each of these follows.

The carbon dioxide (CO_2) laser is very powerful, but its characteristic wavelength of 10,600 nm is much too large to provide the accuracy required for this scheme. The beam diameter of 10-20 mm is also very large. For these reasons, the CO_2 laser is unacceptable for this metrology system.

The neodymium-yttrium-aluminum-garnet (Nd:YAG) laser has a large wavelength of 1064 nm. The long-term stability prohibits its usage.

The helium-neon (He-Ne) laser is characterized by a respectable wavelength of 632.82 nm and a lifetime of 20,000 hr. However, the output power of 0.5-50 mW is rather small. In addition, the beam divergence of 0.5-2 mrad is too large.

The argon laser exhibits a reasonable wavelength of 514.5 nm, a relatively strong maximum output power of 100 mW, and an adequate lifetime (>13000 hr). In addition, this laser exhibits an extremely minuscule beam divergence of 0.4 mrad. The argon laser also has the ability to be pulsed at 100 picoseconds.

The LOITA laser metrology system will employ tunable solid-state lasers having stability of 10^{-12} for internal metrology and 10^{-9} for external metrology.

IV.1.4 Retroreflectors

Reflectors must be incorporated into the metrology system for the purpose of redirecting the laser beam back towards the detection unit. The reflectors must send the laser beams parallel to the incoming rays, but in the opposite direction. The reflectance should be as large as possible so that the strength of the beam returning to the detection unit will have the intensity needed to accurately perform the fringe analysis. The reflective material is normally a metallic layer which is 10,000-20,000 nm thick. Both silver and aluminum exhibit a reflectance in excess of 90%.

A retroreflector returns light back in the direction from which it originated. Some retroreflectors consist of a prism with three edges that intersect at right angles to one another. One such type of retroreflector is the trihedral mirror which consists of three perpendicular plane mirrors. A corner cube is an example of this type of retroreflector. A second type of retroreflector consists of a focusing element with a plane mirror in the focal plane. Several examples of retroreflectors, as well as a plane mirror, are shown in Figure 44. The hemispherical retroreflector will be used for this system because of its simplicity when compared to both the spherical cat's eye and the twin mirror cat's eye reflectors. In addition it has demonstrated an accuracy of 1/12 of a wavelength in the Mark III.[74] This would limit the maximum achievable accuracy to 43 nm.

For the internal metrology system, a total of 18 tiny retroreflectors will be required. Each one will be placed in the center of the secondary mirror of each telescope as shown in Figure 45.

IV.1.5 Detectors

The interferometric metrology system requires a system that is capable of measuring interference fringes. This can be accomplished with a single photodetector which will detect fringes as light and dark periods as they pass over the detector. Alternatively, a CCD could be used to record the interference plane. It appears at this time that the CCD would be best able to observe various fringe patterns.

The metrology system will have to initialize itself each time it starts a new measurement. The laser will not hit the retroreflector and return to the CCD if there exists even the smallest misalignment of mirrors between the laser and the telescope. The system will begin by sweeping a continuous laser beam until the camera detects the returning beam. The interferometer will be used to determine the path length as previously described. These measurements will be fed to the computer controlling the delay system so as to maintain equal paths. Since the interferometric system is continuous, it will maintain the error to a low level at all times. This will be maintained throughout a given exposure. The insertion of the laser beam into the optical path is demonstrated in Figure 46.

IV.2 External Metrology

The external metrology system establishes the topocentric baseline vectors of every possible pair of telescopes. The only change in these topocentric baselines will be a result of shifting in the array configuration.

These baseline vectors are constantly changing in the celestial sphere as the moon rotates relative to the observed source. Ergo, an exact determination of these baseline vectors will be required for uv plane analysis. The measurements of the baseline vectors will be less stringent than the measurements for internal metrology. The same system that is used for internal metrology, therefore, will be more than adequate for external metrology.

Four metrology towers will be positioned within the circular array as seen in Figure 47. The design involves each tower to be located 1.25 km from the center of the array in a square formation.

A single retroreflector shall be placed on the base of each telescope. Again, a plane mirror will not work in this case because four different metrology systems will each require the return of their laser beams from a single retroreflector. As before, the hemispherical retroreflector is selected. In this case, however, they will be approximately 8 cm in diameter to allow for ease in targeting.

IV.2.1 Operations

The first step in determining the geometry of the array will require each metrology station to distance each other metrology station. Hence the coordinate location of each station will be determined. The position of a single tower will be defined as the topocentric origin. Next, all stations will measure the distance to a given telescope. The measurements from the two metrology stations closest to the telescope being distanced, along with the location of these stations, will form a triangle as seen in Figure 47. This determines the location of the telescope in the ascribed coordinate system. The other metrology measurements will similarly define this location with decreasing accuracy. These measurements will be weighted less than the two primary measurements and will be used as verification. A greater number of metrology stations decreases the average distance from a given telescope to its closest station, thereby increasing accuracy.

Due to the curvature of the moon, the metrology towers will have to be at an elevation such that the farthest retroreflector from any given tower will appear above the apparent bulge of the surface. The set of metrology stations which are located in the eastern section of the array will be located closer to the instrument room. An analysis, shown in Table 9, revealed that the towers need to be 1.84 m and 1.92 m high to account for the curvature alone. The laser metrology towers

would require an additional elevation of 8 cm in order to account for the size of the retroreflectors. It is desirable to have the metrology system positioned higher than the point where the light exits the telescope so that the delay lines do not interfere with the path of the laser beams. By constructing the metrology towers so that the laser is positioned 1.92 m and 2.00 m high, the laser beam will travel above the delay lines until it is reflected by the retroreflector, and returned to the detection system.

All of the metrology lasers and retroreflectors will be in a horizontal plane. In this manner, any given laser can point at any given retroreflector by a simple rotation. Each of the four metrology towers will distance each telescope and each other tower in a coordinated cycle. The four systems will aim at a given single telescope and begin ranging via interferometric metrology as seen Figure 48. The location of the telescope will then be determined as discussed above. The four towers will then rotate towards the next telescope or tower to be distanced. Once the complete cycle of ranging is complete, the metrology systems will rest until another cycle is necessary.

The power requirements for each station must be estimated in order to design the power distribution scheme throughout the array as well as to estimate the total power demands of LOITA. Table 10 shows a breakdown of power estimates within the metrology system. A total demand of approximately 692 W is shown. This power consumption is heavily dominated by the lasers themselves. This is due to laser efficiencies on the order of 0.1%. A typical laser emits 1 W for every 1 kW consumed. Therefore an effort to reduce metrology power consumption should focus on creating more efficient lasers or using fewer lasers to perform the same tasks.

TABLE 8. LASER SPECIFICATIONS

Laser Type	CO_2	Nd:YAG	Ar	He-Ne
Wavelength (nm)	10600	1064	514.5	632.82
Output Power (W)	3000	>300 mW	20	0.0005-.05
Beam Divergence(mrad)	1.5-3	<2.4	0.40	0.5-2
Beam Diameter (mm)	10-20	0.9	1.9	0.5-2
Lifetime (hr)	NA	3000	13140	20000

TABLE 9. HEIGHT OF LASER METROLOGY TOWERS REQUIRED TO ACCOUNT FOR CURVATURE OF LUNAR SURFACE

POSITION X (km)	Y	HEIGHT OF STATION meters
1.25	1.25	1.84378
1.25	-1.25	1.84378
-1.25	-1.25	1.91570
-1.25	1.25	1.91570

TABLE 10. ANALYSIS OF POWER REQUIREMENTS

Item	Consumption per item
INTERNAL	
18 Lasers	25 W
18 CCDs	1 W
Total Internal = 468 W	
EXTERNAL	
4 Lasers	25 W
4 CCDs	1 W
4 Radial Motors	30 W
Total External = 224 W	
Total Metrology = 692 W	

Pulse Laser Metrology

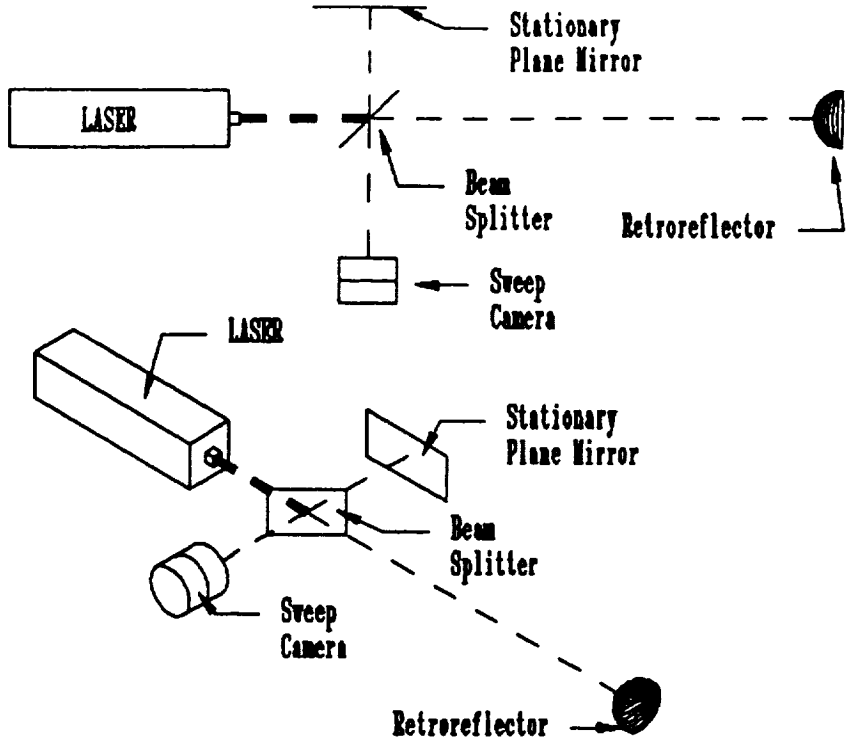

FIG. 42.

Interferometric Laser Metrology

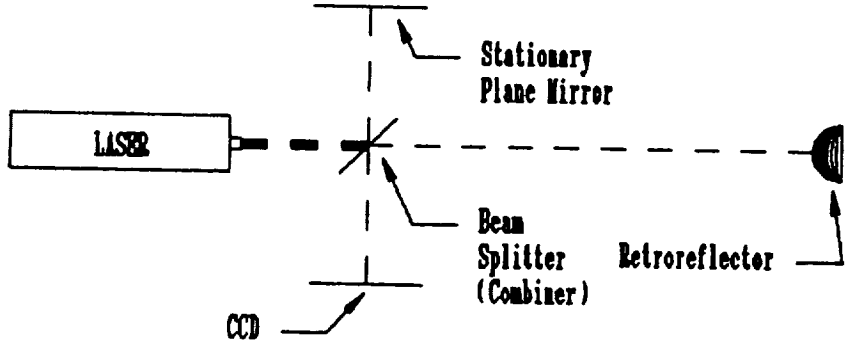

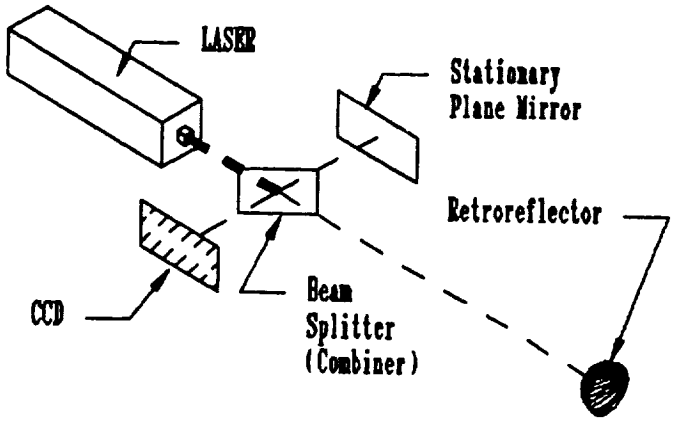

FIG. 43.

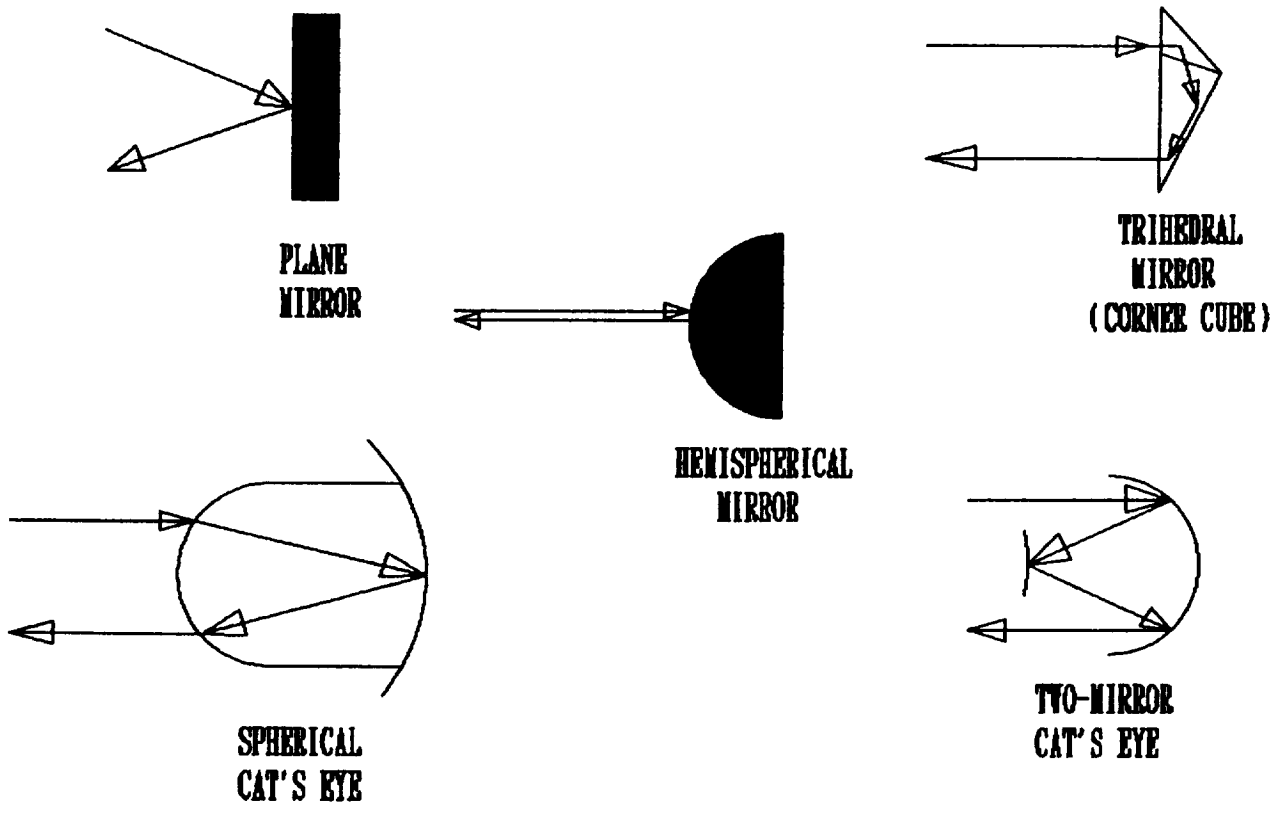

FIG. 44. Types of Retroreflectors

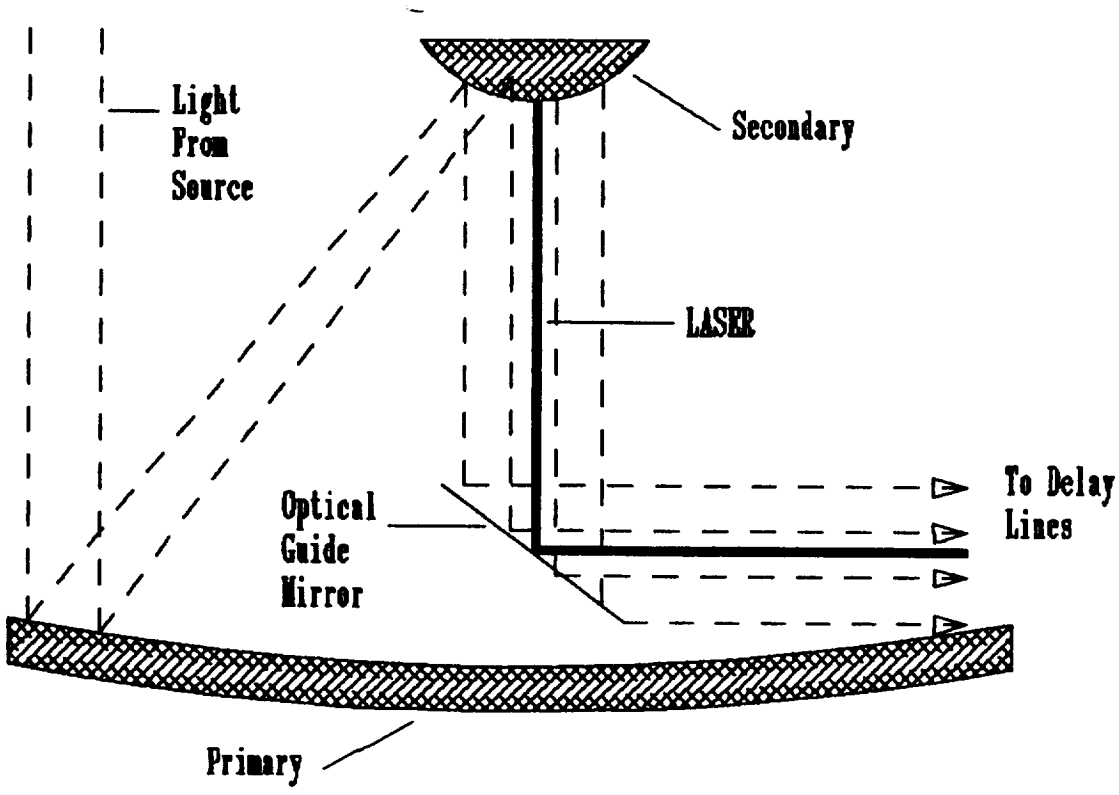

FIG. 45. Location of Retroreflector on Secondary Mirror

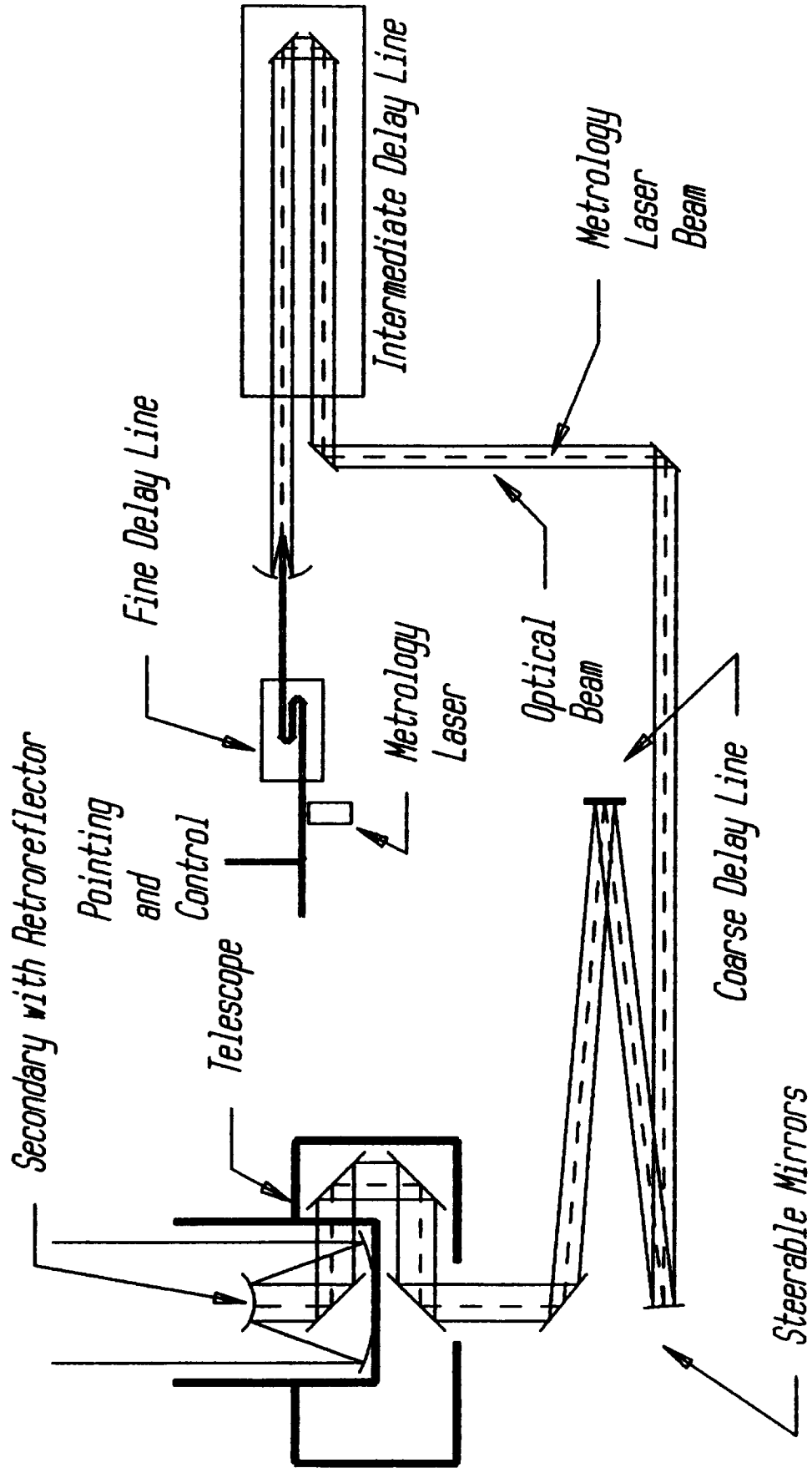

FIG. 46. Insertion of Laser into Optical Path

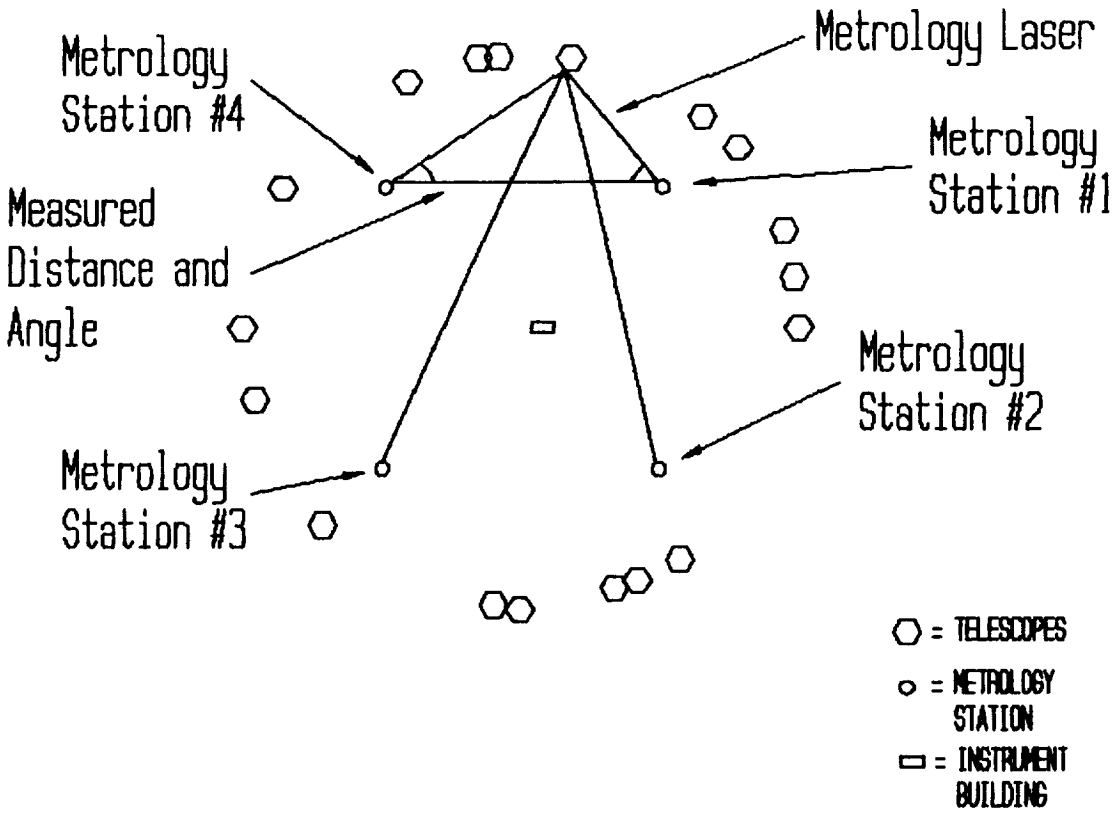

FIG. 47. External Metrology Scheme

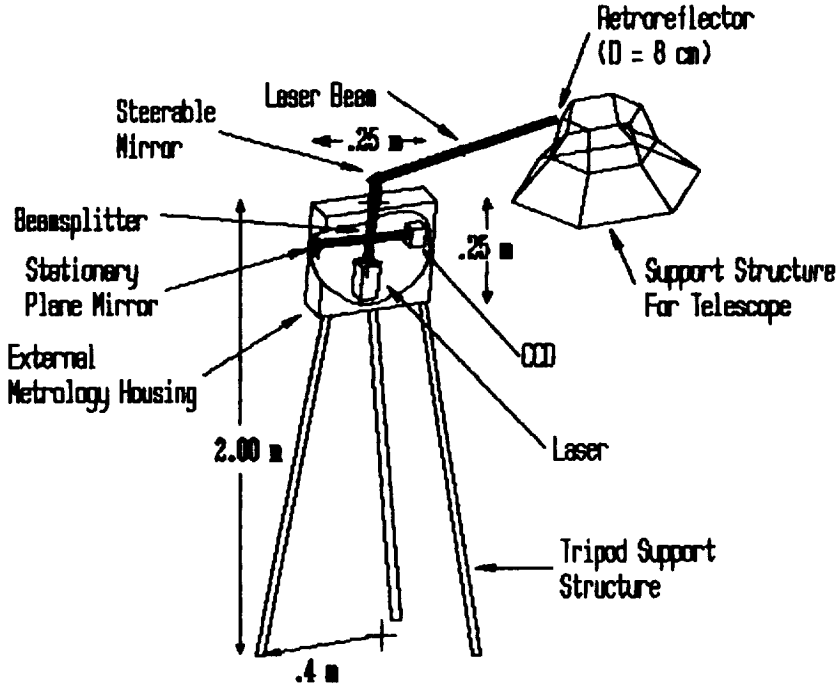

FIG. 48. Schematic of Metrology Tower

V. Pointing and Control System

The telescope array pointing and control system is designed to meet the fine pointing requirement of 10^{-6} arcsec stability, to maneuver each telescope in a combined 180° rotation of the base - 80° vertical rotation of the telescope itself in 15 minutes and to allow for precision tracking of a desired celestial object for up to 12 lunar days.[80] For the planet detection scheme at 10 μm, the needed pointing accuracy is 40 x 10^{-6} arcsec. These objectives are met through the use of a charge-coupled device (CCD) image sensor-driven system used for the determination of the control law, incremental maneuver updates and misaligned telescopes in cooperation with two motor driven precision gear systems used to provide the torque required for maneuvering and pointing. (Note: the motor driven gear systems and their operation are addressed in a later section).

The pointing and control system is driven by a main central command center located external to the telescopes within the instrument room. This central command center generates commands for operation of the telescopes and also serves as an interface between ground control and the telescope array. This interface provides a means of handling real-time commands from ground control in conjunction with stored program commands.[80]

The process of a typical observation, as depicted in the block diagram of Figure 49, begins with the acquisition of the initial target coordinates, predetermined to approximately 10^{-5} arcsec accuracy through astrometry, and the telescope scheme determined from either ground control or through stored program commands. After the coordinates and scheme are determined an initial tracking rate must be calculated and maintained for the entire observation in order to prevent "jerky" movements of the telescope during positioning and to eliminate any errors due to mechanical imperfections, such as "overshooting" a desired position. This initial tracking rate is comprised of two separate parts: 1) A rotation of the telescope base which should not exceed 24°/minute and 2) A vertical rotation of the telescope cylinder itself which should not be greater than 5.3 °/minute. (Note: The maximum rates are based upon the assumption that the telescope should not be repositioned through a 180° base rotation - 80° telescope rotation in less than 15 minutes due to high sensitivity). Both of these rates can be precisely determined to an accuracy of 10^{-3} arcsec given the initial coordinates of the telescope and the target along with the orbital mechanics of the moon itself. Based on this information the pointing and control system will calculate the position of the desired target after a given amount of time and then determine the tracking rate that the telescope must achieve in order for it to point precisely at the target's position at the given time.

After the initial rates are calculated two separate signals are transmitted from the pointing and control system to a motor signal processor located at the base of each telescope. This processor in turn interprets the signals and transmits them to the two motor driven gear systems which then begin the tracking rate.

After initial pointing of the telescopes has been completed the fine pointing stage begins. This stage will achieve and sustain the desired 10^{-6} arcsec accuracy and requires use of the previously mentioned CCD image sensor-driven system, the predetermined tracking rates, and two steerable mirrors which are part of the coarse delay system.

At the beginning of the fine pointing stage the telescope is positioned within 10^{-3} arcsec of the target. Although this is highly precise, it is still not the accuracy that is desired and therefore another system must be used for improving the telescope pointing and eliminating any existing error. First a highly precise device, such as the CCD image sensor-driven system shown in Figure 50, must be used to detect the magnitude of the pointing error. After the error is detected it must be eliminated by one of two means: 1) By updating the tracking rate of the telescopes through the motor driven gear mechanisms or 2) By adjusting the two steerable mirrors in the coarse delay system. The latter of these options must be used during planet detection in order to keep the telescopes' axes precisely aligned. After the necessary adjustments are made in the fine pointing stage it is imperative that updates be made periodically during observation to ensure the accuracy is maintained. These updates should be performed approximately two to three times per hour of surveillance.

Figure 50 shows the main components of the CCD image sensor-driven system: a beamsplitter device, a shutter apparatus, a filtration system, an off-axis mirror and a CCD image-sensor. Each instrument in the system plays an important part in achieving the desired accuracy starting with the first element -- a beamsplitter. The beamsplitter must be positioned in the path of the beams after they have passed through the delay system and entered the instrument room in order to directly utilize the light from the telescopes for pointing and control. This beamsplitter will reflect approximately 10% of the incident beams for use in the fine pointing system and allow the remaining 90% to proceed on to the instruments.

Due to the fact that the telescope scheme will vary from observation to observation it is necessary to be able to associate an incoming beam with its corresponding telescope; therefore, the reflected beams will pass through a shutter device. This device is such that at any given time any one of the eighteen individual shutters may be closed. By alternating the closing of the shutter windows it is possible to determine which telescopes are incorrectly positioned and send correction signals to those specific telescopes through the central command center.

The incoming beams will differ in intensity based upon the brightness of the object being observed. To compensate for this variation and to prevent flooding of the CCD a filtration mechanism is incorporated into the system. Its filtration impact on the reflected beams is directly proportional to the intensity of the incoming light.

A CCD image sensor is used in cooperation with an off-axis mirror in order to determine the pointing error, the actual impact of that error and the updates required to eliminate that error. The off-axis mirror is placed in the beam path and focuses all of the incoming beams onto the face of the CCD which is placed precisely at the focal point of the mirror. If the beams pass from the individual telescopes through the delay system and end up parallel to one another in the pointing and control system then they will all focus at the same point on the face of the CCD, but if they are not there will be a variation in their positions on the CCD and an error will be detected. The significance of the error will then be determined and utilized in determining the magnitude of adjustment needed. This adjustment includes alterations to the tracking rates and/or adjustments to the two steerable mirrors previously mentioned.

All of the individual elements of the fine pointing system have been addressed in minor detail. It is important, however, to examine each piece separately and describe in particular the specifications of each which are critical in order to ensure that the objectives are met and the requirements are fulfilled.

V.1 Beamsplitter

The type of beamsplitter device chosen for use in the pointing and control system is a circular plate beamsplitter. Three separate types of beamsplitters were investigated: 1) Pellicle beamsplitters, 2) Cube beamsplitters and 3) Plate beamsplitters. The first type of beamsplitter examined, the pellicle beamsplitter, was found to have certain advantages over the other options: absorption was very low and ghost image problems were virtually eliminated.[84] There were also several disadvantages as well: there was easier deformation in the beamsplitter due to stress on the mounting frame, there was a high sensitivity to acoustical disturbances, and the beamsplitter itself was intangible due to its high sensitivity.[84] Because of these disadvantages the pellicle beamsplitter was not chosen for use in the system.

At first glance the cube beamsplitter seemed the optimum choice for use in the pointing and control system. The cube beamsplitter was easy to mount, deformed much less than the other options when subjected to mechanical stress, had very small ghost imaging problems and had little trouble with reflection coating degradation over time since the coating was sealed within the body

of the cube.[84] The cube beamsplitter, however, was extremely heavy and hence was not chosen for use in the fine pointing system either.

Two types of plate beamsplitters were investigated: a circular plate and a square plate. Both plate beamsplitters were found to have two main advantages over their cube counterparts; they were significantly smaller and lighter and they were not limited by the endurance level of an optical cement.[84] For this particular beamsplitter application the lack of an optical cement was not necessarily a high consideration, but as Table 11 shows there was a significant weight savings from the use of a plate beamsplitter, especially a circular plate. Because of the weight constraints involved in space applications the obvious choice for the beamsplitter was a circular plate.

The plate beamsplitter chosen is a modified Melles Griot circular plate beamsplitter (See Figure 51) and is placed in the beam path in such a way that the incident beams strike the surface at an angle of 45°. The circular plate is 55 cm in diameter, has a width of 3 cm, and is made of BK 7 grade A fine annealed glass. This material was chosen because it "is a relatively hard glass, does not scratch easily and can be handled without special precautions."[84] The glass also has a very low bubble and inclusion content as well as a fairly low density value and coefficient of linear thermal expansion.[84] Table 12 lists the value of these and other physical constants of BK 7 glass.

There are two types of coatings required for the beamsplitter: a partial reflection coating and an antireflection coating. The partial reflection coating is deposited onto one of the sides of the circular plate (the side facing the incident beams) and will allow a 10% reflection of the incident beams.[84] The antireflection coating is applied to the reverse side of the plate to minimize ghost images and reflection losses.[84] The chosen coating should be comparable to HEBBAR™ (High Efficiency Broadband Antireflection), a Melles Griot antireflection coating. This coating is applied to the surfaces in multilayered films. These films are comprised of alternate layers of various index materials that combine in such a way as to reduce the overall reflection to an extremely low level for the broad spectral bandwidth covered.[84] The reflectance value does not exceed 1.0% over the entire range and is more typically below 0.6%.[84]

In order to provide a stable environment for the cube beamsplitter, a mount such as the modified Melles Griot mount in Figure 52 is suggested. The mount is constructed with dimensions comparable to those of the beamsplitter itself and is specially designed to provide precise angular control of the plate beamsplitter.

V.2 Shutter Apparatus

The shutter device chosen for use in the pointing and control system is an electronic shutter. While a mechanical shutter was also investigated the electronic shutter proved to have several advantages. Because it contains fewer parts and linkages the electronic shutter is inherently more accurate, more stable, and longer-lived than the mechanical shutter (under normal operating conditions a life of 1,000,000 operations may be expected from electronic shutters compared to 200,000 operations from mechanical shutters). Furthermore, variations in opening and closing times are substantially less for electronic shutters than for mechanical shutters, and with electronic shutters the time between command and opening of the shutter blades is constant and repeatable.

Despite these advantages two concerns remain about use of the electronic shutter. First, while the electronic shutter does contain fewer parts and linkages than the mechanical shutter it nevertheless depends upon a mechanical opening and closing mechanism and is therefore still subject to mechanical wear and failure. Second, even with an expected lifetime of 1,000,000 operations this number may be insufficient for our observation purposes. For example, if the shutter was to open/close every 0.5 seconds (2 operations per second) constant observation over a twelve day period would entail 2,073,600 operations.

The actual shutter device chosen is a modified Melles Griot electronic shutter. The apparatus consists of eighteen 2.50 cm diameter electronic shutters (each consisting of five steel shutter blades) placed side by side (0.5 cm spacing between each shutter) and surrounded with a lacquer - finished aluminum housing (See Figure 53). Clearances of 2.0 cm exist between the top of the housing and the shutters, 2.0 cm between the bottom of the housing and the shutters, and 0.5 cm on the two sides resulting in an overall width of 54.5 cm and height of 6.5 cm with the shutters and housing extending to a depth of 2.0 cm. The estimated mass of the electronic shutter system is 1.56 kg.

The electronic shutters were placed with the assumption that if all telescopes are properly pointed at the viewing object then the eighteen incoming beams (which make up 10% of the original light and are separated by the aforementioned beamsplitter) will all be parallel with each 2.0 cm diameter beam spaced 1.0 cm apart, and that the center of each beam will travel down the center axis line of its respective shutter.

The electronic shutter is activated by an electromagnetic solenoid. Standard solenoids are rated at 48VDC.[84] When the solenoid is energized a lever arrangement draws all shutter blades open simultaneously and de-energizing the solenoid causes blades to be redrawn by a spring. An opening DC signal of 4 times the rated solenoid voltage (e.g. 192VDC) should be applied for 3-5 milliseconds[84] and for the shutter to remain open a holding DC current of one-half the solenoid

rating (e.g. 24VDC) must be maintained. Removal of this signal will quickly close the shutter. Each shutter will require between 2 W and 5 W of power; therefore, operation of all eighteen shutters will require a maximum of 90 W of power.

The duration of open time is controlled through an electronic shutter controller (see Figure 53), which may be housed separately and located some distance from the actual shutter. The controller provides precise drive voltage to actuate the electronic shutters and also accurate pre-calibrated timing signals to operate the shutter at speeds ranging from four seconds to 1/125 second. Two cables connect to the electronic shutter controller, one which attaches to the modified Melles Griot electronic shutter apparatus and another which is for connection to a 230VAC power source.

V.3 Filtration Device

To prevent extreme light intensity from flooding the charge-coupled device (CCD) the incoming light beams pass through a filtration device. This device consists of a set of rectangular 2 mm thick neutral density filters (See Figure 54). The filters are made of BK 7 grade A fine annealed glass (the same material used and previously mentioned in the discussion of the beamsplitter). A light meter is used to measure the intensity of the incoming light and transmits a signal for selection and placement of an appropriate density filter into the beams' paths.

V.4 Off-Axis Mirror

The off-axis, or Herschel mounted, mirror used in the fine pointing system has one main purpose: to focus the incoming beams onto the CCD plane which lies directly in the position corresponding to the focal point of the mirror. In order to ensure that the desired accuracy is retained throughout this portion of the fine pointing system the mirror is constructed similar to the primary mirrors of the telescope array. It has the same aluminum reflection coating applied to its surface, is constructed of the same Zerodur™ material and must have a maximum deflection of 3 nm.

The mirror design is based upon a complete parabolic reflector and as Figure 55 shows, the off-axis mirror is actually a section of the entire reflector. The mirror has a focal point of 35 cm (i.e., a curvature of 70 cm), an actual length of 55 cm and a thickness of 1.6 cm. These dimensions will provide a very rigid mirror as well as a minimum value for the mirror mass which is approximately 1.44 kg (See Appendix D for calculations of mass).

V.5 Charge-coupled device

The most important element in the fine pointing system is the silicon charge-coupled device (or CCD). The device is precisely positioned in the system such that the center of the CCD corresponds exactly to the focal point of the off-axis mirror. As the beams are reflected from the mirror they each form a photon "image" on the CCD face having the same shape and dimensions as that of the incoming beam (i.e., a circular shape with a 2 cm diameter). Digital data is developed from the electrical charges on the CCD and becomes a record of the position of the photons in the original array. This information is sent to a computer for analyzing (See Figure 56).

The computer uses the CCD images to determine the initial error during the fine pointing stage and the presence of a pointing error at any time afterwards. As the incoming beams strike the mirror surface their orientation with respect to one other is a key in determining the error. All beams which are exactly parallel to each other will focus precisely onto the same position of the CCD face: the center; whereas, any deviation from a parallel direction will cause the beams to be focused onto an area of the CCD other than the center and will indicate an error. (Note: The error may occur due to the misalignment of the telescope or from an imperfection in the path from the telescope to the pointing and control system). Because the beams are all focused together onto one surface the ability to determine which telescope is in error is not possible directly from the CCD image; therefore, the system will use the shutter device previously described. The computer will systematically send signals to open and close the shutter windows until the misaligned telescope is found. Each time an individual shutter window is closed a new CCD image is processed and the error is determined. If the closing of the shutter did not eliminate any part of the error then the process continues. Figure 57 shows an example of the possible CCD images produced by using two telescopes, one of which is misaligned, and the shutter closure process (described above) to determine the identity of the misaligned telescope.

The CCD device chosen for this application has to be an imager that has a "large" active area, a relatively fast integration time, an anti - blooming circuit and a high quantum efficiency. In order to obtain these desired specifications a specially designed CCD must be developed. It is suggested that the CCD be designed as an array of 9 individual quadrants of 3072 x 3072 with 4 - micron pixels (see Figure 58). The array can be assembled together by edge - butting along the quadrant edges which will leave approximately 400 micron gaps between the quadrants or about 100 pixels.[83] Each quadrant will have an active area of 1.23 cm square resulting in an imager that will measure close to 3.7 cm on each side.[83] It will take approximately 1.75 minutes of integration time for a nine quadrant CCD of this pixel size and overall dimensions.

It is also suggested to include an anti-blooming circuit with the CCD. This device is used to prevent blooming, a condition which occurs when too much light hits a spot on the CCD.[78] When the excess light reaches the CCD the voltage is too much and "spills" over onto the adjacent locations, sometimes affecting an entire row of pixels; therefore, to avoid this harmful situation an anti - blooming circuit is highly recommended.[78]

TABLE 11. BEAMSPLITTER MASS COMPARISONS

		Dimensions (cm)			Mass
Beamsplitter	Radius	Width	Height	Thickness	(kg)
Cube	------	55	55	5	37.96
Plate (Circular)	27.5	-----	------	3	17.89
Plate (Square)	------	55	55	3	22.78

TABLE 12. PHYSICAL CONSTANTS OF BK 7 GLASS

Density	2.51 g/cm^3
Coefficient of Linear Thermal Expansion	
-30 deg to + 70 deg (per deg C)	$7.1 * 10^{-6}$
+20 deg to + 300 deg (per deg C)	$8.3 * 10^{-6}$
Transformation Temperature	559° C
Young's Modulus	$8.10 * 10^9$ dynes/mm^2
Modulus of Rigidity	$3.4 * 10^9$ dynes/mm^2

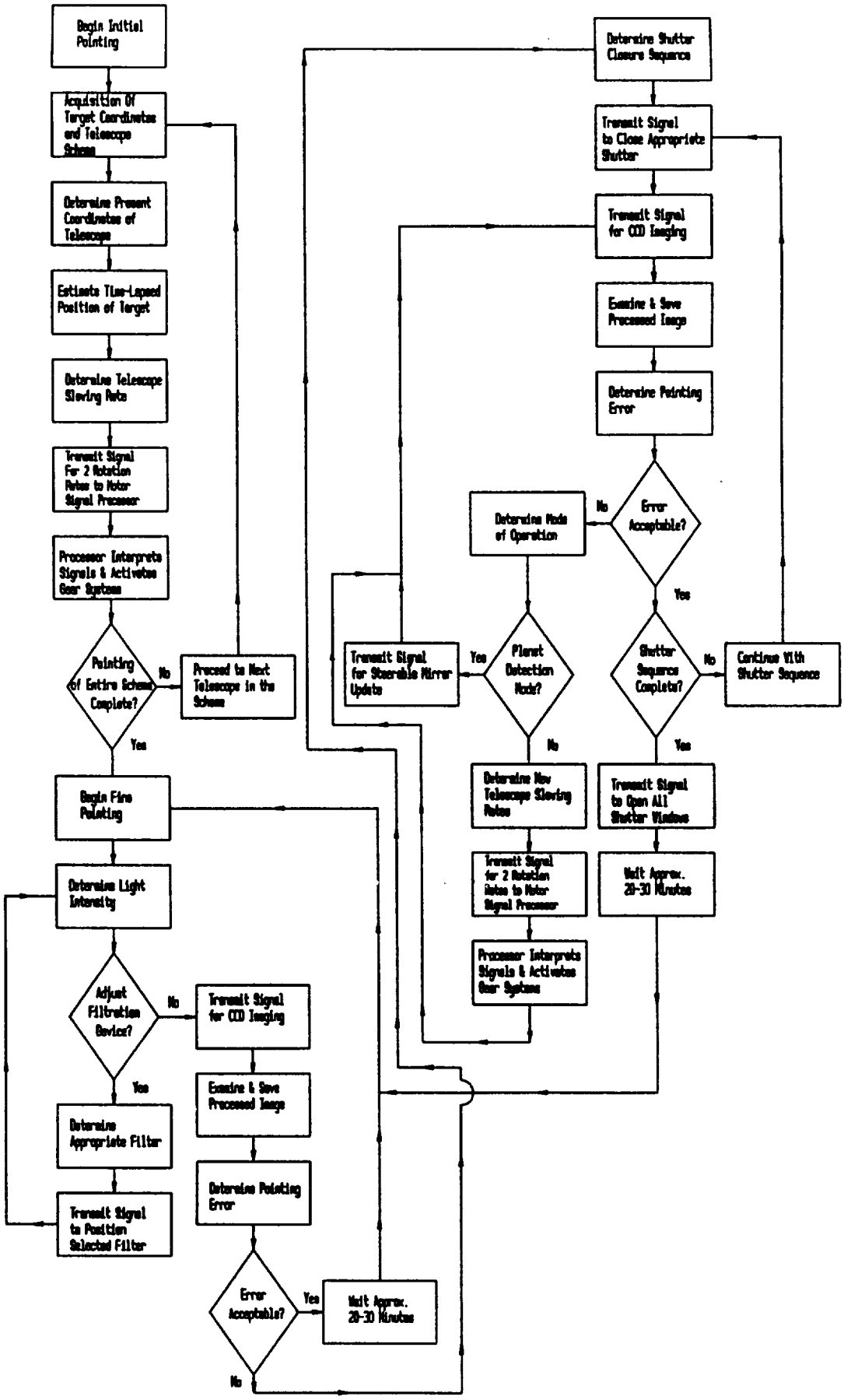

FIG. 49. Pointing & Control System Block Diagram

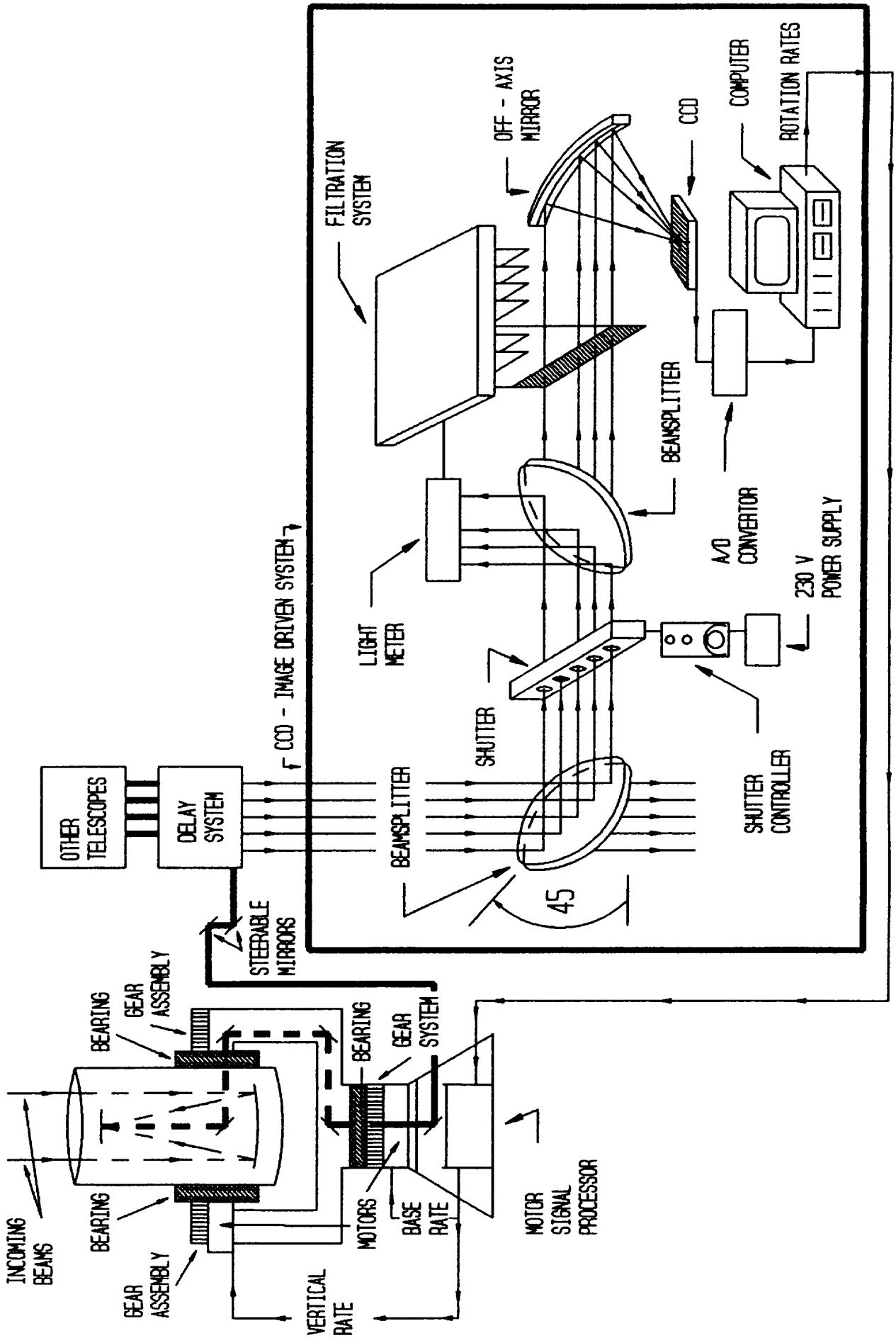

FIG. 50. Schematic of Pointing & Control System

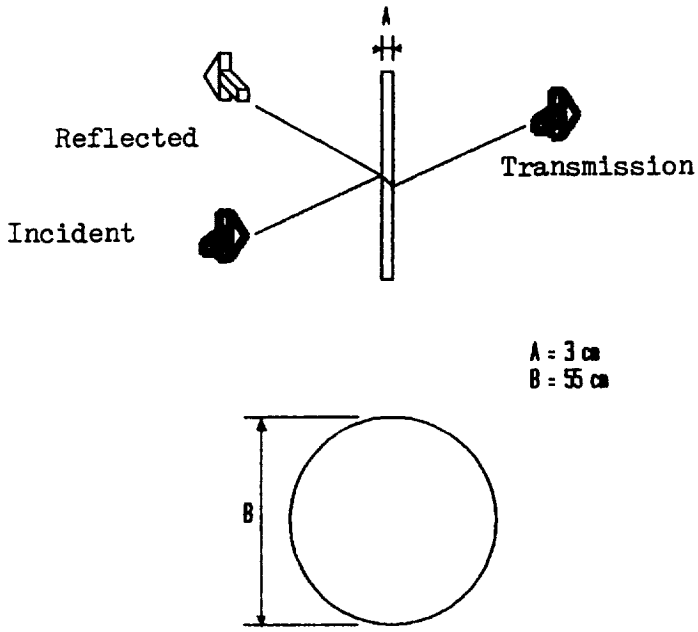

FIG. 51. Circular Plate Beamsplitter

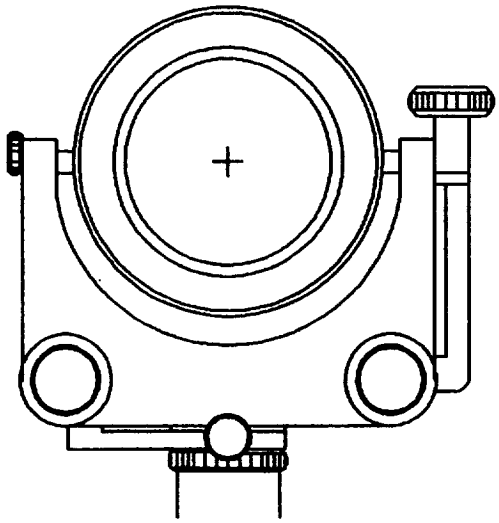

FIG. 52. Beamsplitter Holder

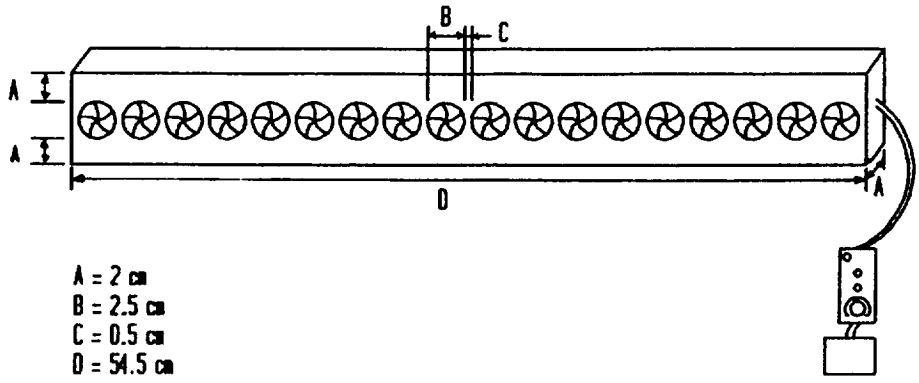

FIG. 53. Shutter Apparatus

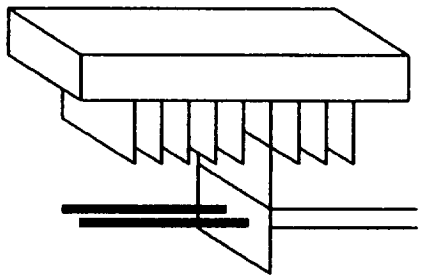

FIG. 54. Filtration Device

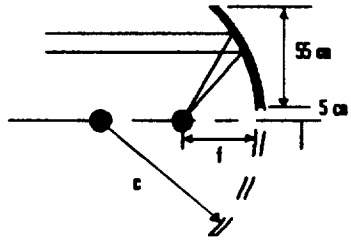

FIG. 55. Off-Axis Mirror

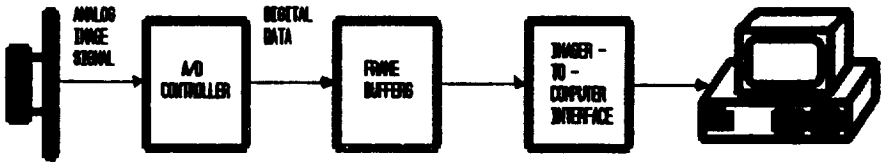

FIG. 56. CCD System

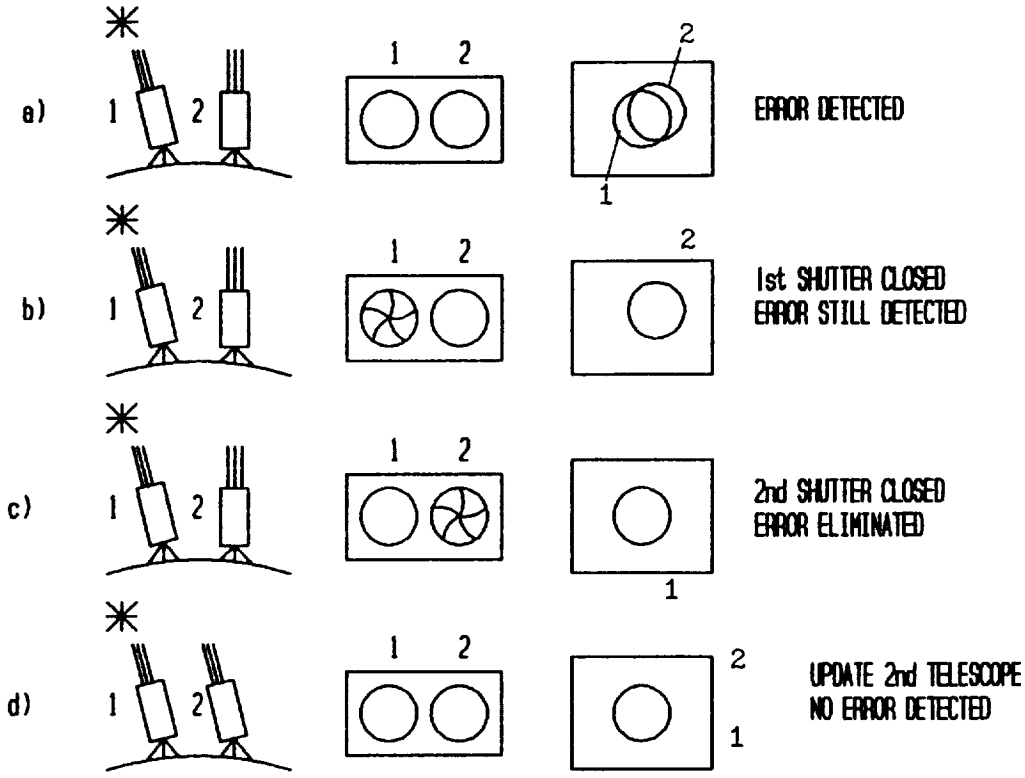

FIG. 57. Error Detection Example

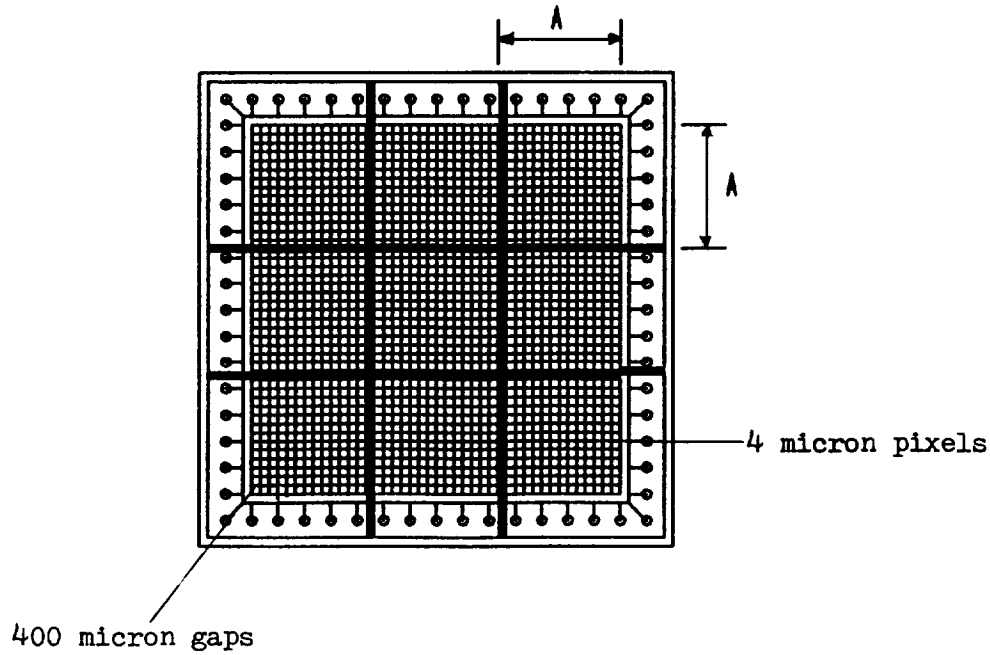

FIG. 58. Charge-Coupled Device (CCD)

VI. Communications

The design of a far side lunar observatory creates communication requirements that have never been encountered before. Clearly, a direct link between the observatory and the processing station on the earth is impossible. Several schemes for maintaining a communication link are examined.

1) One low-altitude lunar satellite
2) Three mid-altitude lunar satellites
3) One geostationary lunar satellite
4) One lunar satellite placed at a Lagrange point

1) A single satellite placed in the proper orbit could upload data from the observatory when it was over the far side of the moon. It could then transmit this data to the earth at a later time when its orbit had carried it to the near side of the moon. This is, in a sense, the simplest option. However, it has, many drawbacks.

First is the fact that the communication link is not continuous. This requires large memory storage capabilities at both the observatory and the satellite due to the massive amount of data being obtained during an exposure.

Choosing the correct orbit also requires a great deal of consideration. Low orbits have the advantage of more frequent flybys but suffer from shorter observatory-to-satellite links. This is partly due to the fact that a closer satellite appears to be moving faster overhead. It is also because the lower the satellite, the closer it needs to be to the observatory to clear the horizon. A higher orbit allows longer links but necessarily exhibits longer blackouts. The optimal orbit would be eccentric. Placing the apoapsis over the observatory would lengthen the link duration and the increased velocity at periapsis would shorten the period. The details of such a communications system are discussed in reference 159. An orbit[159] with a periapsis altitude of 400 km and an eccentricity of 0.47 is shown schematically in Figure 59. Such an orbit would provide an observatory-satellite link duration of about 160 minutes. This is less than half of the 383.4 minute orbit.

The satellite tracking involved in such a system creates further problems. The satellite and observatory must target and track each other during every link. This would involve an approximately 180° track 102 times a month. The satellite must also track the earth while making each orbit. As the satellite passes over the observatory its range decreases and then increases. The

possibility of Doppler effects as well as variable data transmission rates for various observatory-satellite distances would further complicate matters.

2) Three satellites could be placed in equally spaced orbits as also shown in Figure 59. Line of sight telemetry between the three satellites would form an uninterrupted triangle. The observatory would link with whichever satellite was passing overhead at the time. This satellite would then relay the transmission to earth. If the satellite was eclipsed by the moon then the satellite would transmit to either of the other satellites. The second satellite would then transmit directly to earth. Thus a constant link between the earth and the observatory could be established. The most obvious disadvantage of this system is the expense of three satellites. Other problems, however, come in to play as well.

Tracking is a major concern with this scheme. It is shown geometrically that the orbits must have an altitude of 1740 km to provide coverage at any given location on the moon. This is a bare minimum due to the mountainous lunar terrain. Such an orbit has a period of 5.11 hours. During any given period the observatory will have to target and track each of the three satellites across the sky. This would involve acquiring a satellite at the horizon, tracking it across the sky over 102 minutes and then going back to the horizon and finding the next satellite. This demand could be lessened by utilizing higher, and hence slower moving, orbits. Gravitational effects from the earth, however, would soon begin to interfere with the orbits, thus requiring more powerful orbit correcting rockets.

3) An ideal solution would appear to be a single satellite orbiting about the moon with a monthly period. Such a satellite would appear stationary over the surface of the moon and, if positioned correctly, would have an unobstructed view of the earth. Such an orbit would have an altitude of 86,660 km. This is a quarter of the earth - moon distance. Clearly the more massive earth would have a large effect on such a plan. This approach is discarded.

4) A host of alternatives is introduced by examining the Lagrange points. There are five such points where the force vectors of the earth and moon's gravity balance with the centripetal acceleration due to the rotating earth-moon system. Such locations offer the potential of being a non-moving relay directly between the observatory and earth.

The locations of L1 and L3 have no value in communicating to the far side of the moon. The relevant Lagrange points (L2 and L4) are shown in Figure 60. The location of L5, not shown in the figure, is symmetric with L4.

The decision between L4 and L5 would simply depend on which hemisphere of the moon the observatory is located. L4 is examined based on placing the observatory in the mare of Hertzsprung. Figure 60 shows how the geometry allows the L4 relay satellite to communicate about 60° behind the limb of the moon. Therefore, either the L4 or L5 option could be used unless the observatory was placed in the 60° of longitude furthest from the earth. The earth, moon, and L4 satellite roughly form an equilateral triangle. The remoteness of the satellite from the moon demands a more powerful transmission link between it and the observatory.

The L2 point is in a straight line with the moon and earth. The earth, therefore, is always eclipsed by the moon. The satellite is high enough, however, to communicate with the Tracking and Data Relay Satellite System (TDRSS). This fact is demonstrated in Figure 61. Furthermore, a Lissajous orbit could be utilized. Such an orbit is a three dimensional, quasi-periodic motion about the L2 point. The properly chosen orbit could give the satellite enough distance from the earth-moon line that it could communicate directly to the earth. Such an orbit, however, would be relatively hard to predict and track.

Both Lagrange options (L4 - L5 and L2) have advantages with regards to tracking. Since the satellite is approximately stationary relative to the earth and the observatory, it does not require very much motion to stay pointed correctly. Similarly, the observatory does not need to track the satellite across the sky.

A major disadvantage is that of stability. Any errors in the location of a Lagrange satellite will exponentially grow with time into a failed orbit unless corrected. The satellite will in fact be disturbed by the effect of the sun as well as the non-circularity of the moon's orbit. This drifting can be reasonably overcome through the use of small rockets on the satellite. It is predicted[158] that a delta-v capability of approximately 4 m/s per year would be necessary to maintain a satellite at the sun-earth L2 location. The location of L2 is less stable than L5 or L4 because it is much closer to a massive body (the moon). Therefore, a given perturbation at L2 would result in a greater offset of forces away from equilibrium than a similar perturbation at L5 or L4. Figure 62 demonstrates this fact graphically by showing the force vectors that result from 100 meter perturbations in various directions. Therefore, the L4 location is chosen as the site for the relay satellite between LOITA and earth.

VI.1 Data Transmission

The transmission specifications of the satellite(s) and the observatory require consideration of several factors.

1) The transmission system used at the earth

2) The transmission distances (dependent on relay scheme)
3) The data transmission rate

The requirements of the satellite will be molded by the abilities of the system being used at the earth. Its electronics will dictate the operating frequencies, the data bit rate capabilities, and the amount of satellite transmission power that must be collected. Its antenna capabilities will determine the size of the satellite's antenna and its required transmission power. There are two earth systems appropriate for this mission. The array of geostationary satellites called the Tracking and Data Relay Satellite System (TDRSS) and the Deep Space Network (DSN) are examined here.

The TDRSS is presently operational and consists of two primary geostationary satellites positioned at 41° W (over the Atlantic) and 171° W (over the Pacific)[154]. A third backup satellite orbits in between the two. The system is shown in Figure 61. This system allows for radio coverage of any part of the sky by at least one satellite. The receiving satellite relays any transmission to the White Sands Ground Terminal (WSGT) where the data can be processed. The TDRSS satellites have three types of communications systems as seen in Figure 63[154]. There is a 30 element low gain antenna for multiple user applications on the S-band. There are two 4.9 meter parabolic antennas that can each support single user S-band systems or single user Ku-band systems. The low gain antenna works at low data rates (50 kbit/s) and, hence, would not suit the requirements. The parabolic S-band communications can operate up to 6 Mbit/s while the parabolic Ku-band system can relay up to 300 Mbit/s. The Ku-band mode clearly has the best chance of handling the massive amounts of data that will be collected during an observation. The technical data[161] of this system is given in Table 13. The addition of more advanced satellites in the late 1990's will create what is called the Advance TDRSS (ATDRSS). These satellites are planned to operate at even higher frequencies (Ka-band) and may approach data rates of 650 Mbit/s.

The TDRSS is designed primarily to relay data from satellites in a lower orbit than itself to WSGT. It would be necessary, therefore, to make sure that the parabolic dishes have the range of motion to track a communication satellite that is further away from the earth than itself.

The Deep Space Network (DSN) is a distribution of at least three steerable ground based antennas ranging in size from 26 meters to 70 meters. There are twelve such antennas located at three different locations (California, Spain, and Australia). The link is passed from one station to another as the earth spins and the source passes overhead. Hence, a constant link with a given extraterrestrial source can be maintained. There is a disadvantage in the fact that this requires the cooperation of several nations. In addition, certain sites may experience atmospheric interference

or be subjected to man-made signals. One advantage, however, is the need for a less powerful relay satellite because the gain of the DSN is so much higher than that of the TDRSS.

It is in the area of receiver design that the TDRSS truly shows its superiority. The primary disadvantage of the DSN is its increasing technical incompatibility with modern instrumentation. The DSN antennas use a cooled maser amplifier and residual carrier phase modulation with phase-locked loop tracking as shown in Figure 64.[161] The present usage of the DSN has nearly reached the upper data rate limit possible with this system. This is clearly far too slow when one recalls the slow, frame by frame, images from Voyager and then thinks of the many high resolution frames per second that will be generated during a LOITA observation. The TDRSS (as well as the shuttle) operate primarily with Costas-loop, suppressed carrier modulation as shown in Figure 65.[161] All of the transmitted power in such a system is contained in the data itself (rather than mostly in the carrier wave). At this time it appears logical to proceed assuming the best system to use will by the ATDRSS working in the Ka-band.

VI.2 Relay Satellite

The distance between the earth and the relay system must next be factored into the design of the relay satellite. This distance is roughly the earth-moon separation regardless of the relay arrangement decided upon (even for the L4 case). The parameters of the relay system are directly dependent on the data rate used. This will depend on the operation of the CCDs (how long each exposure takes and how often a pair of separate beams are combined). A similar observatory[157] plans to transmit one CCD image every 30 minutes at a data rate of 2.5 Mbit/s. LOITA will most likely require a significantly higher rate of CCD frame transmission. The calculations presented here use the near maximum ATDRSS data rate of 600 Mbit/s to be conservative. This bit rate could theoretically transmit 6 (10,000 X 10,000) frames per sec. Considering the TDRSS data given in Table 13, it is shown that the relay satellite requires a 10 watt transmitter and a 4.15 meter dish to achieve this data rate with an error rate of 10^{-5} as calculated in Appendix F. A more careful study of the losses within the components of the relay satellite itself will no doubt lead to refinements. This configuration leads to a total collecting power of 2.75×10^{-14} W at the TDRSS receiver as calculated in Appendix G.

At any given time, a single satellite antenna can be transmitting to (forward link) or receiving transmissions from (return link) the observatory or earth. The two frequencies must not be the same, however, or the two signals will interfere. The Ka-band consists of the frequency range of 20 - 34 GHz. The subrange of 22.55 - 23.55 GHz has been assigned for forward links. The subrange of 25.25 - 27.50 GHz has been allotted for return. Figure 66 schematically shows

the relay satellite and tabulates its specifications. The overall specifications of the communications system are given in Table 14.

For the L4 option the system at the moon would need to be similar to the transceiver of a typical ATDRSS satellite (because the relay is approximately equidistant from the moon and earth). The array, then, would be equipped with a 20 Watt, 4.9 meter transceiver. This antenna could be mounted atop the instrument room, with the electronics inside the building. Proper shielding of the observation equipment from the radio equipment must be planned. This should not be difficult if one considers the close proximity of the antenna to the sensitive equipment onboard space probes (Voyager). An overall schematic view of the communications system is given in Figure 67.

Table 13. TDRSS DATA

(from reference 161)

BER	10^{-5}
User EIRP, dBW	EIRP
Space Loss, dB	-192.2
Polarization loss, dB	-1.0
TDRS antenna gain at 13°, dB	28.0
P_S at output of antenna, dBW	-165.2 + EIRP
T_S (antenna output terminals), K	824
T_i (due to direct other user interference), K	255
$K(T_S + T_i)$, dBW/Hz	-198.3
$P_S/K(T_S+T_i)$, dB-Hz	33.1 +EIRP
Transponder loss, dB	-2.0
Demodulation loss, dB	-1.5
PN loss, dB	-1.0
Antenna beam forming loss, dB	-0.5
User margin, dB	-3.0
Required E_b/N_O, dB(PSK)	-9.9
FEC gain, R = 1/2, K = 7, dB	5.2
*Achievable data rate, dB	20.4 + EIRP

*This achievable data rate is the user's information rate. It should not be confused with the channel symbol rate, which is twice the information rate.

Table 14. LOITA LINK

Antenna

Diameter = 4.90 m

Area = 18.85 m^2

Efficiency ≅ 0.6

Gain (Ka) = 764,360.9 = 58.83 dB

Transmitter Power = 10 W

EIRP = 68.83 dB

Operating Freq. = Ka Band (24-30 GHz)

Data rate = 600 Mbit/s

Relay Satellite

Antenna

Diameter = 4.15 m

Area = 13.50 m^2

Efficiency ≅ 0.6

Gain (Ka) = 547,265.6 = 57.38 dB

Transmitter Power = 10 W

EIRP = 67.38 dB

Operating Freq. = Ka Band (24-30 GHz)

Data rate = 600 Mbit/s

Solar Power

Type = GaAs Cells with Battery Storage

Power = 1.3 kW

Area = 15.2 m^2

Frequency Allocations

Relay - LOITA

Forward = 22.55 GHz

Return = 25.25 GHz

Relay - Earth

Forward = 23.55 GHz

Return = 27.50 GHz

Life Expectancy = 10 yrs

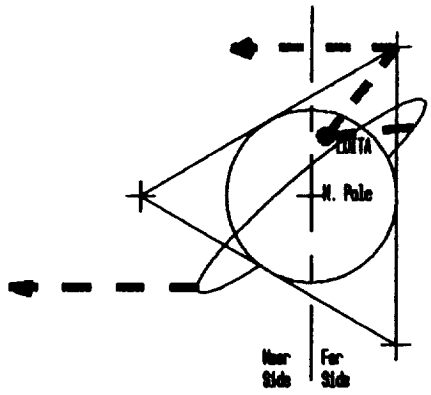

FIG. 59. Single & Three Satellite Communication

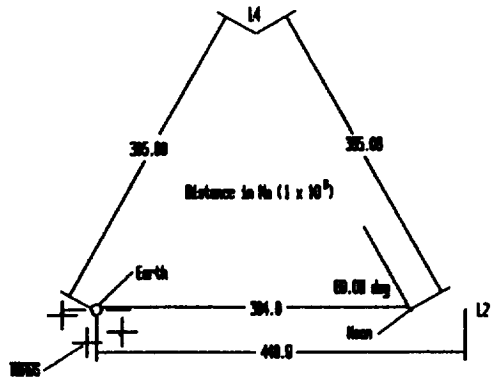

FIG. 60. Viable Earth-Moon Lagrange Points

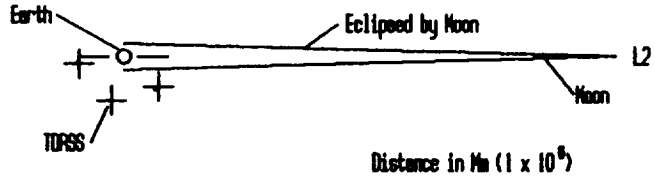

FIG. 61. Comm Link Visibility From L2

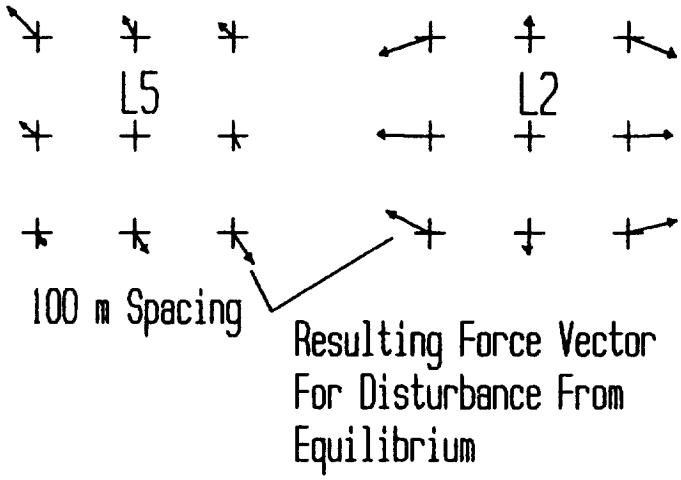

FIG. 62. Stability of L5 and L2

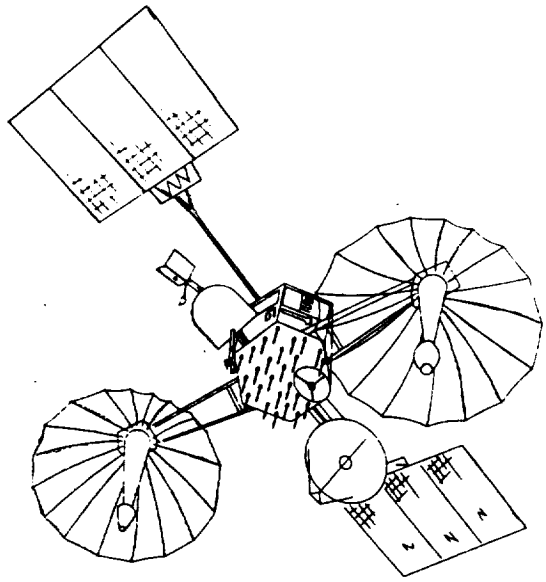

FIG. 63. TDRSS Satellite (taken from ref. 154)

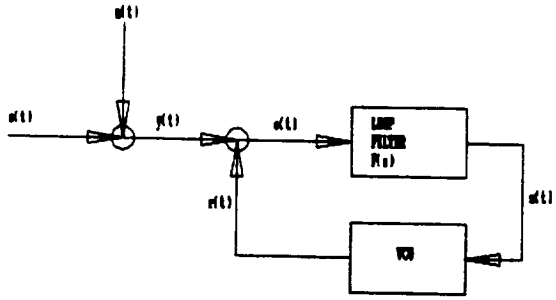

Phased-Locked Loop

FIG. 64. Block Diagram

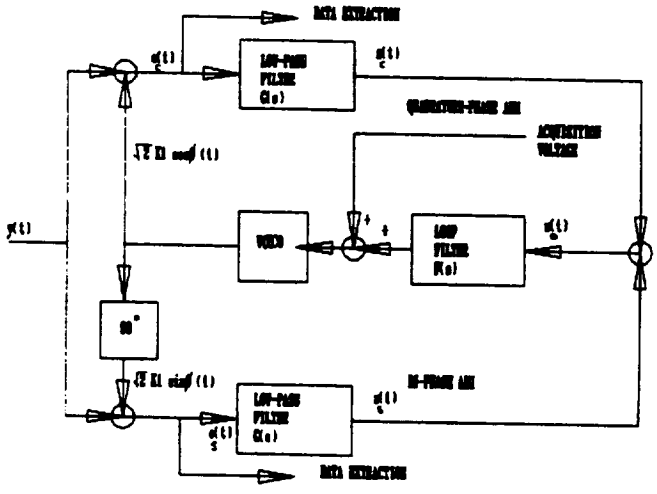

Costas Loop

FIG. 65. Block Diagram

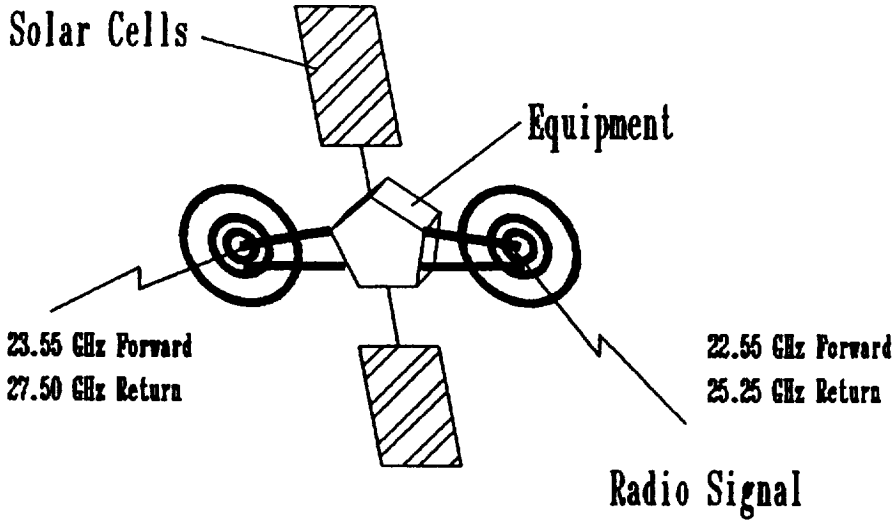

Antenna Diameter = 4.15 m
Antenna Gain = 57.38 dB
Achievable Data Rate = 600 Mbs
Transmiter Power = 10 W
Operating Frequency, Ka Band (20-34 Ghz)

FIG. 66. Schematic of Relay Satellite

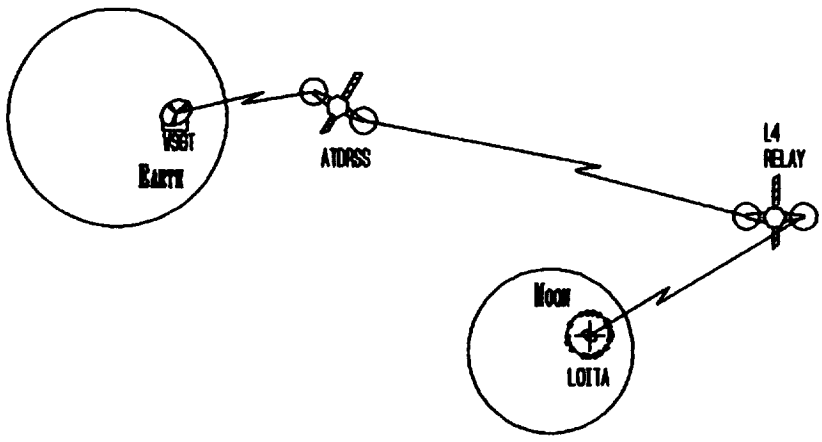

FIG. 67. Schematic of Communications System

VII. Power

VII.1 Power Requirements and Source Consideration

The estimated electrical power requirements for LOITA are tabulated in Table 15. The instrument requirements are representative of the duty cycles of the instrument. Only two instruments will be utilized at any one time and the necessary standby power is shown for the instruments. The mechanisms subsection consists of the required motors for the various subsystems of the array. With a contingency of 25%, total power required is on the order of 10 kW.

Both solar and nuclear power options are considered in the study for a suitable power system. The two nuclear systems examined are the SP-100 and the TOPAZ II nuclear reactors. The solar options considered include InP, GaAs, and Si solar cell arrays with either battery or RFC energy storage systems. Factors considered include: the total mass of the system, resistance to the damaging effects of the lunar environment; required time and effort spent on the moon to initiate operation of the system; and the ability of the system to operate unattended for lengthy periods of time.

VII.2 Nuclear Power

VII.2.1 Reactor Type

The most viable option is the SP-100 nuclear reactor scaled down to 15 kW. Figures 68 and 69 show the current SP-100 design. Figure 68 is a cutaway view of the reactor power system with a diagram of the core. Figure 69 is a representation of the SP-100 in a deployed configuration. In a stowed configuration, the system is approximately 12 meters in length and 5 meters in diameter.

The SP-100 has advantages over the TOPAZ II. It is a modular system, with a specific power of 25 W/kg, designed to produce 100 kW of electrical power. The TOPAZ II has a specific power of 5.7 W/kg and a maximum electrical power output of 6 kW. The use of TOPAZ II for LOITA will require two reactors with a total combined mass of 2122 kg as opposed to a single 15 kW SP-100 type reactor with an estimated mass of 750 kg. The mass of the SP-100 system increases with the increase of electrical power output, as can be seen in Figure 70, however, it is a gradual increase due mainly to the additional shielding requirements. The operational lifetime of the SP-100 source is seven years at full operation and ten years at a reduced power output. By

scaling the SP-100 to 15 kW instead of the required 10 kW, the operational lifetime of the reactor is expected to be ten years. The TOPAZ II system has an operational lifetime of only three years.

The design of the scaled down SP-100 reactor will take into account all aspects of the lunar environment, i.e. lunar gravity, background radiation, dust, micrometeoroids, thermal cycles, and minimal astronaut involvement with deployment and installation while maintaining a minimum 95% reliability.

VII.2.2 Heat Rejection

The heat rejection subsystem will include heat pipes and possibly pumped loops. The radiator panels, which can be seen in Figure 69, consist of modular heat pipe sections. The sections offer a built-in redundancy because of the multitude of individual heat pipes employed in each panel. In essence, each heat pipe acts as a small separate radiator. If penetration of an individual heat pipe by a micrometeoroid occurs the overall ability of the panel will be largely unaffected. Proper orientation of the panels will be necessary to minimize the radiator area and to prevent interference with observations. A horizontal configuration would require a larger area than a vertical configuration because of one-sided heat rejection. The vertical offers two-sided rejection. The total area required is approximately 80 square meters.

VII.2.3 Safety

The system will be non-operational at launch. The accident risk is equal to that accepted in other flight missions. The lithium coolant will be in a solid state. Start-up of the reactor would not take place until it has been deployed on the lunar surface and the lithium has thawed. The entire start-up process will be completed in a twenty-four hour period. The probability of a core melt is less than 10^{-3}. Radiation protection for the astronauts will be the same degree as for workers in terrestrial nuclear power plants. The dose limit will be kept under fifteen milliRems per day.

VII.2.4 Shielding

Maximum use of in-situ materials will be made. The distance between the array and the source will be such to minimize the mass required for the shielding and to remove as much background noise as possible. Figure 71 illustrates three options for the shielding of the reactor. The first option is recommended since it requires the least amount of materials to be transported from earth. The size of the excavated cylinder is approximately 2 m in diameter and 5 m deep. The cylinder wall needs to be lined to prevent the activation of the soil.

VII.2.5 Power Conversion

The next area of study is the conversion of the heat into electricity. The power conversion subsystem to be implemented will be a thermoelectric one. Thermoelectrics is the production of a voltage utilizing the temperature difference between the two junctions of dissimilar materials; this is the Seebeck effect. This conversion method is not the most efficient because of the materials used but the minimization of dynamic machinery is basic to provide a low maintenance schedule. "Good" materials exhibit a high Seebeck coefficient (a), low electric resistance (p), and high thermal resistance (R). The thermoelectric system is designed for a lifetime of five years.

VII.3 Solar Power

The other most viable option for a power generation system is solar power. Three solar cell materials were examined; silicon, gallium arsenide, and indium phosphide. The end of life (EOL) performance of each cell material must be determined in order to accurately compare the three materials and select the lightest most compact array. Table 16 shows the results of this comparison. Table 17 contains properties of the three solar cells. The main criteria affecting the EOL performance of a solar cell material was its ability to cope with the lunar environment. The lunar environment features radiation, high thermal gradients, and dust. In addition to environmental effects, a 3% loss attributed to manufacturing error was included.

VII.3.1 Environmental Effects

Radiation effects were determined using a 3×10^{15} e/cm^2 (1 MeV) irradiation level. In addition a 4% decrease in efficiency was used to simulate ultraviolet radiation damage.[135]

Temperature and thermal cycling also affect a solar cells performance. During the lunar day the surface of the moon reaches a temperature of about 90° C. This value was used as the operating temperature of the array. The temperature of the array could be reduced by use of a reflective backing to decrease absorption of unused wavelengths of light. The effects of thermal cycling were represented by a 2% decrease in performance for Si cells, a 5% decrease for InP cells, and a 4% decrease for GaAs cells.[135]

The effects of lunar dust can not easily be calculated. There is little data on its effects on solar cells. It is known that the lunar dust is made up of charged particles. It will therefore adhere to the charged surface of the solar array, decreasing the amount of incident sunlight and thereby decreasing the output of the array. It has been proposed that a thin conductive film could be placed over the solar array and grounded to eliminate electrostatic charge and reduce adhesion of dust particle.[128]

VII.3.2 Photovoltaic Array

The photovoltaic array will consist of a flexible array of solar cells mounted on a stationary triangular support structure. A stationary system was chosen over a sun-tracking system for two reasons: 1) stationary systems utilize no moving parts, and 2) stationary systems require considerably less time and effort to assemble due to lack of moving parts. The support structure chosen, a NASA patented[137] triangular configuration, mitigates the need for extended construction time since it is transported in a folded state and autonomously erected by way of integrated containers of compressed air. The average angle of inclination selected for the tent array is 45°. This provides the maximum possible incident light to fall on the array over the course of a lunar day.

Three materials were examined for the array: InP, GaAs, and Si. A gallium arsenide solar array was selected. Indium phosphide cells displayed the best EOL performance due to their high radiation resistance. However, though InP cells are currently being used to power at least one orbiting satellite, the amount of real world performance data is not as complete as either the GaAs cells or the Si cells. Another drawback of InP cells is their high cost, estimated at $440 per cell, compared to GaAs at $155 per cell, and Si at $12 per cell.[135]

Silicon cells, though the least expensive by a considerable margin, have a much lower performance level than the gallium arsenide cells. Current reports claim that the older more developed silicon cells have almost reached their performance plateau, 15.8% efficiency, while the newer less developed gallium arsenide cells, with a theoretical predicted efficiency of 23%, still have room for improvement.[138] The higher cost of the gallium arsenide cells should also decrease as production processes are further refined.

Other areas of solar cell research studied include multijunction solar cells and thin film solar cells. Both of these technologies are new and unproven in a space environment, however both have potential to be low mass energy production arrays. Efficiencies above 30% have been achieved by multijunction cells, however, multijunction cells are more susceptible to radiation damage. Thin film solar cells have the attribute of very low specific mass. They have lower efficiencies, on the order of 5-10%, than normal solar cells but they are much thinner, on the order of micrometers. The result is a larger but extremely light weight array.

VII.3.3 Energy Storage

Energy storage for operation of the telescopes during the 354 hour lunar night will be accomplished by gaseous H/O reactant fuel cells. Regenerative fuel cells were chosen over batteries due to the mass penalty associated with a battery system. Ni/H_2 batteries have predicted

near future specific energies in the range of 50-60 Whrs/kg while Na/S batteries have predicted near future specific energies of 153 Whrs/kg. Current H/O RFCs provide specific energies on par with Ni/H_2 systems, however there is tremendous potential for increased energy production. Predicted specific energies for the year 2000 for gaseous RFC systems are around 500 Whrs/kg[142]. Current overall round trip efficiencies of these systems are about 66%[148].

Solar power units are readily adaptable to increases in power required due to their modular deployment. Assuming a total power requirement of 10 kW for the telescope array, plots were created (Figures 72 and 73) to show the relative growth in array area and array mass from 5 kW to 30 kW.

VII.4 System Comparison

A comparison of the most suitable solar and nuclear options, the GaAs array with gaseous regenerative fuel cells and the scaled down SP-100 reactor, is illustrated in the table below. This comparison reveals the SP-100 as being the most viable power source for the array.

Power Source Comparison

Criteria	SP-100	Solar
Weight	1	2
Reliability	1	2
Potential Danger	2	1
Vulnerability	1	2
Lifetime	1	2
Maintenance	1	2
Operation Initiation	1	2
Cost	1	2
Total	9	15

* Lowest total indicates best alternative.

VII.5 Power Profile

Figure 74 represents the power profile during one lunar cycle with the maximum . The minimum requirement occurs during the lunar day while the maximum falls on the time period corresponding to the initial positioning of the telescopes.

VII.6 Distribution

The distribution network consists of the eighteen telescope units being interconnected with four power lines moving outward from a distribution point within the circular array (Figure 75). The circle will be cut into four arcs. Each arc will not contain more than five telescopes. In this configuration with a dual line setup all of the telescopes will be interconnected such that if the lines

along the perimeter between two units are lost then the two telescopes will not become inoperative. The location of the distribution point will be off center in the direction of the source about 1 km away from the instrument room to prevent interference from the high voltage (Figure 75). The source will be located in the area of the lowest unit population, outside of the perimeter, in this case the lower right quadrant about 5 km from the distribution point.

The primary transmission line runs from the source to the power distribution unit (Figure 75). The power distribution unit is designed to distribute the incoming voltage to the five subsystem distribution points where the voltage will be lowered to the proper level. There are six AC-DC or DC-AC converters along the primary line; one in proximity of the source, another one in the proximity of the instrument room and the other four along the perimeter of the array at the intersection of the primary and secondary lines. These converters are necessitated by the transmission voltage in the line, 2 kV. The 2 kV voltage necessitates a line current of 5.0 Amps in the primary. This high voltage is to reduce the line losses to acceptable levels. Also, the high voltage decreases the cable mass by lowering the requisite wire diameter. A block diagram of the proposed system is shown in Figure 76.

The conductor in the transmission lines will be aluminum. Aluminum was chosen due to its low mass, low resistivity, and low cost. A line operating temperature of 300K is sufficient to minimize the power loss incurred by the material and diameter of the conductor. A minimal amount of insulation will be needed for the lines, and will be cross-linked polyethylene (x.l.p.). The two line setup is necessary to minimize the line heating due to one another. It increases the mass but greatly lowers the opportunity for overheating. The lines will be deployed at a depth of about 10 centimeters where the temperature gradient is relatively small. An underground setup is necessary to keep the mass of the insulation to a minimum, to remove thermal strains caused by the greatly varying surface temperature and to offer protection from meteoric and radiation stresses. The diameter of the cable, including insulation will be 3.0 mm. For the conductor, this translates into about 0.034 kg needed per meter. The secondary lines will need to be of a slightly larger size to handle the increased current.

The power system mass is estimated to be 1,050 kg excluding the mass of the cabling. The mass of the cable will be approximately 2,650 kg. The cable mass is such a large percentage (70%) of the system mass due to the required length of approximately 66 km. A breakdown of the masses of the components in shown in Table 18.

TABLE 15. ARRAY POWER REQUIREMENTS (Watts)

Instruments:	Wide Field/Planetary Camera	150 (2 @ 10%)		30
	Faint Object Camera	150 (2 @ 10%)		30
	High Resolution Spectrograph	200 (1 @ 10%)		20
		(1 @ 100%)		200
	Faint Object Spectrograph	200 (1 @ 10%)		20
		(1 @ 100%)		200
			Subtotal:	500
Subsystems:	Central Computers			1500
	Communications			400
	Pointing Control: Pitch	50 (18)		900
	Yaw	100 (18)		1800
	Thermal Control			400
			Subtotal:	5000
Mechanisms:	Shutters	5 (18)		90
	Metrology	50 (22)		1100
	Doors	25 (36)		900
	Additional Motors			500
			Subtotal:	2590
			Contingency 25%:	2023
			Total:	10113

TABLE 16. SIZE AND MASS ESTIMATES FOR INITIAL PHASE SOLAR ARRAY

	Si	InP	GaAs
EOL Power (W)	10000	10000	10000
EOL Power at 90° C (W)	12847	11334	11053
BOL Power after radiation & thermal effects (W)	23440.2	13873.6	16904.6
BOL after 3% assembly losses (W)	24143.4	14289.8	17411.2
Cells required with 66% eff. H/O storage	208004	105310	121912
Array area (m^2, packing factor 0.9)	193.8	93.6	108.4
Array mass (kg) with flexible support structure (1 kg/m^2)	288.6	236.5	281.8
Array area for tent config. (m^2)	255.6	132.4	153.2
Array mass for tent config. (kg)	481.0	334.4	398.6
Total cost ($MIL)	3.7	65.6	26.8

TABLE 17. PROPERTIES OF 2cm x 4cm Si, GaAs, AND InP SOLAR CELLS

	Si	GaAs	InP
Predicted efficiency	15	20	19
Bandgap (eV)	1.13	1.43	1.35
dP/PdT (%/°C)	-0.438	-0.162	-0.206
Decrease in efficiency due to radiation, 3 x 10^{15} e/cm^2 (eff./initial eff.)	0.57	0.68	0.85
Cell mass (gm) with metallization & coating of 0.06 gm/cell)	0.438	1.423	1.357
Cell cost ($/cell)	12	155	440

TABLE 18. POWER SYSTEM MASS

		Total (kg)
SP-100 SRPS with TE Conversion		3200
Converters	10 @ 200	2000
Main Power Distribution		25
Subsystem Distribution	5 @ 10	50
Cable		10550
		15825

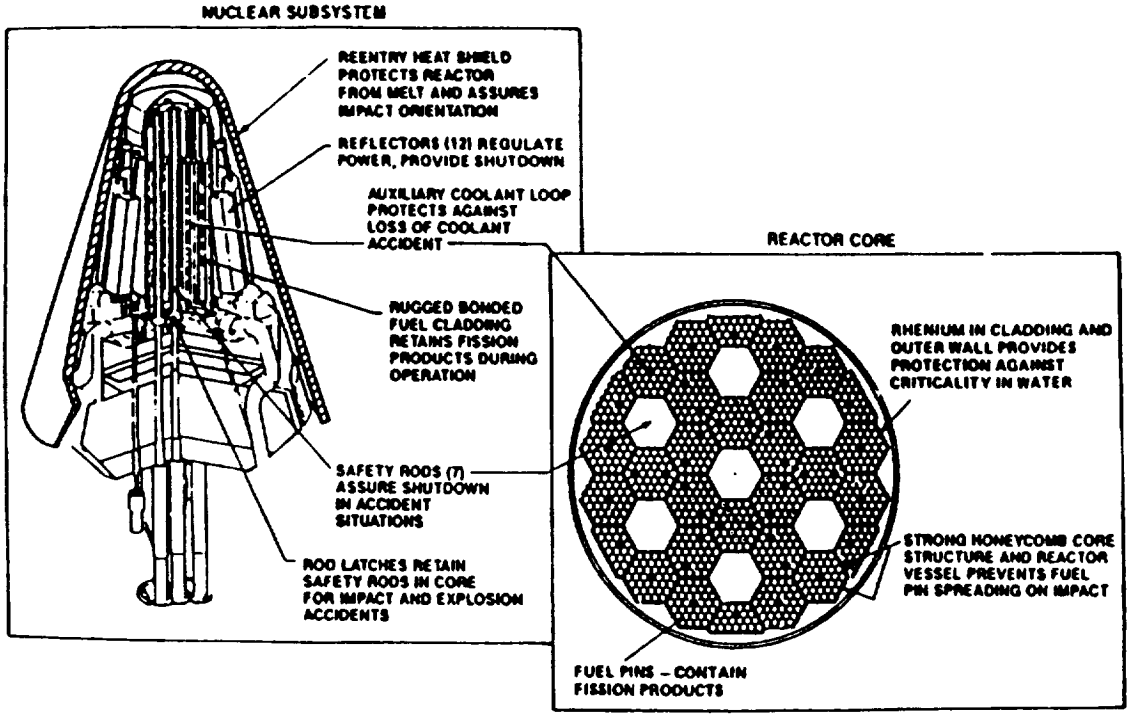

FIG. 68. Cutaway View of SP-100 Reactor Power Assembly (taken from ref. 150)

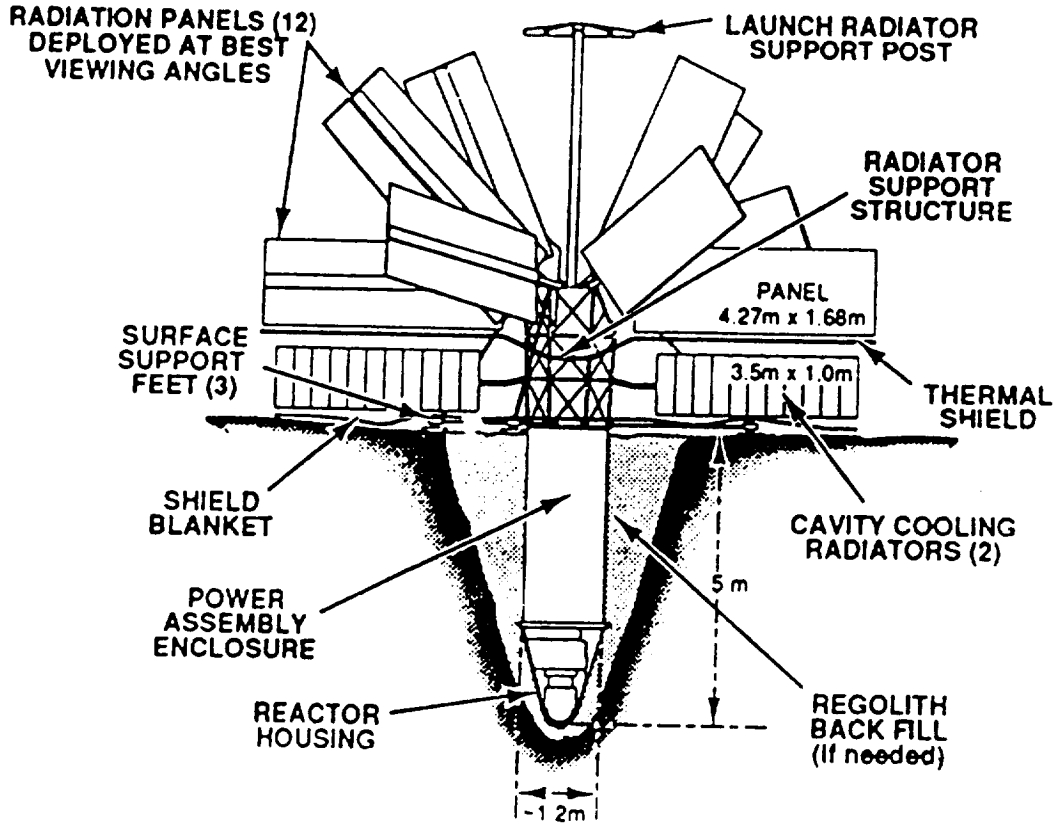

FIG. 69. SP-100 in Deployed Configuration (taken from ref. 152)

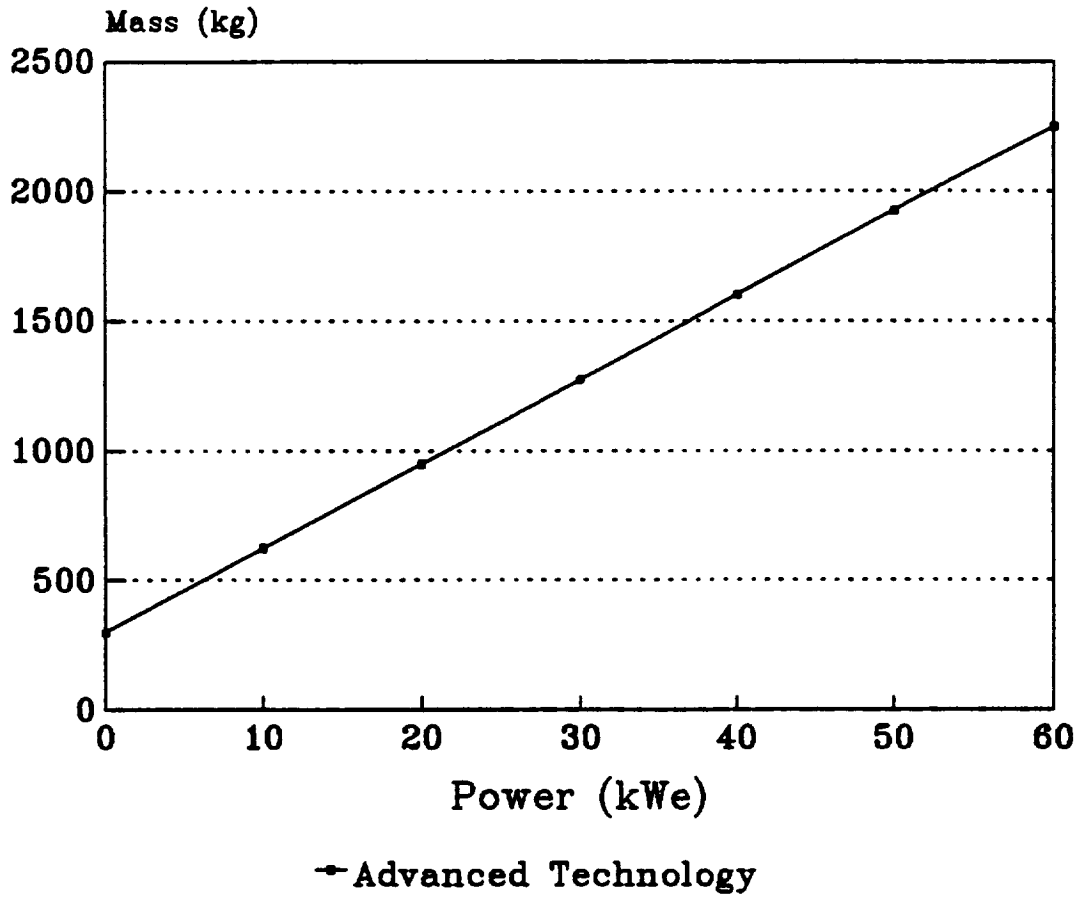

FIG. 70. Mass vs. Power

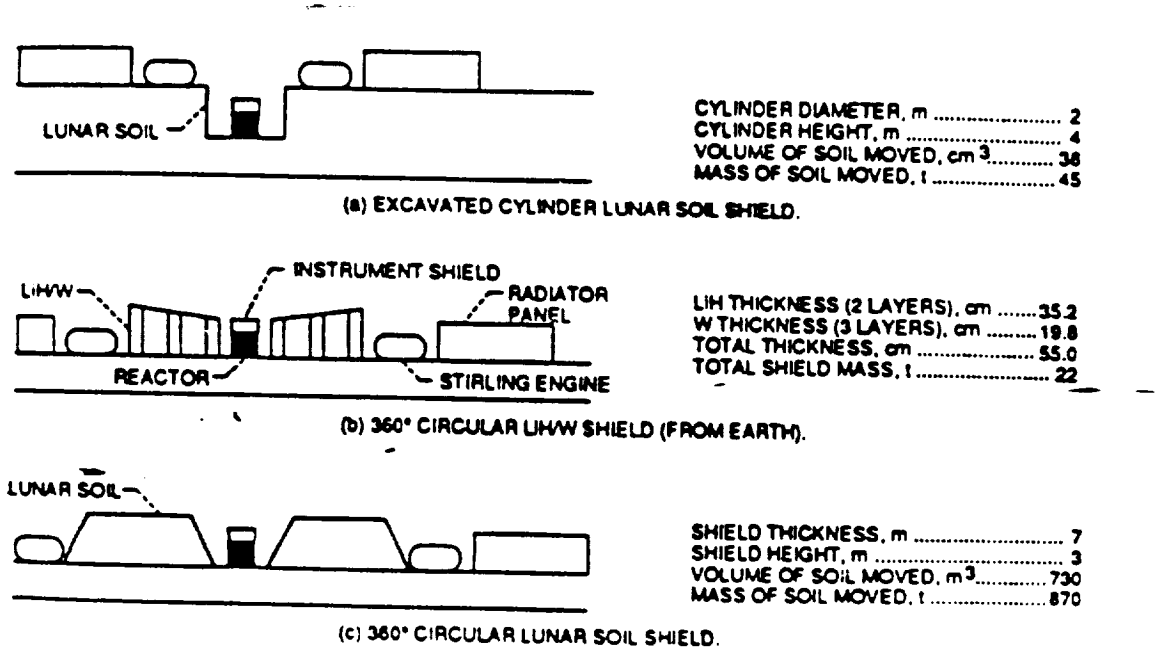

FIG. 71. Shielding Options for SP-100 SRPS
(taken from ref. 150)

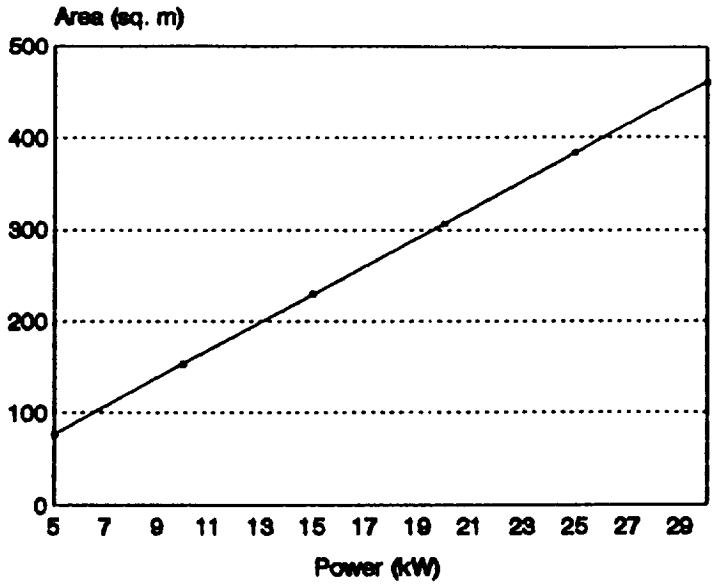

FIG. 72. Power vs. Array Area for GaAs

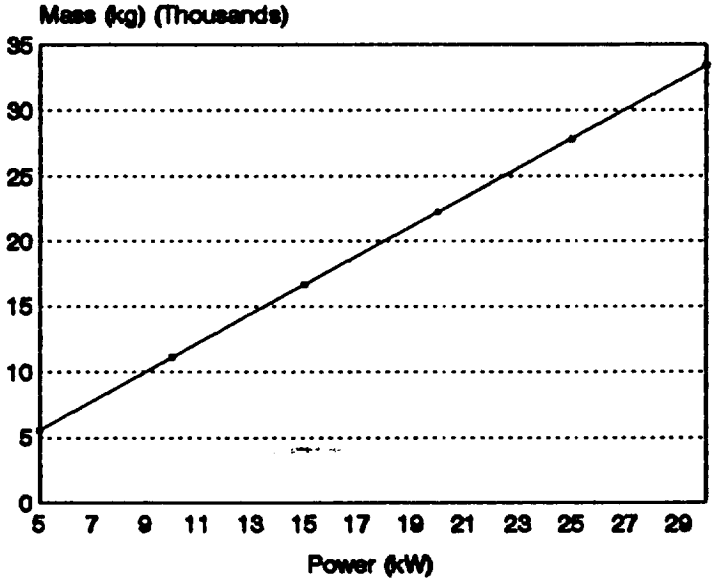

FIG. 73. Power vs. System Mass (GaAs with H/O RFC)

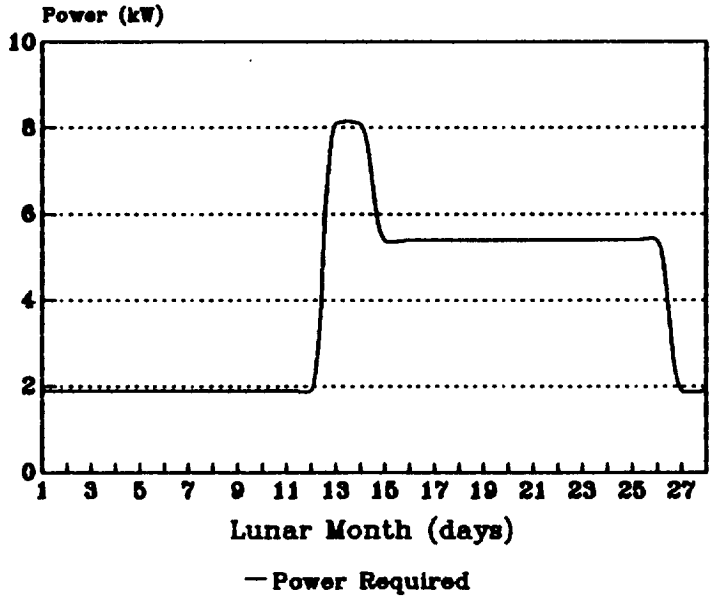

FIG. 74. Power Profile

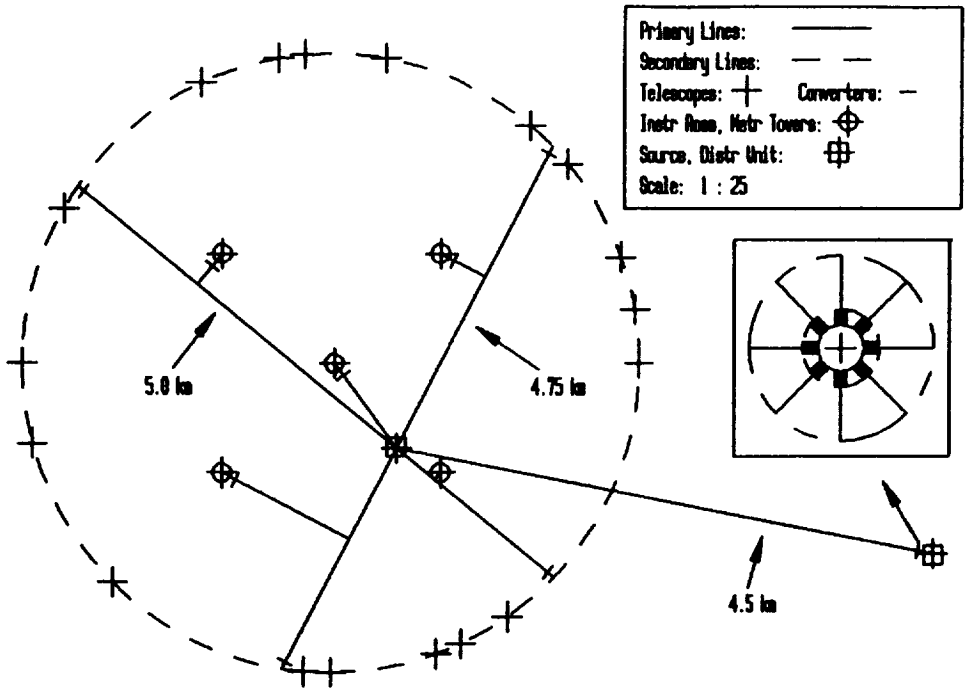

FIG. 75. Power Distribution Network

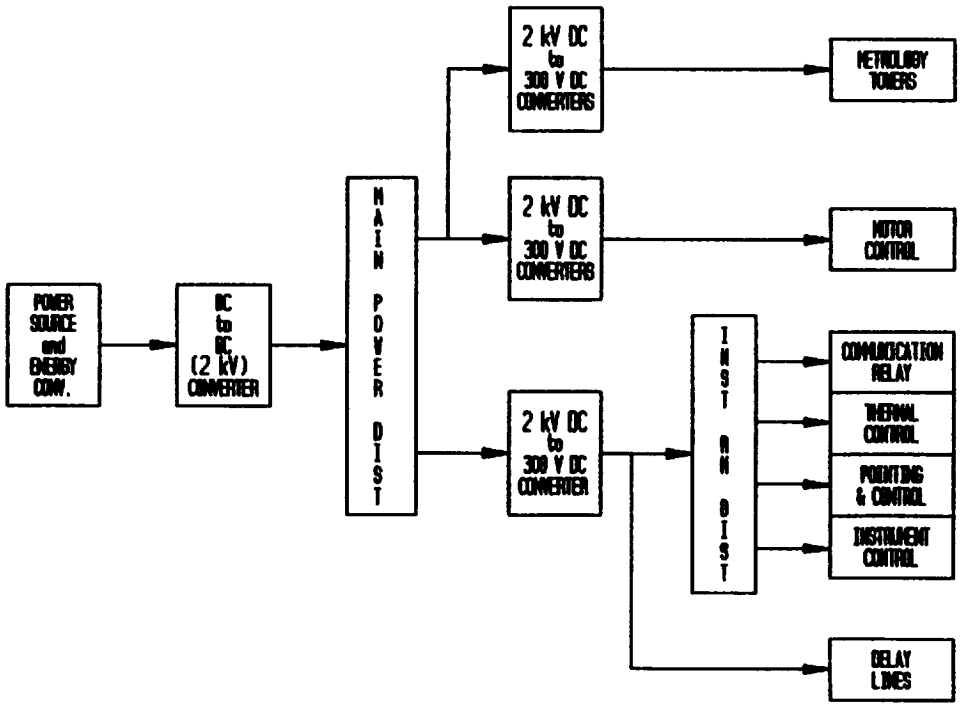

FIG. 76. Power System Block Diagram

VIII. Structures & Thermal Control

VIII.1 Structures

The individual telescope elements will consist of a cylindrical tube that houses the primary and secondary mirrors. The tube is supported by a fork-type mount, providing two degrees of freedom to the system. This fork is supported by a truss base. The tube structure must protect the optics from the hostile environment while maintaining a high level of stiffness. The telescope tube will rotate about its vertical axis by means of a thrust bearing and a set of motor/actuators (fast and slow rotation) mounted to the underside of the fork. Elevating motion will be provided by side mounts using a similar system in the vertical plane. This system will allow for rotation of 360° in the horizontal plane and 160° in elevation (through the zenith). In order to achieve smooth, continuous motion during periods of observation, anti-friction bearings will be used. The entire telescope can be viewed in Figure 77.

VIII.1.1 Telescope Mount

A hydraulic hexapod mount and an altitude-azimuth mount were the primary alternatives studied (types of mounts are shown in Figure 78). Since movement is required about two axes, the best choice for smooth movement is a fork mount with the center of gravity located as close as possible to the rotational axis. The hexapod design was ruled out due to the complicated movements required for the system, the relatively large power requirement for the hydraulic-type lifts, and the questionable reliability of hydraulic systems exposed to the lunar environment. The alt-az fork mount utilizes existing technology with proven reliability and minimal maintenance as well as provide a rigid structure which can be passively balanced. An alt-az mount has been selected for LOITA.

VIII.1.2 Materials

A graphite epoxy composite was chosen as the primary structural material for LOITA. Table 19 contains the critical material properties. Material selection was based on the following requirements:

- High stiffness to minimize deformations.
- Low density in order to minimize weight and decrease transportation costs.
- High strength and modulus of elasticity.

- Very low coefficient of thermal expansion (CTE) to minimize the effects of extreme thermal cycling.

- The ability for the parts to be combined easily without critical surface treatments or bonds. The connections can be molded specifically to interface with other parts during construction.

- The material is very easy to form, allowing contoured shapes which can be specially tailored to the project.

- Very low outgassing properties with maximum losses of 1% gross mass.

The precision alignment of the optical components demands that the structural members supporting the primary and secondary mirrors must not deflect more than 3 nm. The low CTE and high stiffness of the structural material are important in this regard.

Another important factor considered included the strength of the fibers and their volume fraction in the material. A high volume of fibers decreases the possibility of failure. The selected volume of 63% is well within boundaries of safety. The individual fibers will be approximately 10 microns, giving strengths listed in Table 19.

Fiber materials such as Boron were not chosen due to their higher cost and higher coefficients of thermal expansion. A high CTE could cause problems during long periods of heavy thermal cycling. In addition, the tensile strength of many materials decreases when the temperature is increased substantially.

Tensile strength and modulus of elasticity are the highest for graphite composites vs. other composites. Disadvantages of graphite epoxy include poor resistance to high humidity (there is none on the moon) and poor impact resistance. These are not serious problems for our application. Table 20 shows some of these comparisons.

VIII.1.2.1 Structural Considerations

In order to compute estimates of the necessary dimensions of the structural elements, the values of compression, shear, buckling, deflection, and deformation were considered. The following sections explain the analysis undertaken. The numerical results of these analysis appear in Table 21.

VIII.1.2.2 Stress Considerations

The required cross-sectional area of each member was calculated for compressive failure, shear failure, and buckling based on the following assumptions: the weight of the telescope was

placed on a single tube 2 m length and, the diameter of the truss members used in the base was estimated by dividing the load over 6 tubes and performing a simple truss analysis. Extremely small areas were required to eliminate the problems of compressive failure and shearing of the truss members.

VIII.1.2.3 Buckling Considerations

Further calculations were performed to determine the necessary cross-sectional area to support the telescope with its weight evenly distributed across the six 2 m long tubes without buckling. It was determined that the tubing should have an inner radius of 2.75 cm and an outer radius of 3.0 cm. These figures take into account the minimum area needed, as well as a margin of safety to maintain structural stability. The calculations for buckling assumed: the system mass of 500 kg, tube members 2 m long, and material properties from Table 19.

VIII.1.2.4 Deformations and Deflections of the Base

Deformations of the base truss were assumed to be small and evenly distributed since the load of the telescope sits symmetrically over the base and is directed very nearly through the center of the structure's frame. Due to this, any deformations would be carried equally over the structure's base. It was assumed that since the weight was evenly distributed, the base would deform a constant amount at all points.

VIII.1.2.5 Radiation Protection

The constant influx of radiation due to cosmic rays, solar flares and the solar wind has a degradative effect on the material properties of the telescope structure. Of primary concern is the telescope mirrors. It has been calculated that the mirrors can withstand a dose of approximately 10^6 rads before damage occurs.[117]

The radiation dose behind 2 cm of aluminum shielding over a period of 2 years in deep space has been found to be 5022 rads.[117] Extrapolation results in a 50220 rad dose over a 20 year period. This is well below the critical 10^6 limit so 2 cm of aluminum shielding around the optics should be sufficient.

VIII.1.3 Base

The base structure, seen in Figure 79, will utilize a hexagonal truss structure to support the telescope at a height of 3 meters. This height is necessary because the light beam exiting the telescope at the top of the base can travel unimpeded to the instrument room (0.980 meters above

the lunar surface). Calculations performed to account for curvature of the lunar surface were based on the following assumptions: the lunar surface is unobstructed (smooth) and the telescope would be constructed locally vertical. Table 22 shows that the 3 m height provides adequate clearance from the ground to the bottom of the exiting light beam.

The number of legs chosen was based on the thickness and diameter of the tubing. These parameters were crucial in regard to buckling constraints. Results of these studies are shown in Table 21. Twelve tubes were chosen because there was no significant gain in using a larger number of tubes. The tubes will connect together at the upper and lower points of the hexagons with prefabricated joints. These joints will be fabricated on Earth so that they can be easily snapped together during construction. The lowest tier, which connects to the ground through the footings has a distance of 3.0 m between opposing corners of the hexagon. The dimension of the second tier is 2.0 m and the top tier is 1.0 m. The inner and outer radii of the tubes have dimensions of 2.0 cm and 3.0 cm, respectively. This was chosen after a finite element analysis was done using the program EAL.[96] Due to the nature of the program, a two tier truss could not be analyzed because no connections exist between the top and bottom tiers. This adds an extra degree of freedom which could not be corrected in the numerical analysis. Therefore, the scenario used for the computations was that of a one tier truss of 12 members between tiers and 24 total members. The truss was 3 meters high with the six joints on the lunar surface fixed. This assumes the footings to be fully embedded with no movement allowed. Choosing 3 cm as the reference outer radius for the tubing, a series of cross sectional areas was analyzed to determine stress levels and displacements of joints in the x, y, and z directions under a static load due to a 1200 kg mass in lunar gravity. The study showed that a substantial decrease in displacement occurred as the area moved from approximately 0.00025 to 0.001 m^2. From here on, the curve leveled out considerably. This can be seen in Figure 80a. The cross sectional area of 0.0015 m^2 was chosen. This corresponds to an inner radius of 2 cm. It can be seen from Figure 80b that the stresses reduced considerably at this cross sectional area. The data for this tube size (obtained from EAL) can be found in Table 23. The results for the one tier analysis can be extrapolated to the two tier truss. This is done by adding more members to the truss.

In order to guarantee stability, a system of footings will be placed on the base of the structure (one at each joint) to distribute the weight equally to the lunar regolith. The system used will not require the use of bedrock. In addition, little experience has been acquired in driving footings into the lunar surface.

Settlement of the telescope into the soil is of major concern. Resistance to lateral movement also is important, since vehicles and construction efforts could cause ground motion. The three

major types of footings (Figure 81) are rectangular, spudcan, and hemispherical. From tests conducted for NASA to be used in conjunction with a design for a lunar telescope, loads on lunar soil and displacements were studied for a three inch wide footing of the kinds outlined above under loads up to 400 lbs. It was confirmed that the spudcan footing is self installing and performs just as well as the conventional rectangular one. The hemispherical footing was shown to displace more dirt but was seen to be unstable. After a sufficient amount of time, the spudcan footing will show the same stiffness and stability as the rectangular footing. It is known that increased penetration results in stability. The spudcan gives more penetration over time than the rectangular type. Once fully embedded into the soil, the soil's mechanical properties have more effect on future behavior than the type of footing. It has been shown that the spudcan footing can easily be supported by the stiffer layers of regolith found just inches below the surface. The installation of these footings will require only slight entrenching and vibratory compaction to settle the regolith. This will be done during the construction phase. The footings can be drilled directly into the surface to a depth such that the joint connection at the surface is just above ground level. The truss structure can then be built directly atop the footings. Dirt can then be pushed around any open areas to allow the base to settle firmly into the regolith. Furthermore, they allow for adjustment in orientation to achieve a completely level platform. This is done through the use of embedded actuators.

VIII.1.4 Fork Mount

The fork mount was designed with two primary goals: to provide adequate support for the tube structure and to create a suitable enclosed path for the light beam to exit the telescope tube. The fork was designed so that light exiting the tube would strike elliptical mirrors placed along the rotational axes. These mirrors are mounted with ceramic actuators for minute adjustments. For rigidity, the fork mount will be formed as a one piece graphite epoxy structure. The thickness required for the walls of the mount was seen to be 5 cm. The inner region is hollow with a width of 72 cm. The mounting fork will enclose all of the mirrors required for the exit path, as well as the motors required for movement of the telescope. When not in use, this system can be sealed off in order to shield the optics from dust and excess radiation. The motor will sit directly against the bearing on the side opposite the light exit path. This can be seen in the schematic shown in Figure 82.

VIII.1.5 Cylinder Structure

The original truss-ring design of the telescope tube was based on the structure used in the Hubble Space Telescope. This design proved to be inadequate with regards to rigid positioning and deflections of the optical elements with respect to one another.

The tube structure will be comprised of a structural graphite epoxy mirror mount, graphite epoxy tubing from the primary to secondary and primary to stationary exit mirrors. An aluminum shell and door will protect the optics from dust and radiation, as well as shield the aperture from stray light.

The structural graphite epoxy mirror mount will house the primary mirror and provide support for the truss members holding the secondary and stationary exit mirrors in place. The stationary mirror will be held in place by 4 truss members 1.9 cm in diameter. The secondary mirror will also be supported by 4 truss members running from the beyond the outer edge of the primary to the outer edge of the secondary. The diameter of these tubes will be 3.8 cm. The tube diameters were computed such that the deflection of the stationary and secondary mirrors was less than 3 nm when the tube was in a horizontal position. The structural graphite of the cylinder will extend forward, mating with horizontal mounting struts which fit snugly inside the vertical bearings. The cylinder itself is also shown in Figure 82. The thickness of this structure was calculated using the method of finite element analysis. The panel arrangement on EAL is shown in Figure 83. Data from the program indicates thicknesses of 8.0 cm for the mirror backing, 0.8 cm for the large cylinder, and 4.5 cm for the support arms cylinders will provide the necessary rigid support. The graphite epoxy shell tested consisted of eight layers with the fiber laminates aligned at the following angles: 90°, 0°, 45°, -45°, -45°, 45°, 0°, and 90°. This arrangement provides high structural rigidity and eliminates the need for additional rear support of the primary mirror. In Table 24, some of the results for deflections from the EAL method can be seen. The deflections for the rear support ranged from a few nanometers to just over 60 nm. This is a reasonable result due to two factors. First, the two mirrors are connected with rigid truss supports which keep the mirrors in the correct alignment with one another. Second, the EAL program was analyzing a series of panels that came to a point on the back of the cylinder. In this area the panels were irregular in shape and fairly large. This would cause the points to show larger deflections that might actually occur. So, it is reasonable to think that the 60 nm is an overestimate coming from the program's limitations. The deflections of the panels on the sides of the cylinder's tubing are on the order of micrometers. This would be reasonable since the mirrors are held rigidly in place by the four truss members running from the cylinder to the secondary mirror. Further, EAL showed

that all stresses were much less than the yield stress. If further support was deemed necessary, different angles for the layers or a thicker cylinder should be considered.

Around the graphite epoxy support structure, a shell of aluminum 2 cm thick will be used to protect the optics from radiation and micrometeor impacts. This aluminum sheath will extend 0.5 m past the secondary mirror, serving as both a light shield and surface for mounting of the tube door. This 2 cm thickness will keep the bending of the tube to less than approximately 6 micrometers. This will be adequate for our design because the optics are held rigid regardless of the outer aluminum shell.

Affixed to the end of the cylinder tube will be an aperture door similar to the one on the Hubble Space Telescope. Fabricated of 1.5 cm thick graphite epoxy, the door will seal off and protect the telescope's internal optics from dust and micrometeors during periods of non-use. With a total mass of approximately 31 kg, the door will be opened and closed by a small electric actuator. When opened, the door will rotate back and rest on top of the cylinder's casing.

VIII.1.6 Mechanical Control and Error

As previously stated, the telescope will have two degrees of freedom. One mode will be in the horizontal plane where a 360° rotation can be traversed. In the vertical plane it will be possible to traverse 160°. This offers distinct advantages over systems which can only rotate through 90 degrees of elevation. Such systems have difficulty tracking through the vertical (zenith), a condition which requires an impossible acceleration. Permitting the telescope to rotate through 160° allows for smooth, continuous observation.

The altitude-azimuth design chosen requires servomechanism control of rotation about the vertical axis (azimuth) and the horizontal axis (altitude). A thrust bearing mounted on the fixed base will support all of the equipment. The rotating structure, consisting of the entire elevating mechanics and telescope structure, forms the load. Motion will be imparted to the structure by a training motor offset from the rotational center line of the main thrust bearing. The motor will be rigidly mounted to the rotating fork along with the bearings since the resilience of this link directly affects the stiffness of the main drive. The altitude axis will be controlled by a servomotor mounted on the fork unit. The bearing will have an inner diameter of 43 cm to accommodate the light beam out of the system. The bearing will be a tapered roller bearing, which allows for motion in the horizontal. These type of bearings have an excellent load capability in the radial direction and a good running accuracy. The bearings will be made up of cylindrical rollers which have successfully been used in high accuracy applications. The outer diameter is specified for this bearing as 72 cm. The bearings on the side will be mounted roller bearings. Once secured into

position, they will allow for rotation around the horizontal axis. They will have an outer diameter of 72 cm and will also utilize cylindrical rollers. All three bearings will have an approximate width of 30 cm. The positioning of the bearings can be seen in Figure 82.

Bearings made of plastic have several advantages over bearings made of metal and ceramics. Metals require lubrication to reduce friction. Ceramics exhibit the same problem and require fine finishes (i.e. high cost). Therefore, the best choice is that of a plastic. The relatively weak intermolecular bonds of plastics generate less friction and wear than metals do. The plastics also serve best as "dry bearings", especially for low speed applications where freedom is necessary from stick-slip problems. It has been shown in satellite tracking stations that, when flooded with oil, a stick-slip action appears which renders the electronics inoperable. The plastic bearings create a transfer film between contacting surfaces. This, in a sense, performs the function of a lubricant. The choice for our system is that of a metal bearing with a plastic coating. This enhances the abilities of the bearing by giving it extra strength while providing increased heat dissipation. This will also increase the bearing's life. The lifetime for our bearings is estimated at 100,800 hours of operation (25 years).

Selection of the servomechanism is critical to the accuracy of the system, and minimizing the steady-state error is of prime importance. The errors introduced by a servomechanical system can be classified as (i) pointing errors, and (ii) tracking errors.

In the interest of reducing these errors, the system chosen will couple a high precision torque motor and set of bearings. The motors (described in a following section) are mounted against the bearings and will turn at the necessary velocities via a control box.

A closed loop system (detailed in the pointer control section) is required to account for errors which exist in this type of system. A computer will specify the system's direction for pointing, and the motors and gearing will turn the telescope to that position.

VIII.1.7 Mass Estimates

Mass estimates for structural components are computed in Appendix B.

VIII.2 Motors

Each telescope in LOITA will be required to move independently with accuracies on the order of 10^{-6} arcsec over a 12 day period. A crucial element of the pointing and control system will be the drive system used to control the azimuth and elevation rotations of the telescope. There will be two sets of motors for each telescope; one for fast and slow azimuth rotation and one for fast and slow elevation.

To meet the stringent accuracy requirements of the system the motors selected will be direct drive DC torquing motors. As the name implies, these motor directly control the movement of the telescope thus negating the need for a gear system. The disadvantage to this scheme is that a larger, more powerful motor will be required since there will be no mechanical advantage gained from a gear system. However, the accuracy to which the telescopes may be positioned is significantly improved: the limited precision with which gears can be machined will not impact the accuracy of the motion produced by the motor, and unwanted motions due to gear backlash will be eliminated.

VIII.2.1 Types of Motors

There are two types of direct drive DC torquing motors, brush-type DC motors and brushless DC motors. For this application, brushless motors are the best choice. Brushless motors will save weight since they typically produce more torque per pound than brush-type motors. Brushless motors are also more conducive to the space environment. The lack of humidity would not provide sufficient brush filming for a brush-type motor. In addition brushless motors require less maintenance than brush-type motors.

In order to continuously rotate, a motor must receive an alternating current. A direct current power supply requires that the alternating current be provided by a mechanical or electrical process known as commutation. Brushless motors, however, have no means of mechanical commutation and must be commutated electronically. This is accomplished by an amplifier. A sinusoidal commutation amplifier would provide the best possible control of position and velocity at low speeds. Sinusoidal commutation also produces lower ripple torque than the standard six sequence commutation, roughly 1% as opposed to around 5-6%. This allows for more precise position and velocity regulation.

VIII.2.2 Operating Modes

The drive system will have 2 operating modes: 1) fast initial positioning of the telescope, used when first locating the object to be viewed, and 2) slow tracking of the object as it moves with respect to the observatory during the period of observation. The initial pointing operation has been allotted to occur within a time span of approximately 15 minutes. During this 15 minutes, the telescope may have to rotate 180° about it's vertical axis and 80° about it's horizontal axis. The 80° angle of elevation rotation is a result of limiting the telescopes to only 80° of motion from a purely vertical orientation. These time requirements and degrees of motion correspond to an azimuth rotational velocity of about 0.00349 rad/sec and an elevation rotational velocity of about 0.0015514

rad/sec. During the 12 day tracking phase, the angular velocities will be on the order of 2.693 x 10^{-6} rad/sec for elevation and 3.03 x 10^{-6} rad/sec for azimuth. Maximum accelerations required for the system were based on a one second acceleration from a zero initial angular velocity to the maximum required angular velocity. This assumption resulted in a maximum azimuth angular acceleration of 0.00349 rad/sec^2, and a maximum elevation angular acceleration of 0.0015514 rad/sec^2.

The motor will be controlled electronically as shown by the schematic in Figure 84. During the initial pointing phase the position of the telescopes will have to be controlled very accurately, but during the tracking phase both the position and velocity of the telescope will need to be carefully monitored. Two feedback loops will be utilized to accomplish this, one loop will adjust for position errors while the other will compensate for velocity errors. The command signals will be fed into an amplifier which then applies the required voltage to the motor. The error detection devices will find any discrepancies between the actual and the desired position or velocity and send a correction signal back to the amplifier. The amplifier will then supply a correcting input to the motor. The cycle will continue until the error detection devices show that the motor is running at the desired speed or at the desired position. The position feedback loop will utilize a high precision optical encoder for precise motor angle control. The velocity loop will contain either a tachometer or a resolver with which it can accurately determine the velocity of the motor. For these minute angles and velocities of rotation the accuracies of current feedback devices will have to be significantly improved upon.

In order to ensure the best possible accuracy of motion, the motor and telescope should be a critically damped system. The inertia of the load and the inertia of the motor should be matched. This could possibly be achieved by the addition of an inertia wheel, affixed directly to the motor.

The motors finally chosen to drive the telescope system will be designed specifically for this application. Motor parameters have been calculated from the final estimates of the torques required, available voltage and current, and by setting the maximum power consumption of each motor to a specified level. Results of calculations for motor parameters are provided in Table 25. The torques required were multiplied by a factor of 1.5 to account for starting torque and other uncertainties. The static friction value used for calculations was estimated from currently available motors.

The maximum power allotted for the azimuth and elevation drives has been set at 100 W and 50 W, respectively. Since the two motors will be connected in parallel the current, 20 A, must be divided among the motors. 10 A have been allocated for the azimuth drive while 5 A have been

allocated for the elevation drive. This leaves a 5 A for the necessary motor control devices. The voltage supplied to the motors and other equipment has been set at 10 V.

The temperature rise coefficients were determined by the 155° C maximum standard winding temperature for brushless DC motors. Maximum ambient temperatures were taken as 100° C during the lunar day and -150° C during the lunar night.

Table 26 displays the torque calculations and their results. The center of gravity of the telescope, used in the moment calculations, was taken to be at the center of the structure. The moment of inertia was calculated based on a hollow cylinder having a mass equal to the total mass of the telescope, i.e. composite structure, aluminum shell, primary and secondary mirrors. The masses used for the calculations are those mentioned previously, 500 kg for the telescope and 1200 kg for the telescope and fork combination. The accelerations used were the maximum accelerations computed above. Allowable bearing friction was set at 0.05 for static conditions and 0.025 for kinetic conditions. For the calculations of azimuth bearing friction effects, the formula for a block on a flat surface was used. The value for the friction force was then converted into a moment by placing it 15 cm from the center of the support disk which will house the bearings. 15 cm is an approximation for the distance to the center of the bearing ring, allowing for a 24 cm diameter hole at the center of the bearing through which the light beam coming from the telescope will pass. The elevation bearing friction effects were simulated by using friction equations for a journal bearing.

It must also be noted that the torque values used in the calculations are the maximum values which can be expected during operation. During an observation period, the power consumed by the azimuth-axis drive will probably remain fairly constant. The power consumed by the elevation-axis drive however, will fluctuate considerably as the telescope moves during it's operation. As the telescope's angle of inclination increases, the torque and power required will decrease. Conversely as the elevation angle decreases, torque and power required will necessarily increase.

VIII.3 Instrument Room

The fine delay system, instruments and detectors, computers, and communications equipment are housed within the instrument room. The room is located 30 m East of the center of the array along the East-West axis of the array. The light beams will enter the instrument room (fine delay system) 50 m east of the center of the array.

The instrument room is made up of two levels as shown in Figure 85. The upper level houses the fine delay system while the lower level houses the beam combiners, pointing and control equipment, computers, detectors, and other instruments. The communications antenna is mounted above the upper level of the instrument room.

The upper level covers over 83.3 m^2 with its floor at ground level. Most of this area is occupied by the fine delay system which sits 0.5 m off the floor. Access is provided through a set of doors on the western end of the upper level. The doors are situated on the Western side so that dust disturbed by maintenance crews entering the instrument room will not accumulate on the reflectors which are on the eastern side of the room.

The lower level covers 273 m^2 and is 4.5 m below the surface. This depth and the added soil that will be placed on top of the instrument room will aid in the protection and cooling of all of the electronic and optical systems located within. As can be seen in Figure 85, the polarizing arms as well as the beam combiners and instruments are located in an enclosed room. The surrounding walls serve two purposes. First, they will prevent stray light from bleeding into the beam combiners, and second, they will serve as an insulation for the instruments (which will be cooled during observations).

The entire instrument room was designed so that all instruments, computers, and other components could be easily accessible for routine maintenance. Lunar soil will be placed over the top of the entire structure (as shown in Figure 86) to shield the electronic equipment from cosmic rays. The structure itself will be made of aluminum. A power converter will be housed within its own structure next to the instrument room.

VIII.4 Thermal Control

In order for LOITA to operate efficiently into the infrared spectrum, it has been deemed necessary to cool the telescopes and instrumentation to 70K. Additionally, any cooling techniques or apparatus must be highly reliable and of minimum mass. With these requirements in mind, the thermal analysis consists of:

1) Determination of the equilibrium temperature of the telescope structure for both the lunar day and night with and without the use of radiation shields to protect the telescopes from both lunar and solar radiation.
2) Transient temperature analysis of the telescope structure throughout the lunar cycle.
3) A proposed refrigeration system for cooling the instrumentation systems within the central housing.

VIII.4.1 Passive Temperature Equilibrium and Exterior Coatings

To simplify the analysis of the equilibrium temperature reached by the telescope structure, it was assumed that the telescope could be treated as a greybody, the moon and sun as blackbodies, and that there was negligible internal heat generated within the telescopes' cylindrical casing. During the lunar day, two sources of radiative heat effect the telescope: the sun and the moon. The solar heat flux was taken to be constant at 1350 watt/m^2. The moon's albedo is 0.07[134] so the solar flux actually reaching the moon surface was 1256 watt/m^2. Treating the moon as a blackbody radiating at 375K during the lunar day results in a lunar heat flux of 1120 watt/m^2.

The changing position of the sun was not taken into account for the equilibrium calculations. Instead, the sun was taken to be directly overhead at all times throughout the lunar day. This results in the solar heat flux affecting a larger area of the telescope then really occurs, so the maximum temperature calculation is slightly higher than expected. During the lunar night the only source of radiant heat is the lunar surface. The moon was treated as a blackbody radiating at 120K resulting in a heat flux of 12 watt/m^2.

The thermal equilibrium calculations displayed in Appendix H show the defining parameter for the equilibrium temperature to be the absorbtivity to emissivity ratio for the exterior surface. For a given ratio the equilibrium temperatures for the lunar day and night can be determined. This was done for a range of absorbtivity/emissivity ratios with the results plotted in Figure 87. The plot shows an exterior absorbtivity/emissivity ratio in the range of 0.1 to 0.2 which would result in temperature fluctuations of no more than 170K.

In determining the appropriate exterior surface coating, not only does the ratio of absorptivity to emissivity have to be low, but the resistance of the coating to radiative degradation must be considered. Exposure to ultra-violet radiation can trigger chemical reactions within the surface coating that tends to change its radiative properties. With time, the absorptivity to emissivity ratio of some coatings can rise resulting in a change of temperature conditions for the whole structure. Because the telescopes will be exposed to ultra-violet light for extended periods of time, an exterior coating resistant to radiative degradation is necessary.

Two possible exterior surface coatings were considered: anodized aluminum and magnesium oxide aluminum oxide paint. Anodized aluminum has a sufficiently low absorptivity to emissivity ratio of 0.12, but data concerning its resistance to radiative degradation was unavailable. Magnesium oxide aluminum oxide paint also has a low absorptivity to emissivity of 0.098. Additionally, this coating has shown some resistance to radiative degradation.[133] As a result, magnesium oxide aluminum oxide paint was chosen as the exterior coating of the telescopes cylindrical casing.

Using magnesium oxide aluminum oxide paint results in equilibrium temperatures of 212.5K during the lunar day and 58.7K during the lunar night. Assuming the telescope reaches thermal equilibrium in a reasonable amount of time, the use of temperature control systems for the telescope structures may not be necessary.

VIII.4.1.1 Radiation Shield Considerations

The large variations in the equilibrium temperatures of the telescopes cause thermal stresses in the structures. In an attempt to minimize these stresses, the use of radiation shields was considered. These shields would be made of thin aluminum sheets with the possibility of adding insulation to further impede the temperature variations in the shields and, consequently, in the telescope structures. The shields would be coated in a similar manner as the telescope structures in order to reduce their equilibrium temperatures. Calculations similar to those performed in the telescope temperature equilibrium section indicate that the equilibrium temperature of both the lunar and solar shields would be 253.1K during the lunar day. These calculations are conservative as they do not take into account the radiation protection that each shield would provide for one another. They also assume that the temperature distribution is constant throughout the thickness of the shield. Insulation would limit this effect. Using these figures, the maximum temperature of the telescope would be 141K. This is a 70K decrease in temperature when compared to the calculations without the shield.

The primary problem with the use of radiation shields is the additional weight. For one telescope, a shield protecting against radiation from the sun would require a surface area of approximately 7 x 3 m. If a 0.5 cm thickness is used, the mass of that one shield would be 284 kg. The total weight would therefor exceed 10,000 kg. This does not include insulation, supports, and additional motors to uncover the telescopes during operation time.

When comparing the advantages of using radiation shields against the additional mass involved, the shields were deemed unnecessary.

VIII.4.2 Transient Temperature Analysis

Whether or not the telescopes need to be maintained at a constant temperature through the use of thermal control systems depends primarily on how fast the telescopes can dissipate heat with the onset of the lunar night. To determine this, a Crank-Nicholson implicit finite technique was used to model a simplified transient heat conduction problem.

In simplifying the transient heat analysis, an attempt was made to approximate conservatively. As a result, while the analysis does not accurately reflect the problem, the errors involved tend to be pessimistic.

It was assumed that no heat was conducted through the telescope structure either in the direction of the cylinder's length or around the cylinder's perimeter. In actuality, unequal amounts of incident radiation flux would result in cooler parts of the telescope which would dissipate heat more quickly after conduction around the cylinder's perimeter. Also, since the radiation heat flux within the interior of the telescope casing is negligible compared to the conductive heat flux, the cylinder was assumed to be solid. The solid was assumed to be isotropic and the material properties of aluminum were used. With these two simplifications, the situation reduces to a transient heat conduction problem in one dimension.

Incident radiation from both the moon and the sun changed with time in this problem. The moon temperature was taken to vary from 375K to 120K with a 5K/hr linear gradient. The time of sunset was taken to occur in the middle of the moon temperature variation. Before sunset, the incident solar flux was constant. As the sun dipped below the horizon, the solar flux was assumed to vary linearly.

To determine the boundary conditions it was assumed that the thin exterior coating instantaneously came into thermal equilibrium with the incident radiation. The resulting temperature was used as the boundary temperature value. Half the cylinder has assumed to be exposed to both the lunar and solar radiative fluxes while the other half is exposed to only the lunar flux.

Figure 88 shows the changes of the outside boundary temperatures, the temperature at the center of the cylinder, and the temperature of the moon. From this it can be seen that the cylinder center reaches the same temperature as the outer surface roughly eight hours after the variation in the lunar temperature ends, or approximately 32 hours after sunset. This time lag has been deemed a reasonable waiting period for the start-up of telescope operations and the use of active temperature control for the telescope structures should not be necessary according to these results.

VIII.4.3 Refrigeration of Instrumentation

The housing in which the instrumentation is to be stored is at an ambient temperature of 250K below the lunar surface.[130] Therefore, it is necessary to use a refrigeration system to cool the instrumentation to the desired value of 70K.

In cooling the instruments, three design constraints were kept in mind. Two constraints were the high reliability and minimal mass mentioned in the beginning of the section. To

accomplish this, the system needed to be simple with few moving parts. Additionally, the system needed to subject the instrument casing to an extremely low vibration level.

Four instrument encasings need to be cooled. To reduce the required cooling heat loads, the instrument boxes need to be insulated against radiant and conductive heat fluxes. For insulation, multilayered aluminized mylar sheets of 10 micron thickness is proposed. The sheets are crinkled so no spacer material is required between successive layers. Using 3 cm of insulation with 33 sheets per cm thickness results in an effective thermal conductivity of 4.2×10^{-5} watts/(mK). Using Fourier's law of conduction, the heat load through the insulation is 3.65 W. Additionally, heat will leak through the sensor aperture openings which cannot be wrapped in insulation. Radiation fluxes through these areas results in an additional 0.22 W of heat load for approximately 4 W of total heat load per instrumentation box. The cooling system is designed to handle up to six watts of cooling power for each box.

The proposed cooling system is based upon the Stirling refrigerating cycle. Figure 89 depicts the refrigeration system configuration and its positioning with regard to the instrumentation casing. Four identical systems are required, one for each set of instruments. The system works by coupling cold hydrogen gas to a copper plate within the instrument box through stainless steel heat pipes utilizing nitrogen. The copper plate is maintained at a temperature of 70K. All instruments within the casing are thermally coupled to the copper plate. As a thermal sink, another stainless steel heat pipe using Freon-12 and operating at 295K is coupled to 300K hydrogen gas. This pipe radiates heat into the 250K thermal radiation field of the instrument room.

To minimize the vibration levels of the instrument box induced by the refrigeration system, the Stirling refrigerator is not connected to the instrument casing directly. Instead, the refrigerator acts to maintain a 0.2 x 0.2 x 1m pressurized hydrogen tank at 60K. Heat pipes are run from the refrigerator to the hydrogen vessel box and from the hydrogen vessel to the instrument casing. Within the hydrogen vessel, natural convection forces act to transfer heat to and from the heat pipes. Vibrations from the refrigerator are reduced by using elastic seals around the heat pipe entry locations.

Appendices H - N show the heat transfer calculations used to determine the required dimensions of the refrigeration system.

The Stirling refrigeration system works through alternately compressing and expanding hydrogen gas using reciprocating piston machinery. A cross-section of the Stirling engine is shown in figure 90. A reciprocating compressor compresses gaseous hydrogen at 300K from a pressure of 1 atm to 1.88 atm. The hydrogen is then pumped through aluminum tubing at 10 m/s. Six watts of heat is transferred by forced convection from the hydrogen to the Freon-12 heat pipe

and radiated out into the colder 250K housing environment. The hydrogen then passes through a dense bronze metal matrix mesh that is the regenerator of the system. The regenerator acts as a thermodynamic sponge, alternately accepting or rejecting heat from the hydrogen gas as required. For perfect or near perfect regeneration, the regenerator must have a heat capacity much greater than the total heat capacity of the gas passing through it. Based on calculations of the total hydrogen gas mass and the total bronze mesh mass, this requirement was fulfilled (see Appendix N). As a result, perfect regeneration was assumed. The mesh consists of 100 micron diameter bronze strands. The strands are packed together 250 x 250 per cm.

As the hot hydrogen passes through the regenerator, the bronze absorbs heat from the hydrogen, cooling the gas to 55K. The cool gas then flows into aluminum tubing which is coupled to the instrument casing, providing six watts of cooling. As heat is transferred to the working fluid, the fluid temperature is maintained at a constant 55K because of decreased fluid pressure due to expansion. After the fluid passes through the regenerator its pressure is 0.443 atm; after expansion, the pressure is reduced to 0.230 atm.

After the expansion process and refrigeration is complete, the hydrogen flow reverses direction, passing back through the regenerator where it absorbs heat to come to 300K, and goes to the compression tank. At this point the cycle is complete.

The total mass of the system is estimated to be 30 kg.

VIII.4.4 Radiation Shielding

To insure the effective operation of the interferometry instrumentation, it is necessary to shield them from physical damage due to and noise produced by cosmic rays and solar flares. Since the instruments are to housed at least partly beneath the lunar surface, it is proposed to use excavated lunar regolith as shielding material. Calculations have been made suggesting that 5m of compressed lunar regolith of a density of 2 to 3 g/cm^3 would reduce the radiation flux to levels tolerable for telescope instrumentation.[18]

TABLE 19. PROPERTIES OF GRAPHITE EPOXY & ALUMINUM

Graphite Epoxy	
Axial Stiffness	181 GPa
Transverse Stiffness	10.3 GPa
Shear Stiffness	7.17 GPa
Modulus of Elasticity	165 GPa
Poisson's Ratio	0.28
Axial Tensile Strength	1500 MPa
Axial Compressive Strength	1500 MPa
Transverse Tensile Strength	40 MPa
Transverse Compressive Strength	246 MPa
In-Plane Shear Strength	68 MPa
Cured Density	1.6 g/cm^3
Cured Fiber Volume	63%
Aluminum	
Ultimate Tensile Strength	400 MPa
Yield Strength in Tension	250 MPa
Yield Strength in Shear	145 MPa
Modulus of Elasticity	200 GPa
Coefficient of Thermal Expansion	11.7 x 10^{-6}/°C

TABLE 20. RELATIVE PROPERTIES OF HIGH PERFORMANCE FILAMENTS
(taken from reference 100)

			Graphite		
Property	S-Glass	Boron	High Modulus	High Strength	Organic(PRD-49-III)
Mechanical					
Specific Strength	high	high	moderate	high	very high
Specific Modulus	low	high	very high	high	moderate
Uniformity of Properties	excellent	excellent	moderate	moderate	excellent
Impact Resistance	excellent	fair	poor	poor	excellent
Elongation to failure	high	low	low	moderate	moderate
Compression load-carrying ability	low	very high	moderate	high	low
Erosion resistance	moderate	high	low	low	high
Notched fatigue life	low	moderate	moderate	moderate	high
Creep behavior	high	very low	very low	low	moderate
Stress rupture strength	low	high	moderate	moderate	high
Shear bond to matrix	good	excellent	fair-good	good	fair-good
Thermal/physical					
Density	high	high	moderate	moderate	low
CTE	high	moderate	very low	very low	very low
Thermal conductivity	low	moderate	high	high	low
Thermal stability	high	high	high	moderate	limited
Damping ability	good	fair	fair	fair-good	excellent
Dielectric properties	good	poor	poor	poor	excellent
Chemical					
Oxidation resistance	excellent	excellent	poor	poor	not established
Resistance to solvents	high	high	high	high	high
Resistance to high humidity	fair	fair	poor	poor	excellent

TABLE 21. NECESSARY HEIGHT OF TELESCOPE SUPPORT TO OVERCOME CURVATURE OF THE MOON & TO COMPENSATE FOR THE ENTRANCE HEIGHT TO THE INSTRUMENT ROOM

Telescope Position (km) from center of array (x, y)	Height of Structure (m)
2.45, 0	2.707
1.56, 1.92	2.733
-1.11, 2.27	2.809
-2.47, -0.65	2.848
0.81, -2.35	2.754
1.87, 1.61	2.724
-2.56, 0	2.851
1.38, -2.05	2.738
-0.48, 2.46	2.791
-0.05, -2.50	2.779
-0.27, 2.49	2.785
1.01, -2.27	2.748
-2.22, 1.25	2.841
2.30, 0.86	2.711
-0.27, -2.49	2.785
-1.82, -1.77	2.830
0.38, 2.46	2.766
2.41, 0.43	2.708

TABLE 22

Compression
Axial Strength = 1500 MPa
Load:

kg	N	Needed cross-sectional area (m^2)
500	816	5.44×10^{-7}
750	1225	8.17×10^{-7}
1000	1633.3	1.09×10^{-6}

Assuming telescope mass = 500 kg, and astronaut mass of 180 kg x 2 = 360 kg, then total mass is 860 kg.

860	1404.7	9.36×10^{-7}

If using 6 tubes, an area of 1.56×10^{-7} m^2 is needed. Then R_o = 0.03 m and R_i = 0.0299998 m.
If using 8 tubes, an area of 1.17055×10^{-7} m^2 is needed. Then R_o = 0.03 m and R_i = 0.2999 m.

Shear
Supports holding cylinder
Assuming 816 N down, the cross-sectional area needed is 6×10^{-6} m^2. Thus R_o = 0.03 m and R_i = 0.0299681 m.

Buckling
Assuming a truss tube to be 3 m long with the structure held by 6 tubes: $P_{cr} = \pi^2 EI/L_e^2$

R_o (m)	R_i (m)
0.02	0.0199
0.03	0.0300
0.04	0.0400

TABLE 23

Note: All joints 1-6 on surface were considered fixed and carried no displacement or stress. Analysis was done for a single tier truss of 3 m height. Outer radius for the tubes was chosen to be 3.0 cm. The load applied was that of a 1200 kg mass. Results shown here are for a 2.0 cm inner radius.

Static Displacements

Joint	X	Y	Z
7	0.142372	0.082085	0.019766
8	0.002985	-0.159236	-0.018766
9	-0.132347	0.078290	0.018152
10	0.141458	0.081556	-0.019643
11	-0.001082	-0.163538	0.019667
12	-0.141980	0.082085	-0.019729

Stress in Members

Member	Highest Felt (10^5)	Member	Highest Felt (10^5)
7	-1.290360	17	-8.698470
8	0.881711	18	-8.884500
9	-1.317690	19	6.776650
10	0.789611	20	6.383920
11	-1.290280	21	-8.49788
12	0.788826	22	-8.368740
13	-8.367770	23	6.253310
14	-8.367220	24	6.254810
15	6.253840		
16	6.589360		

TABLE 24. RESULTS OF CYLINDER FINITE ELEMENT ANALYSIS

Results shown here are for various panels across the cylinder. The results show a sample of the deflections for the panels on the cylinder.

Main Cylinder Deflections (10^{-6} m)	Rear of Cylinder (10^{-11} m)
-0.01444154	0.0948077
-0.04087860	0.144530
-0.1158740	0.189048
-0.1238980	-8507.13
0.1264690	-6296.40
0.1397350	-6804.56
-0.1493100	-5672.57
-0.1666090	

TABLE 25. REQUIRED MOTOR CONSTANTS

	Azimuth Drive	Elevation Drive
Peak Torque Rating	51.7 Nm	28.1 Nm
Peak Power	100 W	50 W
Motor Constant	5.27 Nm/W	4.03 Nm/W
Static Friction	1.0 N	0.5 N
Max. Winding Temperature	155°C	155°C
Temperature Rise per Watt	0.55°C/W	1.10°C/W
Torque Sensitivity	5.27 Nm/amp	5.72 Nm/amp
DC Resistance	1.0 Ω	2.0 Ω

TABLE 26. MOTOR CALCULATIONS

Moment of Inertia About Rotation Axis:

$I = (1/2)\, mr^2 + (1/12)\, ml^2 + m((3/10)l)^2$

$I = 2.5$ m, $m_a = 1200$ kg, $m_e = 500$ kg, $r = 0.9$ m

$I_a = 1785.6\ m^4$

$I_e = 744.0\ m^4$

Azimuth-Axis Calculations:

$\mu_k = 0.025$, $\mu_s = 0.05$, $a = 0.00349\ rad/sec^2$, $W_m = 1962.0$ N

Friction force:

Static, $F_s = \mu_s W_m = 98.1$ N Dynamic, $F_k = \mu_k W_m = 49.05$ N

Conversion to moments, $M_{Fs} = \mu_s W_m d = 28.25$ Nm, where $d = 0.288$ m, $M_{Fk} = 14.13$ Nm

Summation of moments:

$M_{mas} = I_a a + M_{Fs} = 34.48$ Nm

$M_{norm} = M_{Fk} = 14.13$ Nm

Elevation Axis Calculations:

$a = 0.00155\ rad/sec^2$, $r = 0.05$ m, $W_{pm} = 817.5$ N

Friction moment:

Static, $M_{Fs} = 8.79$ Nm, where $d = 0.215$ m

Dynamic, $M_{Fk} = 4.395$ Nm

$M_{max} = 18.73$ Nm

I_a - estimate for moment of inertia of telescope and fork mount
I_e - estimate for moment of inertia of telescope
m_a - mass of the telescope unit and fork mount
m_e - mass of the telescope unit
W_m - weight of telescope unit and fork mount
W_{pm} - weight of the telescope

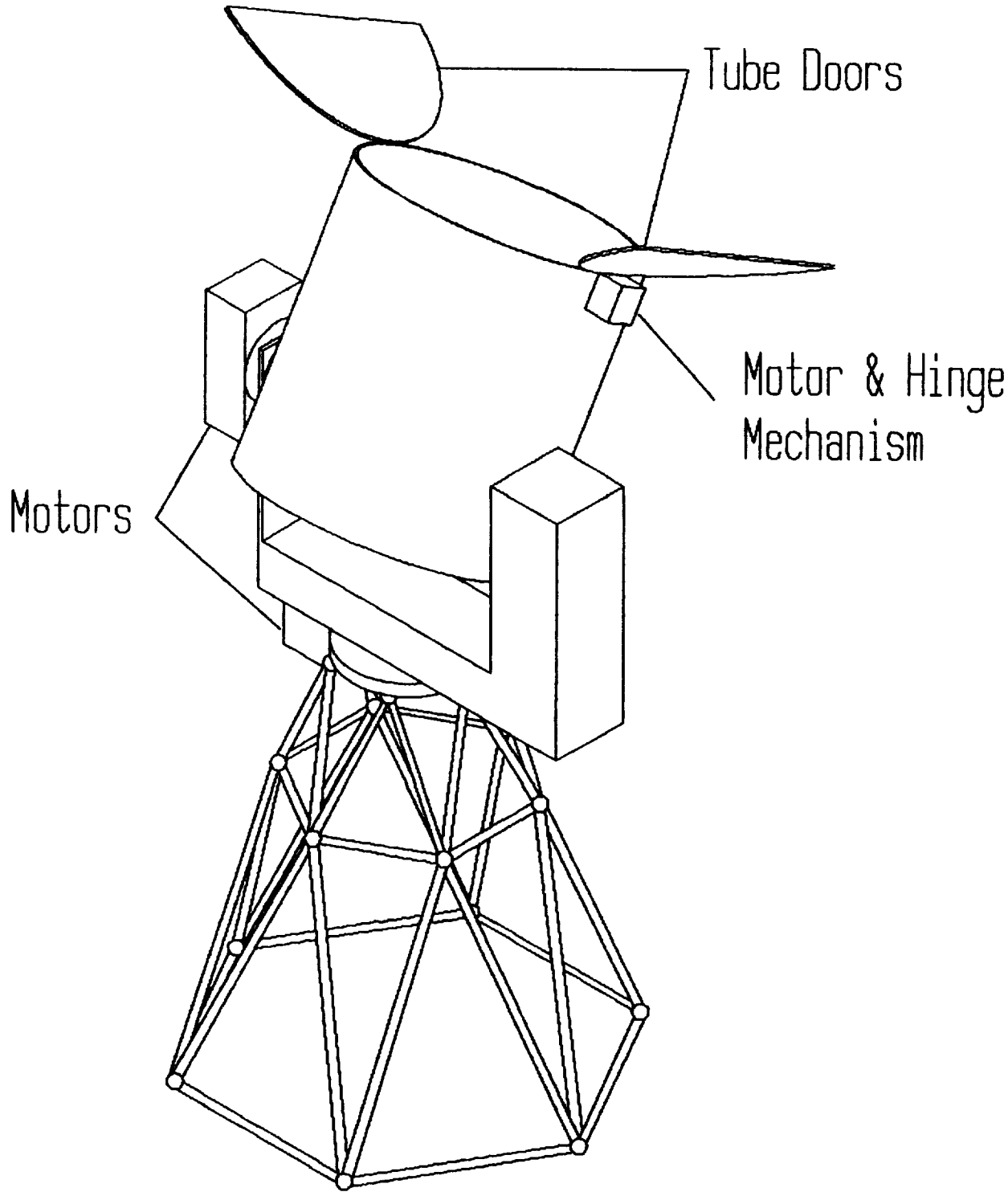

FIG. 77. Telescope

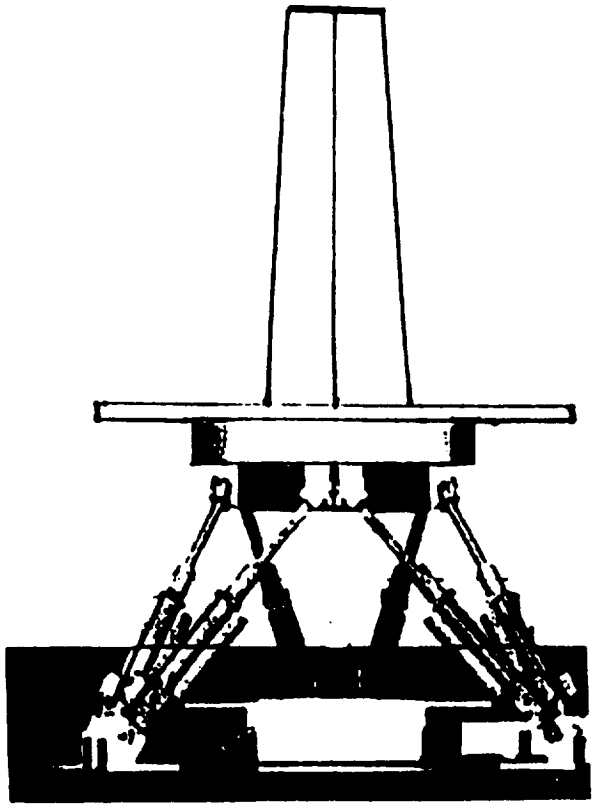

Hexapod Mount

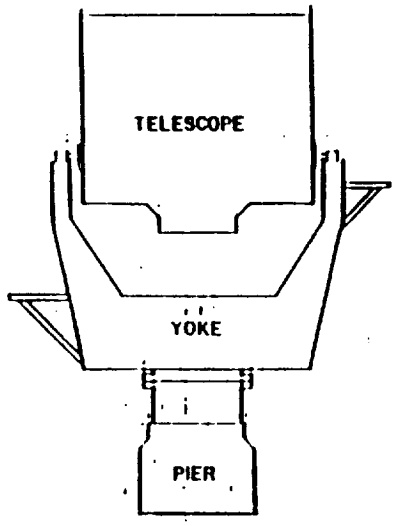

Conventional Alt-Azimuth
Gimbal System

FIG. 78. Types of Telescope Mounts
(taken from ref. 98)

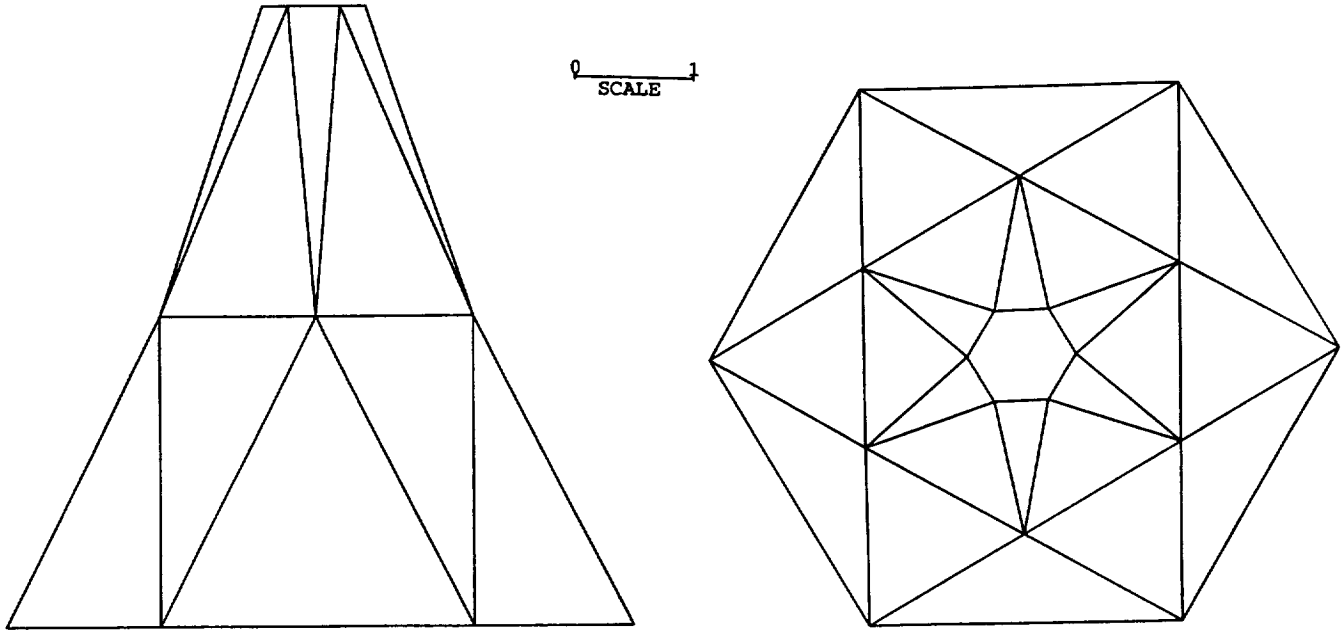

FIG. 79. Base Truss Structure
(from EAL)

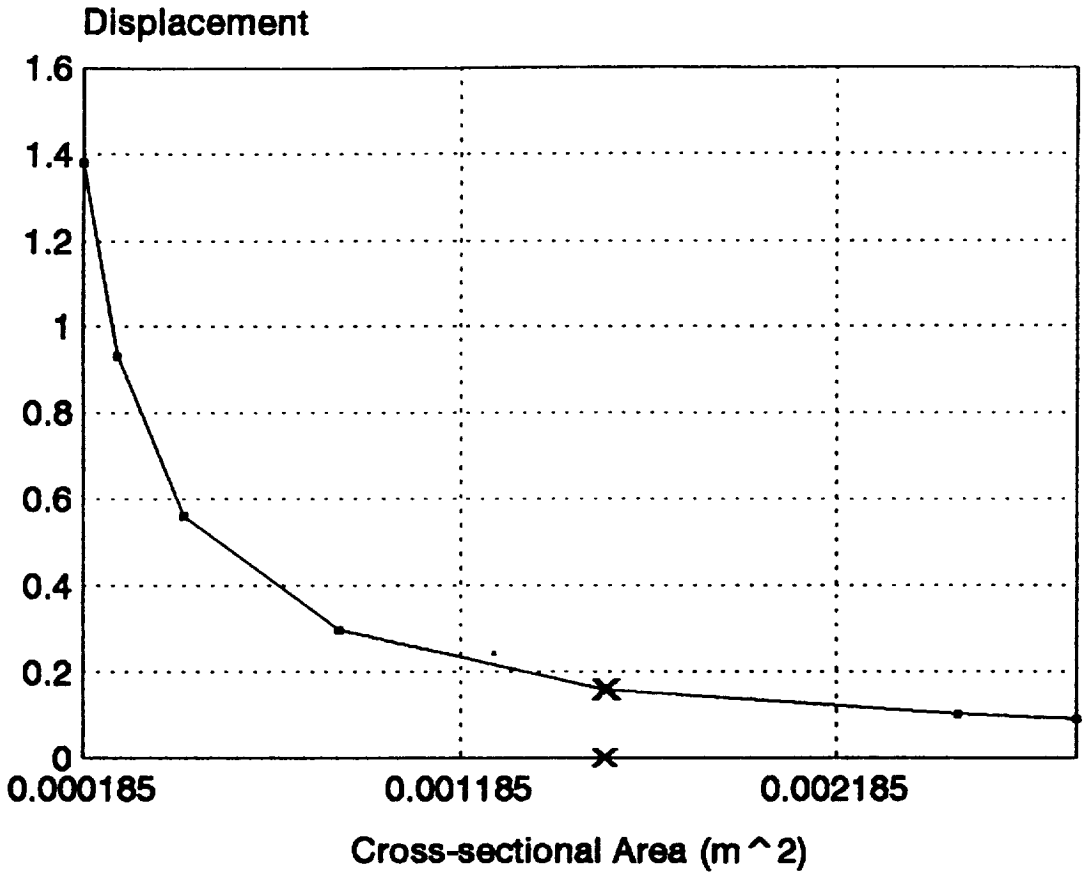

a. Displacement Analysis

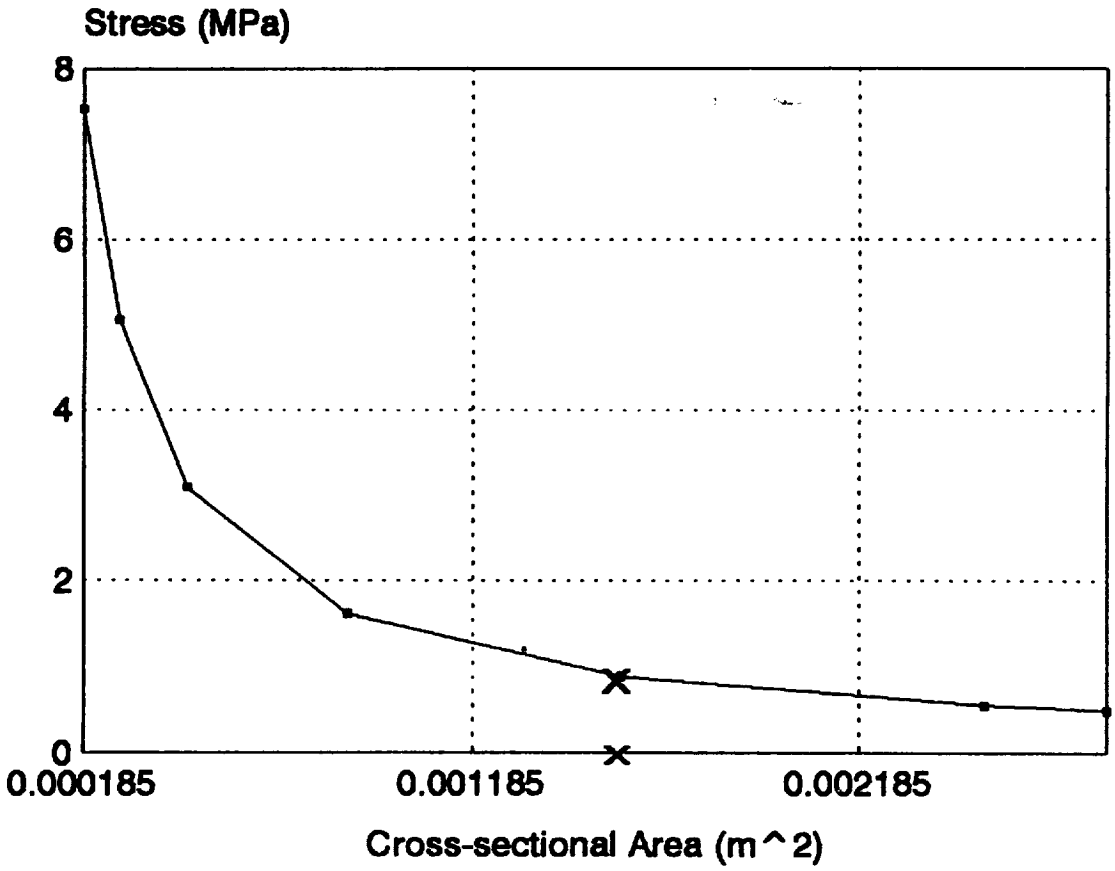

b. Stress Analysis

FIG. 80. Displacement & Stress Analysis

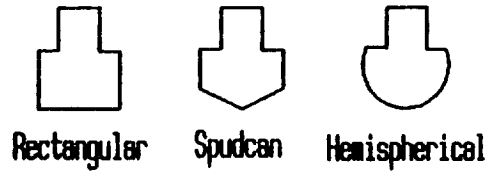

FIG. 81. Types of Footings

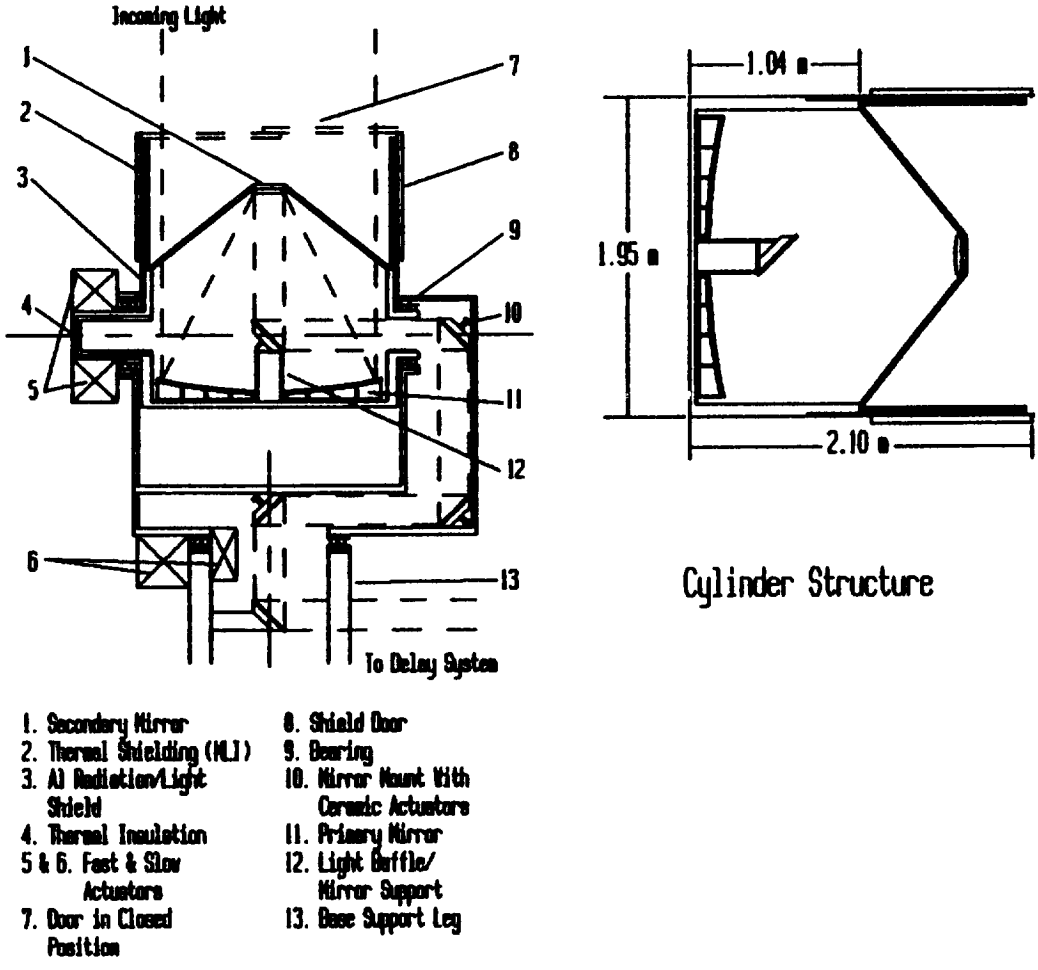

FIG. 82. Telescope Section View

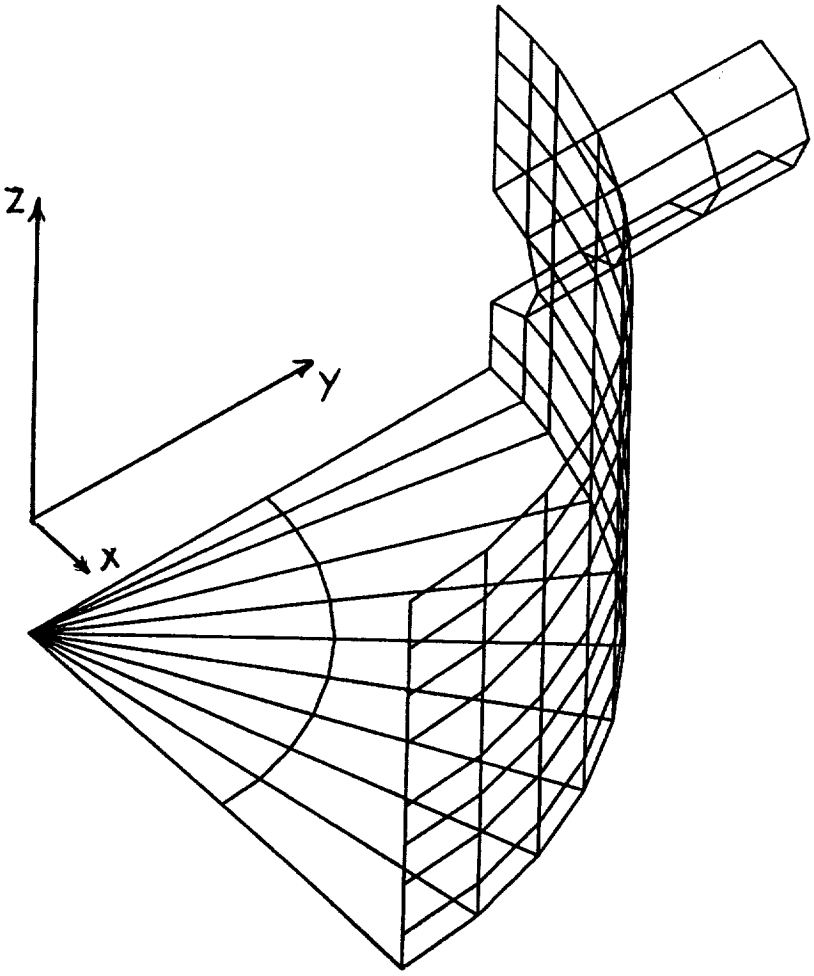

FIG. 83. Cylinder Panels from EAL

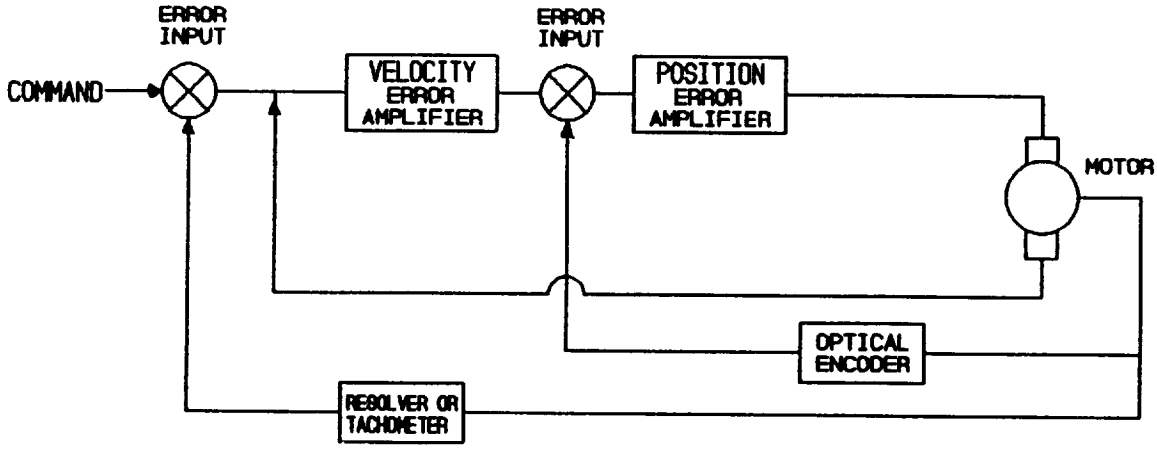

FIG. 84. Motor Control Block Diagram

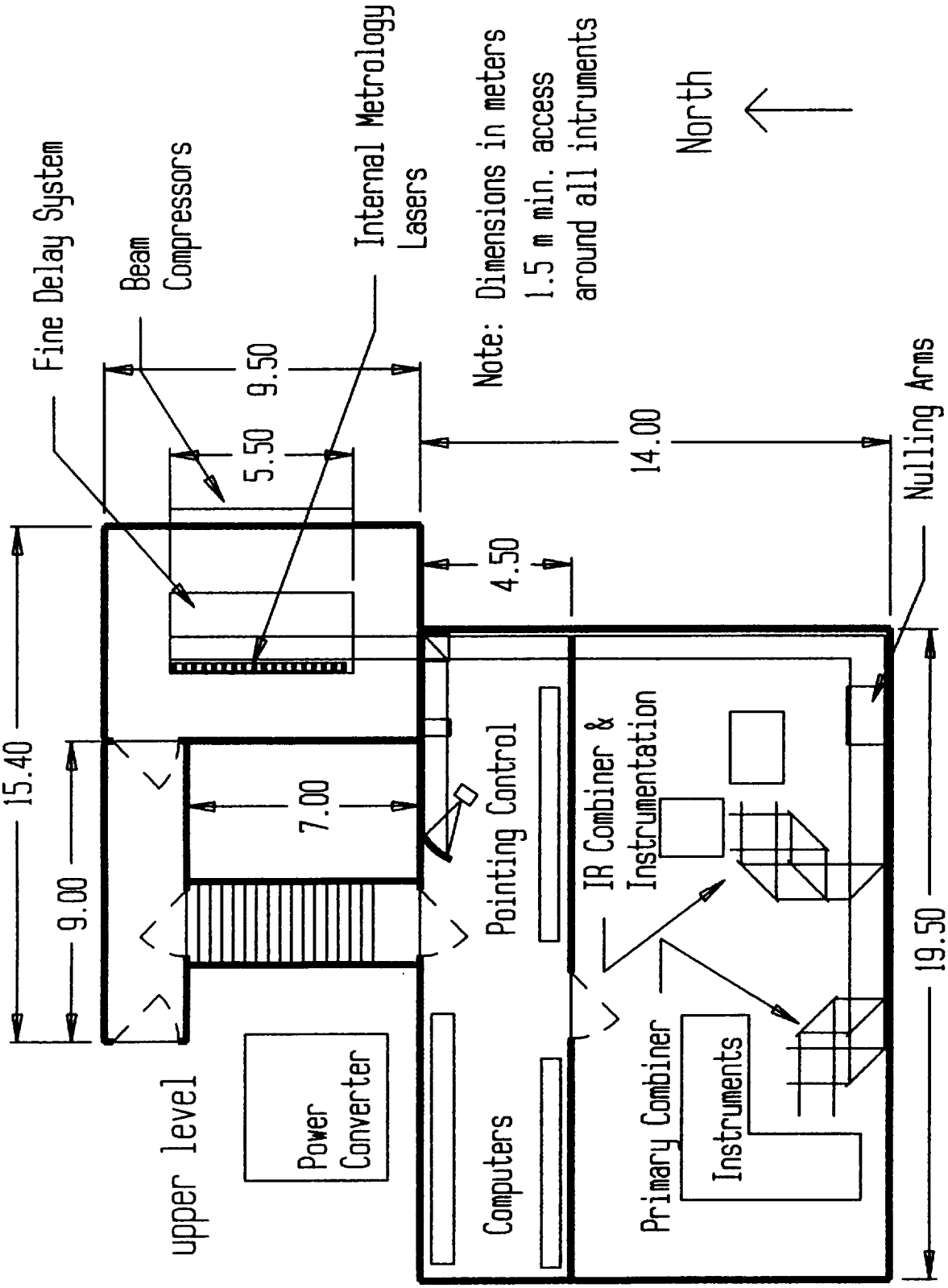

FIG. 85. Instrument Room Floor Plan

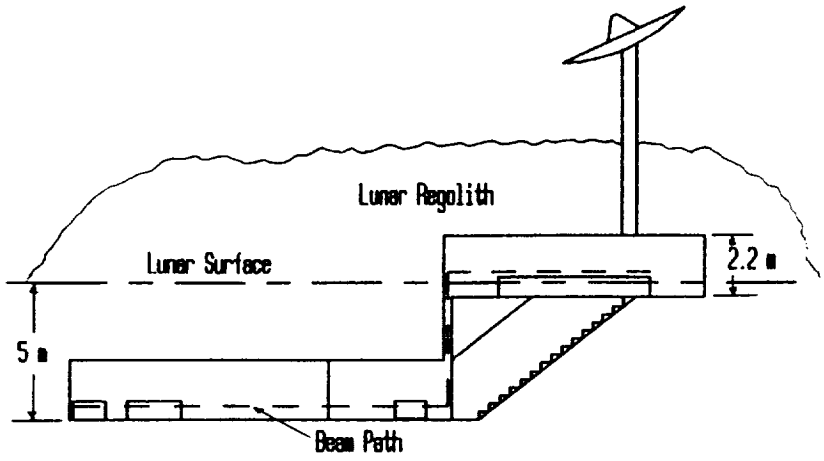

Elevation

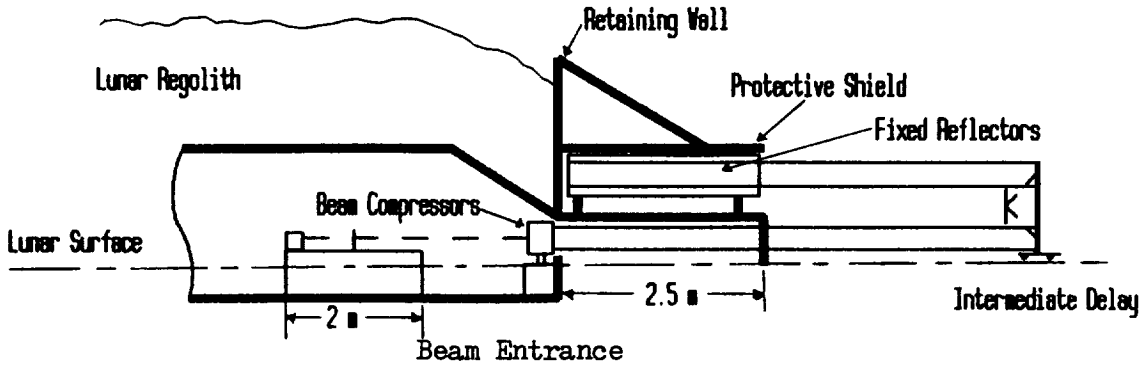

FIG. 86. Elevation View of Instrument Room

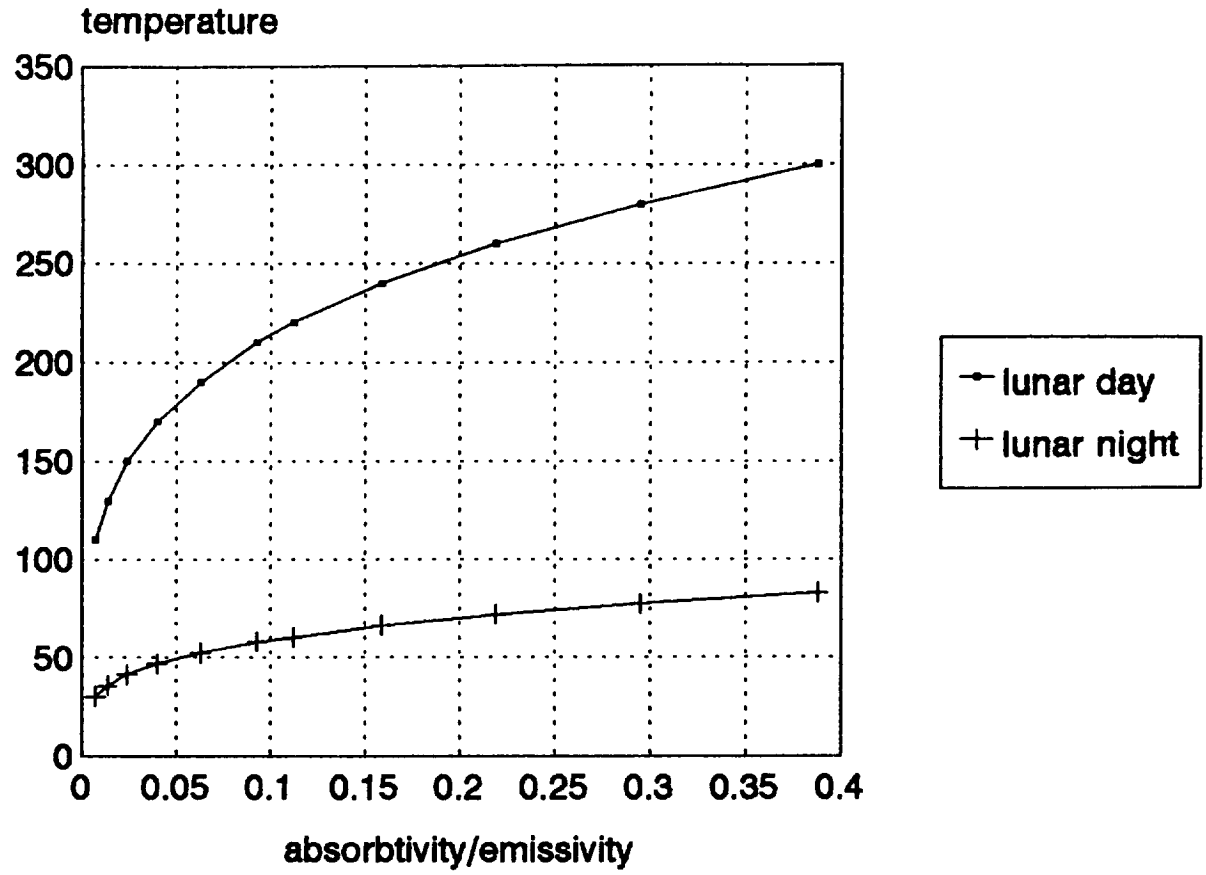

FIG. 87. Temperature vs. Absorbtivity/Emissivity

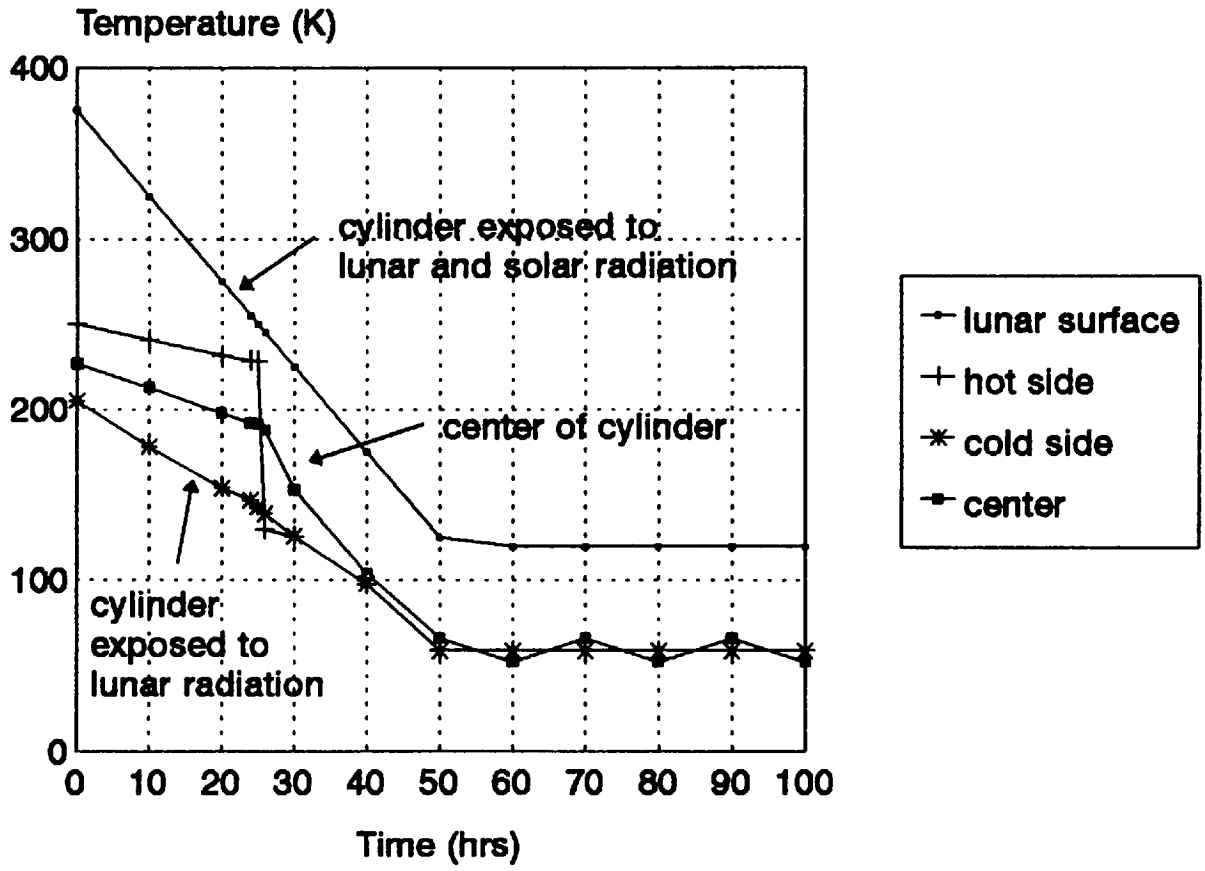

FIG. 88. Transient Temperature vs. Time

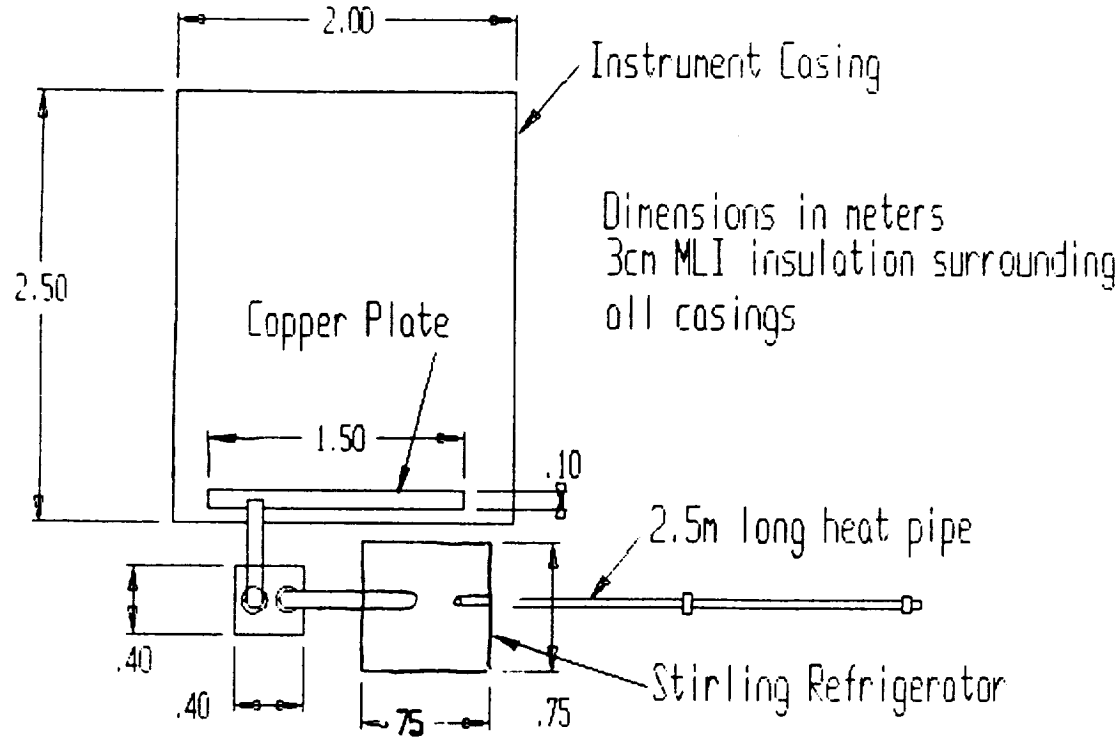

FIG. 89. Cooling System Configuration

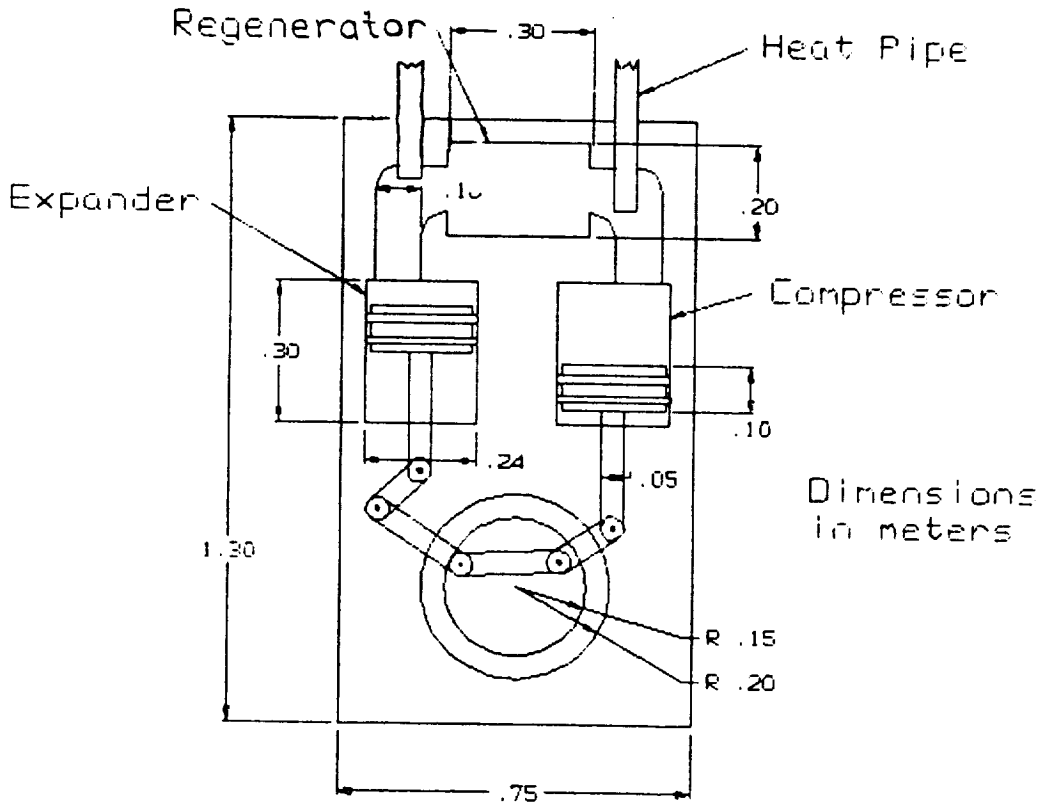

FIG. 90. Cross-Section of Stirling Engine

IX. Launch, Construction, & Cost

IX.1 Launch Scenario

For the successful implementation of LOITA, three requirements must be met. First, the manned space station (Space Station Freedom, SSF) must be operational and useful as a transfer point for lunar transit. Second, a heavy lift vehicle (HLV) capable of launching a larger (bulk) payload must be operational. Third, a new lunar lander and a lunar excursion vehicle (LEV) must be developed. The design of the launch system is beyond the scope of this project and is not addressed.

The launch sequence described here does not include the preliminary site survey which would have to be completed prior to any construction endeavor. Also, the time table for the described launch sequence has not been considered, however, the launch schedule should be developed such that LOITA could begin operations in the years 2010 - 2015.

The proposed launch sequence for the construction and initial operation of LOITA (Phase 1) is listed below.

Launch #	Origin	Vehicle	Payload
1	Earth	Atlas II/Centaur	•Communication satellite to L4
2	Earth	Titan IV/Centaur	•Nuclear reactor/converters to lunar surface
3	Earth	Shuttle	•3 complete telescopes to SSF
4	SSF	LEV	•3 telescopes to lunar surface
5	Earth	Shuttle	•3 remaining telescopes for phase 1 to SSF
6	SSF	LEV	•Remaining telescopes to lunar surface
7	Earth	HLV	•Power cable & remaining power system, metrology towers, coarse delay system, thermal control, utility vehicle, instrument room material, intermediate delay sys., lunar rover to lunar surface
8	Earth	Shuttle	•Instrumentation, control mirrors, computers, fine delay system, metrology lasers, combiners, pointing & control sys., internal thermal control, ground comm. to SSF
9	SSF	LEV	•All equipment from Launch 9 to lunar surface
10	SSF	LEV	•4 astronaut construction crew

As shown in the table, sensitive equipment (including the telescopes) is first transferred to SSF. Once at SSF, the equipment could be examined for any damage and any necessary repairs could be made. Astronauts would not be placed on the lunar surface until all equipment was in place.

IX.2 Construction and Assembly

This section deals with the process of constructing a working array on the moon from prepackaged components sent from the earth. An operation of this magnitude and complexity must be manned. The construction scheme will be designed to minimize the necessary man-hours and equipment, thereby reducing cost. The major equipment will consist of a personnel rover, and a utility vehicle as seen in Figure 91. Construction will be a seven-phase endeavor;

I - Start up
II - Power Activation
III - Instrument Room
IV - Telescopes
V - Delay Lines
VI - Metrology Towers
VII - Testing

Phase I - Start up

The final locations of the array components (the telescopes, instrument room, etc.) will be determined from very high resolution satellite mapping prior to the arrival of any equipment. Everything needed for construction will be safely landed before the manned lander arrives. This prevents costly unproductive time should the astronauts have to wait on a replacement if a shipment is lost. Construction begins with an Apollo-like descent of a four-manned capsule. The landing capsule will need to be somewhat roomier than an Apollo capsule since the astronauts will live out of it for a substantial period of time.

Using the rover for transportation, the astronauts' first task will be to unpack the equipment and test it. Each lander will be inspected to confirm the safe arrival of its package. At this point construction is ready to begin.

Phase II - Power

The equipment consumes large amounts of power in its operation. The power plant is therefore the first item to be placed on-line. The equipment will need to be able to go without power long enough to get this job done.

The necessary cavity (2 m diameter x 5 m deep) is dug by the utility vehicle and the SP-100-like reactor is hoisted in. The reactor is installed and activated. After the 24 hour start-up period, all the equipment can draw power from the reactor.

Next, the utility vehicle is used to lay electrical cable from the reactor into 10 cm deep trenches. The cable will consist of 25 meter long segments to allow for easy repair. This cable is packaged on spools. The necessary pair of cables will be laid simultaneously by the utility vehicle. The power network will be completely laid out to reach each power consumer. At a speed of 1 m/s, the cable laying will take approximately 12 hours plus the time needed to clear the path and change cable spools. A full 14 hours is allotted for this operation.

Phase III - Instrument Room

The construction of the instrument room is the largest single operation in terms of the large amount of materials and excavation. While a majority of the array is only unpacked and placed at the proper location, the instrument room is actually constructed much like any building on the earth.

First, the utility vehicle is used to dig out the (14 x 19.5 x 5.25 m deep) cavity for the two story room. This is the most demanding task for the utility vehicle, and is therefore the primary consideration in its design. Hand shoveling will most likely be required of the astronauts to refine the cavity to its exact dimensions.

Constructing the walls of the building requires 1200 m^2 of paneling. The paneling should be a sturdy but lightweight material with snap together hinges. Each piece should be small enough so that one or two astronauts can handle and connect them without special lifting equipment. The connections should be nearly airtight so as to avoid the entry of dust once the instruments are in place.

The room will be completely assembled except for the roof. This allows the heavy instruments to be hoisted inside by the crane. The astronauts will then mount each instrument in its proper place. Once this is done, the roof is attached. The displaced regolith is then pushed on top of parts of the room by the utility vehicle to provide added protection from radiation.

Once the room is fully assembled it will still contain large amounts of dust left over from construction. Much of it may be shoveled away, but this is not sufficient. Several options exist for removing this last remainder of dust. It might be blown out with pressurized air. Or, it could be gathered by a brush-type vacuum cleaner. Alternatively, the room could be sprayed with some type of adhesive that would bind the dust to the walls.

Lastly the room is connected to the waiting power feed from the reactor. All of the instruments should be checked as thoroughly as possible while there is still time to send replacements without a delay in total construction time.

Phase IV - Telescopes

For the first phase of array operation only six telescope units are to be transported to the moon. A complete telescope unit will consist of a telescope and its supporting structure. The telescope itself will be completely assembled on earth to allow for accurate positioning and testing of the mirrors. The supporting structure and base will be shipped to the moon unassembled: this will minimize the amount of space necessary in the launch vehicle for these components.

Once at the emplacement site, the astronauts will have to prepare the area by removing rocks and filling craters that are too large to be compensated for by the movable feet on the support structure. The base can then be assembled and positioned. Next the telescope will be hoisted onto the structure and locked in place. The final step in constructing the telescope will entail connecting it to the power supply. Once this is accomplished, the telescope's mobility and drive system may be tested.

Phase V - Delay Lines

The 21 coarse delay mirrors will be transported to their sites. Each mirror will be supported by a tripod anchored to the surface. The tripod will be hammered down to a suitable depth. The mirrors will then be properly adjusted.

The intermediate delay system rests on rails 380 meters in length. The rail system can be either a single or dual setup. The rails can either be packaged in sections about 25 meters in length or as a single rail coiled around a spool. The latter option has the advantage of being one entity with no breaks. This would allow easier placement (less work for the astronauts, less time to align the sections, and easier transportation). The rails will be need to be placed on a level surface. This is accomplished by shovels and rakes, the utility vehicle or, if necessary, blasting. The mirrors will be mounted to sleds and placed on the tracks. The system will then be tested and adjusted.

Phase VI - Metrology

The four metrology towers will arrive on the moon unassembled. The tower will be constructed and emplaced in a similar manner to that of the telescope structures. The laser and laser drive system will then be affixed to the tower. The complete unit can then be connected to the power supply. Once powered, the laser and drive system may be tested.

Phase VII - Testing

Each section will be tested as it is completed. However, some systems, such as pointing and control, will only be fully testable once the complete array is assembled. Various functions of the array will be exhaustively tested from the earth as the astronauts prepare for the return trip.

IX.3 Cost Analysis

Before any cost analysis could be completed, a Work Breakdown Structure (WBS) was created. The WBS serves as an outline for the structure of the LOITA program from construction through operations. The WBS is shown in Figure 92. As shown in the figure, the LOITA program has been broken into 9 primary areas. These areas include:

1) Site work: surveying, grading, excavation, foundations
2) Instrument room: interior and exterior walls, doors, roofing, stairways, equipment placement
3) Mechanical systems: motors/servos, cooling system
4) Power system: installation and activation
5) Transportation
6) Subsystems: includes all instrumentation, computers, mirrors, optical components, communications equipment, metrology system
7) Assembly: telescopes, delay lines, alignment of optics
8) Program management: administrative support, technical management, mission planning
9) Engineering services: design, cost estimating, consulting

As with any space-born system, the primary cost incurred is due to transportation. Typically, the launch/transportation cost is in the same range as the system cost. This is true for LOITA. In this analysis, launch costs are assumed to be $10K/kg. The mass of the system is the primary driver of the total cost. The mass estimate for LOITA is shown in Table 27. The estimated launch cost for the 58,820 kg LOITA is approximately $588 million.

A number of assumptions were made in performing this analysis. These include:

- Estimate includes assembly costs on the moon
- Lunar construction/assembly costs are derived from Earth costs for similar work. Earth labor costs are multiplied by a factor of 200 for astronaut EVA.
- All weights are dry weights
- Expected additive project costs for installation and activation are included as well as $5 billion for research and development of new technology (30% Contingency, 5% Program Support)
- Transportation costs are weight driven, a 20% contingency is added to all weights.

- Items not costed are: Ground Systems Development, Data Analysis, Launch Vehicle Development, Checkout of Instruments and Systems Testing

- Annual costs of operation are not included

The following pages contain the preliminary cost estimate for LOITA. The estimate is for construction of Phase 1 (6 elements) and initial start-up of the array. Modifications to the transportation system as well as development of a new transport system (HLV, lunar lander, and LEV) have not been defined; no costs were estimated for this task.

LOITA Cost Estimate

Transportation	$10000/kg			Total: $588,200,000
Construction		time	manpower	cost
Site Preparation	Grading	15h	1	88,762
	Excavation	20h	2	121,290
	Trenching/Cable laying	14h	1	80,770
Instrument Room		20h	3	886,930
Telescopes (ea. 2h/$176000)		12h	2	211,200
Delay Lines				
Coarse Delay		16h	2	140,800
Intermediate Delay		17h	2	149,600
Fine Delay (incl. with Instrument Room)				
Metrology		5h	2	44,000
Power Source		2h	2	17,600
Vehicles			1 x $800000	800,000
			1 x $1600000	1,600,000
			Total (Construction):	4,140,952

Itemized Cost (1st phase)		
Optics:		
Primary Mirror	6 x $500000	3,000,000
Secondary Mirror	6 x $100000	600,000
24 cm dia. Reflectors	75 x $1260	94,500
3 cm dia. Reflectors	144 x $95	13,680
I.Delay Retroreflectors	6 x $2000	12,000
F.Delay Retroreflectors	36 x $1080	38,880
Beam Splitters	72 x $350	25,200
Instruments		500,000,000
Metrology lasers	10 x 120000	1,200,000
Pointing Control		130,500
Motors (altitude 2 ea.)	12 x 10000	120,000
(azimuth 1 ea.)	12 x 20000	240,000
Control Computer		1,000,000
Communications		
satellite/lunar surface		200,000,000

Telescope Structures	6 x 70000	420,000
Thermal Control		1,000,000
Power:		
SP-100 Reactor		200,000,000
Cable	$1.44/m	89,280
Distribution Units	1 x 37500	37,500
Converters	9 x 11000	99,000
	Total (subsystems):	908,120,540
	Total:	1,496,320,540
	Research & Development:	5,000,000,000
	Program Support (5%):	324,816,027
	Total With Program Support:	6,821,136,567
	Contingency (30%):	2,046,340,970
	Total With Contingency:	8,867,477,537

As can be seen from the chart, the estimated initial cost of LOITA (Phase 1) is $8.9 billion. As previously stated, lunar construction costs were derived from Earth construction costs of similar work. The cost of one laborer (heavy construction), is $22/h on Earth. Labor costs on the moon are therefore $4400/h (due to EVA). Time estimates for work on Earth are assumed to be the same for lunar construction. Equipment maintenance costs are included in the site preparation costs and are also assumed to be equal to Earth costs. As shown on the chart, construction costs are $4.1 million. This figure is a preliminary estimate; no data exists for lunar construction costs. This figure does not include life support/habitat for the astronauts.

Maintenance costs are driven by the necessary EVA activity of the astronauts. Routine maintenance can be accomplished by 2 astronauts visiting once every year. The duration of the visit should be no longer than the initial construction time of 8 days. Annual maintenance costs should not exceed $400K (excluding transportation and major repairs) over the expected 20 year life of LOITA.

Table 27: LOITA System Mass

All masses in kilograms

		Phase 1		Complete System	
Telescope		6 * 1198	7,188	18 * 1198	21,564
Delay Lines:	Coarse	21 * 15	315		315
	Intermediate	6 * 20	120	18 * 20	360
	(tracks)	18 * 120	2,160		2,160
	Fine	36 * 0.5	18		18
Other Optics:					
Mirrors (diameters given)					
	(6.4 cm)	108 * 0.01	1.08		1.08
	(25 cm)	36 * 11.2	403.2	72 * 11.2	806.4
	Beam Splitters	72 * 1	72		72
Metrology:	Lasers	10 * 3.2	32	22 * 3.2	70.4
	Towers	4 * 5.6	22.4		22.4
		Total:	10,332		25,389

Remaining systems will be completed during Phase 1:

Instruments:			
Wide Field and Planetary Camera		1 * 250	250
Faint Object Camera		1 * 320	320
High Resolution Spectrograph		1 * 225	225
Faint Object Spectrograph		1 * 250	250
Array Instruments/Detectors			1,500
Pointing Control			50
Computers			500
Power System:	Reactor		750
	Converter/Power Dist.		300
	Cable		2,650
Communications:	surface		420
	satellite		420
Thermal Control			750
Construction Vehicles:	Apollo-like Rover		300
	Utility		5,000
Instrument Room materials			25,000
		subtotal:	38,685
		Total Phase 1:	49,017
		Contingency (20%)	9,803
		Total Phase 1:	58,820

Total Complete System: 64,074

12,815

Total Complete System: 76,889

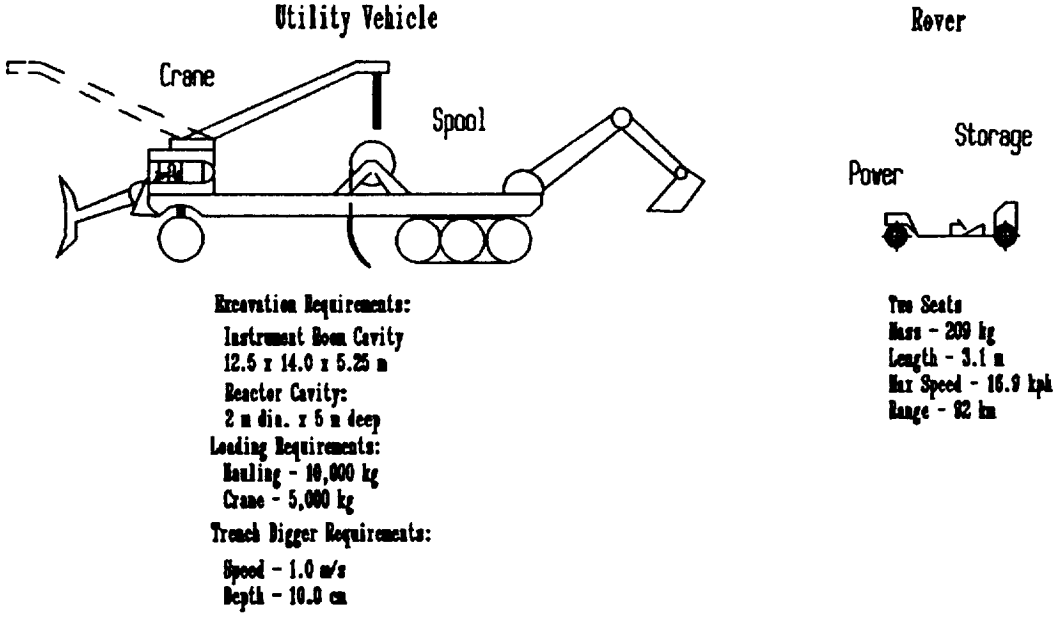

FIG. 91. Construction Vehicles

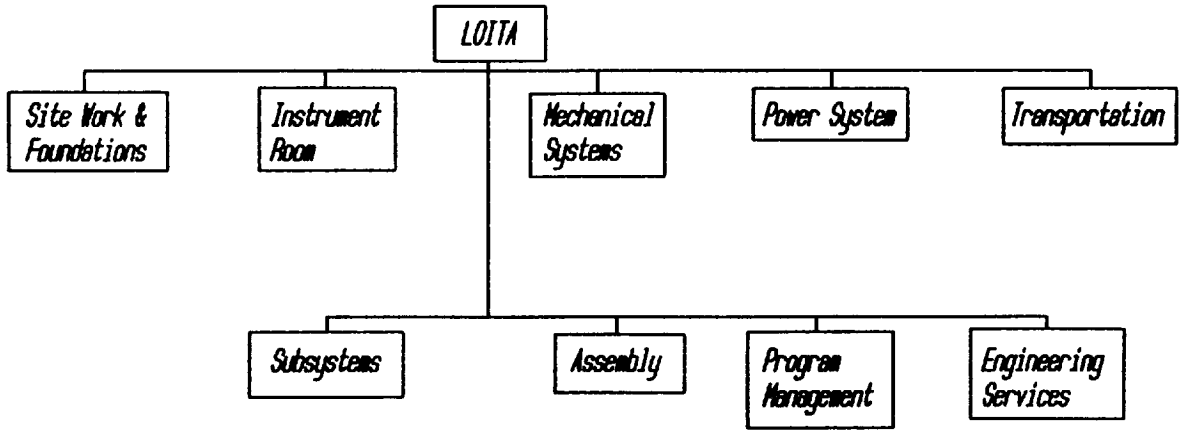

FIG. 92. Work Breakdown Structure

X. Conclusions

LOITA is a lunar-based optical interferometer whose primary mission will be the search for extrasolar planets. The specifications of the complete system are summarized in the table below.

ARRAY SPECIFICATIONS

TELESOPE AND OPTICS

Array Configuration	Circular with Unevenly Spaced Elements
Number of Telescopes	18
System Angular Resolution	0.02 milli-arcseconds

Telescope Configuration:

Type	Cassegrain
Primary Mirror Diameter	1.75 m
Secondary Mirror Diameter	0.24 m
Exit Beam Diameter	0.23 m

Delay Lines:	Coarse	Intermediate	Fine
Number of Mirrors	21	18	18
Mirror Dimensions	24 cm dia.	68 x 24 cm	3 cm dia.
Beam Path Lengths Equalized to within	600 m	1 m	1500 nm

LASER INTERFEROMETRIC METROLOGY

Laser Type	Tunable solid-state (Internal & External)
Frequency Stability	Internal - 10^{-12}
	External - 10^{-9}

TELESCOPE MOTION

Pointing Accuracy	Sub-microarcsec to 10^{-4} arcsec
Azimuth Range	360°
Elevation Range	160°
Maximum Angular Velocities -	
Azimuth	24°/min
Elevation	5.3°/min

COMMUNICATIONS SYSTEM

Antennas:	LOITA Antenna	Relay Satellite Antenna
Diameter	4.9 m	4.15 m
Area	18.85 m	13.5 m
Efficiency	0.6	0.6
Gain (Ka)	58.83 dB	57.38 dB
Transmitter power	10 W	10 W
EIRP	68.83 dB	67.38 dB
Operating Frequency	24-30 GHz	20-34 GHz
Max Data Rate	600 Mbit/s	600 Mbit/s

Relay Frequency Allocations:	Loita	Earth
Forward	22.55 GHz	23.55 GHz
Return	25.25 GHz	27.50 GHz

Transceiver System Life Expectancy - 10 yrs

POWER SYSTEM

Type	SP-100 Derivative
Power Output	15 kW
Start-up Time	24 hr
Radiator Area	80 m^2
Fuel	Uranium Nitride
Coolant	Lithium
Power Grid Cable	66 km
Lifetime	10 yrs

INSTRUMENTATION COOLING SYSTEM

Cycle	Stirling Refrigeration
Cooling Load	6 W
Required Temperature	70 K
System Mass	750 kg

SYSTEM MASS

Phase 1	58,820 kg
Complete System	76,889 kg

OBSERVATORY COST

Phase 1	$8.9 billion

APPENDIX A

Calculations and assistance provided by Dr. Simonetti, Physics Department, Virginia Polytechnic Institute.

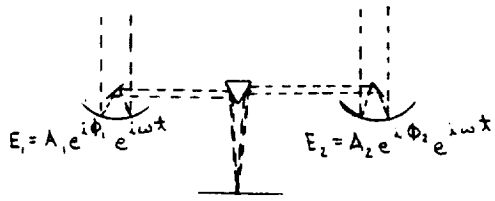

To obtain the pahse of the complex visibility:

$$I = \langle | E_1 + E_2 |^2 \rangle$$

$$= |A_1 e^{i\phi_1} + A_2 e^{i\phi_2} |^2$$

$$= A_1^2 + A_2^2 + A_1 A_2 (e^{i(\phi_1 - \phi_2)} + e^{-i(\phi_1 - \phi_2)})$$

$$= A_1^2 + A_2^2 + 2A_1 A_2 \cos(\phi_1 - \phi_2)$$

amplitude of complex visibility	phase of complex visibility, but only product and cosine of phase, not the phase itself! (i.e. we know $\lvert\Delta\phi\rvert = \lvert\phi_1 - \phi_2\rvert$, but not its sign!)

Now, insert a quarter wavelength phase delay in the path length of E_2:

$$I = \langle |E_1 + E_2 e^{i\pi/2}|^2 \rangle$$

$$= |A_1 e^{i\phi_1} + A_2 e^{i(\phi_2 + \pi/2)}|^2$$

$$= A_1^2 + A_2^2 + A_1 A_2 [e^{i(\phi_1 - \phi_2 - \pi/2)} + e^{-i(\phi_1 - \phi_2 - \pi/2)}]$$

$$= A_1^2 + A_2^2 + 2A_1 A_2 \cos(\phi_1 - \phi_2 - \pi/2)$$

$$= A_1^2 + A_2^2 + 2A_1 A_2 [\cos(\phi_1 - \phi_2)\cos(\pi/2) + \sin(\phi_1 - \phi_2)\sin(\pi/2)]$$

$$= A_1^2 + A_2^2 + 2A_1 A_2 \sin(\phi_1 - \phi_2)$$

So, now that we have both $\cos(\phi_1 - \phi_2)$ and $\sin(\phi_1 - \phi_2)$, we can get the complex visibility which

$$= A_1 A_2 [\cos(\phi_1 - \phi_2) + \sin(\phi_1 - \phi_2)].$$

APPENDIX B. MASS MINIMIZATION ESTIMATES

Compute surface area of primary mirror (m^2): $A = \pi\,(1/4)\,[1.75^2 - 0.23^2]$
Compute thickness of primary mirror (m): $t = (1.75/80)$
Compute volume of primary mirror (m^3): $V = At$
Compute mass of primary mirror (kg): $m = V(2205)$
Reduce mass estimate (honeycomb structure): $m = m(0.25)$
Compute lunar "weight" (N): $w = m(9.81/6)$

A = 2.36373 t = 0.02188 V = 0.05171 m = 28.50331 w = 46.60291

Compute surface area of secondary mirror (m^2): $A = \pi(1/4)(0.24^2)$
Compute thickness of secondary mirror (m): $t = 0.01$
Compute volume of secondary mirror (m^3): $V = At$
Compute mass of secondary mirror (kg): $m = V(2205)$
Reduce mass estimate (honeycomb structure): $m = m(0.25)$
Compute lunar "weight" (N): $w = m(9.81/6)$

A = 0.04155 t = 0.01 V = 0.00042 m = 0.22903 w = 0.37447

Estimate structural graphite tube volume:

$$V = \pi(1/4)[1.85^2 - 1.75^2] + 2\pi(1/4)[0.33^2 - 0.22^2](0.25) + \pi(1.4)(1.85^2)(0.05)$$

Compute tube mass (kg): $m = V(1600) = 705.44463$
Compute mass of secondary support struts and truss structure:
$V = 22\pi(0.019^2)(2)$
$m = V(1600) = 79.84169$
Estimate mass of aluminum shielding:
$V = \pi(1/4)[1.87^2 - 1.85^2] + 0.02\pi(1/4)(1.87^2)$
$m = V(2710) = 307.21319$
Mass estimate for door: $m = 40$
Total mass estimate: $m_{total} = 1161.22$

APPENDIX C. UV COVERAGE PROGRAM

```
REM*************************************************************************************
REM* Program by Neil Thomas, Jr.                                        Design 1992-1993
REM* Advisor: Prof. A. Jakubowski                                       VPI & SU
REM* This program is designed to allow for the calculation of uv plane visibility for any user specified array
REM* configuration, any topocentric location, and any source location. The program initially reads in the
REM* coordinates of the telescopes from the file "ARRAY#.DAT" where # is a number corresponding to the
REM* particular configuration. All of the possible baseline vectors are calculated and output to the data file
REM* "VECTOR.DAT". A small plot of the array configuration along with critical observation parameters
REM* is displayed in the upper right corner. The coordinates of the array and the observed source are next read
REM* in from the file "ARRAY.DAT". The intersections of the baseline vectors of the telescopes make with
REM* the celesteal sphere are next calculated. The program then allows the option of a full exposure in which
REM* the source travels 360° through the celestial sphere or the option of a specified exposure length. Although
REM* the full exposure can never be experimentally attained, it compiles much faster and gives the user a
REM* comprehensive feel for the coverage. The limited exposure option provides analysis for particular
REM* observations. In addition, the duration can be set so that the "snapshot" coverage is obtained. It is re-
REM* commended that the full exposure mode be used when making qualitative analysis between broadly
REM* different configurations. The limited exposure mode can then be used to refine a system and judge between
REM* similiar designs for particular observations. The units on the uv plane are ignored since this program is
```

```
REM* intended for qualitative assessment, not detailed simulations. Indeed, a detailed simulation of coverage
REM* on the moon would need to take into account the nonalignment of the moon's topocentric coordinates
REM* and celestial coordinates due to its tilt and inclined orbit.
REM*
REM* Variables:
REM*   MODE = INPUT OF DESIRED EXPOSURE MODE
REM*   E(#), N(#) = EAST, NORTH COORDINATES OF TELESCOPES RELATIVE TO THE CENTER OF
REM*                THE ARRAY
REM*   NUM = NUMBER OF TELESCOPES IN ARRAY
REM*   J, K, C1, C2, C3, C4, C5 = COUNTING VARIABLES IN DO LOOPS
REM*   DE, DN = EAST, NORTH COORD OF VECTORS BETWEEN TELESCOPES
REM*   D(1), D(2), D(3) = COMPONENTS OF DE, DN IN CELESTIAL COORDINATES
REM*   DEL = DECLINATION OF ARRAY ON MOON
REM*   H = HOUR ANGLE OF ARRAY ON MOON
REM*   DELS = DECLINATION OF SOURCE ON CELESTIAL SPHERE
REM*   HS = HOUR ANGLE OF SOURCE ON CELESTIAL SPHERE
REM*   DMAG = MAGNITUDE OF BASELINE VECTOR LENGTH
REM*   HBASE = HOUR OF THE INTERSECTION OF THE BASELINE VECTOR AND CELESTIAL
REM*           SPHERE
REM*   DBASE = DECLINATION OF THE INTERSECTION OF THE BASELINE VECTOR AND THE
REM*           CELESTIAL SPHERE
REM*   LAMDA = WAVELENGTH OF OBSERVATIONS
REM*   SWEEP = HOUR ANGLE OF SOURCE MOTION DURING LIMITED EXPOSURE TIMES
REM*   U, V = COORDINATES OF INSTANTANEOUS UV COVERAGE DURING LIMITED EXPOSURE
REM*   A, C, VO = PARAMETERS OF ELLIPSES SWEPT OUT OVER A COMPLETE EXPOSURE
REM*   NORMA, NORMC, VON = A, C, VO NORMALIZED TO FIT NICELY ON THE SCREEN
REM*************************************************************************************

5  CLS
   PRINT "WHICH OPTION DO YOU PREFER?"
   PRINT "      (1) FULL EXPOSURE"
   PRINT "      (2) LIMITED EXPOSURE"
   INPUTE MODE

10  DIM E(35)
20  DIN N(35)
30  OPEN "ARRANG.DAT" FOR INPUT AS #1
40  OPEN "VECTOR.DAT" FOR OUTPUT AS #2
50  INPUT#1, NUM
60  FOR C1=1 TO NUM
70  INPUT#1,E(C1),N(C1)
90  NEXT C1
105  REM GOTO 240
110  REM **************TELESCOPE LOCATION BYPASS
     REM * IF LINE 105 IS TURNED INTO A REM STATEMENT THEN THE DATA LISTED BELOW
     REM * WILL BE ANALYSED.  THIS IS USEFUL FOR SMALL NUMBERS OF ELEMENT (6) WHERE
     REM * IT WOULD BE HARDER TO CREATE A DATA FILE FOR EACH CASE.
111  NUM=6
120  E(1)=0
130  N(1)=200
140  E(2)=200
150  N(2)=0
160  E(3)=-200
170  N(3)=0
180  E(4)=0
190  N(4)=-1000
200  E(5)=866
210  N(5)=500
220  E(6)=-866
230  N(6)=500
235  REM **************CONVERTING E, N TO DE, DN
```

```
240 FOR J=1 TO NUM
250     FOR K=1 TO NUM
260     IF J=K THEN GOTO 320
290     DE=E(J)-E(K)
300     DN=N(J)-N(K)
310     PRINT#2,DE,DN
320     NEXT K
330 NEXT J
    CLOSE

340 REM **************PLOTTING ARRAY
360  SCREEN 2
370 FOR C2=1 TO NUM
380 CIRCLE (520+(E(C2)/20),50-(N(C2)/48)),2,,,,.41667
390 NEXT C2
440 DIM D(3)
470 OPEN "ARRAY.DAT" FOR INPUT AS #2
480 INPUT #2,DEL,H,DELS,HS
490 DEL=.00001
500 DELS=20*3.14159265359/180
    HS = 1.57
    H=1.57
510 CLOSE #2
530 PRINT"                                          TARGET"
540 PRINT"                                         DECLINATION"IN
    PRINT"                                         EXPOSURE = 1 H

550 OPEN "VECTOR.DAT" FOR INPUT AS #3

560  C3=C3+1
570  INPUT #3,DE,DN
580  REM ***************COORDINATES OF BASELINE VECTORS
590 D(1)=-DN*COS(H)*SIN(DEL)-DE*SIN(H)
600 D(2)=-DN*SIN(H)*DIN(DEL)+DE*COS(H)
610 D(3)=DN*COS(DEL)
620 REM ***************INTERSECTION OF BASELINE VECTOR AND CELESTIAL SPHERE
630 DMAG=SQR(D(1)*D(1)+D(2)*D(2)+D(3)*D(3))
640 HBASE=ATN(D(2)/D(1))
650 IF D(1)<0 THEN HBASE=3.1515926539+HBASE
660 DBASE=ATN(D(3)/(D(1)*D(1)+D(2)*D(2))^.5)
670 REM ***************TRANSFORM TO UV PLANE
    LAMDA=.0000005
    LINE(0,100)-(639,100)
    LINE(320,0)-(320,199)
    LINE(322,0)-(322,199)
    IF MODE=1 THEN GOTO 710

701 REM ***************LIMITED INTEGRATIONS
    REM 1 DEGREE = 2 HRS
702  SWEEP = 8.7266E-3/100
703  FOR C3B=1 TO 100
704 U=(DMAG*2.4/25)*(COS(DBASE)*SIN(HS-HBASE)+.0000001)
706 V=(DMAG/25)*(SIN(DBASE)*COS(DELS)-COS(DBASE)*SIN(DELS)*COS(HBASE-HS))
    IF C3B=1 THEN GOTO 707
    LINE (320+U,1000-V)-(320+UOLD,100-VOLD)
707 UOLD=U
    VOLD=V
708 HBASE=HBASE-SWEEP
709 NEXT C3B
    IF C3=NUM*(NUM-1) THEN GOTO 1040
    GOTO 560
```

```
    REM ***************FULL EXPOSURE TIME
710 A=(DMAG/LAMDA)*COS(DBASE)
    C=A*SIN(DELS)
    VO=(DMAG/LAMDA)*SIN(DBASE)*COS(DELS)
920 DL=5E07
930 SCREEN 2
940 NORMA=(A/DL)*2.4
950 NORMC=(C/DL)
960 VON=(VO/DL)
970 A=NORMC/NORMA
1010 CIRCLE (320,100-VON),NORMA,,,,A
1022 GOTO 1030
1030 IF C3=NUM*(NUM-1) THEN GOTO 1040
1035 GOTO 560
1040 END
```

APPENDIX D. INTERFEROMETRIC ERROR (given by referance 70)

$$\delta z = \{\delta\phi_L + (\delta\lambda/\lambda) + \phi(\delta\lambda)/(\delta\lambda)\}$$

where, the first term is error from a finite SNR, the second term is the error in the measurement of the laser wavelengths being used, and the third term is from expressing the dirrerence between two wavelengths as a fraction of those two wavelengths.

For estimates of: λ = wavelength = 500 nm
$\delta\lambda = 0.1 \times 10^{-10}$
$\delta\phi$ = 0.001 waves rms

this yields, $\delta z = \lambda_L \{10^{-3} + 2\times10^{-5} + 5.6\times10^{-5} \times \lambda_L\}$, where λ_L is the synthetic wavelength in microns.

1ST measurement with λ_L = 500 microns --> δz = 14.51 microns
2ND measurement with λ_L = 20 microns --> δz = 0.2 microns

APPENDIX E. SAMPLE CALCULATION OF OFF-AXIS MIRROR MASS

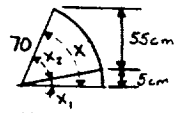

$\sin(x) = 60/70$
$x = 1.0297$ rad = 58.997°

$\sin(x_1) = 5/70$
$x_1 = 0.07149$ rad = 4.096°

$x = x_1 + x_2$
$x_2 = x - x_1$
$x_2 = 1.0297 - 0.07149 = 0.95821$ rad

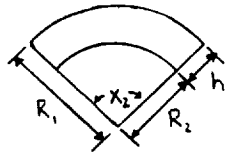

area = $(1/2)hx_2(R_1 + R_2)$ = (1/2)(1.6 cm)(0.95821 rad)(71.6 cm + 70 cm) = 108.545 cm^2

volume = (area)(height) = (108.545)6 = 651.27 cm^3 = 0.00065127 m^3

mass = (wolume)(density) = (0.00065127)(2205) = 1.436 kg

APPENDIX F. DATA RATE CALCULATIONS

Achievable Data Rate, dB = 20.4 + EIRP[155]
Desired Rate = 600 Mbits/s = 87.78 dB
EIRP = 67.38 dB

EIRP = $P_s + G_s$ (W/m^2) effective isotropically radiated power[156]
P_s = Power transmitted by relay satellite = 10 W = 10 dB
G_s = Gain of relay satellite

$G_s = 4\pi + A_e - (\lambda)^2$ [157] = 48.298 dB + A_e
A_e = Effective area = n x Actual Area, $n \cong 0.6$
λ = wavelength = c/f = 0.013636 m (λ^2 = -37.306 dB)
f = frequency = 22 GHz

Therefore, EIRP = 10 dB + 48.298 dB + A_e = 67.38 dB
A_e = 9.082 dB = 8.094 m^2

A = 13.5 m^2 --> D_s = 4.15 m

APPENDIX G. POWER COLLECTED BY TDRSS ANTENNA

$P_r = EIRP + G_r - L_p$ dBW [155]

EIRP = 67.38 dB, effective isotropically radiated power
G_r = 28.0 dB[155], Gain of the receiver
$L_p = 20 \log(4\pi R/\lambda)$ [156], Space loss
R = 3.84 x 10^8 m, Earth - moon distance
λ = transmission wavelength = $20 \log(4\pi(3.84 \times 10^8))/0.013636$ = 230.9 dB
P_r = 67.38 dB + 28.0 dB - 230.9 dB = -135.60 dB

$P_r = 2.75 \times 10^{-14}$ W

APPENDIX H. TELESCOPE TEMPERATURE EQUILIBRIUM CALCULATIONS

Notation:
q_r - heat radiated away from telescope (W/m^2)
q_l - incident lunar radiation (W/m^2)
A_l - cylinder surface area exposed to lunar radiation
T - equilibrium telescope temperature (K)
ε - exterior coating emissivity
D - cylinder diameter (m)
q_s - incident solar radiation flux (W/m^2)
A_t - total telescope cylinder surface area (m^2)
A_s - cylinder surface area exposed to solar radiation
α - exterio coating abserbtivity
σ - Stephan-Boltzmann constant = 5.67×10^{-8} W/m^2K^4
L - cylinder length (m)

At thermal equilibrium: $q_r = q_s + q_l$

$$\sigma\varepsilon A_t T^4 = q_s A_s \alpha + q_l A_l \alpha \quad \text{so,} \quad T = [\alpha(q_s A_s + q_l A_l)/\varepsilon\sigma A_t]^{1/4}, \text{ where}$$

$$A_t = \pi DL + (\pi/2)D^2$$
$$A_l = (\pi/2)(DL + D^2)$$
$$A_s = (\pi/2)DL, \text{ or } T = k(\sigma/\varepsilon)^{1/4}$$

$$\text{where} \quad k = \frac{[(\pi/2)D(q_s L + q_l(L+D))]^{1/4}}{[\sigma\pi D(L + (D/2)]^{1/4}} = 380.0 \text{ K}$$

so, $T_{max} = 380.0(\alpha/\varepsilon)^{1/4}$. For (σ/ε)=0.098 (Magnesium Oxide Aluminum Oxide Paint), T_{max} = 212.6 K.

APPENDIX I. NATURAL CONVECTION IN THE PRESSURIZED H_2 CONTAINER

Purpose: Determine the surface area of a heat pipe necessary to transfer 6 W of heat

Notation:
- P - pressure
- ρ - density
- μ - viscosity
- h - convective heat transfer coefficient
- Pr - Prandtl number
- Nu - Nusselt number
- Q - total heat transfer
- L - heat pipe length
- T_w - temperature of heat pipe
- g - lunar force of gravity
- T - temperature
- k - thermal conductivity
- ν - kinematic viscosity
- C_p - specific heat
- Gr - Grashof number
- q - heat flux
- d - heat pipe diameter
- β - temperature coefficient of thermal conductivity
- T_h - temperature of the H_2

Properties of H_2 at P = 1 atm, T = 60K:
$\rho = 0.45$ kg/m$_3$
$k = 0.031$ W/mK
$\mu = 3.0 \times 10^{-6}$ kg/ms
$C_p = 18.9$ kJ/kgK

then, $\nu = \mu/\rho = 6.67 \times 10^{-6}$ (m^2/s), $Pr = C_p(\mu/k) = 1.83$, $\beta = 1/T = 0.0167$ K^{-1}

for L = 1 m:
$Gr_L = [g\beta(T_w - T_h)L^3]/\nu^2 = 3.07 \times 10^9$
$Nu_L = 0.508Pr^{1/2}(0.952 + Pr)^{-1/4}Gr_L^{1/4} = 125.3$
$h_L = (kNu_L)/L = 3.88$ W/m^{2}K

so the heat transfer values may be calculated: $h = (4/3)h_L = 5.18$ W/m^{2}K (for isothermal surface).
When a 5K difference is maintained between the heat pipes and the H_2:
$q = h(T_w - T_h) = 25.9$ W/m^2
$Q = q\pi dL = 6$ W

so the required heat pipe diameter is $d = Q/(qpL) = 0.078$ m

Conclusion: A 1 m length, 0.1 m diameter heat pipe is sufficient to transfer 6 W of heat to and from a vessel containing hydrogen at 1 atm pressure with a 5K temperature difference between the heat pipe and the hydrogen. Only free convection forces are necessary.

APPENDIX J. HEAT TRANSFER FROM COMPRESSED H_2 TO HEAT PIPE

Purpose: Determine the required surface area of a heat pipe exposed to compressed H_2 flow.

Notation:
- u_h - velocity of the H_2 flow
- d_{HP} - diameter of heat pipe
- Re - Reynolds number
- d_r - diameter of refrigerator tubing

set conditions of the hydrogen:
$u_h = 10$ m/s
P = 1 atm
T = 300 K
$\rho = 0.08185$ kg/m^3
$C_p = 14.314$ kJ/kgK
$k = 0.182$ W/m^{2}K
Pr = 0.706
$\mu = 8.963 \times 10^{-6}$ kg/ms
$\nu = 109.5 \times 10^{-6}$ m^2/s

check Reynolds number for turbulence condition: if Re > 2300 the flow is turbulent
$Re = (\rho u_h d_r)/m = 9130$ (turbulent flow)

then, $Nu = C (u_h d_r/\nu)^n Pr^{1/3}$, where C and n are constants set by the Reynolds number (C = 0.193, n = 0.618)
so, $Nu = hd_r/k = 31.4$, $h = 114.3$ W/m^{2}K

maintaining the temperature of the heat pipe at 275K results in, $q = 2856$ W/m^2 and $Q = q\pi d_{HP}L = 36.8$ W.

setting $d_{HP} = 0.05$ m results in $L = 0.082$ m

Conclusion: For a heat pipe with a 0.05 m diameter, a length of 0.09 m must be exposed to the refrigerator flow to transfer the heat load plus the heat generated by the refrigerator.

APPENDIX K. HEAT TRANSFER AT THE INSTRUMENT CASING

Purpose: Determine the surface area of contact between a heat pipe and the copper plate within the instrument casing to transfer 6 W of heat.

Notation: dT - temperature difference
dx - maximum distance of heat transfer throughout the instrument casing

set the heat pipe diameter at 0.1 m, use k = 407 W/mK

use Fourier's Law: $q = k(dT/dx)$

Assume the maximum heat transfer path through the instrument box is 2.5 m (= dx) and that the instruments are maintained at 70K with the heat pipe at 60K (dT = 10K).

so, $q = 407\ (10/2.5) = 814$ W/m^2, and $L = Q/\pi dq = 0.023$ m

Conclusion: For a heat pipe with a 0.1 m diameter, a length of 0.03 m is sufficient to transfer 6 W of heat if a 10K temperature difference is maintained.

APPENDIX L. HEAT TRANSFER AWAY FROM THE STIRLING REFRIGERATOR

Purpose: Determine the amount of heat required to be transferred away from the refrigeration unit. Determine the required length of heat pipe operating at 275K necessary to radiate the heat into a radiation field of 250K.

Notation:
COP - coefficient of performance
T_H - refrigerator hot temperature
T_L - refrigerator cold temperature
W_{NET} - net refrigerator work

Calculate the carnot cycle efficiency. Assume the Stirling refrigerator can operate at half the carnot value.

$COP = T_L/(T_H - T_L) = 0.389$ (carnot)
$COP_{stirling} = 0.195$
$W_{NET} = Q/COP = 30.8$ W
$Q_{TOT} = Q + W_{NET} = 36.8$ W

Radiation heat pipe claculations: use $\varepsilon = 0.92$ (Magnesium Oxide Aluminum Oxide Paint Coating)

$d = 0.05$ m
$Q = \sigma\varepsilon\pi dL(T_{HP}^4 - T_w^4)$
$L = Q/(\sigma\varepsilon\pi d(T_{HP}^4 - T_w^4)) = 2.47$ m

Conclusion: A heat pipe of 2.5 m is necessary to discharge a total of 36.8 W of heat.

APPENDIX M. HEAT TRANSFER FROM EXPANDED H_2 TO HEAT PIPE

Purpose: Determine the amount of surface area of the heat pipe exposed to the expanded H_2 flow to transmit 6W of heat.

Properties of H_2: $u_h = 10$ m/s, $P = 0.2$ atm, $T = 55K$, $\rho = 0.45$ kg/m^3, $k = 0.31$ W/mK, $\mu = 3.0 \times 10^{-6}$, $\nu = 6.67 \times 10^{-6}$, $Pr = 1.83$

Calculate the Reynolds number: $Re = 1.5 \times 10^5$ (turbulent flow), so $C = 0.0266$, $n = 0.805$, and $Nu = 477$

For a 0.05 m diameter heat pipe at 60K, $h = Nu(k/d_{HP}) = 296$ W/m^{2}K

$q = h(T_{HP} - T_{H_2}) = 1480$ W/m^2

$L = 0.025$ m

Conclusion: A heat pipe running at 60K with a 0.05 m diameter must be inserted 0.025m into the expanded H_2 flow to transmit 6 W of heat.

APPENDIX N. REGENERATOR REQUIRED MASS/VOLUME

Purpose: Determine the required mass and volume of the regenerator matrix for perfect regeneration. The assumption of perfect regeneration is allowed when the heat capacity of the regenerator is much greater than the heat capacity of the fluid.

Notation: Q - heat capacity, m - mass, V - volume, c - specific heat for a solid

Heat capacity of the H_2 (total fluid mass = 0.812 kg)

$Q_{H_2} = m_{H_2}C_p dT = 2533$ kJ

Let the heat capacity of the bronze matrix be ten times the heat capacity of the hydrogen fluid.
Find the required regenerator volume: $Q_{BR} = \rho V c dT$, for bronze, $\rho = 8666$ kg/m^3 and $c = 0.410$ kJ/kgK

so, $V = Q/(\rho c dT) = 0.0297$ m^3

Let the regenerator be a 0.2 m diameter tube filled with a bronze matrix mesh, 5000 x 5000 strands, with a 100 μm diameter strand. Meshes are packed 200/cm.
Find the required length of the tubing:

Vol (strand) = $\pi d^2 L/4 = 1.571 \times 10^{-9}$ m^3

Vol (mesh) = 10000 x Vol (strand) = 1.571×10^{-5} m^3

Vol (length) = 250 x Vol (mesh) = 3.92×10^{-3} m^3

L = V/Vol (length) = 7.56 cm

Note: The analysis was done for a square cross-section tube instead of a circular one. Assume the required length of the circular cross-section is twice that of the square one.

so, $L_{eff} = 15.1$ cm

REFERENCES

Optics

[1]Abel, I.R., "Mirror Systems: Engineering Features, Benefits, Limitations and Applications," Geometrical Optics, Robert E. Fisher, William H. Price, Warren J. Smith, Editors, Proc. SPIE 531, pp 121-134 (1985).

[2]Angel, R., "Use of 16m Telescope to Detect Earthlike Planets," see ref. 3.

[3]Bely, Pierre-Yves (ed.), The Next Generation Space Telescope, Space Telescope Science Institute, Baltimore, Maryland, 1989.

[4]Black, David C. (ed.), Project Orion: A Design Study of a System for Detecting Extrasolar Planets, NASA Ames Research Center.

[5]Bracewell, R.N., "Detecting Nonsolar PLanets by Spinning Infrared Interferometer," Nature, vol. 274, pp. 780-781, 1978.

[6]Bracewell, R.N., MacPhie, R., "Searching for Nonsolar Planets," Icarus, vol. 38, pp. 136-147, 1979.

[7]Brueggemann, H.P., Conic Mirrors, The Focal Press, New York, 1968.

[8]Burke, B.F., "Detection of Planetary Systems and the Search for Evidence of Life," (1986).

[9]Burns, Jack O. (ed.), "Future Astronomical Observatories on the Moon," NASA Conference Publication 2489, Lyndon B. Johnson Space Center, January 1986.

[10]Burns, J.O., Nebojsa Duric, "A Lunar Far-Side Very Low Frequency Array," NASA Conference Publication 3039, 1989.

[11]Cheimets, Peter, "Design of Two Delay Lines for Optical Interferometers," Amplitude and Intensity Spatial Interferometry, Jim B. Breckinridge, Editor, Proc. SPIE 1237, pp. 183-196, 1990.

[12]Colavita, Mark, A Strawman Lunar Interferometer, Jet Propulsion Laboratory/California Institute of Technology, Workshop on technologies for Space Interferometry, 1990.

[13]Cox, Arthur, A System of Optical Design, The Focal Press, New York, 1964.

[14]Diner, D.J., "IBIS: An Interferometer-Based Imaging System for Detecting Extrasolar Planets with a Next Generation Space Telescope," see ref. 3.

[15]Diner, D.J., J. van Zyl, D.L. Jones, E. Tubbs, V. Wright, J.F. Appleby, and E. Ribak, "Direct and Interferometric Imaging Approaches for Detecting Earth-Like Extrasolar Planets," AIAA-88-0553, AIAA 26th Aerospace Sciences Meeting, Reno, Nevada, 1988.

[16]Elachi, C., T. Cooley, "Lunar Optical Interferometer System Study Final Report," California Institute of Technology, 1990.

[17]Faucherre, M., R.V. Stachnik, S. Aram, "Numerical Experiments in Image Reconstruction," see ref. 29.

[18]Johnson, S.W., "Extraterrestrial Facilities Engineering," Encyclopedia of Physical Science and Technology - Yearbook 1989.

[19]Kingslake, Rudolf, Applied Optics and Optical Engineering, vol. 2 and 5, Academic Press, New York, 1969.

[20]Kutner, Marc L., Astronomy: A Physical Perspective, Harper & Row, Publishers, Inc., New York, 1987.

[21]Labeyrie, A., Mourard, D., "The Optical Very Large Array and its Moon-based Successor," Amplitude and Intensity Spatial Interferometry, Jim B. Breckinridge, Editor, Proc. SPIE 1237, pp. 102-119, 1990.

[22]Labeyrie, A., "Problems in Image Reconstruction With Optical Arrays," see ref. 29.

[23]Labeyrie, A., "Results and Limitations of Ground-Based Optical Arrays," see ref. 29.

[24]Levy, E.H., G.D. Gatewood, R.J. Terrile, "The Astrometric Imaging Telescope: Near-Term Discovery and Study of Other Planetary Systems," Observatories in Earth Orbit and Beyond, 287, Y. Kondo (ed.), Kluwer Acedemic Publishers, 1990.

[25]"Large Lunar Telescope (LLT)," Program Development, NASA Marshall Space Flight Center, 1991.

[26]Lukachko, Stephen P., "LOVLBI, End of Term Report," SEIO, 1992.

[27]McAlister, H.A., et al, "Multiple-telescope Optical Interferometric Array," Amplitude and Intensity Spatial Interferometry, Jim B. Brechinridge, Editor, Proc. SPIE 1237, pp. 22-30, 1990.

[28]Noordam, J.E., P.D. Atherton, A.H. Greenaway, "OASIS: Optical Aperture Synthesis in Space," see ref. 29.

[29]Proceedings of Colloquium on "Kilometric Optical Arrays in Space," Corsica, 1984 (ESA SP-226, April 1985).

[30]Shao, M., Colvita, M.M., "Long-Baseline Optical and Infrared Stellar Interferometry," Annual Review of Astronomy and Astrophysics, vol. 30, Annual Reviews, Inc., Palo Alto, California, 1992, pp. 457-498.

[31]Shao, M., "Lunar Optical Interferometer," Astrophysics From the Moon, Michael J. Mumma and Harlan J. Smith, Editors, AIP Conference Proceedings 207, pp. 486-494, 1990.

[32]Shao, M., "Direct Interferometric Detection of Extra Solar Planets," see ref. 3.

[33]Simonetti, J.H., Calculations in Appendix B, Private Communication.

[34]Smith, Warren J., Modern Optical Engineering: The Design of Optical Systems, Second Edition, McGraw-Hill Inc., New York, 1990.

[35]Stachnik, R.V., D.Y. Gezari, "SAMSI: An Orbiting Spatial Interferometer for Micro-Arcsecond AStronomical Observations," see ref. 29.

[36]Terrile, R.J., "Direct Imaging of Extra-Solar Planetary Systems with the Circumstellar Imaging Telescope (CIT)," AIAA-88-0555, AIAA 26th Aerospace Sciences Meeting, Reno, Nevada, 1988.

[37]Traub, W.A., N.P. Carleton, "COSMIC: A High Resolution, Large Collecting Area Telescope," see ref. 29.

[38]Walker, Gordon, "Astronomical Observation - An Optical Perspective."

[39]Wyman, Charles L., "A Systematic Study of Focal Ratio and Effects of optical misalignment for LST (NASA)." NASA Technical Note (TN/D-7627), Marshall Space Flight Center, May 1974.

[40]"The Naval Research Lab Big Optical Array, An Imaging Interferometer," 1990.

Instrumentation

[41]Abrahams, Tony, National Optical Observatory, Private Communication.

[42]Bely, Pierre Y., ed., Space Astronomical Telescopes and Instrumentation, SPIE-The International Society of Optical Engineering, 1991.

[43]Black, David D., see ref. 4.

[44]"Charge-Coupled Devices," McGraw-Hill Encyclopedia of Science and Technology, vol. 3, 1992, pp. 475-477.

[45]Crawford, David L., ed., Instrumentation in Astronomy VII, SPIE-The International Society of Optical Engineering, Bellingham, WA, 1990, parts 1 and 2.

[46]Duncan, David K., ed., Hubble Space Telescope Goddard High Resolution Spectrograph Instrument Handbook, Version 3.0, Space Telescope Science Institute, 1992.

[47]Griffiths, R.E., "The Development and Applications of Charge-coupled Devices for Space Astronomy", U.S. Government Publication, No. 82-1836.

[48]Humphries, C.M., Instrumentation for Astronomy with Large Optical Telescopes, 1981.

[49]"Infrared Image Devices," McGraw-Hill Encyclopedia of Science and Technology, vol. 9, 1992, pp. 163-165.

[50]"Instrumentation '89: Charge-coupled Devices", Chemical and Engineering News, March 20, 1989, p.36.

[51]Jernhomme, Luc. B., Single-Mode Fiber Optics, Marcel Dekker, Inc, New York, 1983.

[52]Kinney, Anne L., ed., Hubble Space Telescope Faint Object Spectrograph Instrument Handbook, Version 3.0, Space Telescope Science Institute, 1992.

[53]MacKenty, John W., ed., Hubble Space Telescope Wide Field and Planetary Camera Instrument Handbook, Version 3.0, Space Telescope Science Institute, 1992.

[54]"Optical Materials," see ref. 49, pp. 425-429.

[55]Paresce, F., ed., Hubble Space Telescope Faint Object Camera Instrument Handbook, Version 3.0, Space Telescope Science Institute, 1992.

[56]Pearson, A. David, ed., Single-Mode Optical Fibers, SPIE-The International Society of Optical Engineering, Bellingham, Washington, 1983.

[57]Schroeder, Daniel J., Astronomical Optics, Academic Press, Inc., San Diego, CA, 1987.

[58]Van Der Hucht, K.A. and G. Vaiana, eds., New Instrumentation for Space Astronomy, Pergamon Press, 1977.

[59]Woodgate, Bruce E., "Visible and Ultraviolet Detectors for High Earth Orbit and Lunar Observations," NASA Goddard Space Flight Center, Sept. 1989.

Metrology

[60]Arecchi, F.T., E.O. Schulz-Dubois (ed.), Laser Handbook, vol. 2, American Elsevier Publishing Company, Inc., New York, 1972.

[61]Beesley, M.J. Lasers and Their Applications. Taylor & Francis LTD, London, 1971.

[62]Burger, Raymond W. and Thomas C., Electronic Distance Measuring Instruments, Tomlinsin, American Congress on Surveying and Mapping, Falls Church, VA, 1977.

[63]Cutler, Paul H. and Lucas, A.A., Editors, Quantum Metrology and Fundamental Physical Constants, Plenum Press, New York, 1983.

[64]Ealey, Mark A., Editor, Active and Adaptive Optical Systems, Proc. SPIE 1542, 1991.

[65]Elion, Herbert A. Laser Systems and Applications. Pergamon Press, New York, 1967.

[66]Grosman, Michel, and Meyrueis, Patrick, Editors, Optics Applied to Metrology, Proc. SPIE, 136, 1977.

[67]Hecht, Jeff and Teresi, Dick, Laser Supertool of the 1980's, Ticknor & Fields, New York, 1982, pp. 156-157.

[68]Kennie, T.J.M., and G. Petrie, Engineering Survey Technology, John Wiley & Sons, Inc., New York, 1990, pp. 48-82.

[69]"Lasers," McGraw-Hill Encyclopedia of Science & Technology, Vol. 9, 1991.

[70]Massie, N.A., "Absolute distance Interferometry," Interferometric Metrology, Proc. SPIE 816, pp. 149-155, 1987.

[71]Meyers, Robert A., Encyclopedia of Lasers and Optical Technology, Academic Press, Inc., New York, 1991.

[72]Mollennauer, L.F., and White, J.C., Editors, Tunable Lasers, New York, 1987.

[73]Prokhorov, A. M., "US-Russian Streak Cameras Offer Picosecond Resolution," Technology Guide: Electronic Signal-Analysis Equipment, pp. 125-128, 1991.

[74]Shao, M., "The Mark III Interferometer and Its Successors," Smithsonian Astrophysical Observatory.

[75]Steel, W.H., Interferometry, Cambridge University Press, New York, 1983.

[76]Tomlienson, Raymond W., and Thomas C. Burger, Electronic Distance Measuring Systems, American Congress on Surveying and Mapping, Falls Church, VA, 1977.

[77]Young, Matt, Optics and Lasers, Springer-Verlag, New York, 1986.

Pointing Control and Guidance

[78]Chibnik, Michael. "CCD Cameras: Digital Astrophotography is Here." Astronomy, October 1990, pp. 66-73.

[79]Dougherty, H., and others. Space Telescope - Meeting the Pointing Control Challenge With Today's Technology. NASA-32697.

[80]Dougherty, H., and others. Space Telescope Pointing Control System. Paper 80-1784 presented at the AIAA Guidance and Control conference, Danvers, Massachusetts.

[81]Kollsman Instrument Company. Target Acquisition and Positioning Study (TAPS). New York: Kollsman Instrument Company, 1974.

[82]Field, George, and Donald Goldsmith. The Space Telescope. Chicago: Contemporary Books, Inc., 1989.

[83]Geary, John C. "Large-format CCD's for Astronomical Applications," International Conference on Scientific Optical Imaging, M. Bonner Denton (ed.), Proc. SPIE 1439, pp 159-168 (1992).

[84]Melles Griot, "Optics Guide 5," 1990.

[85]Morton, Hudson. Anti-Friction Bearings. 2nd ed. Ann Arbor, Michigan: Hudson T. Morton, 1965.

[86]O'dell, C. R. The Space Telescope Observatory.

[87]Smith, Eric A., ed. Mechanical Drives. England: Morgan-Grampian Publishers Ltd., 1970.

[88]Zlotykamien, Herve. Active Magnetic Bearings. Paper presented at the 7th Cheltenham Bearing Conference, 1986.

Telescope Optics and Structures

[89]Anderson, E.H., D.M. Moore, J.L. Fanson, and M.A. Ealey, "Development of an active truss element for control of precision structures," Optical Engineering, 29(11), 1333-1341 (November 1990).

[90]Burnick, Craig, Inland Motor, Private Communication.

[91]Beer, Ferdinand P. and E. Russel Johnston, Jr., Mechanics of Materials, McGraw-Hill, New York, 1981.

[92]Broutman, Lawrence J. and Richard H. Krock, Composite Materials, vol. 3, Academic Press, New York, 1974.

[93]Chua, Koon Meng, Zehong Yuan, and Stewart W. Johnson, "Foundation Design for a Radio Telescope on the Moon," Engineering, Construction, and Operations in Space, vol. 1, Proc. Space '90, 1990.

[94]Corning ULE[tm] Corning Code 7971 Titanium Silicate Zero Expansion Material

[95]Heiland, K.P., "Recent advancements in passive and active vibration control systems," Vibration Control in Microelectronics, Optics, and Metrology, Proc. SPIE, Vol. 1619, 22-33, (1991).

[96]Huang, Xiaming, Finite Element Computer Model, Private Communication.

[97]Inland Motor, Brushless D.C. Motors and Servo Amplifiers, Kollmorgen Corporation, 1990.

[98]Large Lunar Telescope (LLT), Program Development, NASA George C. Marshall Space Flight Center, March 1991.

[99]Lee, S.M., "Smart Structures", International Encyclopedia of Composites, S.M. Lee, ed., pp. 158-251.

[100]Lee, Stuart M., International Encyclopedia of Composites, vol. 5, VCH Publications, New York, 1990.

[101]Lunar Transit Telescope (LTT), Program Development, NASA George C. Marshall Space Flight Center, January 1992.

[102]Mantell, Charles L., Carbon and Graphite Handbook, Interscience Publishers, New York, 1968.

[103]Marker III, A, J, Fuhromann, H., "Lightweight Large Mirror Blanks of Zerodur," Large Optics Technology, Gregory M. Sanger, Editor, Proc. SPIE 571, 1986.

[104]Nostrand, N., "Graphite Fibers and Composites," Handbook of Composites, G. Lubin, ed., pp. 234-239.

[105]Piggot, Michael R., Load Bearing Fibre Composites, Pergamon Press, New York, 1980.

[106]Podnieks, E. R., "Environmental Considerations for Lunar Base Engineering," Engineering, Construction, and Operations in Space, Proc. Space '88, S. W. Johnson and J. P. Wetzel, eds., 1988.

[107]Roark, Young, Formulas For Stress and Strain, Fifth Edition, 1975.

[108]Sadeh, Willy Z., Stein Sture, and Russel J. Miller (eds.), Engineering, Construction, and Operations in Space III, American Society of Civil Engineers, New York, 1992.

[109]Schmitt, H.H., "Constraints on Lunar Base Construction," Engineering, Construction, and Operations in Space," Proc. SPACE 88, S.W. Johnson and J.P. Wetzel, eds., pp. 35-54.

[110]Smith, pp. 196-201, See Reference 34.

[111]Wilson, D.R., ed., Modern Practice in Servo Design, Pergamon Press, New York, 1970.

[112]Wilson, W.H., "Why So Many Bearing Materials," Selecting Bearings for Economical and Reliable Design, Mechanical Engineering Publications Limited, United States, 1986, pp. 19-30.

Lunar Environment

[113]Andersson, Leif E., and Ewen A. Whitaker, NASA Catalogue of Lunar Nomenclature, NASA Report 1097, 1982.

[114]Briggs, G.A., and F.W. Taylor, The Cambridge Photographic Atlas of the Planets, Cambridge University Press, New York, 1982, pp. 106-107.

[115]Heiken, Grant, David Vaniman, and Bevan M. French, Lunar Sourcebook. A User's Guide to the Moon, Cambride University Press, New York, 1991.

[116]Hess, Wilmot, Donald H. Menzel and John A. O'Keefe, The Nature of the Lunar Surface: Proceeding of the 1965 IAU-NASA Symposium, The Johns Hopkins Press, Baltimore, 1966.

[117]King, Henry C., The World of the Moon, Thomas Y. Crowell Company, New York, 1964, p. 124.

[118]Kopal, Zdenek, An Introduction to the Sudy of the Moon, D. Reidel Pulblishing Company, New York, 1966.

[119]Kopal, Zdenek, and Robert W. Carder, Mapping of the the Moon: Past and Present, D. Reidel Publishing Company, Boston, 1974.

[120]Lowman, Jr., Paul D., Lunar Panorama, Weltfulgbild, Zurich, Switzerland, 1969.

[121]Masursky, Harold, G. W. colton, and Farouk El-Baz, Apollo Over the Moon: A View from Orbit, NASA, Washington, D.C., 1978.

[122]Moore, Patrick, The Moon, Rand McNally & Company, New York, 1981.

[123]Moore, Patrick, Guide to the Moon, Lutterworth Press, London, 1976.

[124]Mutch, Thomas A., Geology of the Moon. A Stratigraphic View, Princeton University Press, Princeton, New Jersey, 1970.

[125]Parkinson, Bob, High Road to the Moon, The British Interplanetary Society, London, 1979.

[126]Rukl, Antonin, Maps of Lunar Hemispheres, D. Reidel Publishing Company, dordrecht, Holland, 1972, Map #3, Vol. 33.

[127]Tatsch, J.H., The Moon: It's Past Development and Present Behavior, Tatsch Associates, Sudbury, Massachussetts, 1974.

[128]Taylor, G. Jeffrey, "Site Selection Criteria," Potential Lunar VLFA Site.

[129]Taylor, Stuart Ross, Lunar Science: A Post-Apollo View, Pergammon Press, Inc., New York, 1975, pp. 28-33.

Thermal Control

[130]See ref. 9.

[131]Haffner, James W. (1967). Nuclear Science and Technology. Academic Press, New York.

[132]Hands, B.A. (1986), Cryogenic Engineering, Academic Press, New York.

[133]Henniger, John H. (1984), Solar Absorptance and Thermal Emittance of Some Common Spacecraft and Thermal-Control Coatings, NASA Reference Publication 1121.

[134]Van Vliet, Robert M. (1965), Passive Temperature Control in the Space Environment, The Macmillan Company, New York.

Power

[135]Bailey, Shelia G. and Geoffrey A. Landis, "Photovoltaic Superiority For Space Station Freedom Power In The 21st Century", 21st IEEE Photovoltaic Speciealists Conference-1990, IEEE Publishing Services, New York, NY. 1990, pp 1356-1361.

[136]Burghart, J. Robert, "Loss Evaluation for Underground Transmission and Distribution Cable Systems," IEEE Transactions on Power Delivery, November 1990, vol. 5, no. 4, pp. 1652-1658.

[137]Colozza, Anthony J., "Award Abstract Self Deploying Photovoltaic Power System", NASA Case No. Lew-15,308-1, NASA Lewis Research Center, 1992.

[138]DiNetta, L. C., Hannon, M. H., Cummings, J. R., McNeely, J. B., and Allen M. Barnett, "AlGaAs Top Solar Cell For Mechanical Attatchment In a Multi-Junction Tandem Concentrator Solar Cell Stack", Proceedings of the 25th Intersociety Energy Conversion Engineering Conference, AIChE, 1990, pp 587-592.

[139]Eaton, J. Robert, Electric Power Transmission System, Prentice-Hall, Inc., New Jersey, 1972.

[140]Gaustad, Krista L., and Lloyd B. Gordon, "Transmission Line Design for the Lunar Environment", 25th Intersociety Energy Conversion Engineering Conference, 1990, Vol. 1, pp. 490-495.

[141]Goldmeer, Jeffrey S., "Power Distribution on the Moon", 25th Intersociety Energy Conversion Engineering Conference, 1990, Vol. 1, pp. 440-445.

[142]Hickman, Mark J, Curtis, Henry B., and Geoffrey A. Landis, "Design Considerations For Lunar Base Photocoltaic Power Systems", 21st IEEE Photovoltaic Speciealists Conferance-1990, IEEE Publishing Services, New York, 1990, pp 1256-61.

[143]Hickman, M. J., and H. S. Bloomfield. "Comparison of Solar Photovoltaic and Nuclear Reactor Power Systems For a Human-Tended Lunar Observatory," NASA Lewis, 1990.

[144]Hord, R. Michael, CRC Handbook of Space Technology: Status and Projections, Florida: CRC Press, Inc., 1985.

[145]Josloff, A. T., et al, "SP-100 Space Reactor Power System Readiness," General Electric Company, 1992.

[146]Keshishian, Vahe, et al, "Space Reactor Shield Technology," AIAA Paper 88-9243, 1988.

[147]King, S.Y. and N.A. Halfter, Underground Power Cables, Longman Group Ltd., New York, 1982.

[148]Linden, David., Handbook of Batteries and Fuel Cells, McGraw-Hill Book Company, Ney York, 1984, p 42-7.

[149]Slifer, Luther W., Jr. "Performance, Size, Mass, and Cost Estimates For 1KW EOL Si, InP and GaAs Arrays", NASA Document N91-19199, 1991.

[150]Smith, John M., et al, "Trade Studies For Nuclear Space Power Systems," NASA Lewis, 1992.

[151]Stephen, J. D., "SP-100 Nuclear Subsystem Design," AIAA Paper 88-9320, 1988.

[152]Upton, H. A., et al, "The Application of SP-100 Technology In a Lunar Surface Power System," AIAA Paper 91-3587, 1991.

[153]Weinberg, I., Swartz, C. K., and D. J. Brinker, "New Directions In InP Solar Cell Research," Proceedings of the 25th Intersociety Energy Conversion Engineering Conference, AIChE, 1990, pp 593-597.

Communications

[154]Brandel, L. Daniel., "NASA'a Advanced Tracking and Data Relay Satellite System for the Years 2000 and Beyond," Proceedings of the IEEE, 1990.

[155]Hastrup, R., A. Weinberg, and R. McOmber, "Evolving Earth-Based and In-Situ Satellite Network Architectures for Mars Communications and Navigation Support," AIAA/NASA/OAI Conference on Advanced SEI Technologies, Cleveland, OH, September 4-6, 1991.

[156]Kitsuregawa, Takashi, Advanced Technology in Satellite Communication Antennas, Electrical & Mechanical Design, Artech House, Boston, 1990.

[157]See ref. 25.

[158]Lo, Martin., "The Application of Lissajous Orbits for the SIRTF Mission," Advances in the Astronautical Sciences, 1991.

[159]Swenson, L. Byron., "Providing Relay Communications Support for the Mars Environmental Survey (MESUR) Mission," Advances in the Satronautical Sciences, 1991.

[160]Wertze., Space Mission, Proceedings of the IEEE, 1984.

[161]Yuen, H. Joseph. Deep Space Telecommunications System Engineering, JPL Publication 82-76, 1982.

Launch, Construction, & Cost

[162]"Atlas/Centaur Fact Sheet," General Dynamics Space Systems Division, Public Affairs, 1992.

[163]Furnas, Randall B., "Space Logistics: Launch Capabilities," see referance 3.

[164]Krause, Robert B., United States Launch Vehicle Systems, Kluwer Academic Publishers, Netherlands, 1990.

[165]Lenorovitz, Jeffrey M., "GD Goal: Lower-Cost Manned Lunar Missions," Aviation Week & Space Technology, January 18, 1993.

[166]McMahon, Leonard A., Heavy Construction Cost Guide 1991, Annual Edition No. 3, 1990.